Dynamical complexity and model reduction of driven quantum systems

Michiel Burgelman

PSL UNIVERSITÉ PARIS

THÈSE DE DOCTORAT

DE L'UNIVERSITÉ PSL

Préparée à MINES ParisTech

Complexité dynamique et réduction de modèle de systèmes quantiques forcés

Dynamical complexity and model reduction of driven quantum systems

Soutenue par

Michiel BURGELMAN

Le 1 juillet 2022

École doctorale n°621

Ingénierie des Systèmes, Matériaux, Mécanique, Énergétique

Spécialité

Mathématique et automatique

Composition du jury :

Michel DEVORET Professeur, Yale University	*Président*
Anja METELMANN Professeur, Karlsruher Institut für Technologie	*Rapporteur*
Bernhard MASCHKE Professeur, Université Claude Bernard Lyon 1	*Rapporteur*
Jacques FÉJOZ Professeur, Université Paris Dauphine - PSL	*Examinateur*
Alain SARLETTE Chargé de Recherche, INRIA Paris	*Co-directeur de thèse*
Pierre ROUCHON Professeur, Mines ParisTech - PSL	*Directeur de thèse*

MINES ParisTech | PSL

Acknowledgements

I am indebted to many people, without whom this work would not have been possible. First and foremost, I want to thank my advisors Mazyar Mirrahimi, Alain Sarlette and Pierre Rouchon for their passionate and excellent scientific guidance, and their constant support throughout. I would like to warmly thank Mazyar for the opportunities he gave me to get acquainted with the international scientific community, often alongside him, which helped me to grow as a scientist. Alain, thank you for introducing me to the research of the team, and through a tremendous amount of your time and patience, to research in general. Lastly, I must thank Pierre, whose experience made for a mathematical jump-start of the project, and made sure all was on track when wrapping up.

I owe my gratitude to a great number of people for important insights and discussions, the following of which I must thank in particular: Jacques Féjoz, Abed Bounemoura, Michel Devoret, Jayameenakshi Venkatraman, Xu Xiao, Cyril Elouard, Alexandru Petrescu, Benjamin Huard, Simon Apers, Christian Siegele and Paolo Forni. I would like to thank Michel Devoret for hosting me in his group for three months. Exchanging with Jayameenakshi Venkatraman and Xu Xiao helped shape part I of this manuscript early on, and discussions with experimentalists and all of the scientific activity at the Yale Quantum Institute were very enriching experiences for me.

I have been blessed with a fertile scientific environment at the Quantic team, in close connection with experimental research led by Zaki Leghtas and Philippe Campagne-Ibarcq, and with theoretical expertise brought by Antoine Tilloy and Alexandru Petrescu. I would like to thank all for their valuable input, and complementary points of view.

Thank you Paolo, Lucas and Gerardo for giving me a warm welcome in the team. There is a wonderful ambiance in the team, and the daily office life was more amicable than I could wish for. I would like to thank Louis, Mathys, Masaaki, Ronan, Lev-Arcady, François-Marie, Jérémie, Vincent, Christian, Fred, Derya and many others for the good times, many memorable moments, and for their support. A special thanks goes to Christian, who was there during also the most isolated of covid times.

Finally, I want to thank my parents, my brothers and Natalie for their never-wavering support throughout these past few years.

Contents

Chapter 1

Introduction (version française)

Au cours des dernières décennies, des ingénieurs, des physiciens et des mathématiciens ont travaillé ensemble à la réalisation de dispositifs de calcul quantique opérationnels. [39, 102]. Ces dispositifs utilisent une méthode de stockage et de manipulation de l'information fondamentalement différente de celle des ordinateurs classiques, car l'information est codée dans l'état quantique du système lui-même. Le bit quantique, ou qubit, est l'unité indivisible de l'information quantique, par analogie avec un bit classique. Cette information intrinsèquement quantique, associée à la possibilité d'effectuer des opérations logiques appelées "portes quantiques", permettrait de créer une toute nouvelle famille d'algorithmes qui ne peuvent être exécutés que sur des systèmes quantiques et qui surpassent largement la performance de tous les algorithmes classiques connus pour certains problèmes [3, 56, 118]. De cette façon, le matériel quantique opérationnel pourrait améliorer les systèmes de cryptage modernes [10], rechercher une liste non triée quadratiquement plus vite [56] (étant donné un oracle quantique fournissant les données), et peut-être plus important encore, simuler les systèmes mécaniques quantiques eux-mêmes beaucoup plus rapidement [116]. L'obstacle majeur à la réalisation de cet objectif est la fragilité des états de superposition complexes nécessaires pour effectuer les calculs. En raison des interactions inévitables du dispositif quantique avec son environnement, une partie de l'information codée dans son état quantique sera irrévocablement perdue. Ce processus de décohérence [133] peut être décrit par un processus de bruit stochastique au sens mathématique, et il est la source la plus importante d'erreurs physiques dans les dispositifs quantiques. Puisque les informations quantiques doivent être protégées de la corruption afin de bénéficier d'un avantage de l'informatique quantique, l'objectif principal d'un ordinateur quantique est de réaliser un nombre souhaité de portes quantiques pendant la durée de vie du système. Pour atteindre cet objectif dans un modèle de circuit pour le calcul quantique, plusieurs aspects doivent être pris en compte, comme par exemple la réduction du bruit intrinsèque au matériel physique, les techniques de correction d'erreurs quantiques qui utilisent un encodage redondant de l'information, et des implémentations physiques plus rapides des portes quantiques.

Cette thèse s'inscrit dans le contexte général de la protection contre le bruit physique au niveau du matériel et au niveau du contrôle, en se concentrant sur deux approches différentes et complémentaires : Les codages bosoniques dans des états de chat de Schrodinger [92] utilisant des circuits supraconducteurs d'une part, et le découplage dynamique (DD) [129] d'autre part. Dans les deux contextes, nous réalisons une étude théorique des systèmes dynamiques pour caractériser les performances et les régimes de fonctionnement possibles de l'approche. Une

base de calcul composée d'état de chat est un schéma prometteur pour la correction d'erreur quantique bosonique tolérante aux fautes [58, 103], avec un seuil d'erreur et une surcharge matérielle favorables [59], et pour créer de tels états, l'on pilote des éléments non linéaires à base de jonctions Josephson [55, 80]. Le DD est une méthode dynamique qui élimine les interactions indésirables entre le système et son environnement en appliquant au système cible que l'on souhaite protéger des opérations de contrôle cohérentes à variation rapide, afin d'annuler efficacement son couplage Hamiltonien avec l'environnement. Le dénominateur commun de ces deux approches contre le bruit, dont chacune sera présentée plus en détail ci-après, est que l'on applique des signaux de pompe au système pour obtenir le régime de fonctionnement souhaité. Les dispositifs quantiques étant par nature des systèmes ouverts, ces domaines d'application impliquent la difficulté générale d'analyser des *systèmes quantiques ouverts pilotés*. Un axe parallèle de cette thèse est de rechercher des méthodes d'analyse améliorées pour cette classe de systèmes.

Le régime de fonctionnement souhaitable des systèmes quantiques ouverts pilotés ne peut généralement être compris qu'en termes d'un modèle réduit, obtenu après avoir éliminé les degrés de liberté rapides de la description, afin de conserver une description efficace de l'évolution du système à l'échelle de l' intervalle de temps d'intérêt. Ces degrés de liberté rapides peuvent impliquer la fréquence du pilotage, mais aussi la décroissance rapide des degrés de liberté dissipatifs. Dans un premier temps, pour les systèmes sans perte (dits "high-Q"), les termes de pilotage à oscillation rapide peuvent être éliminés par des *méthodes de moyennisation*, qui sont particulièrement bien établies dans le cas Hamiltonien [15, 34, 88, 91, 125]. Cependant, le domaine de validité des modèles réduits obtenus est souvent peu clair, et pour le cas des oscillateurs anharmoniques quantiques pilotés employés dans les circuits supraconducteurs, cette thèse établit une limite fondamentale à la réduction des modèles, en étudiant la dynamique chaotique des jonctions. En même temps, nous fournissons une recette pour choisir les paramètres du circuit afin d'éviter ce comportement chaotique préjudiciable. Cette étude, objet de la partie I, se situe donc dans le contexte des limitations d'excitation forte des expériments actuels sur les circuits supraconducteurs. Le contexte de ce domaine de recherche est à nouveau résumé au début de la partie I.

Afin d' éliminer rapidement les degrés de liberté dissipatifs, les techniques d'*élimination adiabatique* [5, 6, 66] fournissent une méthode de réduction systématique des modèles, en profitant de cette séparation des échelles de temps dissipatives. Cette technique étant relativement nouvelle, de nombreuses questions restent ouvertes par rapport aux échelles de temps qui peuvent être éliminées, et par rapport à quels degrés de liberté il faut éliminer afin d' arriver à un modèle réduit qui est physiquement interprétable, par exemple de forme Lindblad [51, 83]. Cette thèse apporte deux contributions à ce domaine, en fournissant une extension à la méthode de pilotage périodique, et une extension aux degrés de liberté plus généraux à éliminer. Ces deux extensions sont directement applicables dans le contexte de le DD, et ouvrent la possibilité d'appliquer la méthodologie de le DD d'une façon nouvelle : nous proposons de piloter un sous-système de l'environnement de manière à le découpler du système cible, chaque fois que le premier peut être facilement identifié et représente la principale source de bruit pour la cible. Cette approche de découplage côté environnement présente l'avantage immédiat que les actions imprécises ne détériorent pas directement le système cible. A notre connaissance, cette stratégie n'a pas été envisagée avant, et nous l'avons étudiéee en détail pour le cas d'un environnement de système à deux niveaux (TLS), obtenant ainsi des expressions explicites pour les vitesses de décohérence induits du système cible. Ce travail fait l'objet de la partie II de la thèse.

Le reste de cette section est organisé comme suit. Tout d'abord - après un bref intermezzo sur la correction d'erreur quantique basée sur les codes correcteurs - une introduction aux codages bosoniques et au DD est fournie, comme complément à ces stratégies contre le bruit au niveau physique. Ensuite, nous exposons le contexte des problèmes qui sont abordés dans cette dissertation. Dans la Section 1.2, nous nous concentrons sur les circuits supraconducteurs et le problème de la dynamique chaotique sous pilotage fort. Dans la Section 1.3, nous détaillons les défis que pose une approche de découplage côté environnement. Enfin, nous résumons les contributions de cette thèse dans la section 1.4, et le plan du manuscrit dans la section 1.5.

1.1 Contre le bruit

Les techniques de correction quantique des erreurs (CEQ) [44, 52, 123] consistent à coder de manière redondante le même qubit d'information logique dans un système physique plus grand. Ce système physique plus vaste peut être un réseau de qubits physiques bien connectés. La redondance permet de mesurer plusieurs syndromes d'erreur différents, en mesurant différents sous-systèmes physiques. Si les différents enregistrements de mesure donnent un résultat contradictoire, nous savons qu'une erreur physique a dû se produire dans un sous-système. Si les erreurs individuelles ne sont pas trop nombreuses, alors nous pouvons déduire de l'enregistrement des mesures quelle erreur est la plus probable et nous pouvons la corriger. Toutefois, dans le cas de nombreuses erreurs individuelles, le qubit logique peut être corrompu de manière irréversible, ce qui entraîne une erreur logique. Dans l'hypothèse de bruit local et non corrélé, il a été démontré que la probabilité qu'une erreur logique se produise peut être rendue arbitrairement petite en augmentant le nombre de sous-systèmes matériels physiques dans lesquels l'information est codée, à condition que la probabilité d'erreur physique de chaque composant soit inférieure à un certain seuil de probabilité d'erreur, et à condition que les erreurs produites par l'application de portes logiques imparfaites manipulant l'information soient également inférieures à un seuil similaire. Cette propriété est appelée *tolérance aux défauts* [1, 72]. La redondance requise augmente avec la probabilité d'erreur logique souhaitée, tandis qu'elle diminue en fonction de combien la probabilité d'erreur physique est inférieure au seuil d'erreur physique. De cette manière, la caractéristique de tolérance aux erreurs permet d'effectuer de manière fiable des calculs arbitrairement longs, à condition de disposer d'une réserve matérielle suffisante pour y encoder les informations. La difficulté principale est que les qubits peuvent subir un continuum d'erreurs quantiques, qui sont typiquement décomposées par le codage en deux types fondamentaux : les erreurs de renversement de bit et les erreurs de renversement de phase, respectivement. Le concept d'erreur de calcul par renversement de phase est un concept inhérent à la mécanique quantique et ne s'applique pas aux ordinateurs classiques. Puisque la CEQ doit corriger les deux types d'erreurs, le seuil d'erreur physique des codes quantiques (s'il existe) peut être plutôt bas (pensez à 1%), et en plus de la surcharge matérielle peut être beaucoup plus défavorable que pour les codes classiques, rendant de nombreux schémas CEQ irréalistes d'un point de vue pratique. La présente thèse explore les méthodes de réduction des erreurs *au niveau physique* qui peuvent compléter, et faciliter la tâche des approches de correction d'erreurs quantiques par code correcteur.

Une première approche qui vise à alléger ce problème de surcharge matérielle est ce qu'on appelle les *codes bosoniques*, qui visent à établir une première protection de l'information quantique au niveau physique, soit pour les deux types d'erreurs, comme pour les codes GKP [21, 53], soit pour un seul type d'erreur, comme pour les codes chat de Schrödinger [92].

Dans les deux cas, le dimensionnement de la surcharge matérielle nécessaire à la CEQ est drastiquement réduite. Afin de réaliser cette protection au niveau physique, l'espace d'état de dimension infinie d'un oscillateur harmonique quantique est utilisé, fournissant une redondance naturelle pour le codage. Une classe importante de codes bosoniques, étudiée dans cette thèse, est donnée par les états de chat de Schrödinger [78, 92], à savoir les superpositions de deux amplitudes classiques cohérentes d'un champ bosonique. L'avantage des codes de chat provient du fait qu'un qubit de chat bénéficie d'un biais de bruit : le taux d'erreur de renversement de bit est plus petit que le taux d'erreur de renversement de phase par un facteur qui varie exponentiellement avec la taille du chat, défini comme l'amplitude du champ bosonique correspondant aux états cohérents susmentionnés. En utilisant ce biais de bruit, un schéma de CEQ préservant le biais a été développé qui passe à l'échelle beaucoup plus favorablement [58, 103] en termes de surcoût matériel que les schémas pour des codes plus traditionnels composés de qubits physiques ordinaires. La manière dont les états du chat sont stabilisés dépend de la plate-forme physique, mais implique généralement un couplage de l'oscillateur harmonique à un élément non linéaire qui est également soumis à des signaux d'excitation [80]. En effet, il a été démontré qu'il était impossible de créer de tels états non-classiques en utilisant uniquement des systèmes linéaires, alors qu'il est connu que les états quantiques des systèmes purement linéaires ne présentent aucun avantage par rapport à un ordinateur classique [85]. En résumé, une base de calcul d'états de chats est un schéma très prometteur pour la correction d'erreur quantique bosonique tolérante aux fautes, avec un seuil d'erreur et une surcharge matérielle favorables, et pour créer de tels états, il faut forcer des éléments non-linéairs.

Dans cette thèse nous étudions une deuxième approche pour atténuer directement au niveau physique les erreurs: le Découplage Dynamique (DD) [129]. Il s'agit d'une méthode dynamique qui filtre les interactions indésirables entre le système et l'environnement en appliquant des opérations de contrôle cohérentes et à variation rapide au système cible que l'on souhaite contrôler, afin d'annuler efficacement son couplage Hamiltonien avec l'environnement. La validité de cette approche repose sur une séparation temporelle entre les impulsions de contrôle appliquées et le taux de couplage avec l'environnement. En permettant des opérations de contrôle arbitrairement fortes et arbitrairement rapides, le DD a la capacité de rendre le taux de décohérence effectif du système cible arbitrairement petit, en supposant que les processus de bruit qui doivent être découplés présentent une fréquence de coupure finie. En pratique, les stratégies de DD doivent être envisagées dans le cadre d'hypothèses de contrôle réalistes, en utilisant des ressources de contrôle finies. Un tel cadre a conduit à l'établissement de schémas de DD qui utilisent ces ressources de manière optimale [76, 104]. Contrairement aux codages bosoniques, les techniques de DD ont été essentiellement établies pour les systèmes de basse dimensionnalité en agissant directement au niveau d'un seul qubit physique stockant l'information, alors que les codages bosoniques exploitent intrinsèquement un espace d'états à dimension infinie. Tout comme pour les codages bosoniques, les stratégies de DD peuvent être combinées avec la correction quantique des erreurs [99, 127], et elles peuvent également fournir une protection lors de l'exécution de portes logiques [68, 69].

Les deux sections suivantes présentent les contextes physiques spécifiques dans lesquels nous proposons de poursuivre les codages bosoniques, resp. les DD, et les défis à surmonter. Pour les codages bosoniques, il s'agira de la plate-forme matérielle quantique des circuits supraconducteurs, où la non-linéarité sans perte fournie par la jonction Josephson est centrale. En revanche, pour la stratégie de découplage dynamique, au lieu de nous limiter à une seule plate-forme matérielle nous considérons une classe générale de systèmes quantiques ouverts,

présentant des sous-systèmes et des séparations d'échelle de temps bien définis. Dans ce cadre, nous proposons une nouvelle stratégie pour contrer le bruit, qui va de pair avec les techniques de réduction de modèle que le cadre physique exige. Les contributions scientifiques résultant de ces deux approches sont ensuite résumées dans la Section 1.4.

1.2 Circuits supraconducteurs pilotés

Une plateforme physique de premier plan pour la construction de dispositifs de calcul quantique est celle des circuits supraconducteurs [97], car ils ont fait des progrès significatifs en matière de préparation d'état et de fonctionnement de porte fiables, ainsi que de temps de cohérence plus longs [14, 71]. Les circuits supraconducteurs sont des circuits électriques qui sont refroidis jusqu'à quelques dizaines de mK et qui se couplent fortement aux photons micro-ondes. A ces températures extrêmement basses, toutes les observables physiques obéissent aux équations de mouvement de la mécanique quantique. Des éléments non linéaires sans perte sont introduits dans les circuits, qui sont utilisés soit pour stocker et manipuler l'information quantique elle-même dans deux de leurs niveaux d'énergie, soit pour servir de médiateur aux interactions entre les résonateurs micro-ondes qui stockent l'information dans des modes bosoniques. L'élément non linéaire par excellence est une jonction Josephson [64], constituée de deux électrodes supraconductrices séparées par une barrière isolante. Il est possible de créer différents types d'interactions entre les différents modes en les pilotant avec des champs micro-ondes simples ou en modulant un paramètre du circuit. Cette ingénierie paramétrique des interactions est un sujet clé de la recherche, et de nouveaux types d'interactions sont continuellement développés, que ce soit dans le but de créer une interaction ou une porte logique plus exotique [29, 89], ou dans le but de stabiliser un état quantique désiré [79, 117]. De cette façon, la stabilisation par réservoir des états quantiques chat de Schrödinger du rayonnement micro-onde a été réalisée [80].

D'autre part, la thématique générale d'oscillateurs non linéaires pilotés entre dans le domaine des systèmes possiblement chaotiques, comme l'ont découvert les pionniers van der Pol [124] et Duffing [33]. Ces phénomènes chaotiques ont été largement étudiés pour les circuits Josephson dans le régime classique, notamment dans les années 80. Un grand *accroissement du bruit* a été observé pour les amplificateurs paramétriques à base de Josephson [26, 122]. On savait que ce phénomène n'était pas dû à des fluctuations thermiques, mais l'origine exacte de cette augmentation soudaine du bruit restait incertaine. Ceci jusqu'à ce que Huberman, Crutchfield et Packard l' ont attribuée purement à une propriété des équations *classiques*non linéaires complètes du mouvement : le chaos [62]. Le bruit était dû à une dynamique de jonction chaotique, mais néanmoins déterministe. Pour une jonction simple, qui est équivalente à un simple pendule piloté, des voies de doublement de période vers le chaos ont été observées et étudiées dans [32]. En effet, il est bien connu qu'un pendule piloté périodiquement peut avoir un comportement chaotique. Pour un modèle de jonction shuntée piloté par un courant, [62] et [107, 108] ont trouvé un comportement simple et périodique avec le pilotage, mais aussi un comportement subharmonique compliqué, et des cascades de doublement de période dans un régime chaotique lorsque l'amplitude du pilotage est augmentée.

La technologie de la jonction Josephson ayant évolué (elle est par exemple entrée dans le régime quantique et dans la gamme de fréquences des micro-ondes), ces résultats ont apparemment été mis de côté. Récemment aussi, dans le régime quantique, les limitations expérimentales ont été attribuées à un comportement dynamique mal compris [81, 110]. Un

effort pour résoudre ce problème consiste à développer des théories de perturbation raffinées, obtenir des modèles réduits d'ordre supérieur de la dynamique plus précis [100, 101, 110]. Un deuxième effort a été de modifier la conception du circuit afin de le rendre plus robuste par rapport aux instabilités dynamiques. Notamment, l'ajout d'un shunt inductif au transmon traditionnel [73] a rendu le circuit plus stable sous un pompage paramétrique fort [126]. Dans la partie I, nous montrons comment ce transmon à shunt inductif peut être réglé pour être résistant au comportement nuisible qui, par définition, ne peut être capturé par aucun modèle réduit intégrable : le chaos classique. Ce régime chaotique peut être supprimé alors que le dispositif conserve la capacité de confiner une classe d'états non classiques utiles pour la CEQ bosonique, à savoir les états de chat de Schrödinger.

1.3 Approche de découplage activée sur l'environnement

L'idée du découplage dynamique quantique est de réduire le couplage effectif entre un système cible et son environnement, en utilisant des actions de contrôle sur le système cible, adaptées à une échelle de temps plus rapide que le couplage Hamiltonien avec l'environnement. La validité de cette approche dépend crucialement de la manière dont cet environnement peut être modélisé. En effet, pour un processus de décohérence purement markovien, correspondant au cas d'un environnement sans mémoire, on ne peut s'attendre à pouvoir découpler la cible en utilisant des actions de contrôle. Lorsqu'on modélise une grande partie pertinente de l'environnement comme un seul (peut-être très grand) système Hamiltonien, il a été démontré que le DD est valide dans des conditions très générales [129]. Dans ce cas, on peut prouver que le couplage effectif peut être rendu arbitrairement petit dans la limite théorique de contrôles arbitrairement forts et arbitrairement rapides. Ceci est typiquement prouvé en utilisant une méthode d'analyse telle que l'expansion de Magnus [16, 88] ou une technique équivalente de moyenne Hamiltonienne [35].

Plusieurs réalisations expérimentales pour le matériel quantique rencontrent une situation intermédiaire pour l'environnement pertinent. Ici, la cible est directement couplée à un système de dimension finie, bien identifié, qui agit comme la principale source de décohérence induite sur la cible. Ce *sous-système* environnemental est ensuite couplé à un bain environnemental qui n'est pas directement couplé à la cible. Un exemple immédiat de tels sous-systèmes environnementaux sont les défauts de système à deux niveaux (TLS) dans la couche d'oxyde des jonctions Josephson supraconductrices, qui décohèrent typiquement par des canaux de phonons et sont un mécanisme principal induisant la décohérence des qubits supraconducteurs [84, 95].

En partant de cette observation, nous proposons d'appliquer la méthodologie DD de la manière suivante : appliquer des actions *sur l'environnement*, de manière à réduire la décohérence induite sur le système cible. Un avantage potentiel de l'application de ces actions au sous-système environnement est une tolérance accrue par rapport aux actions imprécises. En effet, les méthodes de DD qui agissent avec des impulsions de contrôle directement sur le système cible doivent être particulièrement précises, et toute imprécision de contrôle détériore directement l'information quantique stockée dans la cible.

Un deuxième avantage potentiel du découplage côté environnement est que les actions sont compatibles avec toutes les portes logiques que l'on pourrait vouloir exécuter sur le système cible. Bien que des schémas de DD qui assurent de la protection pendant l'exécution de portes logiques aient été développés [70], ils présentent l'inconvénient d'augmenter les ressources,

comme la complexité des signaux de contrôle. En contrepartie, on ne peut évidemment espérer agir sur l'environnement que si celui-ci est bien identifié et de dimension raisonnablement réduite.

Il y a deux points principaux sur lesquels la méthodologie DD doit être étendue pour établir la performance de l'activation par l'environnement. Tout d'abord, comme les pilotages de découplage sont appliquées sur un sous-système d'environnement *avec pertes rapides*, cela nécessite de nouvelles méthodes d'analyse pour caractériser les performances de le DD de cette approche, car les performances de le DD sont traditionnellement étudiées à l'aide de techniques de calcul de moyenne dans un cadre purement Hamiltonien. La technique générale de réduction de modèle pour éliminer les degrés de liberté *dissipatifs* tels que le sous-système environnement avec perte est l'élimination adiabatique [5, 6, 66]. Un premier défi est d'étendre cette technique au cas de pilotage périodique, car jusqu'à présent la technique n'avait été développée que pour des systèmes stationnaires. Notre approche axée sur l'environnement présente un deuxième défi. Alors que le fait d'agir sur l'environnement offre la sécurité de ne pas détériorer l'état cible directement en cas d'imprécision du contrôle, nous ne pouvons pas non plus nous attendre à contrôler un système d'environnement d'une manière bien calibrée. Nous ne pouvons pas non plus espérer d' avoir une connaissance précise de l'Hamiltonien de l'environnement. La partie II de cette thèse détaille comment ces deux problèmes généraux peuvent être résolus, fournissant une nouvelle stratégie pour contrer le bruit dans les dispositifs quantiques pratiques.

1.4 Contributions

- Premièrement, nous fournissons une recette pour choisir les paramètres de circuit des dispositifs supraconducteurs quantiques afin d'éviter un comportement chaotique préjudiciable, tout en bénéficiant d'un régime fortement non linéaire du dispositif. Nous illustrons ce potentiel fortement non linéaire en confinant de manière robuste une classe d'états hautement non classiques, connus sous le nom d'états chats de Schrödinger. Ces états chats ont des applications immédiates dans le domaine des codages bosoniques, qui ont montré qu'ils permettaient une correction des erreurs quantiques efficace sur le plan matériel. L'ensemble de ces résultats permet de préciser l'extension des régimes de fonctionnement des circuits supraconducteurs.

- Une deuxième contribution réside dans la méthodologie générale développée pour analyser l'avènement et l'effet de la dynamique chaotique dans le contexte de tels systèmes quantiques "high-Q" pilotés périodiquement. Pour ce faire, nous établissons une connexion entre l'application Poincaré classique et la décomposition de Floquet du système. En utilisant des techniques analytiques sur le système classique, nous fournissons un résultat bloquant la route principale vers le chaos du système pour des paramètres du circuit bien choisis. De plus, nous caractérisons les différents régimes de fonctionnement non linéaires une fois que le dispositif est dans le régime régulier, non chaotique, par des techniques de réduction de modèle basées sur la théorie de la moyenne géométrique. A notre connaissance, une telle analyse de moyenne n'a pas été réalisée précédemment en tenant compte du potentiel cosinus de Josephson complet, et devrait fournir des résultats plus précis vers le réglage des dispositifs pratiques.

Ce travail est en finalisation pour être soumis à Physical Review Letters.

- Troisièmement, nous proposons une nouvelle stratégie pour contrer le bruit sur une classe pratique de dispositifs quantiques cibles qui est intrinsèquement robuste et efficace sur le plan matériel. La méthodologie DD existante fournit des techniques pour découpler une cible d'un environnement en agissant sur le système cible avec des opérations de contrôle fortes et précises. Nous avons étendu cette méthode au cas où l'on actionne le sous-système d'environnement lui-même pour le découpler de la cible. Les performances d'une telle approche sont évaluées pour le cas d'un environnement à deux niveaux (TLS), et analysées dans un cadre de théorie des systèmes, du modèle à la figure de mérite principale, à savoir le taux de décohérence induit du système cible. Le type de pilotage côté environnement pour lequel nous avons prouvé l'efficacité de l'approche comprend des pilotages périodiques cohérents d'une part, et la limite du pilotage avec du bruit pur d'autre part, où les actions ajoutées correspondent à des canaux de dissipation ajoutés à l'environnement, établissant une nouvelle variante dissipative de le DD. L'étude d'optimisation qui en résulte conduit à une conclusion physique générale qui est d'une pertinence immédiate pour les scénarios expérimentaux typiques : peut-être contre-intuitivement, isoler l'environnement des sources de bruit autant que possible n'est souvent pas le meilleur plan d'action.

- Une dernière contribution réside dans les méthodes d'analyse développées pour cette approche de découplage côté environnement, qui établissent une connexion entre le domaine de la réduction de modèle pour les systèmes quantiques ouverts dissipatifs et le problème de contrôle du découplage dynamique. Nous avons développé une extension de la méthode d'élimination adiabatique pour inclure le pilotage périodique, permettant d'analyser les avantages du DD pour le premier type de pilotage côté environnement, qui a été choisi pour être périodique. De plus, la méthode d'élimination adiabatique a également été étendue à l'élimination des dégrés de liberté plus généraux, dans le contexte de la variante dissipative du découplage dynamique.

Ces deux dernières contributions constituent des travaux [20] soumis au Journal du Franklin institute.

1.5 Présentation du manuscrit

Dans la partie I de cette thèse, nous fournissons une recette pour obtenir un régime subharmonique robuste d'oscillateurs quantiques non linéaires pilotés, correspondant au confinement d'un ensemble d'états de chat de Schrödinger.

- Dans le chapitre 3, nous commençons par présenter le modèle du transmon piloté périodiquement et shunté par induction. Nous examinons comment ce système monomode combine les trois éléments de base des circuits supraconducteurs, ce qui le rend prototypique. Plus précisément, nous effectuons un changement de variables global qui transforme le système en une forme normale qui sera utilisée tout au long de cette partie. Cela permet d'identifier quatre paramètres principaux dont nous discutons brièvement les rôles. Il s'agit de deux paramètres de circuit effectifs appelés le *paramètre de régularité* et le *paramètre d'échelle quantique*, ainsi que des versions renormalisées des paramètres de pilotage. Une fois que cette forme normale du système est établie, dans la Section 3.2, des éléments d'introduction sur les méthodes générales d'analyse des systèmes à pilotage périodique sont fournis. Pour les systèmes périodiques classiques, les

concepts pertinents de la théorie des systèmes dynamiques sont introduits, notamment la carte de Poincaré, ainsi que la notation qui sera utilisée dans les chapitres suivants de cette partie. Du côté quantique, une introduction à la théorie de Floquet est donnée, y compris son extension aux systèmes (quantiques ouverts) interagissant faiblement avec un bain environnemental. Enfin, les méthodes numériques que nous avons utilisées pour simuler le système sont résumées.

- Dans le chapitre 4, nous utilisons le langage de la théorie de Floquet pour établir un régime subharmonique robuste et non chaotique du transmon piloté par induction et shunté. Après une brève introduction sur les qubits cat, nous établissons une connexion entre la carte de Poincaré du système classique d'une part, et les modes de Floquet du système quantique d'autre part, en assimilant les solutions classiques sous-harmoniques stables à l'existence d'un ensemble dégénéré de modes de Floquet de chat de Schrödinger. En nous concentrant sur une classe de sous-harmoniques donnée, nous caractérisons les signatures quantiques du chaos classique qui s'installe lorsque l'on augmente l'amplitude de forçage. Nous observons un régime asymptotique hautement entropique pour le système quantique dans ce cas chaotique. Ensuite, nous montrons comment choisir les paramètres du circuit de manière à supprimer efficacement ce régime hautement entropique, en abaissant le paramètre de régularité. Nous proposons une explication théorique pour ceci en montrant que les voies possibles vers le chaos du système classique sont supprimés pour des petites valeurs du paramètre de régularité. Enfin, nous montrons que dans le régime non chaotique, le paramètre de d'échelle quantique peut être réglé indépendamment pour augmenter le taux de confinement de la variété invariante sous-tendue par des chats de Schrödinger, fournissant un régime régulier fortement non-linéaire.

- Dans le chapitre 5, nous nous concentrons sur la dépendance du système aux paramètres de pilotage, afin de caractériser les conditions de résonance qui mènent à des solutions sous-harmoniques stables du système classique, en utilisant un modèle moyenné du premier ordre. Après une brève introduction sur la théorie de la moyennisation géométrique, nous obtenons un modèle réduit qui élimine la dépendance du temps. Nous discutons des symétries globales du modèle résultant, ainsi que des cas limites, et fournissons un compte rendu numérique d'une classe particulière de solutions sous-harmoniques prédites par le modèle.

Dans la partie II, nous proposons une nouvelle approche pour contrer le bruit pour les systèmes quantiques pratiques basée sur la méthodologie du découplage dynamique.

- Dans le chapitre 6 nous montrons comment le découplage dynamique côté environnement peut être réalisé en pilotant continuellement l'environnement avec un seul pilotage à fréquence unique. Après avoir passé en revue les travaux pertinents dans le domaine des approches de DD à pilotage continu, nous introduisons un pilotage DD qui présente une double séparation temporelle et qui atténue efficacement les imprécisions de contrôle actuelles. Ensuite, nous étendons la technique de réduction de modèle de l'élimination adiabatique au cas du pilotage périodique, afin d'obtenir des formules explicites pour la décohérence induite sur le système cible sous cet actionnement périodique de l'environnement. Nous discutons l'efficacité du découplage en termes de dépendance du taux de décohérence induit aux d'actionnement, et nous concluons en analysant la

limite où la force des actions DD devient comparable à la fréquence du TLS, confirmant à nouveau les avantages de le DD.

- Dans le chapitre 7, nous étendons la stratégie de découplage côté environnement à la limite des pilotages désorganisés, en les considérant comme des canaux de dissipation supplémentaires sur l'environnement. Nous commençons par réviser les formules d'élimination adiabatique d'ordre supérieur qui décrivent la décohérence induite sur la cible. En cherchant à minimiser la décohérence induite sur la cible, nous mettons en évidence les caractéristiques générales du problème d'optimisation résultant pour les taux de dissipation sur l'environnement. Une étude de cas pour le cas d'un environnement TLS est fournie, y compris la limite d'un environnement partiellement décohérent, qui ne perd qu'une partie de ses cohérences.

Les deux parties peuvent être lues indépendamment. Une conclusion dans la Partie III donne un aperçu des questions ouvertes et des travaux futurs possibles.

Chapter 2

Introduction

Over the last few decades, engineers, physicists and mathematicians have been working together towards the realization of operational quantum computational devices [39, 102]. These devices make use of a fundamentally different way of storing and manipulating information as compared to conventional classical computers, as information is encoded in the quantum state of the system itself. The quantum bit, or qubit, is the indivisible unit of quantum information, in analogy with a classical bit. This inherently quantum-like information, together with the ability to perform logical operations called quantum gates, would enable a whole new family of algorithms that can only be run on quantum hardware, and that outperform any known classical algorithm for certain problems [3, 56, 118]. In this way, operational quantum hardware could improve on modern encryption systems [10], search an unsorted list quadratically faster [56] (given a quantum oracle providing the data), and perhaps most importantly simulate quantum mechanical systems themselves much faster [116]. The major obstacle towards achieving this goal is the fragility of the intricate superposition states required to perform the computations. Due to inevitable interactions of the quantum device with its environment, some of the information encoded in its quantum state will be irrevocably lost. This decoherence process [133] can be described by a noise process in the mathematical sense, and it is the most prominent source of physical errors in quantum devices. Since quantum information must be protected from corruption to be able to benefit from a quantum computing advantage, the main goal for a quantum computer is to perform a desired number of quantum gates within the lifetime of the system. To achieve this goal within a circuit model for quantum computation several aspects must be pursued, such as the reduction of intrinsic hardware noise on the physical level, quantum error correction techniques which make use of redundant encoding of information, and faster physical implementations of quantum gates.

This dissertation is set in the general context of countering physical noise on a hardware and control level, focusing on two different and complementary applications: Schrödinger cat-state bosonic encodings [92] using superconducting circuits on the one hand, and dynamical decoupling (DD) [129] on the other hand. In both contexts, we perform a theoretical dynamical systems study to characterize the performance and possible working regimes of the approach. A cat state computational basis is a promising scheme for fault-tolerant bosonic quantum error correction [58, 103], with a favorable error threshold and hardware overhead [59], and to engineer such states one typically drives Josephson-junction-based nonlinear elements [55, 80]. DD is a dynamical method that filters out unwanted system-environment interactions by applying coherent and fastly-varying control operations to the target system that we wish

to protect, in order to effectively cancel its Hamiltonian coupling to the environment. The common denominator of these two noise-countering approaches, each to be introduced more in detail further on, is that one applies time-dependent Hamiltonian drives to the system to obtain the desired operating regime. Since quantum devices are inherently open systems, these application domains come with the general difficulty of analyzing *driven open quantum systems*. A parallel axis of this dissertation is to pursue improved analysis methods for this class of systems.

The desirable operating regime of driven open quantum systems can generally only be understood in terms of a reduced model, obtained after eliminating fast degrees of freedom from the description, to retain an effective description of the evolution of the system at the timescale of interest. These fast degrees of freedom can entail the driving frequency, but also the fast decay of dissipative degrees of freedom. As a first case, for very lossless (called high-Q) systems, fastly-oscillating drive terms can be eliminated by *averaging methods*, which are particularly well established in the Hamiltonian case [15, 34, 88, 91, 125]. The range of validity of the obtained reduced models is often unclear however, and for the case of driven quantum anharmonic oscillators employed in superconducting circuits, this dissertation establishes a fundamental limit to model reduction, by studying chaotic junction dynamics. At the same time, we provide a recipe for choosing the circuit parameters as to avoid this detrimental chaotic behavior. This study, subject of Part I, is thus situated in the context of strong-drive limitations of current superconducting circuits experiments. The context of this field of research is again summarized at the beginning of Part I.

To eliminate fastly dissipative degrees of freedom, *adiabatic elimination* techniques [5, 6, 66] provide a systematic model reduction method, leveraging this dissipative timescale separation. This technique being relatively novel, many open questions remain about which timescales can be eliminated, and the elimination of which degrees of freedom leads to a reduced model that is physically interpretable, for example of Lindblad form [51, 83]. This dissertation makes two contributions to this field, providing an extension of the method to periodic driving, and to a new class of degrees of freedom to be eliminated. Both of these extensions are directly applicable in the context of DD, and opened up the possibility for applying the DD methodology in a novel way: we propose to drive an environment subsystem as to decouple it from the target system, whenever the former can readily be identified and presents the main source of noise for the target. This environment-side decoupling approach has the immediate advantage that imprecise actions do not directly deteriorate the target system. This strategy had not been considered to the best of our knowledge, and we benchmarked it for the case of a two-level system (TLS) environment, obtaining explicit expressions for the induced decoherence rates of the target system. This work is the subject of Part II of the dissertation.

The rest of this section is organized as follows. First an introducion to both bosonic encodings and DD is provided, after a short intermezzo on code-based quantum error correction, as a complement to these noise countering strategies at the physical level. Next we state the context of the problems that are tackled in this dissertation In Section 2.2, we focus on superconducting circuits and the problem of chaotic dynamics under strong drives. In Section 2.3, we detail the challenges that come with an environment-side decoupling approach. We finally summarize the contributions of this dissertation in Section 2.4, and the layout of the manuscript in Section 2.5.

2.1 Countering noise

Quantum error correction (QEC) [44, 52, 123] techniques consist of encoding the same qubit of logical information in a larger physical system in a redundant manner. This larger physical system can be a network of well-connected physical qubits. The redundancy allows for multiple different error syndromes to be measured, by measuring different physical subsystems. If the different measurement records yield a conflicting result, we know that a physical error must have occurred in some subsystem. If not too many individual errors have occurred, then we can infer from the measurement record which error is most likely to have occurred, and we can correct for it. However, in the case of many individual errors the logical qubit may be irreversibly corrupted, resulting in a logical error. Under the assumption of local and uncorrelated noise, it was shown that the probability of a logical error occurring can be made arbitrarily small by scaling up the number of physical hardware subsystems in which the information is encoded, provided the physical error probability of each constituent be below a certain error-probability threshold, and provided also the errors produced by the application of imperfect logical gates manipulating the information be below a similar threshold. This property is called *fault-tolerance* [1, 72]. The required redundancy scales up with the desired logical error probability, while it scales down with how much the physical error probability is below the physical error threshold. In this way the property of fault tolerance allows for reliably performing arbitrarily long computations, as long as we have enough hardware overhead to encode the information in. The main difficulty is that qubits can undergo a continuum of quantum errors, which can be shown to be decomposable by the encoding into two fundamental types: bit-flip errors and phase-flip errors respectively. The concept of a phase-flip computational error is something inherently quantum mechanical, and does not apply to classical computers. Since QEC has to correct for both types of errors, the physical error threshold of quantum codes (if one exists) can be rather low (think 1%), and furthermore the scaling of the hardware overhead can be much more unfavorable than for classical codes, rendering many QEC schemes unfeasible from a hardware point of view. This dissertation explores methods for reducing errors *at the physical level* that can complement, or even be leveraged by quantum error correction approaches.

One approach that sets out to alleviate this hardware-overhead problem are so-called *bosonic encodings*, which aim to establish a first protection of the quantum information at the physical level, either for both types of errors, as in GKP-codes [21, 53], or just one type of error, as in the case of Schrödinger cat codes [92]. In both cases, the scaling of the necessary hardware overhead for QEC is drastically reduced. To achieve this protection at a physical level, the infinite-dimensional state space of a quantum harmonic oscillator is utilized, providing a naturally-present redundancy for the encoding. One prominent such class of bosonic codes that is studied in this dissertation are given by Schrödinger cat states [78, 92], namely the superpositions of two coherent classical amplitudes of a bosonic field. The advantage of cat codes stems from the fact that a cat qubit benefits from a noise bias: the bit-flip error rate is smaller than the phase-flip error rate by a factor that scales exponentially with the size of the cat, which is defined as the amplitude of the bosonic field corresponding to the aforementioned coherent states. Using this noise-bias, a bias-preserving QEC-scheme has been developed that scales much more favorably [58, 103] in terms of hardware overhead than schemes for more traditional codes composed of regular physical qubits. The way in which the cat states are stabilized depends on the physical platform, but typically involves a coupling of the harmonic oscillator to some nonlinear element that is also *driven* [80]. Indeed, it has been shown im-

possible to create such non-classical states using only linear systems, while it is known that quantum states of purely linear systems provide no advantage over a classical computer [85]. In summary, a cat state computational basis is a very promising scheme for fault-tolerant bosonic quantum error correction, with a favorable error threshold and hardware overhead, and to engineer such states one typically drives a coupled nonlinearity.

A second approach for mitigating errors directly on the physical level studied in this thesis is Dynamical Decoupling (DD) [129]. This is a dynamical method that filters out unwanted system-environment interactions by applying coherent and fastly-varying control operations to the target system that we wish to protect, in order to effectively cancel its Hamiltonian coupling to the environment. The validity of this approach hinges on a timescale separation between the applied control pulses and the coupling rate to the environment. When allowing for arbitrarily strong and arbitrarily fast control operations, DD has the ability to render the effective decoherence rate of the target system arbitrarily small, under the assumption that the noise processes that are to be decoupled exhibit a finite cut-off frequency. In practice, DD strategies should be considered within realistic control assumptions, utilizing finite control resources. Such a setting has led to the establishing of DD schemes that use these resources in an optimal manner [76, 104]. In contrast to bosonic encodings, DD techniques have essentially been established for low-dimensional systems by acting directly on the level of a single physical qubit storing the information, whereas bosonic encodings inherently exploit an infinite-dimensional states space. Just as for bosonic encodings, DD strategies can be combined with quantum error correction [99, 127], and they can also provide protection while performing logic gates [68, 69].

The next two sections introduce the specific physical settings in which we set out to pursue bosonic encodings, resp. DD, and which challenges are to be overcome. For bosonic encodings this will be the quantum hardware platform of superconducting circuits, where the lossless nonlinearity provided by the Josephson junction stands central. For the dynamical decoupling strategy on the other hand, instead of limiting ourselves to one hardware platform we consider a general class of open quantum systems, exhibiting well-defined subsystems and timescale separations. Within this framework, we propose a new strategy for countering noise, that goes hand-in-hand with the model reduction techniques the physical setting calls for. The scientific contributions that resulted from pursuing both these approaches are subsequently summarized in Section 2.4.

2.2 Driven superconducting circuits

A leading physical platform for building quantum computing devices is that of superconducting circuits [97], as these have made significant strides towards reliable state preparation and gate operation, and longer coherence times [14, 71]. Superconducting circuits are electrical circuits that are cooled down to a few tens of mK and couple strongly to microwave-photons. At these extremely low temperatures, all physical observables obey quantum mechanical equations of motion. Lossless nonlinear elements are introduced in the circuits, which are used either to store and manipulate the quantum information itself within their two lowest-lying energy levels, or to mediate interactions between microwave resonators storing information in bosonic modes. The go-to nonlinear element is a Josephson junction [64], consisting of two superconducting electrodes separated by an insulating barrier. Different types of interactions between different modes can be engineered by driving with simple microwave fields, or by

parametrically modulating a circuit parameter. This parametric engineering of interactions is a key topic of research, and new types of interactions are continuously being engineered; be it for the purpose of a more exotic interaction or logical gate [29, 89], or for reservoir-engineering purposes stabilizing a desired quantum state [79, 117]. In this way, the reservoir-engineered stabilization of quantum Schrödinger cat states of microwave light was achieved [80].

On the other hand, the general combination of driven nonlinear oscillators enters into the domain of possibly chaotic systems, as has been the pioneering discovery of van der Pol [124] and Duffing [33]. These chaotic phenomena have been extensively studied for Josephson circuits in the classical regime specifically during the 80's. A large *noise rise* was observed for Josephson-based parametric amplifiers [26, 122]. This phenomenon was known not to be due to thermal fluctuations, but the exact origin of this sudden noise rise remained unclear. This until Huberman, Crutchfield and Packard attributed it purely to a property of the full nonlinear *classical* equations of motion: chaos [62]. The noise was due to chaotic, but nonetheless deterministic junction dynamics. For a simple junction, which is equivalent to a simple driven pendulum, period-doubling routes to chaos were observed and studied in [32]. Indeed, it is well-known that a periodically kicked pendulum can behave chaotically. For a current-driven shunted-junction model, [62] and [107, 108] found simple behavior periodic with the drive, but also complicated subharmonic behavior, and period-doubling cascades into a chaotic regime when the drive amplitude is increased.

Josephson junction technology having evolved, for example having entered the quantum regime and the microwave frequency range, these results have seemingly been sidelined. Also recently in the quantum regime, experimental limitations have been attributed to ill-understood dynamical behavior [81, 110]. One effort to resolve this issue is by developing refined perturbation theories, obtaining more accurate higher-order reduced models of the dynamics [100, 101, 110]. A second effort has been to alter the circuit design as to render it more robust with respect to dynamical instabilities. Notably the addition of an inductive shunt to the traditional transmon [73] has been shown to render it more stable under strong parametric driving [126]. In Part I, we show how this inductively-shunted transmon can be tuned to be resistant against the detrimental behavior that can per definition not be captured by any integrable reduced model: classical chaos. This chaotic regime can be suppressed while the device retains the ability to confine a class of non-classical states useful for bosonic QEC, namely Schrödinger cat states.

2.3 Environment-actuated decoupling approach

The idea of Quantum Dynamical Decoupling is to reduce the effective coupling between a target system and its environment, by applying tailored control actions to the target system, at a faster timescale than the Hamiltonian coupling to the environment. The validity of this approach crucially depends on the way this environment can be modeled. Indeed, for a purely Markovian decoherence process, corresponding to the case of a memoryless environment, one cannot expect to be able to decouple the target using control actuations. When modeling a large relevant part of the environment as one (possibly very large) Hamiltonian system, DD has been shown to be valid under very general conditions [129]. In this case, one can prove that the effective coupling can be made arbitrarily small in the theoretical limit of arbitrarily strong and arbitrarily fast controls. This is typically proven using an analysis method such as the Magnus expansion [16, 88] or an equivalent Hamiltonian averaging technique [35].

Several experimental realizations for quantum hardware encounter an intermediate situation for the relevant environment. Here, the target is directly coupled to a finite-dimensional, well-identified system that acts as the main source of induced decoherence on the target. This environment *subsystem* is then coupled to an environmental bath that is not directly coupled to the target. One immediate example of such environment subsystems are two-level system (TLS) defects in the oxide layer of superconducting Josephson junctions, which typically decohere through phonon channels and are a main mechanism inducing decoherence of superconducting qubits [84, 95].

Starting from this observation, we propose to apply the DD methodology in the following way: applying actions on the *environment side*, such as to reduce induced decoherence on the target system. One potential advantage of applying these actions to the environment subsystem is an increased tolerance with respect to imprecise actions. Indeed, DD methods that act with control pulses directly on the target system need to be particularly precise, and any control imprecision directly deteriorates the quantum information stored in the target. A second potential advantage of environment-side decoupling is that the actions commute with any logical gates one might want to perform on the target system. Although DD schemes have been developed that provide protection while performing logical gates [70], these come with the drawback of increased resources, such as the complexity of the control signals. On the downside, of course we can hope to act on the environment only if it is well identified and of reasonably small dimension.

There are two main points in which the DD methodology is to be extended to establish the performance of environment-side driving. Firstly, as the decoupling drives are being applied on a *lossy* environment subsystem, this calls for novel analysis methods to characterize the DD performance of this approach, as the performance of DD is traditionally studied using averaging techniques in a purely Hamiltonian setting. The general model reduction technique to eliminate *dissipative* degrees of freedom such as the lossy environment subsystem is adiabatic elimination [5, 6, 66]. A first challenge is to extend this technique to the case of periodic driving, as so far the technique had only been developed for stationary systems. Our environment-side approach comes with a second challenge. While acting on the environment comes with the security of not deteriorating the target state directly in the case of control imprecision, we also cannot expect to control an environment system in a well calibrated manner. Neither can we expect to have accurate knowledge of the bare environment Hamiltonian. Part II of this dissertation details how these two general problems can be resolved, providing a novel strategy for countering noise in practical quantum devices.

2.4 Contributions

The general scope of this dissertation being two complementary approaches for countering physical noise, with a common denominator of periodically-driven quantum systems, its contributions can be summarized in four main points.

- First, we provide a recipe for choosing the circuit parameters of practical superconducting devices in order to avoid detrimental chaotic behavior under strong driving, all the while benefiting from a strongly nonlinear regime of the device. We exemplify this strongly nonlinear potential by robustly confining a class of highly non-classical states, known as Schrödinger cat states. These cat states have immediate applications

in the field of bosonic encodings, which have been shown to allow for hardware-efficient quantum error correction.

- A second contribution lies in the general methodology that is developed to analyze the advent and the effect of chaotic dynamics in the context of such periodically-driven high-Q quantum systems. We do this by laying a connection between the classical Poincaré map and the Floquet decomposition of the system. Using analytical techniques on the classical system, we provide a result blocking the main route to chaos of the system for well-chosen circuit parameters. Furthermore, we characterize the different nonlinear operating regimes once the device is in the regular, non-chaotic regime, through model reduction techniques based on geometric averaging theory. To our knowledge, such an averaging analysis has not been performed accounting for the full Josephson cosine potential, and should prove more accurate towards tuning practical devices.

This work is in preparation for submission to Physical Review Letters.

- Thirdly, we provide a novel and robust variation of DD for countering noise in a practical class of target quantum devices. Existing DD methodology provides techniques for decoupling a target from an environment by acting on the target system with strong and precise control operations. We extended this method to the case where one drives an identifiable environment subsystem to decouple it from the target. The performance of such an approach is benchmarked for the case of a two-level-system (TLS) environment, and analyzed in a system-theoretical setting from model to the main figure of merit, namely the induced decoherence rate of the target system. The type of environment-side driving for which we proved the effectiveness of the approach comprises coherent periodic drives on the one hand, and the limit of driving with pure noise on the other hand, where the decoupling actions correspond to added dissipation channels to the environment, establishing a novel dissipative flavor of DD. The analysis of this dissipative flavor of DD leads to an overall physical conclusion that is of immediate relevance for typical experimental scenarios: maybe counterintuitively, isolating the environment from noise sources as much as possible is often not the best course of action.

- A last contribution lies in the analysis methods developed for this environment-side decoupling approach, which lay a connection between the field of model reduction for dissipative open quantum systems and the system-theoretic control problem of dynamical decoupling. We developed an extension of the method of adiabatic elimination to include periodic driving, allowing to analyze the DD benefits for the first type of environment-side driving, which was chosen to be periodic. Moreover, the adiabatic elimination method was likewise extended to more general degrees of freedom to be eliminated, in the context of the dissipative flavor of dynamical decoupling.

These last two contributions constitute work [20] submitted to the Journal of the Franklin institute.

2.5 Layout of the manuscript

In Part I of this dissertation, we provide a recipe for obtaining a robust subharmonic regime of driven quantum nonlinear oscillators, corresponding to the confinement of a manifold of Schrödinger cat states.

- In Chapter 3 we start by introducing the model of the periodically-driven inductively-shunted transmon. We discuss how this single-mode system combines the three basic circuit elements of superconducting circuits, making it ubiquitous. More specifically, we perform a general change of variables that transforms the system into a normal form that will be used throughout this part. This identifies four main parameters of which we briefly discuss the roles. These comprise two effective circuit parameters called the *regularity parameter* and the *quantum scaling parameter*, as well as renormalized versions of the drive parameters. Once this normal form of the system is established, in Section 3.2, introductory material on the general analysis methods of periodically-driven systems is provided. For classical periodic systems, the relevant concepts from dynamical systems theory are introduced, most notably the Poincaré map, as well as notation to be used in the subsequent chapters of this part. On the quantum side, an introduction to Floquet theory is given, including its extension to (open quantum) systems interacting weakly with an environmental bath. Lastly, the numerical methods we used to simulate the system are summarized.

- In Chapter 4 we use the language of Floquet theory to establish a robust, non-chaotic subharmonic regime of the driven inductively-shunted transmon. After a short introduction on cat qubits, we lay a connection between the Poincaré map of the classical system on the one hand, and the Floquet modes of the quantum system on the other hand, equating stable subharmonic classical solutions to the existence of a degenerate set of Schrödinger-cat Floquet modes. Focusing on one class of subharmonics, we characterize the quantum signatures of classical chaos occurring when ramping up the drive strength. We observe a highly entropic asymptotic regime for the quantum system in this chaotic case. Next, we show how to choose the circuit parameters as to effectively suppress this high-entropic regime, by lowering the regularity parameter. We propose a theoretical explanation for this by showing that the possible routes to chaos of the classical system are blocked for a small-enough regularity parameter. Finally, we show that in the non-chaotic regime, the quantum scaling parameter can be tuned independently to increase the confinement rate of the manifold of Schrödinger cat states, providing a strongly nonlinear, regular regime.

- In Chapter 5 we focus on the dependence of the system on the drive parameters, in order to characterize the resonance conditions that lead to stable subharmonic solutions of the classical system, using a first-order averaged model. After a short introduction on the theory of geometric averaging, we obtain a reduced model that eliminates the dependence on time. We discuss global symmetries of the resulting model, as well as limiting cases, and provide a numerical account of one particular class of subharmonic solutions predicted by the model.

In Part II, we propose a novel noise-countering technique for practical quantum systems based on the dynamical decoupling methodology.

- In Chapter 6 we show how environment-side dynamical decoupling can be achieved by continuously driving the environment with only a single-frequency drive. After reviewing the relevant work in the field of continuous-drive DD approaches, we introduce a DD drive that exhibits a double timescale separation that effectively mitigates the present

control imprecisions. Next, we extend the model reduction technique of adiabatic elimination to the case of periodic driving, to obtain explicit formulas for the decoherence induced on the target system under this periodic driving of the environment. We discuss the effectiveness of the decoupling in terms of the dependence of the induced decoherence rate on drive parameters, and conclude by analyzing the limit where the strength of DD drives becomes comparable to the bare frequency of the TLS, again confirming the DD benefits.

- In Chapter 7, we extend the environment-side decoupling strategy to the limit of completely disorganized drives, by considering them as added dissipation channels onto the environment. We start by revising the leading-order adiabatic elimination formulas that describe the induced decoherence on the target. Setting out to minimize the induced decoherence on the target, we highlight general properties of the resulting optimization problem for the dissipation rates on the environment. A case-study for the case of a TLS environment is provided, including the limit of a partly decohering environment, that only loses part of its coherences.

The two parts can be read independently. A conclusion in Part III gives an insight into possible open questions and future work.

Part I

Structurally-stable subharmonic regime of a driven quantum Josephson circuit

This first part of the dissertation sets out to provide solutions for strong-drive limitations of current superconducting-circuits experiments. Our contribution is to identify these limitations as chaotic dynamics, and to provide a clear recipe of how to suppress this chaos for a ubiquitous single-mode nonlinear device: the inductively-shunted transmon. To display the remaining nonlinear potential of the device in the non-chaotic regime, we focus on the application of the robust confinement of a manifold of Schrödinger cat states.

The language that will be used throughout this part has a strong classical component. Indeed, we will perform as much analysis of the classical equations of motion of the inductively-shunted transmon, as we will of their quantized version. The methods used to perform this study likewise leverage dynamical systems theory techniques that have been developed for general classical driven nonlinear oscillators specifically. Since chaotic dynamics is inherently a classical concept, this is maybe not surprising. We will introduce the confinement of the cat states in a classical language as well, however, which we consider a contribution in and of itself. We will tie classes of *subharmonic* solutions of the classical system to a manifold of confined cat states of the quantum system. The goal is to be able to establish such a subharmonic regime in a robust way, and hence we speak of a robust subharmonic regime of driven quantum nonlinear oscillators in the title of this part. Alongside this classical study, to quantify the quantum signatures of classical chaos, we have opted for a numerical approach characterizing the long-time behavior of the quantum system, based on Floquet-Markov theory.

We begin by introducing strong-drive limitations in various state-of-the-art superconducting-circuits experiments, giving an overview of recent work on theoretical explanations, and of a new circuit design to alleviate these very limitations. Next, in Chapter 3 the model of the driven inductively-shunted transmon is introduced, as well as the theoretical methods that are used to study this driven system throughout this part: Floquet theory for the quantum system, and the Poincaré map for the classical system. Chapter 4 then provides the main result. Guided by numerical Floquet simulations, we define the figures of merit for cat state confinement, and exhaustively characterize the roles of two main circuit parameters. The *regularity parameter* can be lowered to a finite value to avoid chaotic regimes, and a second, the *quantum scaling parameter*, can be augmented independently to obtain strong confinement of the cat states in the non-chaotic regime. These numerical results focus on the dominant subharmonic regime of the device, corresponding to three-component cat states confined by a four-photon process. Lastly, in Chapter 5, we characterize the roles of the drive parameters as to be able to select different classes of subharmonics for the classical system, linked to corresponding classes of cat states.

Context

Superconducting circuits have proven to be a leading platform for quantum information processing [13]. A variety of applications hinge on strong parametric interactions, such as high-fidelity gates [27] and readout [105], tunable couplers [47], efficient reservoir engineering [80, 117], or bosonic encodings [55, 82]. For many of these applications, the desired system behavior has been shown to break down when driving the system too strongly. Moreover, the radical change in system response is discontinuous in the drive power, indicating a structural instability of the system. These strong-drive limitations have been demonstrated experimentally in the context of unwanted heating [110] or ionization [81] caused by strong-drive effects. As a first effort, theoretical explanations have been pursued for readout [100, 110] and para-

metric gates [101], focusing on terms in the parametric Hamiltonian that cannot be captured by low-order rotating-wave approximations (RWA). While these refined perturbation theories have been successful in explaining the unwanted behavior, either analytically or numerically, they do not provide a recipe to retain structural stability under strong driving. As a second effort, in [126], a new circuit design was proposed that behaves more stable, thanks to an extra harmonic confining potential provided by adding an inductive shunt to the traditional transmon.

In this part, we study the classical and quantum dynamics of the periodically-driven inductively-shunted transmon as a function of circuit and drive parameters, and we explicitly identify chaotic dynamics as the cause of structural instability of the system. Recently, limitations on performance caused by chaotic motion has been reported for a quasi-classical detector model [77], and chaotic states for a large number of coupled transmons [73] have been predicted to limit future architectures [12], showing a breakdown of many-body localization. Therefore, laying a connection between classical chaos and superconducting-circuits parametric engineering is a first important step towards alleviating strong-drive limitations.

Chapter 3

Model and preliminaries

Ce chapitre introduit le modèle du transmon shunté d'une inductance, forcé de maière périodique. Ce système représente un oscillateur non-linéaire omniprésent dans le domaine des circuits supraconducteurs. Nous réalisons d'abord un changement de variables pour mettre le systme sous une forme normale, qui guidera les analyses à venir. Ce changement de variables permet d'identifier des nouveaux paramètres renormalisés du circuit, qui déterminent chacun des propriétés complémentaires du système, que l'on discute brièvement, en anticipant les résultats des chapitres à venir. Dans la Section 3.2, nous introduisons le baggage technique nécessaire pour analyser ce genre de système dynamique périodique. Du côté classique, l'application de Poincaré permet de décrire toutes les propriétés dynamiques pertinentes, et du côte quantique, ce rôle est joué par la théorie de Floquet, composée des modes de Floquet et leur quasi-energies. Vu que la définition de l'application Poincaré ansi que de la décomposition de Floquet nécessite la connaissance des solutions exactes du systèmes, nous expliquons comment les trouver par des simulations numériques. Ces simulations numériques ont permi d'établir la plupart des résultats dans le chapitre 4 à venir.

In this chapter, we introduce the model of the periodically-driven inductively-shunted transmon, highlighting its character as a ubiquitous nonlinear oscillator central to quantum information applications. Through an exact change of variables, the system is rewritten in a normal form that allows for the definition of new effective circuit parameters that each govern distinct and complementary system properties. A brief summary of this dependence on parameters is given, anticipating some of the results of later chapters. In Section 3.2, we introduce the technical tools used to analyze the dynamical behavior of periodically driven systems. We start by introducing the classical Poincaré map, which allows us to define all the relevant dynamical behavior for the classical system. We proceed to introduce Floquet theory as the analogous language to fully characterize the dynamical behavior of the quantum system, consisting of the Floquet eigenmodes together with the Floquet quasi-energies. The definition of both the Poincaré map and the Floquet decomposition requires the knowledge of exact solutions of the system, and we detail what numerical methods were implemented to compute these quantities numerically. The majority of the results presented in Chapter 4 are obtained through these numerical simulations. Of particular importance is the Floquet-Markov theory outlined in Section 3.2.2, as we will mainly be interested in characterizing the long-time asymptotic behavior of the quantum system in Chapter 4.

3.1 Model description

In this chapter, we study the inductively-shunted transmon subjected to periodic driving. While this nonlinear element is general enough to encompass a large class of superconducting devices designed for quantum information processing, it is concrete enough to allow for a systematic study of its behavior when applying drives. Indeed, the number of circuit parameters that have to be chosen at fabrication of the device amount to three. A schematic depiction of the device is given in Figure 3.1.

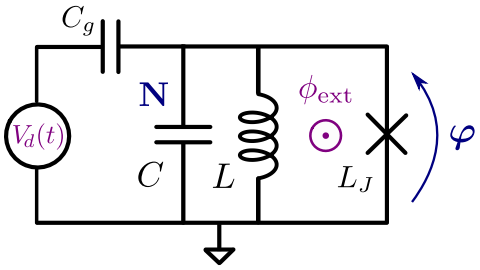

Figure 3.1: Circuit diagram of a driven superconducting circuit comprising a Josephson junction (black cross) as nonlinear element, in parallel to a linear inductance and capacitance. The circuit is capacitively driven by an AC voltage source $V_d(t)$ and could be biased by an external magnetic flux ϕ_{ext} threading the superconducting loop. This circuit is dubbed the inductively-shunted transmon.

The corresponding quantum Hamiltonian model derived from quantizing the circuit (see e.g. [130]) reads

$$\mathbf{H}(t) = 4E_C\left(\mathbf{N} - \frac{C_g V_d(t)}{2e}\right)^2 + \frac{E_L}{2}\boldsymbol{\varphi}^2 - E_J\cos\left(\boldsymbol{\varphi} - 2\pi\frac{\phi_{\text{ext}}}{\phi_0}\right), \tag{3.1}$$

where e is the electron charge, $\phi_0 = \hbar/(2e)$ is the reduced magnetic flux quantum with $\hbar$ the reduced Planck constant, E_J is the Josephson energy, $E_C = e^2/2(C + C_g)$ is the charging energy, and $E_L = (\phi_0/2\pi)^2/L$ is the inductive energy.

The quantum observables $\mathbf{N} = \mathbf{Q}/2e$ and $\boldsymbol{\varphi} = 2e\boldsymbol{\phi}/\hbar$ respectively describe the number of Cooper pairs that have tunneled through the junction, and its conjugate, the reduced flux operator. These observables correspond to dimensionless versions of the charge $\mathbf{Q}$ on the capacitor and the magnetic flux $\boldsymbol{\phi}$ through the inductor respectively. We will systematically denote quantum observables in boldface throughout this part, whereas classical variables are typeset normally. The two Hermitian operators satisfy the canonical commutation relations

$$[\boldsymbol{\varphi}, \mathbf{N}] = i, \tag{3.2}$$

with i the imaginary unit, $i^2 = -1$.

We consider a single-frequency drive

$$V_d(t) = \overline{V}_d\cos(\omega_d t) \tag{3.3}$$

with frequency $\omega_d > 0$ and amplitude $\overline{V}_d > 0$, applied through a capacitive coupling to an AC-voltage source, as depicted in the circuit model of Figure 3.1. In this work, we consider

the case of zero external magnetic flux:

$$\phi_{\text{ext}} = 0.$$

We will see that the methods developed in this dissertation can be extended towards other flux bias points, however, and that many of the main results remain valid.

As a last point, present day nonlinear oscillators in superconducting circuits experiments are becoming better and better isolated from the environment, but still present finite losses, mediated through a coupling to their environment. We model this dissipation as a capacitive coupling of the oscillator to a thermal bath [48]. The coupling Hamiltonian can be described in terms of the different modes of the bath,

$$\mathbf{H}_{\text{SB}} = \sum_{\omega} \hbar\omega \mathbf{b}[\omega]^\dagger \mathbf{b}[\omega] + \hbar g[\omega] \mathbf{N} \otimes (\mathbf{b}[\omega] + \mathbf{b}[\omega]^\dagger). \tag{3.4}$$

where $\mathbf{b}[\omega]$ (resp. $\mathbf{b}^\dagger[\omega]$) is the annihilation (resp. creation) operator of the bosonic mode with frequency ω, satisfying the commutations relations $\left[\mathbf{b}, \mathbf{b}^\dagger\right] = 1$, and $g[\omega]$ is a frequency-dependent coupling rate. We will address how to capture the effect of (3.4) in the limit of weak coupling (i.e. small $g[\omega]$) in Section 3.2.2.

3.1.1 Change of variables to normal form

To obtain a form of our system that is amenable to both perturbation theory and numerical simulations, we will carry out a change of variables with the aim of diagonalizing the *unbounded* part of the Hamiltonian. As it happens, the unbounded part of (3.1) is a driven *linear* system, and can be diagonalized exactly, yielding just a normalized Harmonic oscillator. Concretely, we will rescale the variables $(\boldsymbol{\varphi}, \mathbf{N})$, rescale time, and displace the system to take the effect of the drive into account. The Josephson cosine potential will then be transformed along with the given change of variables.

Consider the rescaled variables

$$\mathbf{x} = \frac{\boldsymbol{\varphi}}{\sqrt{2}\lambda}, \tag{3.5}$$

$$\mathbf{p} = \sqrt{2}\lambda\, \mathbf{N}, \tag{3.6}$$

with

$$\lambda = \left(\frac{2E_C}{E_L}\right)^{1/4}.$$

Dropping a term proportional to the identity operator, we can write

$$\mathbf{H}(t) = \sqrt{8E_C E_L}\frac{\mathbf{x}^2 + \mathbf{p}^2}{2} - E_J \cos\Big(\sqrt{2}\lambda\mathbf{x}\Big) - 2^{2/3} E_C \frac{C_g \bar{V}_d}{e\lambda} \cos(\omega_d t)\mathbf{p}. \tag{3.7}$$

Next we can eliminate one parameter by rescaling time by the system frequency $\sqrt{8E_C E_L}$:

$$\tau \coloneqq \sqrt{8E_C E_L}\, t.$$

The Hamiltonian then has to be rescaled with the same factor, yielding

$$\tilde{\mathbf{H}}(\tau) = \frac{\mathbf{x}^2 + \mathbf{p}^2}{2} - \frac{\beta}{2\lambda^2} \cos\Big(\sqrt{2}\lambda\mathbf{x}\Big) - \sqrt{\frac{E_C}{E_L}} \frac{C_g \bar{V}_d}{e\lambda} \cos(\nu_d \tau)\mathbf{p}, \tag{3.8}$$

with

$$\beta \coloneqq \frac{E_J}{E_L}, \tag{3.9a}$$

$$\nu_d \coloneqq \frac{\omega_d}{\sqrt{8E_C E_L}}. \tag{3.9b}$$

Finally, a part of the drive-effect can be taken into account by moving to a displaced frame. Since we only consider the response of the unbounded, linear part of the system (putting $\beta = 0$), an exact expression for the amplitude of this displacement is available:

$$\tilde{\mathbf{x}} = \mathbf{x} - \frac{\xi_d}{\sqrt{2}\lambda}\sin(\nu_d \tau), \tag{3.10a}$$

$$\tilde{\mathbf{p}} = \mathbf{p} - \frac{\xi_d}{\sqrt{2}\lambda\nu_d}\cos(\nu_d \tau). \tag{3.10b}$$

This yields the following final model:

$$\tilde{\tilde{\mathbf{H}}}(\tau) = \frac{\mathbf{p}^2}{2} + \frac{\mathbf{x}^2}{2} - \frac{\beta}{2\lambda^2}\cos\Big(\sqrt{2}\lambda\mathbf{x} + \xi_d \sin(\nu_d\tau)\Big), \tag{3.11}$$

where we have defined

$$\xi_d = \frac{\overline{V}_d C_g}{e}\sqrt{\frac{2E_C}{E_L}}\frac{\nu_d}{1-\nu_d^2}. \tag{3.12a}$$

With a slight abuse of notation, we drop the double tilde-notation $\tilde{\tilde{\cdot}}$ in (3.11), and simply write $\mathbf{H}(\tau)$, the distinction with original Hamiltonian $\mathbf{H}(t)$ in (3.1) being made by the time argument τ, resp. t. It should be noted that (3.1) and (3.11) are exactly equivalent in describing the system dynamics, as no approximations have been made in the change of variables.

In the next chapter it is shown that the four parameters $(\beta, \lambda, \nu_d, \xi_d)$ are well chosen, in the sense that they individually govern different and complementary system properties.

3.1.1.1 Classical equations of motion

The change of variables we performed on the quantum observables were all *canonical*, preserving the commutation relations $[\boldsymbol{\varphi}, \mathbf{N}] = [\mathbf{x}, \mathbf{p}] = i$. We can thus consider $\mathbf{x}, \mathbf{p}$ as classical variables of a corresponding classical model with Hamiltonian

$$H(\tau) = \frac{p^2}{2} + \frac{x^2}{2} - \frac{\beta}{2\lambda^2}\cos\Big(\sqrt{2}\lambda x + \xi_d \sin(\nu_d\tau)\Big), \tag{3.13}$$

leading to classical equations of motion (EOM)

$$\frac{\mathrm{d}x}{\mathrm{d}\tau} = \quad \frac{\partial H}{\partial p}(\tau) = p, \tag{3.14a}$$

$$\frac{\mathrm{d}p}{\mathrm{d}\tau} = -\frac{\partial H}{\partial x}(\tau) = -x - \frac{p}{\tilde{Q}} - \frac{\beta}{\sqrt{2}\lambda}\sin\Big(\sqrt{2}\lambda x + \xi_d \sin(\nu_d\tau)\Big), \tag{3.14b}$$

where we have accounted for a finite loss rate $1/\tilde{Q}$. It is easily verified that when interpreting (3.1) as a classical Hamiltonian system, and performing the analogous classical change

of variables, one obtains exactly (3.13). In this work, the nonlinear oscillator is assumed to present a very low loss rate, as superconducting devices are becoming increasingly lossless. We will take $\tilde{Q}$ of the order of 10^5 typically.

It turns out that one can perform an additional, non-canonical rescaling of the quadratures to eliminate λ from the EOM. By defining

$$x_\lambda = \sqrt{2}\lambda\, x, \tag{3.15a}$$

$$p_\lambda = \sqrt{2}\lambda\, p, \tag{3.15b}$$

we obtain the EOM

$$\frac{\mathrm{d}x_\lambda}{\mathrm{d}\tau} = p_\lambda, \tag{3.16a}$$

$$\frac{\mathrm{d}p_\lambda}{\mathrm{d}\tau} = -x_\lambda - \frac{p_\lambda}{\tilde{Q}} - \beta \sin(x_\lambda + \xi_d \sin(\nu_d \tau)). \tag{3.16b}$$

This will be the standard form in which we analyze the classical system throughout this part, as λ drops out, and one circuit parameter is eliminated in this way. It should be remembered that the correct quantum-classical correspondence involves a rescaling with λ however. Since λ only plays a role for the quantum version of the system, we call it the *quantum scaling parameter*. Indeed, in Chapter 4 we will see that λ governs purely quantum effects. Anticipating one more result of the next chapter, we call β the *regularity parameter*, as for small enough values of β, the system is in a regular, non-chaotic regime.

3.2 Preliminaries on periodic systems

3.2.1 Periodic dynamical systems

In this section, we introduce the mathematical language needed to study the dynamics of periodically-driven dissipative nonlinear oscillators on a classical level. We will consider oscillators with only one degree of freedom (i.e. two variables), since this is the case for the inductively-shunted transmon introduced in Section 3.1, and all of the theory developed in this section will be applied to this case in later chapters. We focus on the concepts that are most relevant for the results obtained in the rest of this chapter. Of key importance for the remainder of this part is the Poincaré map introduced in (3.23). This tool allows us to define saddle-points and stable nodes (see Section 3.2.1.2), which will be a central concept throughout the rest of this part. A general idea of the *saddle-node* and *period-doubling bifurcation* is required to be able to follow Chapter 5 and Section 4.3 respectively. For a detailed discussion of these bifurcations, we refer to chapter 3 of [57]. Chapter 1 of [57] was the main inspiration for the content of this section. A less mathematically flavored but very physically insightful introduction to the relevant concepts can be found in [120].

The state of the oscillator is described by a vector $z \in \mathbb{R}^2$, whose evolution over time satisfies the set of ordinary differential equations

$$\dot{z} = f(z,t), \quad z \in \mathbb{R}^2, t \in \mathbb{R}, \tag{3.17}$$

where $\dot{z} \coloneqq \frac{\mathrm{d}}{\mathrm{d}t} z$ stands for the ordinary time-derivative, and where $f : \mathbb{R}^2 \times \mathbb{R} \to \mathbb{R}^2$ is a smooth vector field that is periodic in time with period $T > 0$:

$$f(z, t+T) = f(z,t), \quad \forall z \in \mathbb{R}^2. \tag{3.18}$$

The vector field f is often called *non-autonomous*, since it depends on time. The model (3.17) is fully general, in that it can describe any periodically forced oscillation with one degree of freedom.

We denote a particular *solution* (or *trajectory*) of (3.17) corresponding to an initial condition $z_0 \in \mathbb{R}^2$ at time $t = 0$ by $z(t)$, with $z(0) = z_0$. We also speak of $z(t)$ as the solution of (3.17) *based at* z_0. Of particular interest for this work are *periodic solutions* for which

$$z(t + nT) = z(t), \forall t \in \mathbb{R}, n \in \mathbb{N}, n \geq 1, \tag{3.19}$$

as these solutions represent an integral part of the asymptotic behavior of the oscillator. Indeed, a periodic solution is bound to repeat itself indefinitely. When $n = 1$, we call the solution a *harmonic*, and when $n \geq 2$, we speak of a *subharmonic solution*, as it contains frequencies that are necessarily lower than that of the periodic driving modeled by $f(\cdot, t)$.

3.2.1.1 Flow and Poincaré map

Families of solutions can be considered by defining the *flow* Ψ_t corresponding to (3.17). By definition, $\Psi_t : \mathbb{R}^2 \to \mathbb{R}^2, t \in \mathbb{R}$ maps an arbitrary initial condition z_0 to the solution based at z_0, evaluated at time t:

$$\Psi_t(z_0) = z(t), \text{ with } \quad \dot{z}(s) = f(z(s), s), \quad 0 \leq s \leq t, \text{ and } \quad z(0) = z_0, \tag{3.20}$$

An equivalent definition is to interpret Ψ as a function of (t, z) and directly impose

$$\frac{\partial}{\partial t}\Psi_t(z_0) = f(\Psi_t(z_0), t), \quad \forall t \in \mathbb{R}, z_0 \in \mathbb{R}^2. \tag{3.21}$$

Remark that to define the flow, we require knowledge of the exact solution based at any point z_0. Hence, an explicit representation of the flow as a 2D map is almost never available for realistic systems. Nevertheless, thinking of dynamical systems in a geometric way, in terms of the flow that transforms subsets of phase space, can bring useful insight.

In the discussion so far, the choice of starting point $t = 0$ has been somewhat arbitrary, as the system is T-periodic, and one can translate time by any multiple of the period T. Explicitly, for every two trajectories $z_1(t)$ and $z_2(t)$ that share a point $z_1(t_0) = z_2(t_0 + kT), k \in \mathbb{Z}$ at some time t_0, it follows that $z_1(t) = z_2(t + kT), \forall t \in \mathbb{R}$. z_1 and z_2 are in fact one and the same solution. This observation leads to the following (discrete) group property for the flow:

$$\Psi_{nT} = \Psi_{(n-1)T} \circ \Psi_T = \Psi_{(n-2)T} \circ \Psi_T^2 = \cdots = \Psi_T^n. \tag{3.22}$$

Here, the powers and open circle $\circ$ stand for the composition of maps, defined by $\Psi_T^2(z_0) = \Psi_T \circ \Psi_T(z_0) = \Psi_T(\Psi_T(z_0))$. We now define the *Poincaré map* as the flow corresponding to one system period, mapping any initial condition to its solution a time T later:

$$\mathcal{P} \coloneqq \Psi_T. \tag{3.23}$$

One additional possible interpretation is that given a continuous-time solution $z(t)$ of (3.17), powers of $\mathcal{P}$ allow us to sample the solution at multiples of the drive period:

$$\mathcal{P}^k(z_0) = z(kT). \tag{3.24}$$

Once we have defined the Poincaré map, we can consider the discrete dynamical system

$$z_{k+1} = \mathcal{P}(z_k), k \in \mathbb{N}, \tag{3.25}$$

which can be studied in its own right. We call $\{z_k | k \in \mathbb{N}\}$ the *orbit* of $\mathcal{P}$ based at z_0. When considering the discrete-time dynamical system (3.25), we can identify the powers $\mathcal{P}^k$ of the Poincaré map as the flow of this discrete-time dynamical system. We say that $\mathcal{P}$ generates the discrete flow. To simplify the terminology, we will refer to $\mathcal{P}^k$ simply as *the flow*, as the context should make it clear whether we are talking about the continuous-time system, or its discrete version (3.25).

The Poincaré map allows us to define all the relevant system behavior in the context of this work. An immediate example is that subharmonic solutions $z(t)$ of period nT correspond to an n-periodic orbit (or simply n-orbit) $\{z_k^* := z(kT) | k = 0, 1, \ldots, n-1\}$ of $\mathcal{P}$, with

$$\begin{aligned} \mathcal{P}(z_k^*) &= z_{k+1}^*, \quad k = 0, 1, \ldots, n-2, \\ \mathcal{P}(z_{n-1}^*) &= z_0^*. \end{aligned}$$

This is easily verified given the relation (3.24). One last equivalent formulation is that to a subharmonic of period nT are associated n *fixed points* z_k^* of $\mathcal{P}^n$, in the sense that

$$\mathcal{P}^n(z_k^*) = z_k^*, \quad k = 0, 1, \ldots, n-1. \tag{3.27}$$

In summary, an nT-periodic subharmonic continuous-time solution corresponds to an n-orbit of the corresponding Poincaré map $\mathcal{P}$, which in turn corresponds to a set of n distinct fixed points of $\mathcal{P}^n$.

3.2.1.2 Local properties of the flow

For notational simplicity, we will focus on a fixed point of $\mathcal{P}$ in this section, instead of fixed points of $\mathcal{P}^n$ for a general $n \geq 1$. The discussion of this section is completely analogous for $n \geq 2$ however. Denote the fixed point of $\mathcal{P}$ by z^*. We can ask ourselves the question what the dynamics in its immediate vicinity is like. Do neighboring points converge to z^*, are they repelled by it, or do they remain at a bounded distance from it indefinitely? Such questions are the subject of a *stability analysis* of the fixed point. We will first provide a rather informal discussion of the possible cases that can be concluded from a local linearization analysis, yielding a few distinct possibilities for the stability type of the fixed point.

Since an analysis based on a linearization is only approximately valid a priori, we next detail in which cases a linearization analysis yields provably correct conclusions regarding the true, exact flow around fixed points. This is the subject of so-called *invariant manifold theorems*, providing the existence of one-dimensional manifolds that are invariant under the flow. This allows us to locally reduce $\mathcal{P}$ to a one-dimensional map, by restricting it to the appropriate one-dimensional invariant manifold.

One last question one could ask is through what mechanism fixed points can appear or disappear, or change stability type, upon changing a system parameter μ. We define a *bifurcation* of a fixed point to be any process where fixed points are created or disappear, or any process where a fixed point changes stability type, where μ is the corresponding *bifurcation parameter*. Lastly we will briefly discuss the possible bifurcations that can take place for fixed points of $\mathcal{P}$ upon changing the parameters of our system, concluding this subsection on local properties of the flow.

Stability type of fixed points through linearization

Consider an initial condition $z^* + \Delta z_0$, with $\mathcal{P}(z^*) = z^*$, and Δz_0 a small variation. We can define variations Δz_k at later times kT such that

$$z^* + \Delta z_{k+1} = \mathcal{P}(z^* + \Delta z_k).$$

Letting the variations Δz tend to zero, formally replacing it by the infinitesimal δz, we obtain

$$\delta z_{k+1} = \boldsymbol{\nabla}\mathcal{P}(z^*)\ \delta z_k. \tag{3.28}$$

For small variations, we can thus study the linear system generated by the linearized Poincaré map $\boldsymbol{\nabla}\mathcal{P}(z^*)$ to obtain the stability type of the fixed point z^*. When both the eigenvalues ζ, η of $\boldsymbol{\nabla}\mathcal{P}(z^*)$ lie outside the unit circle ($|\zeta|, |\eta| > 1$), we call z^* a *source*, as neighboring points diverge from it at an exponential rate. When both eigenvalues lie in the interior of the unit circle, we speak of a *sink*, or a *stable node*, as neighboring orbits converge exponentially to z^*. When $|\zeta| > 1$, but $|\eta| < 1$, the fixed point corresponds to a *saddle point*, displaying one unstable, and one stable direction. Indeed, considering the eigenvectors $v, w \in \mathbb{R}^2$ of $\boldsymbol{\nabla}\mathcal{P}(z^*)$, we find one contracting direction since $\left(\boldsymbol{\nabla}\mathcal{P}(z^*)^k\right)v = \eta^k v$, and one expanding direction, as $\left(\boldsymbol{\nabla}\mathcal{P}(z^*)\right)^k w = \zeta^k w$, with $|\zeta| > 1$. The stable (resp. unstable) manifold theorem then states that locally, there exists an exact corresponding manifold $\mathcal{W}_s$ (resp. $\mathcal{W}_u$), locally tangent to $\{z^* + hv | h \in [-l, l]\}, l > 0$ (resp. $\{z^* + hw | h \in [-l, l]\}, l > 0$) that remains invariant under the application of $\mathcal{P}$. More precisely, points in $\mathcal{W}_s$ are mapped to points in $\mathcal{W}_s$, and the system can be reduced to a one-dimensional map when restricted to $\mathcal{W}_s$. This manifold is dubbed the *stable manifold*, since for this one-dimensional (1D) flow, z^* is exponentially stable.

Sinks, sources and saddles are three so-called *hyberbolic fixed points*, since a linearization analysis allows us to classify their stability type. When one of the eigenvalues of $\boldsymbol{\nabla}\mathcal{P}(z^*)$ lies exactly on the unit circle, a linearization analysis is inconclusive to characterize the flow in the vicinity of z^*, and a higher-order normal form calculation should be pursued, involving higher powers of the variations δz. When $|\eta| = 1$, but $|\zeta| \neq 1$, we can still find one stable (resp. unstable) direction corresponding to the eigenvector w if $|\zeta| < 1$ (resp. $|\zeta| > 1$). To the eigenvector v corresponding to η is now associated an invariant manifold called the *center manifold*. The 1D flow restricted to this center manifold is structurally-stable, but instead corresponds to a bifurcation point. We will briefly classify the types of fixed points and the types of bifurcations that can take place, for the specific case of the model introduced in (3.16).

3.2.1.3 Specifics for dissipative driven oscillators

Consider now the system introduced in (3.16), with a nonzero dissipation rate $\frac{1}{\tilde{Q}} > 0$. For the state vector we have

$$z = \begin{pmatrix} x_\lambda \\ p_\lambda \end{pmatrix},$$

and we can readily identify the vector field as

$$f(z, \tau) \coloneqq \begin{pmatrix} p_\lambda \\ -x_\lambda - \frac{p_\lambda}{\tilde{Q}} - \beta \sin(x_\lambda + \xi_d \sin(\nu_d \tau)) \end{pmatrix}. \tag{3.29}$$

For this case of a dissipative oscillator, it is easy to see that only stable nodes and saddle points can occur as fixed points of $\mathcal{P}^n$, whereas sources cannot occur. This is due to the

area-contracting nature of the system. Indeed the local flow Ψ around a source could never be area-contracting. For a mathematical proof we can use Lemma 3.1, providing an explicit representation for the eigenvalues $\eta_\pm$ of $\boldsymbol{\nabla}(\mathcal{P}^n)(z_0^*)$, with $\mathcal{P}^n(z_0^*) = z_0^*$. Through this lemma, it is easy to see that at least one eigenvalue of $\boldsymbol{\nabla}(\mathcal{P}^n)(z_0^*)$ must lie inside the unit circle, so the fixed point z_0^* cannot correspond to a source. Another immediate consequence of Lemma 3.1 is that the only possible local bifurcations of fixed points of $\mathcal{P}^n$ correspond to either a *saddle-node bifurcation*, for which

$$\eta_+ = 1 \text{ , for } \quad L = \exp\left(\frac{\pi n}{\nu_d \tilde{Q}}\right) \text{ in (3.31)} \quad ,$$

or a *period-doubling bifurcation*, or flip bifurcation, for which

$$\eta_+ = -1 \text{ , for } \quad L = -\exp\left(\frac{\pi n}{\nu_d \tilde{Q}}\right) \text{ in (3.31)} \quad .$$

For a general introduction to these bifurcation mechanisms, we refer to chapter 3 of [57].

Lemma 3.1. *Consider a fixed point z_0^* of $\mathcal{P}^n, n \in \mathbb{N}, n \geq 1$, where $\mathcal{P}$ is the Poincaré map associated to the vector field* (3.29)*. The eigenvalues of $\boldsymbol{\nabla}(\mathcal{P}^n)(z_0^*)$ can either be written as*

$$\eta_\pm = \exp\left(-\frac{\pi n}{\nu_d \tilde{Q}}\right) e^{i\theta}, \theta \in [0, 2\pi), \tag{3.30}$$

or as

$$\eta_\pm = \exp\left(-\frac{\pi n}{\nu_d \tilde{Q}}\right) L^{\pm 1}, L \in \mathbb{R}, |L| \geq 1. \tag{3.31}$$

.

Proof. The main idea of the proof is to exploit the fact that the system exhibits a constant contraction rate given by

$$\mathrm{Tr}(\boldsymbol{\nabla} f) \equiv -\frac{1}{\tilde{Q}},$$

as

$$\boldsymbol{\nabla} f(z) = \begin{pmatrix} 0 & 1 \\ -1 - \beta\cos(x + \xi_d \sin(\nu_d \tau)) & -\frac{1}{\tilde{Q}} \end{pmatrix}.$$

To work towards the final result, we perform a similar linearization of the flow Ψ_τ corresponding to the continuous-time system (3.17) around the point z_0^*, and integrate the resulting equation over n drive periods, yielding

$$\boldsymbol{\nabla} \Psi_{\frac{2n\pi}{\nu_d}}(z_0^*) = \boldsymbol{\nabla}(\mathcal{P}^n)(z_0^*).$$

To conclude the proof, we only need an expression for the product of the eigenvalues of $\boldsymbol{\nabla}(\mathcal{P}^n)$ (i.e. $\det(\boldsymbol{\nabla}(\mathcal{P}^n))$), as one easily sees that $\eta_+\eta_- = \exp\left(-\frac{2\pi n}{\nu_d \tilde{Q}}\right)$ for both cases (3.30) and (3.31). We now summarize the derivation.

By definition the flow satisfies

$$\frac{\partial}{\partial \tau}\Psi_\tau(z) = f(\Psi_\tau(z), \tau), z \in \mathbb{R}^2 \tag{3.32}$$

We can linearize this equation around the continuous-time $2\pi n/\nu_d$-periodic solution $\Psi_\tau(z_0^*) = z(\tau) = (x(\tau), p(\tau))$, analogous to the reasoning on the discrete-time system given in (3.28):

$$\frac{\partial}{\partial\tau}\boldsymbol{\nabla}\Psi_\tau(z_0^*) = \boldsymbol{\nabla} f(z(\tau),\tau)\boldsymbol{\nabla}\Psi_\tau(z_0^*). \tag{3.33}$$

This is now a linear time-dependent equation enabling the study of the system in the vicinity of $z(\tau)$, and since $z(\tau)$ is $2\pi n/\nu_d$-periodic, the linear system (3.33) is of the same period. The dissipative nature of the system can be exploited by considering $\det(\boldsymbol{\nabla}\Psi_\tau)$, as this quantity captures the local expansion of oriented surfaces around the given solution:

$$\frac{\partial}{\partial\tau}\det(\boldsymbol{\nabla}\Psi_\tau(z_0^*)) = \mathrm{Tr}(\boldsymbol{\nabla} f(z(\tau),\tau))\det(\boldsymbol{\nabla}\Psi_\tau(z_0^*)), \tag{3.34}$$

where we have used Jacobi's formula. Now we can leverage the local contraction rate, by substituting

$$\mathrm{Tr}(\boldsymbol{\nabla} f(z(\tau))) \equiv -\frac{1}{\tilde{Q}},$$

as

$$\boldsymbol{\nabla} f(z(\tau)) = \begin{pmatrix} 0 & 1 \\ -1-\beta\cos(x(\tau)+\xi_d\sin(\nu_d\tau)) & -\frac{1}{\tilde{Q}} \end{pmatrix}.$$

Integrating the resulting equation over a time $2\pi n/\nu_d$ readily yields

$$\det\left(\boldsymbol{\nabla}\Psi_{\frac{2n\pi}{\nu_d}}(z_0^*)\right) = \det(\boldsymbol{\nabla}(\mathcal{P}^n)(z_0^*)) = \exp\left(-\frac{2\pi n}{\nu_d\tilde{Q}}\right),$$

independently of the exact fixed point z_0^*. Since $\boldsymbol{\nabla}(\mathcal{P}^n)$ is a matrix with real entries (obtained by integrating a system with real variables), its eigenvalues $\eta_\pm$ must either be real, or come in complex conjugate pairs, with still

$$\eta_+\eta_- = \exp\left(-\frac{2\pi n}{\nu_d\tilde{Q}}\right).$$

This concludes the proof. □

3.2.1.4 Numerical scheme

In this work, phase portraits of the Poincaré map were simulated using time-domain simulations, orbit per orbit for different chosen initial conditions. The system was simulated in a form where the dissipation rate on the two variables is equal, after an extra change of variables − see Section 4.3.1 later, the result of which is (4.28), anticipated here:

$$\begin{aligned} \frac{\mathrm{d}}{\mathrm{d}s}\tilde{x} &= \quad \tilde{p} - \kappa\tilde{x}, \\ \frac{\mathrm{d}}{\mathrm{d}s}\tilde{p} &= -\tilde{x} - \kappa\tilde{p} - \tilde{\beta}\sin(\tilde{x} + \xi_d\sin(\tilde{\nu}_d s)). \end{aligned}$$

We used a first-order integration scheme that is symplectic for $\kappa = 0$, defined as

$$\tilde{x}_{k+1} = \tilde{x}_k + \mathrm{d}s(\tilde{p}_{k+1} - \kappa\tilde{x}_k), \tag{3.36a}$$

$$\tilde{p}_{k+1} = \tilde{p}_k - \mathrm{d}s\Big(\tilde{x}_k + \kappa\tilde{p}_{k+1} + \tilde{\beta}\sin(\tilde{x}_k + \xi_d\sin(\tilde{\nu}_d\, k\,\mathrm{d}s))\Big). \tag{3.36b}$$

Note that the updated value $\tilde{p}_{k+1}$ must be used in the right hand side of (3.36a) for the scheme to be symplectic for $\kappa = 0$. Since the unknown $\tilde{p}_{k+1}$ only appears in linear terms, we can solve for it, and the update rule can readily be written down explicitly:

$$\tilde{p}_{k+1} = \frac{\tilde{p}_k - \mathrm{d}s\Big(\tilde{x}_k + \tilde{\beta}\sin(\tilde{x}_k + \xi_d \sin(\tilde{\nu}_d\, k\, \mathrm{d}s))\Big)}{1 + \kappa \mathrm{d}s}, \tag{3.37a}$$

$$\tilde{x}_{k+1} = \tilde{x}_k + \mathrm{d}s(\tilde{p}_{k+1} - \kappa \tilde{x}_k). \tag{3.37b}$$

We chose $\mathrm{d}s = \frac{\pi}{500\tilde{\nu}_d}$ for all numerical simulations shown in this work, which corresponds to 1000 samples per period of the drive.

3.2.2 Floquet theory and numerical simulations

In this section, we will review the basics of Floquet theory [40, 109], both for closed Hamiltonian systems, as for a weak coupling to a bath where the Born-Markov approximation is valid. This Floquet formalism is used to perform the numerical simulations of this part of the dissertation. The main goal is to describe the long-time asymptotic behavior of the system.

Consider a time-dependent Hamiltonian $\mathbf{H}(t)$ that is time-periodic, with period $T = 2\pi/\omega_d$, acting on Hilbert space $\mathcal{H}$. The Floquet theorem states that there exists solutions of the corresponding Schrödinger equation

$$\frac{\mathrm{d}}{\mathrm{d}t}\left|\psi(t)\right\rangle = -\frac{i}{\hbar}\mathbf{H}(t)\left|\psi(t)\right\rangle, \tag{3.38}$$

of the form

$$\left|\psi_r(t)\right\rangle = e^{-\frac{i}{\hbar}\varepsilon_r t}\left|\phi_r(t)\right\rangle, \tag{3.39}$$

where the *Floquet modes* $\{|\phi_r(t)\rangle\}$ form an orthonormal basis of the Hilbert space $\mathcal{H}$ at any time t, and are T-periodic:

$$\left|\phi_r(t+T)\right\rangle = \left|\phi_r(t)\right\rangle, \forall t \in \mathbb{R}, \tag{3.40a}$$

$$\left\langle\phi_r(t)|\phi_l(t)\right\rangle = \delta_{rl}, \forall t \in \mathbb{R}. \tag{3.40b}$$

Here, $\{\varepsilon_r\}$ are called the *Floquet quasi-energies*. Clearly, ε_r is defined up to multiples of $\hbar\omega_d$ as the Floquet modes $|\phi_r(t)\rangle$ can be multiplied by $e^{-ik\omega_d t}$. Without, loss of generality we choose the quasi-energies ϵ_r to lie in the *first Brillouin zone* $[-\hbar\omega_d/2, \hbar\omega_d/2]$. An equivalent viewpoint is that the Floquet modes (resp. quasi-energies) are the eigenvectors (resp. eigenvalues) of the generalized Hamiltonian

$$\mathbf{H}(t) - i\hbar\frac{\partial}{\partial t},$$

considered to act on the Hilbert space of square integrable T-periodic wave functions in $\mathcal{H}$. Since the Floquet modes at any time t form an orthonormal basis of the Hilbert space $\mathcal{H}$, one can obtain the solution of the Schrödinger equation corresponding to an arbitrary initial state $|\psi(0)\rangle$ by decomposing it into the basis of Floquet modes:

$$\left|\psi(t)\right\rangle = \sum_r e^{-\frac{i}{\hbar}\varepsilon_r t}\left|\phi_r(t)\right\rangle\left\langle\phi_r(0)|\psi(0)\right\rangle. \tag{3.41}$$

The Floquet modes can be numerically computed as the eigenstates of the unitary evolution $\mathbf{U}(t)$ generated by (3.38). Indeed, we note that the solution of the following equation

$$\frac{d}{dt}\mathbf{U}(t) = -\frac{i}{\hbar}\mathbf{H}(t)\mathbf{U}(t), \qquad \mathbf{U}(0) = \mathbf{I}$$

with $\mathbf{I}$ representing the identity operator, is given by

$$\mathbf{U}(t) = \sum_r e^{-\frac{i}{\hbar}\varepsilon_r t} \left|\phi_r(t)\right\rangle\!\left\langle\phi_r(0)\right| .$$

Therefore, one obtains the Floquet quasi-energies and the correct basis of Floquet modes at time $t = 0$ by numerically diagonalizing $U(T)$. Next, we can again numerically integrate the Schrödinger equation with initial conditions $|\phi_r(0)\rangle$ to obtain the Floquet modes at any time $t \in [0, T[$.

Floquet theory can be extended to describe the effect of a weak coupling to a thermal bath. In particular, the asymptotic behavior of the system is described by an extension of Fermi's golden rule ([54], section 9). We will give a quick summary of this Floquet-Markov theory here, and explain the numerical approach that we use in the manuscript. For concreteness, recall that in (3.4) , we modeled the system coupled capacitively to a thermal bath through the Hamiltonian

$$\mathbf{H}_{SB} = \sum_\omega \hbar\omega \mathbf{b}[\omega]^\dagger \mathbf{b}[\omega] + \hbar g[\omega] \mathbf{N} \otimes (\mathbf{b}[\omega] + \mathbf{b}[\omega]^\dagger), \tag{3.42}$$

where $\mathbf{b}[\omega]$ is the annihilation operator of the bosonic mode with frequency ω, and $g[\omega]$ is a frequency-dependent coupling rate. Assuming the coupling rates $g[\omega]$ to be the slowest timescale in the joint system, and assuming a non-resonance condition on the quasi-energies (detailed here-under), one can apply the standard Floquet-Markov-Born approximation ([54], section 9). This Floquet-Markov-Born approximation yields a Lindblad type master equation for the system alone, that can easily be solved in the Floquet basis. When parameterizing the density matrix of the system in terms of its components in the Floquet basis (corresponding to the first Brillouin zone),

$$\rho_{rl} \coloneqq \left\langle \phi_r(t)|\rho(t)|\phi_l(t)\right\rangle , \tag{3.43}$$

one obtains a set of decoupled rate equations for ρ_{rl}:

$$\frac{\mathrm{d}}{\mathrm{d}t}\rho_{rr}(t) = \sum_l L_{rl}\rho_{ll}(t) - L_{lr}\rho_{rr}(t), \tag{3.44a}$$

$$\frac{\mathrm{d}}{\mathrm{d}t}\rho_{rl}(t) = -\frac{1}{2}\sum_m (L_{mr} + L_{ml})\rho_{rl}(t). \tag{3.44b}$$

The transition rates L_{rl} are given by an extension of Fermi's golden rule:

$$L_{rl} \coloneqq \sum_m \gamma_{r,l,m} + n_{\mathrm{th}}(|\Delta_{rlm}|)(\gamma_{r,l,m} + \gamma_{l,r,-m}). \tag{3.45}$$

Here,

- $\hbar\Delta_{rlm} \coloneqq \varepsilon_l - \varepsilon_r + m\hbar\omega_d$,

- $n_{\text{th}}(\omega)$ represents the average number of thermal photons in the bath mode at frequency ω, given by the Bose-Einstein distribution at thermal equilibrium with bath temperature T_{bath}:
$$n_{\text{th}} = \frac{1}{\exp\left(\frac{\hbar\omega}{k_B T_{\text{bath}}}\right) - 1}.$$

- The coefficients γ_{rlm} are in turn given by
$$\gamma_{r,l,m} \coloneqq 2\pi\Theta(\Delta_{rlm})J(\Delta_{rlm})|P_{rlm}|^2, \tag{3.46}$$
where $J(\omega)$ is the spectral function of the coupling rate to the bath, defined in turns of the $g[\omega]$ and to be evaluated mode by mode, and Θ is the Heaviside function.

- Lastly, the matrix elements P_{rlm} are defined by
$$i\left\langle\phi_r(t)|a - a^\dagger|\phi_l(t)\right\rangle = \sum_m P_{rlm} e^{im\omega_d t}. \tag{3.47}$$

The above rate equation can be contrasted to Fermi's golden rule for stationary systems as follows. The transition frequency between two Floquet modes is now not simply given by one unique difference in energy. Instead there are an infinite number of possible transition frequencies, shifted by harmonics of the drive frequency ω_d. This is consistent with the fact that the Floquet modes themselves can contain any harmonic of the drive in principle. The total transition rate between two Floquet modes $r \leftrightarrow l$ induced by the coupling to the bath is now the sum of the rates of these different possible transitions, obtained by evaluating the bath spectral noise density at these different transition frequencies.

It is easy to see that the rate equations (3.44) ensure that the asymptotic density matrix $\rho_\infty(t)$ is diagonal in the Floquet basis, since $\rho_{rl} \to 0, r \neq l$, and that the state converges to a unique classical mixture over the Floquet modes,
$$\rho(t) \to \rho_\infty(t) = \sum_r p_r \left|\phi_r(t)\right\rangle\!\left\langle\phi_r(t)\right|.$$

To compute the probability distribution $\{p_r\}$ corresponding to this mixture, it suffices to solve the linear system of equations $Rp = 0$, with
$$R_{rl} \coloneqq L_{rl} - \delta_{rl}\sum_m L_{rm}. \tag{3.48}$$

The fact that the asymptotic density matrix is diagonal in the Floquet basis derives from a secular approximation as part of the Floquet-Born-Markov approximation, where one neglects time-dependent terms that oscillate at frequencies $(\varepsilon_r - \varepsilon_l)/\hbar - m\omega_d$, whenever either $r \neq l$ or $m \neq 0$. We will see later on that indeed no (near-)degeneracies occur in the quasi-energy spectrum typically, so this secular approximation is justified.

3.2.2.1 Assumptions in this work, and numerical implementation

In this work, we assume the limit of a cold bath, and hence assume $T_{\text{bath}} = 0$, so $n_{\text{th}} = 0$. We furthermore assume $J(\omega) = J$ to be constant. We observe that the maximal Brillouin-zone difference that has to be chosen in (3.45) for the simulations to converge amounts to $m_{\max} = 5$.

We use the Floquet toolbox of the QuTiP [63] open source package to compute the Floquet decomposition, using a modified version of the subroutine calculating the rate matrix R in (3.48). The number of Fock states that has to be used to simulate the system depends on the type of asymptotic cycle $\rho_\infty(\tau)$ obtained. We will address this question in Section 4.2.

One numerical difficulty that occasionally presents itself lies in the numerical evaluation of the eigenvector of the transition matrix R corresponding to the eigenvalue zero. Numerically we see that R shows at least one eigenvalue that is 0 up to machine precision. For some system parameters we encountered the possibility of the transition matrix R exhibiting *two* very-nearly degenerate eigenvectors, both corresponding to eigenvalues very close to 0. At this point the employed numerical diagonalization algorithm becomes unstable, and whether the steady-state ρ_∞ is uniquely defined cannot be concluded based on the numerics. Such parameter values will be removed from the numerical data in the next chapter, as mentioned there.

Chapter 4

Robust Floquet cat-confinement

Dans le chapitre précédent, nous avons présenté l'application de Poincaré et la théorie de Floquet comme les deux langages permettant de décrire le comportement à long terme de notre système forcé. Dans ce chapitre, nous commençons par utiliser ces outils pour fournir une définition physique concrète de l'objectif principal de cette partie: le confinement des états chats de Schrödinger de manière robuste. Pour définir ce confinement des états chats, nous établissons un parallèle fort entre des solutions sousharmoniques classiques et des modes de Floquet sous forme de chats quantiques, d'un nombre de composants correspondant. En effet, nous montrons qu'une même condition de résonance satisfaite par le forçage est responsable à la fois des processus multi-photons qui confinent les états chats, ainsi que de l'existence des solutions subharmoniques correspondantes. Dans la Section 4.2, les effets du chaos classique sur le confinement des états chats sont étudiés. Pour cette étude, nous nous concentrons sur une condition de résonance $(3:1)$*, correspondant à une variété de trois d'états chats de Schrödinger à trois composants. Plutôt que de converger vers une variété protégé d'états chats, le régime asymptotique est fortement entropique, et l'état quantique se disperse sur une grande surface de l'espace des phases. Nous montrons que l'abaissement d'un paramètre effectif du circuit (appelé paramètre de régularité) introduit dans le chapitre précédent supprime complètement ce comportement chaotique. Nous présentons ensuite une explication théorique en correspondance avec cette transition en fonction du paramètre de régularité, celle-ci basée sur le blocage d'une route principale vers le chaos. Enfin, dans la Section 4.4, nous étudions la protection de la variété d'états chats dans le régime non-chaotique, appelé régulier. Nous montrons que l'augmentation du second paramètre effectif du circuit, appelé paramètre de redimensionnement quantique, augmente lécart spectral de quasienergie entre les états chats et leurs états de premi'ere excitation, sans jamais mener à des régimes chaotiques. Nous concluons dans la Section 4.5 en ce concentrant sur les extensions possibles de la méthode développée.*

In the previous chapter we introduced both the Poincaré map and Floquet theory as the two languages in which to describe the long-time asymptotic behavior of our driven system, for the classical and the quantum version respectively. In this chapter, we first use these tools to provide a concrete physical definition of the main goal of this part, namely the confinement of Schrödinger cat states that are robust against perturbations. Our way of defining this cat-state confinement draws a strong parallel between classical subharmonic solutions and the different coherent-state components of the quantum cat states. In Section 4.2, we study the breakdown of cat-state confinement due to classical chaotic dynamics. For this we focus

on a $(3:1)$-resonance condition, corresponding to a manifold of 3-component Schrödinger cat states. Rather than converging to a degenerate manifold of cat states, the asymptotic regime is highly entropic, and the quantum state mixes over a large area in phase space. We show that one effective circuit parameter (dubbed the regularity parameter) introduced in the previous chapter can be lowered to eliminate the highly entropic regimes of the quantum system. Next, we present a theoretical explanation in accordance with this phase transition as a function of the regularity parameter β, based on the blocking of a main route to chaos for the system. This suggests that for a small but finite value of β the chaotic behavior can be suppressed altogether. Lastly, in Section 4.4, we show that in the non-chaotic regime, a second effective circuit parameter dubbed the quantum scaling parameter can be tuned independently to increase the spectral gap separating the cat state manifold from higher-excited states, without ever running into chaotic behavior. We conclude in Section 4.5, focussing on possible extensions of the developed method.

4.1 $(n:m)$-resonances and Schrödinger cat states

In this section, we will show that the inductively-shunted transmon introduced in Section 3.1 can be used to provide Hamiltonian confinement of a degenerate manifold of Schrödinger cat states. On the one hand, this is a proof that the studied system is well-chosen, as it can exhibit highly-nonclassical behavior. On the other hand, our definition of cat qubit confinement lays a connection between the classical and quantum system that we believe to be novel. The presentation serves to introduce the desired behavior of the system, expressed in terms of the Floquet decomposition of the system, without considering the influence of system and drive parameters on the behavior of the system. This dependence on parameters is the subject of Sections 4.2,4.3 and 4.4.

We start with a general introduction on the benefits of cat codes. This is done using examples of general idealized models that confine the manifold of cat states. Next, in Section 4.1.2, we detail how a degenerate manifold of three-component cat states can be confined by appropriately driving the inductively-shunted transmon. We define this cat state confinement in terms of the Floquet decomposition, and more specifically in terms of the long-time asymptotic behavior characterized by Floquet-Markov simulations. In Section 4.1.3, we discuss an observed connection between the phase portrait of the classical Poincaré map on the one hand, and the degenerate manifold of cat states on the other hand. We conclude that the confinement of general n-component cat states goes hand in hand with stable n-orbits of the Poincaré map, and vice versa.

4.1.1 Confined cat qubits

Let $\alpha \in \mathbb{C}$ be a given complex number, and denote by $\mathbf{a}$ the annihilation operator of a bosonic mode, $\left[\mathbf{a}, \mathbf{a}^\dagger\right] = 1$. A *coherent state* $|\alpha\rangle$ is the normalized quantum state parametrized by $\alpha \in \mathbb{C}$ such that

$$\mathbf{a}\,|\alpha\rangle = \alpha\,|\alpha\rangle\,,$$

A coherent state can be considered the most "classical" a quantum state can be, as in a phase-space picture, $|\alpha\rangle$ adheres to a Gaussian distribution centered around the classical point (x, p) with $\alpha = \frac{x+ip}{\sqrt{2}}$, with equal and minimal standard deviations Δx, Δp of the two quadratures

given by the Heisenberg uncertainty principle:

$$\Delta x = \Delta p = \frac{1}{\sqrt{2}}.$$

The corresponding Wigner quasiprobability distribution is represented in Figure 4.1(left). Given this classical correspondence, for $\alpha = |\alpha|e^{i\theta} \in \mathbb{C}$, we will call $|\alpha|$ the amplitude and θ the *classical phase* of the state $|\alpha\rangle$.

We can then define the normalized opposite-phase superpositions

$$\left|\mathcal{C}^{\alpha}_{\pm}\right\rangle = \frac{|\alpha\rangle \pm |-\alpha\rangle}{\mathcal{N}_{\pm}}. \tag{4.1}$$

These states go by the name of Schrödinger cat states, as they form the quantum superposition of two opposite classical phases θ and $\theta + \pi$ of the oscillator, which can be considered macroscopic when $|\alpha|$ is large. The states $|\mathcal{C}^{\pm}_{\alpha}\rangle$ are orthogonal, whereas $|\pm\alpha\rangle$ are not. The normalization constant $\mathcal{N}_{\pm}$ amounts to

$$\mathcal{N}_{\pm} = \sqrt{2(1 \pm \langle -\alpha|\alpha\rangle)} = \sqrt{2\Big(1 \pm e^{-2|\alpha|^2}\Big)},$$

so for a large amplitude $|\alpha|$, the two coherent states do become orthogonal for all practical purposes. The basic idea behind the exact orthogonality of $|\mathcal{C}^{\pm}_{\alpha}\rangle$ is a parity argument. To see this, it is instructive to consider the representation of a coherent state in the basis of *Fock states* $|n\rangle$, namely the eigenstates of the photon number operator $\mathbf{a}^{\dagger}\mathbf{a}$:

$$|\alpha\rangle = e^{-\frac{|\alpha|^2}{2}} \sum_{n\in\mathbb{N}} \frac{\alpha^n}{\sqrt{n!}} |n\rangle \,, \text{ with } \quad \mathbf{a}^{\dagger}\mathbf{a}\,|n\rangle = n\,|n\rangle \,. \tag{4.2}$$

Indeed, in this way it can be verified that $|\mathcal{C}^{+}_{\alpha}\rangle$ involves only states with an even number of photons, and similarly $|\mathcal{C}^{-}_{\alpha}\rangle$ involves only states with an odd number of photons.

The cat states $\left|\mathcal{C}^{\alpha}_{\pm}\right\rangle$ have been proposed as basis states of a quantum bit (or qubit), to be used for universal quantum computation [78, 92]. The logical code space is spanned by the computational basis states

$$|0_L\rangle \coloneqq \frac{\left|\mathcal{C}^{\alpha}_{+}\right\rangle + \left|\mathcal{C}^{\alpha}_{-}\right\rangle}{\sqrt{2}} = |\alpha\rangle + \mathcal{O}\Big(\exp\Big(-2|\alpha|^2\Big)\Big), \tag{4.3}$$

$$|1_L\rangle \coloneqq \frac{\left|\mathcal{C}^{\alpha}_{+}\right\rangle - \left|\mathcal{C}^{\alpha}_{-}\right\rangle}{\sqrt{2}} = |-\alpha\rangle + \mathcal{O}\Big(\exp\Big(-2|\alpha|^2\Big)\Big), \tag{4.4}$$

In terms of protection of information against errors, the merit of the proposed cat-qubit stems from the fact that bit flips (errors mapping $|0_L\rangle$ into $|1_L\rangle$ and vice versa) are exponentially suppressed in $|\alpha|^2$. Increasing $|\alpha|^2$ (also called the *size of the cat*, coinciding with the mean photon number $\bar{n} \coloneqq \langle\alpha|\mathbf{a}^{\dagger}\mathbf{a}|\alpha\rangle$) thus exponentially suppresses the occurrence of bit flips. This fact is not trivial to see, but we can generally understand this bit-flip protection in two steps. First, mechanisms must be put in place to confine the physical state to the manifold of cat states. For now assume the state remains within the code space, as we elaborate on these possible confinement mechanisms hereunder. If the state remains within the code space, we can look at the matrix element $|\langle\alpha|\mathbf{E}|-\alpha\rangle|^2$ proportional to the rate of *direct* transitions

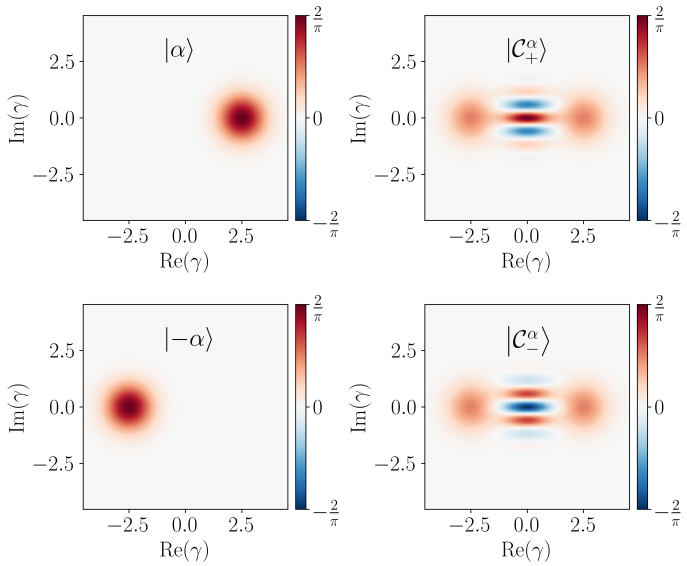

Figure 4.1: Wigner representations of $|\alpha\rangle$, $|-\alpha\rangle$, $\left|\mathcal{C}^\alpha_+\right\rangle$ and $\left|\mathcal{C}^\alpha_-\right\rangle$, for $\alpha = 2.5$. The two coherent states are well-separated in phase space, even for this moderate mean number of photons $\bar{n} = 6.25$. One can see that the sign of the interference fringes is interchanged for the two cat states. The larger the value of $|\alpha|$, the closer the positive and negative interference fringes alternate each other. This proximity may be another way to understand why larger cat states become (linearly) more fragile to phase-flip errors.

between $|\alpha\rangle$ and $|-\alpha\rangle$ induced by an error operator $\mathbf{E}$. One can show that this matrix element is exponentially small in $|\alpha|^2$ for any error operator $\mathbf{E}$ that acts locally in phase space. This is for example the case for displacement errors ($\mathbf{E} = \mathbf{a} + \mathbf{a}^\dagger$), and in fact for most physically relevant error mechanisms. For the case of displacement errors we can calculate:

$$\Big| \langle -\alpha | \mathbf{a} + \mathbf{a}^\dagger | \alpha \rangle \Big|^2 = |\alpha - \alpha^*|^2 \exp\Big(-4|\alpha|^2\Big).$$

A physical intuition for this scaling is that the two coherent states become more and more separated in phase space when $|\alpha|$ becomes large, and operators that act locally in phase space can only couple them with exponentially small rates. Using the same reasoning, one can show that the rate of phase-flips (errors mapping $\left|\mathcal{C}^\alpha_+\right\rangle$ into $\left|\mathcal{C}^\alpha_-\right\rangle$ and vice versa) is expected to *increase* with $|\alpha|^2$. Indeed, still considering displacement errors, we obtain

$$\Big| \big\langle \mathcal{C}^\alpha_\mp \big| \mathbf{a} + \mathbf{a}^\dagger \big| \mathcal{C}^\alpha_\pm \big\rangle \Big|^2 \simeq |\alpha + \alpha^*|^2,$$

when neglecting terms that are exponentially small in $|\alpha|^2$. Note that the resulting increase in phase-flip rate is only *linear* in $|\alpha|^2$ however, and this remains true for error operators that act locally in phase space. This noise-bias allows for more hardware efficient quantum error correction, by ramping up $|\alpha|^2$ as to render bit-flip errors negligible, and subsequently correcting only for the (linearly) increased phase-flip errors using quantum error correction techniques. For this, the present noise-bias has to be preserved while performing a universal set of logical gates [58, 103].

As we mentioned the two-dimensional code space spanned by the cat states is embedded in a larger, in fact infinite-dimensional Hilbert space. Hence, there is not only the danger of logical errors occurring directly within the code space, but the physical state can also *leak* out of the code space. Protection against this leakage can be provided in two different and complementary ways, and state-of-the-art experiments have succeeded in confining a manifold of cat states using either a dissipative stabilization mechanism [80, 82] or a Hamiltonian confinement mechanism [55]. Recent theoretical work has shown that these two complementary ways can also be combined [49], using well-chosen adaptations of the Hamiltonian providing the confinement. The first approach [80, 82] stabilizes the computational manifold by engineering a dissipative mechanism where pairs of oscillator photons are exchanged with single photons of a strongly dissipative environment, typically composed of a second, low-Q oscillator. The effective coupling Hamiltonian that has to be engineered is of the form

$$g_2\big(\mathbf{a}^2-\alpha^2\big)\otimes\mathbf{b}^\dagger+g_2^*\Big(\mathbf{a}^{\dagger 2}-\alpha^{*2}\Big)\otimes\mathbf{b}, \tag{4.5}$$

which takes place at a rate $|g_2|$, and where the $\mathbf{b}$ mode is designed to be low-Q, and in interaction with a cold bath. In summary, in the dissipative case, a quantum state that has leaked outside the code space is actively made to reconverge to the code space, due to the dissipative stabilization of the cat qubit manifold. The local reconvergence rate due to this effective *two-photon dissipation* process is of the order [92]

$$\kappa_2\sim\frac{|g_2|^2}{\kappa_b}|\alpha|^2,$$

where κ_b stands for the photon loss rate of mode $\mathbf{b}$.

As a second flavor of cat-qubit confinement [55], a Kerr-Hamiltonian of the following form is engineered,

$$\mathbf{H}_{\text{Kerr}}=K\Big(\mathbf{a}^{\dagger 2}-\alpha^{*2}\Big)\big(\mathbf{a}^2-\alpha^2\big),K>0. \tag{4.6}$$

The cat qubit code space thus coincides with the kernel of $\mathbf{H}_{\text{Kerr}}$. For this Hamiltonian cat-qubit confinement, once the state is perturbed out of the code space, there is no active mechanism to bring it back. However, for a given strength of *Hamiltonian* perturbations, one can determine how much the cat qubit manifold is perturbed as a whole by considering the gap in the spectrum of $\mathbf{H}_{\text{Kerr}}$. When applying *sufficiently weak and sufficiently slowly-varying* Hamiltonian perturbations, typical results from perturbation theory [65] tell us that the perturbed eigenspace will remain very close to that of the cat qubit manifold. For the case of the Kerr Hamiltonian, this spectral gap is shown to scale as

$$4K|\alpha|^2$$

in the limit of large $|\alpha|$. In the next subsection, we define an analogous spectral gap on the quasi-energies of the driven system, capturing the analogous robustness of the cat subspace as a whole to sufficiently weak and sufficiently slowly-varying Hamiltonians.

As a last point, the question remains how to engineer Hamiltonians that confine cat states, such as (4.5) or (4.6), starting from the available superconducting circuit elements, preferably with large g_2 and K respectively in order to achieve strong cat confinement. The Josephson junction plays the central role of the nonlinear element with which such nonlinear processes are engineered. To engineer a given nonlinear process, one typically applies one or several

microwave drives called *pumps* [55, 80]. For example, (4.5) can be seen a four-wave mixing process mediated by the junction that is made resonant by applying a microwave pump satisfying the frequency-matching condition [82]

$$2\omega_a = \omega_p + \omega_b,$$

where ω_a is the frequency of the **a**-mode, ω_b is the frequency of the **b**-mode, and ω_p stands for the frequency of the applied pump.

The engineering of such parametric interactions through basic first-order analysis methods (such as first-order rotating-wave approximation [132], and first-order adiabatic elimination [8]) is now state-of-the-art knowledge. Our contribution will be to show how these can be kept robust in more extreme regimes corresponding to large driving amplitudes, and we will perform this study for the benchmark system of the inductively-shunted transmon. We will do this for the exact system, considering the full Josephson nonlinearity and true time-dependence due to the driving. This creates a first difficulty to be overcome, namely characterizing the correct resonance condition that selects the desired parametric interaction. In this chapter, we adopt a numerical approach for this based on numerical Floquet-Markov simulations of the driven quantum system, while in Chapter 5, such resonance conditions are characterized in the limit where the oscillator can be considered to be classical. We there perform an approximate analytical study. In the remainder of this section, we will focus on drive parameters for which a given resonance condition is satisfied. The benefit of considering the full cosine potential and the exact time-dependence through numerical Floquet-Markov simulations is that effects are captured that go beyond approximate models such as rotating-wave approximations. We identify these effects as chaotic dynamics in Section 4.2, and show how these can lead to the breakdown of the desired parametric process if the circuit parameters are not well chosen.

4.1.2 Floquet-Markov signatures of cat confinement

In this section, we will show that the inductively-shunted transmon can be used to confine a degenerate manifold of Schrödinger cat states. We focus on a fixed set of appropriately chosen drive parameters, and we define the cat state confinement based on the Floquet decomposition. We focus on the asymptotic regime of our system with Hamiltonian (recalled from (3.11))

$$\mathbf{H}(\tau) = \frac{\mathbf{p}^2}{2} + \frac{\mathbf{x}^2}{2} - \frac{\beta}{2\lambda^2}\cos\Big(\sqrt{2}\lambda\mathbf{x} + \xi_d \sin(\nu_d \tau)\Big), \tag{4.7}$$

and consider a weak dipolar coupling to an environmental bath, as modeled in (3.42). Recall from Section 3.2.2 that numerical Floquet-Markov simulations then allow us to find the unique infinite-time asymptotic state $\rho_\infty(\tau)$ as a probabilistic mixture over the Floquet modes $|\phi_r(\tau)\rangle$,

$$\rho_\infty(\tau) = \sum_r p_r \, |\phi_r(\tau)\rangle\langle\phi_r(\tau)| \, .$$

We recall that for these Floquet-Markov simulations we assume a zero-temperature bath, and frequency-independent coupling rates to the different modes of the bath.

With well-chosen drive parameters (ν_d, ξ_d), we obtain the asymptotic regime displayed in Figure 4.2. A joint account is given of the quasi-energies of the driven system (3.11), as well as the occupation probabilities of the corresponding Floquet modes in ρ_∞. In plot (a), one can see that the probability vector p_r only has considerable support on a triplet of dominant

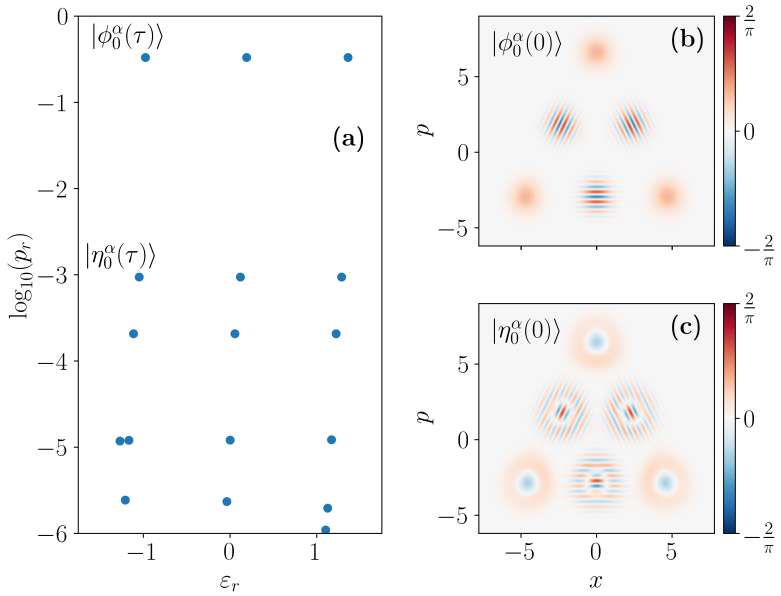

Figure 4.2: Numerical account of the infinite-time Floquet state $\rho_\infty(\tau)$, for $\beta = 0.5, \lambda = 0.2, \xi_d = 0.75$ and $\nu_d = 3.5$. **(a)** The Floquet quasi-energies are plotted against their respective occupation probabilities. The quasi-energy spectrum shows three branches that are separated by $\nu_d/3$, making ε_r mod $\nu_d/3$ threefold degenerate to good approximation. The corresponding occupation probabilities show the same trend, with 3 states being equally occupied in triplets. ρ_∞ mainly has support on one dominant triplet of modes $|\phi_k^\alpha\rangle$ only. This signature of resonance is confirmed in the plots on the right. **(b)** Wigner representation of one of the three dominantly occupied Floquet modes, at time $\tau = 0$. The mode is seen to represent a three-component Schrödinger cat state. The other two modes $|\phi_k^\alpha\rangle, k = 1, 2$ in the triplet correspond to three-component cat states with complementary interference pattern. **(c)** Wigner representation of one of the three Floquet modes $|\eta_k^\alpha\rangle$ with next-highest occupation probability, at time $\tau = 0$. The $|\eta_k^\alpha\rangle$ show a close resemblance to the three analogous symmetric superpositions of displaced Fock $|1\rangle$-states. These excited states are seen to be the most coupled to the cat states, as they have the next-highest occupation probability. The quasienergy spectral gap $\Delta\varepsilon$ between the $|\phi_k^\alpha\rangle$ and the $|\eta_k^\alpha\rangle$ amounts to 0.073.

Floquet modes, that each share the same occupation probability ($\simeq 1/3$). We will denote these dominant Floquet modes by $|\phi_k^\alpha\rangle, k = 0, 1, 2$. We also observe that the quasienergies $\varepsilon[|\phi_k^\alpha\rangle]$ of $|\phi_k^\alpha\rangle$ are degenerate modulo $\nu_d/3$ up to very good accuracy. This is a signature of resonance in the driven system. A Wigner representation at time $\tau = 0$ mod $2\pi/\nu_d$ of one of these dominant modes can be seen in plot (b), showing that within good approximation, $|\phi_0^\alpha\rangle$ corresponds to the symmetric coherent superposition of three coherent states, namely a Schrödinger cat state. The other two states $|\phi_k^\alpha\rangle, k = 1, 2$ correspond to the two other three-component cat states with the complementary interference pattern. Further numerical simulations (not shown) indicate that the $|\phi_k^\alpha(\tau)\rangle$ represent cat states at any time τ, and that, moreover, for the physical state $|\psi_k^\alpha(\tau)\rangle = e^{-i\varepsilon[|\phi_k^\alpha\rangle]}\,|\phi_k^\alpha(\tau)\rangle$ (recall (3.39) from Floquet

theory) which is a solution of the Schrödinger equation with Hamiltonian (4.7) we can write, up to an insignificant accumulated global phase:

$$|\psi_k^\alpha(\tau)\rangle \simeq \left|\mathcal{C}^\alpha_{k\,(\mathrm{mod}\,3)}(\tau)\right\rangle \coloneqq \frac{1}{\mathcal{N}_k^{(3)}} \sum_{l=0}^{2} e^{2i\frac{lk}{3}\pi} \left|\alpha e^{-2i\frac{l}{3}\pi} e^{-i\frac{\nu_d}{3}\tau}\right\rangle, \alpha \in \mathbb{C}, k = 0, 1, 2, \tag{4.8}$$

where $\mathcal{N}_k^{(3)}$ is an appropriate normalization constant. The $|\psi_k^\alpha(\tau)\rangle$ are therefore approximately given by the completely symmetric superposition of three coherent states, uniformly rotating at angular frequency $\nu_d/3$.

In Figure 4.2(a), we can see that the next-most occupied triplet $|\eta_k^\alpha\rangle$ of Floquet modes is populated with a probability that is a few orders of magnitude smaller ($p_r \sim 10^{-3}$). These correspond to the Floquet modes that are most coupled to $|\phi_k^\alpha(\tau)\rangle$ (defined by Fermi's golden rule (3.45) of Section 3.2.2), resulting in the next-highest occupation probability. These can be considered to be excited states of the $|\phi_k^\alpha\rangle$, in this non-equilibrium driven system, and we will denote them by $|\eta_k^\alpha(\tau)\rangle$. Figure 4.2(a) shows that this process continues in three separate branches that can still be labeled by $k = 0, 1, 2$, with every next-most coupled state down the branch being ordered in decreasing occupation probability. We see that also every excited triplet of states shares the same occupation probability, and furthermore, the quasienergies of each triplet are likewise approximately degenerate modulo $\nu_d/3$. They thus form resonant triplets, just as the cat states $|\phi_k^\alpha(\tau)\rangle$, and this process continues until the occupation probabilities become negligible ($p_r \sim 10^{-6}$) for these system parameters.

We can get some basic intuition into this asymptotic, infinite-time regime, based on the possible transition rates between Floquet modes induced by the coupling to the cold bath. With such a dipolar coupling, we can expect the environment to be able to discern the different possible cat states from one another. Moreover, the transition rates between $|\phi_k^\alpha\rangle, k = 0, 1, 2$ are equal in all directions. For the case of two-component cat states (see (4.1)) for example, the transition matrix element induced by single photon loss errors reads

$$\left|\langle \mathcal{C}^\alpha_\mp | \mathbf{a} | \mathcal{C}^\alpha_\pm \rangle\right| \simeq |\alpha|^2,$$

up to terms that are exponentially small in $|\alpha|^2$, which indeed implies equal transition rates in both directions. One can generalize this argument to three-component (and general multi-component) cat states, and so the asymptotic state $\rho_\infty(\tau)$ within the degenerate cat manifold essentially mixes equally over the 3 different cats:

$$\rho_\infty(\tau) \simeq \frac{1}{3}\sum_{k=1}^{3} |\phi_k^\alpha(\tau)\rangle\langle\phi_k^\alpha(\tau)| \simeq \frac{1}{3}\sum_{k=1}^{3} \left|\mathcal{C}^\alpha_{k\,(\mathrm{mod}\,3)}(\tau)\right\rangle\left\langle\mathcal{C}^\alpha_{k\,(\mathrm{mod}\,3)}(\tau)\right|, \tag{4.9}$$

which can be rewritten as

$$\rho_\infty(\tau) \simeq \frac{1}{3}\sum_{k=1}^{3} \left|\alpha e^{-2i\frac{l}{3}\pi} e^{-i\frac{\nu_d}{3}\tau}\right\rangle\left\langle\alpha e^{-2i\frac{l}{3}\pi} e^{-i\frac{\nu_d}{3}\tau}\right|. \tag{4.10}$$

Also for the higher-excited states we can attribute this triplet-structure of p_r to the transition rates being equal in all directions. The transition rates between the cats $|\phi_k^\alpha\rangle$ and next-excited states $|\eta_k^\alpha\rangle$ are highly unidirectional, for this specific bath model, with $|\eta_k^\alpha\rangle$ transitioning into $|\phi_k^\alpha\rangle$ at a much higher rate than vice versa, which explains the convergence of ρ_∞ to a mixture of

essentially only the $|\phi_k^\alpha\rangle$. For this non-equilibrium driven system, the $|\eta_k^\alpha\rangle$ are still occupied to some extent, even for the case of a bath at zero temperature. Up to this residual population of excited states (0.1% for the case of Figure 4.2), which we will neglect in the following argument, the coupling to the bath respects the cat code space, however.

Apart from characterizing the limit of infinite time, the obtained Floquet decomposition also allows us to describe the transient behavior of the system, for which we can neglect the weak coupling to the bath. Consider an initial state within the cat code space, and suppose we want to apply logical operations on the cat qubit. A prominent approach is to apply an extra drive that is resonant with the transitions between the $|\phi_k^\alpha\rangle$ (see e.g. Zeno gates for two-component cats [49, 58]). For this one needs to drive at the frequency

$$\nu_{\text{gate}} \coloneqq \pm\frac{\nu_d}{3}, \tag{4.11}$$

or possibly shifted over a number of Brillouin zones, in which case $\nu_{\text{gate}} = \pm\frac{\nu_d}{3} + l\nu_d, l \in \mathbb{Z}$. If this driving also induced transitions between the $|\phi_k^\alpha\rangle$ and *other* Floquet modes however, the state is driven out of the logical code space. Transitions to the first-excited states $|\eta_k^\alpha\rangle$ will be the most prominent when driving with frequencies around approximately ν_{gate}, as their quasi-energy difference to the cat states is the smallest modulo $\nu_d/3$ (see Figure 4.2(a)), and hence transitions between $|\eta_k^\alpha\rangle$ and $|\phi_k^\alpha\rangle$ are the next-most resonant. To maximally benefit from *strong* driving, which enables fast Hamiltonian gates, we want the quasi-energy gap between the $|\eta_k^\alpha\rangle$ and $|\phi_k^\alpha\rangle$ to be as large as possible, so the state remains within the logical code space. Hence we define the *quasienergy spectral gap* as

$$\Delta\varepsilon \coloneqq \min_{k,k'=1,\dots,3} \min_{l\in\mathbb{Z}} |\varepsilon[|\phi_k^\alpha\rangle] - \varepsilon[|\eta_k^\alpha\rangle] + l\nu_d|, \tag{4.12}$$

where $\varepsilon[|\phi_k^\alpha\rangle]$ corresponds to the quasienergies of the cat states $|\phi_k^\alpha\rangle$, and $\varepsilon[|\eta_k^\alpha\rangle]$ stands for the quasienergies of the first-excited states $|\eta_k^\alpha\rangle$. This definition is directly analogous to the spectral gap reported to provide protection during fast gates in the case of Kerr cats [55]. One of the main conclusions of this chapter is to identify the quantum scaling parameter λ as the main parameter governing the magnitude of this spectral gap $\Delta\varepsilon$, hence increasing the confinement rate (and therefore the protection) of the cat qubit during such Hamiltonian driving. We will study this in Section 4.4

4.1.3 Correspondence with classical subharmonics

As mentioned, this part of the dissertation sets out to understand the behavior of the quantum system by also studying the equations of motion of the corresponding classical system. A first connection between the quantum and classical system can be established in the context of the desired behavior of Section 4.1.2, namely the confinement of Schrödinger cat states. We establish this connection by numerically simulating the Poincaré map $\mathcal{P}$ associated to the classical equations of motion, recalled here from (3.14)

$$\frac{\mathrm{d}x}{\mathrm{d}\tau} = \quad p, \tag{4.13a}$$

$$\frac{\mathrm{d}p}{\mathrm{d}\tau} = -x - \frac{p}{\tilde{Q}} - \frac{\beta}{\sqrt{2}\lambda}\sin\Big(\sqrt{2}\lambda x + \xi_d \sin(\nu_d\tau)\Big). \tag{4.13b}$$

We recall from Section 3.2.1.1 that $\mathcal{P}$ samples continuous-time solutions of (4.13) at multiples of the drive period, as

$$\mathcal{P}^k(x_0, p_0) = \left(x\left(\frac{2k\pi}{\nu_d}\right), p\left(\frac{2k\pi}{\nu_d}\right)\right),$$

with $x(0) = x_0, p(0) = p_0$.

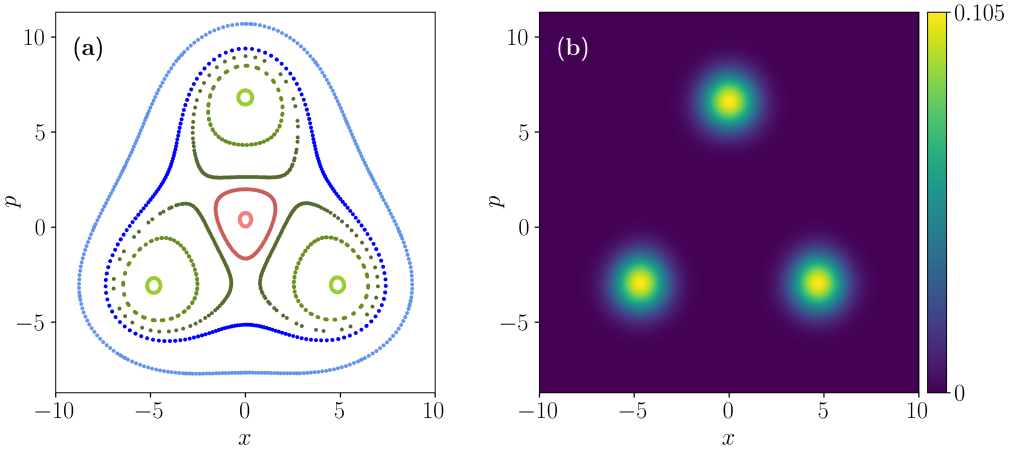

Figure 4.3: Quantum-classical correspondence of the asymptotic regime for $\tilde{Q} = \infty, \beta = 0.5, \nu_d = 3.5, \xi_d = 0.75$ and $\lambda = 0.2$. (a) 6 orbits of the Poincaré map $\mathcal{P}$ are plotted over 300 iterations of $\mathcal{P}$. Each different orbit is plotted in a different color. The red-shaded orbits correspond to irrational flow on nested invariant tori [2, 45, 74, 94] encircling the nominal fixed point of $\mathcal{P}$ (corresponding to a harmonic, $2\pi/\nu_d$-periodic continuous-time trajectory). The green-shaded orbits are seen to encircle a 3-orbit of $\mathcal{P}$ with three different phases. The blue-shaded orbits encircle both the nominal fixed point, as well as the 3-orbit of $\mathcal{P}$ corresponding to this $(3:1)$-resonance. For a finite $\tilde{Q}$, the red orbits slowly spiral into the nominal fixed point, which then corresponds to a stable node. A similar conclusion holds for the green orbits and the 3-orbit of $\mathcal{P}$. (b) Husimi Q-function of ρ_∞ at time $\tau = 0 \bmod 2\pi/\nu_d$. Note the uniform distribution of ρ_∞ over the three cat states $|\phi_k^\alpha(0)\rangle, k = 0, 1, 2$, or equivalently over three coherent states $|\alpha_l\rangle, l = 0, 1, 2$. The locations of the 3 coherent states displayed in the Husimi Q-function are seen to correspond to the classical phases of the 3-orbit of $\mathcal{P}$ up to very good accuracy.

Figure 4.3 shows the phase portrait of $\mathcal{P}$ in the dissipationless case of $\tilde{Q} = \infty$ (a) alongside the Husimi-Q function of the asymptotic state ρ_∞ at times $\tau = 0 \bmod 2\pi/\nu_d$ (b). The Husimi-Q function will be the preferred representation for ρ_∞, as the Wigner representation does not show an interference pattern for ρ_∞ in any case, and the Husimi-Q representation shows a closer analogy to the classical system. Encircled by a family of quasiperiodic orbits [1] shown in red in Figure 4.3(a), $\mathcal{P}$ admits a fixed point $(x^{(\mathrm{h})}, p^{(\mathrm{h})})$,

$$\mathcal{P}\left(x_1^{(\mathrm{h})}, p_1^{(\mathrm{h})}\right) = (x_1^{(\mathrm{h})}, p_1^{(\mathrm{h})}),$$

[1] These quasiperiodic orbits correspond to irrational flow on nested two-dimensional invariant tori [2, 74, 94] of the suspended system (where τ is considered a dynamical variable with $\dot{\tau} = 1$), enclosing the subharmonic orbit.

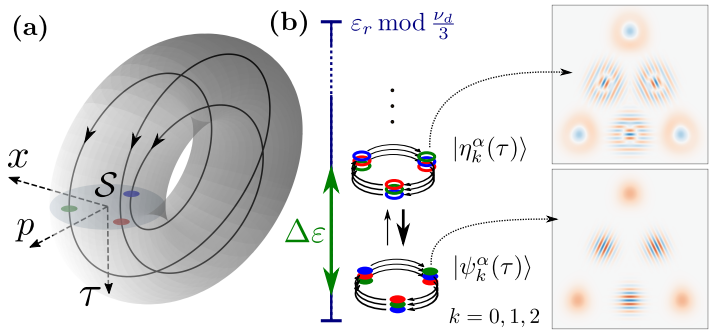

Figure 4.4: Schematic depiction of the observed quantum-classical correspondence in the context of Schrödinger cat Floquet modes. (a) Illustration of the dynamics of the classical periodic planar system (4.13) with two standard axes x, p and time τ considered as a third periodic variable. A (3:1) subharmonic trajectory is shown in black, intersecting the surface of the Poincaré section $\mathcal{S}$ in three points (red, blue and green). (b) Schematic depiction of the equivalent quantum system given by the Hamiltonian (4.7). The periodically driven system is characterized by the Floquet modes of the Hamiltonian. At the (3:1)-resonance, we observe three Floquet modes $|\phi_k^\alpha(\tau)\rangle$ with quasi-energies degenerate modulo $\nu_d/3$. The Floquet modes superposition $|\phi_k^\alpha(\tau)\rangle$ can be mapped, qualitatively and quantitatively, to the three amplitudes on (a), with Floquet choice $\tau = 0 \bmod 2\pi/\nu_d$ corresponding to the choice of intersection time for the Poincaré section $\mathcal{S}$. Concerning the cat-confinement, assuming a zero-temperature flat spectrum bath (see (3.42)), the $|\phi_k^\alpha(\tau)\rangle$ are dominantly populated in the asymptotic regime. The three Floquet modes $|\eta_k^\alpha(\tau)\rangle$ represent the most coupled excited states that are also populated in this asymptotic regime. The gap $\Delta\varepsilon$ between the quasi-energies of $|\eta_k^\alpha(\tau)\rangle$ and $|\phi_k^\alpha(\tau)\rangle$ provides protection of the three-component Schrödinger cat state during fast Hamiltonian gates. Wigner functions associated to these Floquet modes are represented for $k = 0$ and at time $\tau \equiv 0$ modulo $2\pi/\nu_d$.

corresponding to a $2\pi/\nu_d$-periodic *harmonic* solution $(x^{(\mathrm{h})}(\tau), p^{(\mathrm{h})}(\tau))$ of (4.13), with $x^{(\mathrm{h})}(0) = x_1^{(\mathrm{h})}, p^{(\mathrm{h})}(0) = p_1^{(\mathrm{h})}$. Encircled by a family of quasiperiodic orbits shown in green, $\mathcal{P}$ admits a 3-orbit $\left\{(x_l^{(3:1)}, p_l^{(3:1)}), l = 0, 1, 2\right\}$, corresponding to 3 fixed points $(x_l^{(3:1)}, p_l^{(3:1)})$ of $\mathcal{P}^3$. The corresponding $6\pi/\nu_d$-periodic solution $(x^{3:1}(\tau), p^{(3:1)}(\tau))$ completes one lap around the harmonic solution $(x^{(\mathrm{h})}, p^{(\mathrm{h})})$ during its period $6\pi/\nu_d$ (not shown here). Hence the superscript $(n : m) = (3 : 1)$, since the subharmonic is of period $n = 3$ times the drive period, and completes $m = 1$ lap around the harmonic solution during its period (see Definition 4.1).

Definition 4.1. Consider a harmonic, $2\pi/\nu_d$-periodic solution $(x^{(\mathrm{h})}(\tau), p^{(\mathrm{h})}(\tau))$ of (4.13). An $(n : m)$-*subharmonic* is defined as a $2\pi n/\nu_d$-periodic solution $(x^{(n:m)}(\tau), p^{(n:m)}(\tau))$ of (4.13) that completes m laps[2] around the harmonic solution $(x^{(\mathrm{h})}(\tau), p^{(\mathrm{h})}(\tau))$ during its period $2n\pi/\nu_d$.

Now let us again consider the Husimi-Q representation of the asymptotic quantum state ρ_∞ in Figure 4.3(b). Consistent with (4.10), ρ_∞ predominantly has support on three coherent

[2]Note that two different solutions at the same time τ cannot cross, so this is well-defined.

states $|\alpha_l\rangle, l = 0, 1, 2$, and, moreover, we approximately have that

$$\alpha_l \simeq \frac{x_l^{(3:1)} + ip_l^{(3:1)}}{\sqrt{2}}.$$

This general quantum-classical correspondence is depicted schematically in Figure 4.4. In Figure 4.4 (a), the subharmonic orbit is shown in a representation where the time τ is considered a third dynamical variable, with $\dot{\tau} = 1$. This lifts the classical equations of motion to an autonomous dynamical system in 3D (so solutions are not allowed to cross), where τ should be considered a periodic variable, such that the state space corresponds to that of a torus if we consider a bounded domain for x and p. A $(3:1)$-subharmonic trajectory is shown in black. The three fixed points of $\mathcal{P}^3$ correspond to the intersection points of the trajectory with the Poincaré surface of section $\mathcal{S}$, which is defined by $\tau = 0 \bmod 2\pi/\nu_d$. The corresponding Floquet modes $|\phi_k^\alpha(\tau)\rangle$ are depicted schematically in Figure 4.4(b), and a Wigner representation at time $\tau = 0 \bmod 2\pi/\nu_d$ is included, showing that the $|\phi_k^\alpha(\tau)\rangle$ resemble cat states.

Comparing the Floquet-Markov simulations of the quantum system with the phase portrait of the classical Poincaré map for different drive parameters (ν_d, ξ_d), this quantum-classical correspondence is seen (simulations not shown here) to be valid for general $(n:m)$-subharmonics and general multi-component Schrödinger cat states. This leads us to Observation 4.1, summarizing the conclusions of this section.

Observation 4.1. *Consider a pair of positive coprime integers (n, m) and define the parity $r \coloneqq (n+m) \bmod 2$, so either $r = 0$ or $r = 1$. The existence of an $(n:m)$-subharmonic of (4.13) indicates the existence of $(1+r)n$ associated Floquet modes $|\phi_k^\alpha(\tau)\rangle$ of (4.7) that correspond to $(1+r)n$-component Schrödinger cat states. The corresponding quasi-energies $\varepsilon[|\phi_k^\alpha\rangle]$ are degenerate modulo $\frac{m}{n}\nu_d$, due to a multi-photon process where $(1+r)m$ drive photons at frequency ν_d are converted into $(1+r)n$ photons of the oscillator at frequency $\frac{m}{n}\nu_d$, and vice versa. Moreover, this manifold of cat states is spanned by states approximately of the form*

$$\begin{aligned} |\psi_k^\alpha(\tau)\rangle &\simeq \left|\mathcal{C}^\alpha_{k(\bmod (1+r)n)}\right\rangle \qquad (4.14)\\ &= \frac{1}{\mathcal{N}_k^{((1+r)n)}} \sum_{l=0}^{(1+r)n-1} e^{2i\frac{lk}{(1+r)n}\pi} \left|\alpha e^{-2i\frac{lm}{(1+r)n}\pi} e^{-i\frac{m}{n}\nu_d\tau}\right\rangle, \quad k = 0, \ldots, (1+r)n-1. \end{aligned}$$

This general correspondence motivates the study of classical $(n:m)$-subharmonics of the classical system as to find the drive parameters that lead to the confinement of a manifold of general multi-component cat states. Characterizing the set of $(n:m)$-subharmonics using perturbative techniques will be the subject of Chapter 5. To understand the role of the parity $r = (m+n) \bmod 2$ in Observation 4.1, we need to consider a global symmetry of the system which is due to the parity of the Josephson cosine potential, and which is treated in Section 4.1.4. Section 4.1.4 is not essential to follow the remainder of this chapter however.

4.1.4 Global symmetry from parity considerations

The system exhibits a global symmetry, linked with the parity of the Josephson cosine potential. We will discuss the consequences of this symmetry on the corresponding classical system, and link back to the consequences for the quantum system at the end of this subsection. This will allow us to explain the role of the parity $r = (m+n) \bmod 2$ in Observation 4.1.

Recalling the classical equations of motion (4.13) here,

$$\frac{\mathrm{d}x}{\mathrm{d}\tau} = p, \tag{4.15a}$$

$$\frac{\mathrm{d}p}{\mathrm{d}\tau} = -x - \frac{p}{\tilde{Q}} - \frac{\beta}{\sqrt{2}\lambda}\sin\Big(\sqrt{2}\lambda x + \xi_d \sin(\nu_d \tau)\Big), \tag{4.15b}$$

one can see that the transformation

$$\begin{cases} x & \to & -x, \\ p & \to & -p, \\ \tau & \to & \tau + \frac{\pi}{\nu_d}. \end{cases} \tag{4.16}$$

leaves (4.15) invariant, as all individual terms change sign. This symmetry implies that for any given solution $(x(\tau), p(\tau))$ of (4.15), another exact solution of the system is given by $(-x(\tau+\frac{\pi}{\nu_d}), -p(\tau+\frac{\pi}{\nu_d}))$. This observation has the consequence that when considering periodic orbits of $\mathcal{P}$, we can classify them into two distinct categories. Consider a harmonic solution $(x_1(\tau), p_1(\tau))$ with the period of the drive, i.e. $\frac{2\pi}{\nu_d}$-periodic. As a first case, we can have that

$$x_1\left(\tau + \frac{\pi}{\nu_d}\right) = -x_1(\tau), \quad \forall \tau \in \mathbb{R}, \tag{4.17a}$$

$$p_1\left(\tau + \frac{\pi}{\nu_d}\right) = -p_1(\tau), \quad \forall \tau \in \mathbb{R}, \tag{4.17b}$$

in which case we merely obtained a particular symmetry of the given solution. We will call harmonic solutions for which (4.17) is valid *symmetric harmonics*. Note that (4.17) immediately implies that the solution has the period of the drive, as $x_1(\tau) = -x_1(\tau + \frac{\pi}{\nu_d}) = (-1)^2 x_1(\tau+\frac{2\pi}{\nu_d}) = x_1(\tau+\frac{2\pi}{\nu_d})$, and analogously for p_1. As a second case, assume the orbit does not exhibit the symmetry (4.17), in which case we can immediately identify a second, different solution of the system. Both of the considered harmonics will then be called *non-symmetric harmonics*.

The same reasoning can be applied to n-orbits of $\mathcal{P}$, so considering a solution $(x_n(\tau), p_n(\tau))$ for which $(x_n(\tau), p_n(\tau)) = (x_n(\tau + \frac{2n\pi}{\nu_d}), p_n(\tau + \frac{2n\pi}{\nu_d}))$. Indeed, applying the symmetry (4.16) n times, we have a derived symmetry of the system:

$$\begin{cases} x & \to & (-1)^n x, \\ p & \to & (-1)^n p, \\ \tau & \to & \tau + \frac{n\pi}{\nu_d}. \end{cases} \tag{4.18}$$

We can similarly classify the n-orbits by asking the question if

$$x_n\left(\tau + \frac{n\pi}{\nu_d}\right) = (-1)^n x_n(\tau), \tag{4.19a}$$

$$p_n\left(\tau + \frac{n\pi}{\nu_d}\right) = (-1)^n p_n(\tau), \tag{4.19b}$$

holds or not. We can see that when n is even, this leads to a contradiction, as the period of the solution would be given by $\frac{\pi n}{\nu_d}$, corresponding to an $n/2$-orbit of $\mathcal{P}$. We can conclude

that an n-orbit of $\mathcal{P}$ cannot exhibit the symmetry (4.18) when n is even. However, when n is odd, the symmetry is well-defined. We then either have a so-dubbed *symmetric* n-orbit for which (4.19) is satisfied, or we can identify a second, different n-orbit of $\mathcal{P}$ corresponding to $(-x_n(\tau + \frac{n\pi}{\nu_d}), -p_n(\tau + \frac{n\pi}{\nu_d}))$.

The remaining question to be answered is which n-orbits of $\mathcal{P}$ adhere to the symmetry (4.18), and which do not. In numerical simulations of the Poincaré map, we observe that (not shown here) for the specific class of $(n:m)$-subharmonics defined in Definition 4.1, the subharmonic adheres to the symmetry whenever $n+m$ is even, whereas $(n:m)$-subharmonics where $m+n$ is odd are non-symmetric, and hence always come in pairs. While we do not have a general proof of this fact, we can gain some intuition by anticipating some of the results of Chapter 5. In Chapter 5, we show that for small enough values of β, for any pair of positive integers (m, n) that are *coprime*, there exists a prominent class of $(n:m)$-subharmonic solutions of the form

$$x^{(n:m)}(\tau) \simeq R\sin\Big(\frac{m}{n}\nu_d\tau + \theta\Big), \tag{4.20a}$$

$$p^{(n:m)}(\tau) \simeq R\cos\Big(\frac{m}{n}\nu_d\tau + \theta\Big), \tag{4.20b}$$

for some distance $R > 0$ and angle $\theta \in [0, 2\pi)$ that depend intricately on β and the drive parameters (ν_d, ξ_d). We can see that when $n+m$ is even (so both m and n are odd, as they are coprime), the solution (4.20) exhibits the symmetry (4.19), corresponding to a *symmetric* n-orbit of $\mathcal{P}$. When $n+m$ amounts to an odd number, the solution in question is *non-symmetric*. In this latter case, a second $(n:m)$-subharmonic resonance can readily be identified, by applying (4.18) to the original solution. We see numerically that this discussion remains valid for any $(n:m)$-subharmonic where n and m are coprime, whether they be approximately of the form (4.20) or not.

An analogous discussion for the quantum system can be made. We can make use of the following lemma to show that certain Floquet modes must necessarily come in pairs.

Lemma 4.2. *Consider a Floquet mode $|\phi(\tau)\rangle$ of the quantum Hamiltonian $\mathbf{H}(\tau)$ given in* (4.7) *with corresponding quasienergy ε,*

$$\left(H(\tau) - i\frac{\partial}{\partial\tau}\right)|\phi(\tau)\rangle = \varepsilon\,|\phi(\tau)\rangle\,.$$

Then

$$\left|\tilde{\phi}(\tau)\right\rangle \coloneqq e^{i\pi\mathbf{a}^\dagger\mathbf{a}}\left|\phi\left(\tau + \frac{\pi}{\nu_d}\right)\right\rangle$$

is also a Floquet mode of $\mathbf{H}(\tau)$, with the same quasienergy ε.

Proof. Recalling

$$\mathbf{H}(\tau) = \frac{\mathbf{p}^2}{2} + \frac{\mathbf{x}^2}{2} - \frac{\beta}{2\lambda^2}\cos\Big(\sqrt{2}\lambda\mathbf{x} + \xi_d\sin(\nu_d\tau)\Big),$$

it is easy to see that $\mathbf{H}(\tau)$ adheres to the symmetry

$$e^{i\pi\mathbf{a}^\dagger\mathbf{a}}\mathbf{H}\left(\tau + \frac{\pi}{\nu_d}\right) = \mathbf{H}(\tau)e^{i\pi\mathbf{a}^\dagger\mathbf{a}}.$$

This readily implies that

$$\begin{aligned}\left(H(\tau)-i\frac{\partial}{\partial\tau}\right)\left|\tilde{\phi}(\tau)\right\rangle &= \left(H(\tau)-i\frac{\partial}{\partial\tau}\right)e^{i\pi\mathbf{a}^\dagger\mathbf{a}}\left|\phi\left(\tau+\frac{\pi}{\nu_d}\right)\right\rangle \\ &= e^{i\pi\mathbf{a}^\dagger\mathbf{a}}\left(H\left(\tau+\frac{\pi}{\nu_d}\right)-i\frac{\partial}{\partial\tau}\right)\left|\phi\left(\tau+\frac{\pi}{\nu_d}\right)\right\rangle \\ &= \varepsilon e^{i\pi\mathbf{a}^\dagger\mathbf{a}}\left|\phi\left(\tau+\frac{\pi}{\nu_d}\right)\right\rangle \\ &= \varepsilon\left|\tilde{\phi}(\tau)\right\rangle.\end{aligned}$$

□

Lemma 4.2 implies that the Floquet modes must either be *symmetric*, with

$$e^{i\pi\mathbf{a}^\dagger\mathbf{a}}\left|\phi\left(\tau+\frac{\pi}{\nu_d}\right)\right\rangle = |\phi(\tau)\rangle\,, \tag{4.21}$$

or they must necessarily come in pairs of two *non-symmetric* Floquet modes $\left(|\phi(\tau)\rangle\,,\left|\tilde{\phi}(\tau)\right\rangle\right)$ with

$$\left|\tilde{\phi}(\tau)\right\rangle \coloneqq e^{i\pi\mathbf{a}^\dagger\mathbf{a}}\left|\phi\left(\tau+\frac{\pi}{\nu_d}\right)\right\rangle.$$

The question is again which Floquet modes of the system are symmetric and which are not. Using the approximate relation

$$|\psi_k^\alpha(\tau)\rangle \simeq \left|\mathcal{C}^\alpha_{k(\mathrm{mod}\ n)}\right\rangle \coloneqq \frac{1}{\mathcal{N}_k^{(n)}}\sum_{l=0}^{n-1} e^{2i\frac{lk}{n}\pi}\left|\alpha_0 e^{-2i\frac{lm}{n}\pi}e^{-i\frac{m}{n}\nu_d\tau}\right\rangle, k=0,\dots n-1, \tag{4.22}$$

with

$$\alpha_0 = \frac{iRe^{-i\theta}}{\sqrt{2}},$$

a completely analogous discussion as for the classical system shows that for a given pair of coprime integers (n,m), these correspond to symmetric Floquet modes only when $m+n$ is even (so both m and n are odd), and have to come in pairs when $m+n$ is odd. This explains why for $m+n$ odd, Observation 4.1 shows a doubling of the number of cat-state Floquet modes.

As a last point of this section, note that if we had considered a DC-biased Josephson potential

$$\beta\cos(\lambda x+\phi_{\text{bias}}+\xi_d\sin(\nu_d\tau)) \quad , \quad \phi_{\text{bias}}\neq 0,$$

then the symmetry (4.16) would be broken, as the corresponding term in the vector field (last term of (4.15b)) no longer exactly switches sign. Hence, if we had taken a different flux bias point in Section 3.1, this discrete symmetry would not have been present, and the condition that $m+n$ must be even would not be necessary in Observation 4.1.

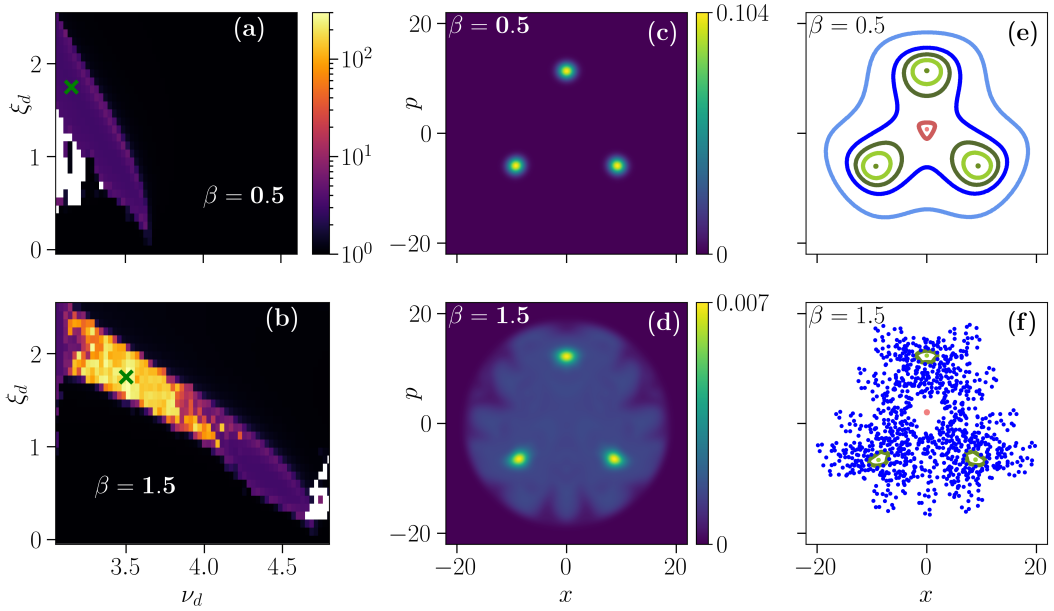

Figure 4.5: Floquet-Markov simulations of the weakly-dissipative quantum system governed by Hamiltonians (3.11) and (3.42), identifying the asymptotic quantum state ρ_∞ as a function of drive parameters ξ_d and ν_d. We target a (3:1)-resonance, for a fixed value of the quantum scaling parameter $\lambda = 0.2$ and two different values of the regularity parameter $\beta = 0.5$ (plots (a),(c),(e)) and $\beta = 1.5$ (plots (b),(d),(f)). Plots (a) and (b) show the effective number of Floquet modes N_{occ} over which the asymptotic periodic orbit is mixed (see (4.23)). We observe black zones with essentially one Floquet mode (harmonic regime), purple zones with essentially three Floquet modes $(\{|\phi_k^\alpha\rangle\}_{k=1,2,3}$ of Figure 4.4(b), representing the (3:1)-subharmonic regime), and yellow zones indicating a highly entropic ρ_∞. The white points in plots (a,b) indicate that the numerical simulations are inconclusive to determine ρ_∞, see Remark 4.1 for an explanation. The Husimi Q-functions shown in plots (c) and (d) correspond to the green cross on the associated plot of N_{occ}. Plot (c) essentially corresponds to an equal mixture of the degenerate Floquet modes $\{|\phi_k^\alpha\rangle\}_{k=1,2,3}$. Plot (d) shows the wave-packet explosion [23] characterizing a highly entropic asymptotic regime (note the different color map compared to (c)). Plots (e) and (f) show phase portraits of the Poincaré map $\mathcal{P}$ of the associated classical dynamics (3.14) in the limit of infinite $\tilde{Q}$. Each color corresponds to a different orbit of $\mathcal{P}$. In (e), we see a center close to the origin, associated to a harmonic solution, encircled by orbits in shades in red corresponding to nested invariant tori [2, 74, 94] enclosing the harmonic center. The orbits in green are seen to encircle three fixed points (centers) of $\mathcal{P}^3$ which appear as three distinct phases of the corresponding 3-orbit of $\mathcal{P}$. Finally, the blue orbits correspond to nested invariant tori enclosing the harmonic and subharmonic orbits. In plot (f), the harmonic and subharmonic solutions are still present but are enclosed by a vast chaotic region, densely covered by a single orbit plotted in blue. This chaotically covered region resembles the region covered by the wave-packet explosion in (d)

4.2 Signatures of classical chaos in asymptotic quantum regime

In this section, we perform a numerical study of the quantum system to analyze the effect of a first circuit parameter, namely the regularity parameter $\beta \coloneqq E_J/E_L$ that was introduced in Section 3.1.1. For this we focus on the asymptotic behavior of the system, captured by a classical probability distribution over the different Floquet modes:

$$\rho_\infty(\tau) = \sum_r p_r \left|\phi_r(\tau)\right\rangle\!\left\langle\phi_r(\tau)\right| .$$

Both the Floquet modes $|\phi_r\rangle$ and the occupation probabilities are calculated through the numerical Floquet-Markov simulations introduced in Section 3.2.2, according to the model introduced in Section 3.1, where the system is weakly coupled to a cold bath. We characterize this asymptotic behavior by the von Neumann entropy S of $\rho_\infty(\tau)$,

$$S(\rho_\infty) \coloneqq -\operatorname{Tr}(\rho_\infty \ln(\rho_\infty)) = -\sum_r p_r \ln(p_r),$$

i.e. the standard entropy of the classical probability distribution over Floquet modes. The effective number of occupied Floquet modes can subsequently be defined as

$$N_{\text{occ}} \coloneqq \exp(S(\rho_\infty)). \tag{4.23}$$

A state that is the uniform mixture of N_{occ} Floquet modes leads to the same von Neumann entropy as ρ_∞.

We fix $\lambda = 0.2$ and study the asymptotic regime for various values of β, while varying the drive parameters, focusing on the case of a $(3:1)$-resonance. Our findings are summarized in Figure 4.5, where we focus on two possible values of $\beta = 0.5, 1.5$. Plots (a) and (b) of Figure 4.5 show the effective number of modes N_{occ} as a function of the drive parameters. Plot 4.5(a), for $\beta = 0.5$, features two zones: the black one, corresponding to a dominant harmonic solution, and the purple one, corresponding to a dominant (3:1)-subharmonic solution. Indeed, a Husimi-Q function of $\rho_\infty(0)$ for drive parameters chosen in this subharmonic zone shows essentially a mixture of the three states $\left|\phi_k^\alpha(0)\right\rangle, k = 0, 1, 2$ (Figure 4.5(c)). In plot 4.5(b), for $\beta = 1.5$, a high-entropy zone appears in yellow. In this zone the subharmonic regime is essentially lost, and $\rho_\infty(\tau)$ spreads over a large portion of phase space, as seen in plot 4.5(d). This spreading is called *wave-packet explosion* and is a quantum signature of classical chaos in the weakly-dissipative regime [23]. Stronger dissipation (with respect to the Lyapunov exponents of classical chaos) would instead induce *wave-packet collapse* along a classical chaotic trajectory [23]. To investigate this classical dynamics, Figures 4.5(e,f) show the Poincaré maps corresponding to (3.16), for the same parameter values β, ν_d, ξ_d and in the limit of infinite $\tilde{Q}$. Each color represents an orbit associated to a different initial condition. Close to the origin of plot (e), a fixed point indicates a harmonic solution of (3.16), surrounded by closed orbits corresponding to invariant tori enclosing the harmonic center. Further from the origin, orbits encircling three points of the same color indicate a $6\pi/\nu_d$-periodic solution of (3.16), corresponding to three fixed points of $\mathcal{P}$. For a large yet finite $\tilde{Q}$ (not shown), the closed orbits become slowly winding spirals, indicating the asymptotic stability of the stable nodes. In plot (f), for $\beta = 1.5$ these regular features reduce to very small zones, while a large portion of phase space is covered by a single dense orbit, indicating a dominantly chaotic regime. The densely covered region is very similar to the wave packet explosion of plot (d).

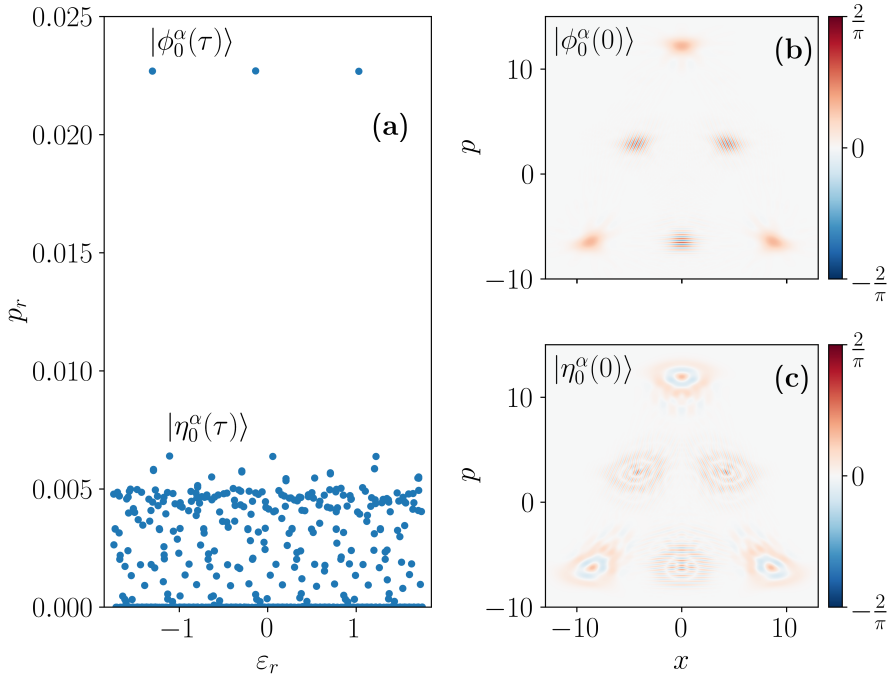

Figure 4.6: Characterization of ρ_∞ for the parameter values of Figure 4.5 (d) ($\beta = 1.5, \lambda = 0.2, \xi_d = 1.75, \nu_d = 3.5$). (a) The Floquet quasi-energies are plotted against their respective occupation probabilities in ρ_∞. We observe a triplet of most occupied states whose quasienergies are degenerate modulo $\nu_d/3$, indicating a $(3:1)$ resonance. The next-most occupied Floquet modes are seen to all be occupied to similar extents, and together make up 93% of the total population (mind the linear scaling for p_r). (b) Wigner representation of the most occupied Floquet mode, at time $\tau = 0$. We still roughly observe a symmetric superposition of three coherent states as in Figure 4.2, which however appear squeezed and distorted. (c) Wigner representation of the fourth-most occupied Floquet mode, at time $\tau = 0$. Instead of a symmetric coherent superposition of displaced Fock-$|1\rangle$-states as in Figure 4.2, we observe a distorted state closer to a symmetric superposition of displaced Fock-$|2\rangle$-states. The quasienergies of the next-occupied states densely fill up the first Brilluoin zone, showing the absence of an energy gap wth respect to the cat state manifold.

Remark 4.1. The white points in plots 4.5(a,b) indicate where the numerical Floquet-Markov simulations are inconclusive to determine the asymptotic behavior. We recall from Section 3.2.2, that the probabilities p_r are determined as the unique vector making up the kernel of the matrix R describing the transition rates between Floquet modes (see (3.48)). For the parameter values corresponding to the white points in plots 4.5(a,b), R exhibits two different eigenvectors of probabilities $(p_{A,r})$ and $(p_{B,r})$ that correspond to very small eigenvalues:

$$R\begin{pmatrix} p_{A,1} \\ p_{A,2} \\ \vdots \end{pmatrix} \simeq R\begin{pmatrix} p_{B,1} \\ p_{B,2} \\ \vdots \end{pmatrix} \simeq 0.$$

The kernel of R is then spanned by a probabilistic (convex) combination of situation A and situation B. In other words there is no unique steady state ρ_∞ for which to plot N_{occ}. For the white points of plot (a), both the harmonic regime (displaced vacuum) as well as the $(3:1)$ subharmonic regime are eigenvectors in the kernel of R. The white points in plot (b) represent a similar situation, but where both the $(3:1)$ and a $(5:1)$-resonance appear to approximately make up the kernel of R. In any case, the two situations A and B are always seen to correspond to *regular* situations, where only a handful of states are occupied (in case of a resonance), or where the system is in a pure state (displaced vacuum), and no chaotic regime is observed for the white points in plots 4.5(a,b). We would also like to stress that the computation of the Floquet modes that make up situation A and B have themselves fully converged in terms of the truncation of the Hilbert space. For the physical long-time evolution of the system, we can expect any distribution in the kernel of R to be long-lived, so both situations A and B should be metastable.

To get a different view on how the cat-confinement is broken by the chaotic regime, we plot the Floquet quasienergies ε_r against their respective occupation probabilities in Figure 4.6, for the drive parameters of Figure 4.5(d). Comparing to the regular case of Figure 4.2, we can see that a triplet of most-occupied Floquet modes can still be identified, vaguely resembling Schrödinger cat states, which appear severely distorted however. Moreover, together these three modes only make up 7% of the total population, as opposed to 99.6% in the regular case of Figure 4.2. The remaining Floquet modes are all occupied with probabilities that are of the same order of magnitude ($\sim 1/200$), and together make up 93% of the asymptotic state ρ_∞. Notably, the quasienergy spectral gap defined in (4.12) is ill-defined here, as no clear exited state can be designated that is most coupled to the cat state triplet, and we can see that quasi-energies corresponding to occupied Floquet modes seem to become dense.

Further Floquet-Markov simulations (not displayed here) show that for the range of drive parameters displayed in Figure 4.5(a,b), no highly entropic points are observed for any $\beta \leq 0.5$, and the plots of N_{occ} looks essentially similar (except for an AC-Stark shift [115] of the resonant drive frequencies that scales with β). Furthermore, also when varying λ (see the simulations in Figure 4.9, in Section 4.4), no chaotic behavior is observed for $\beta = 0.5$. This suggests the following general picture: for low enough values of $\beta \lesssim 0.5$, target subharmonics remain robustly stable when varying the drive amplitude and accounting for the AC Stark shift [115]. For larger values of $\beta \gtrsim 0.5$, ramping up the drive amplitude carries with it the danger of inducing a highly entropic regime instead of the target resonance. In the next section we propose a theoretical explanation compatible with these observations. Performing a system theoretical analysis on the classical equations of motion, we study what can be concluded using analytical tools, for small enough β.

4.3 Avoiding chaos in the classical system

In the previous section, numerical Floquet-Markov simulations indicated that when choosing the regularity parameter β small enough, we can seemingly suppress high-entropy asymptotic regimes for the periodically-driven dissipative nonlinear quantum system governed by 4.7. We further argued that such high entropy regimes go hand in hand with large chaotic regions in phase space for the corresponding classical system. In this section, we hence study the

behavior of the classical system (3.16), recalled here:

$$\frac{\mathrm{d}x_\lambda}{\mathrm{d}\tau} = p_\lambda, \tag{4.24a}$$

$$\frac{\mathrm{d}p_\lambda}{\mathrm{d}\tau} = -x_\lambda - \frac{p_\lambda}{\tilde{Q}} - \beta \sin(x_\lambda + \xi_d \sin(\nu_d \tau)). \tag{4.24b}$$

The goal of this section is to prove that taking β small enough would prevent (4.24) from displaying chaotic behavior. This would exclude the observed wave-packet explosion of Figure 4.5(d), and allow for a robust subharmonic regime of the system, corresponding to the confinement of Schrödinger cat states.

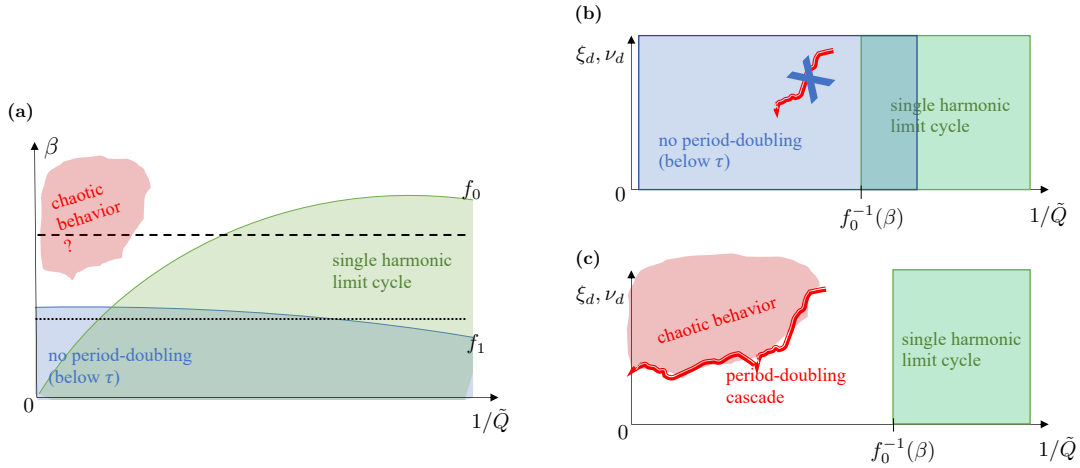

Figure 4.7: Schematic representation of the study on avoiding chaos in system (4.24). **(a)** For $\beta < f_0(1/\tilde{Q})$ given in (4.37), corresponding to dissipation dominating nonlinearity, the system is contracting [86] and all solutions are attracted towards a single asymptotic limit cycle (green region), regardless of the values of the drive parameters (ξ_d, ν_d). For $\beta < f_1(1/\tilde{Q}, \bar{\tau})$ given by (4.58), which admits arbitrarily low dissipation, a period-doubling bifurcation is excluded, regardless of the values of the drive parameters (ξ_d, ν_d), for all solutions of period shorter than $\bar{\tau}$ (blue region). This is useful, as the Gambaudo-Tresser conjecture (here Conjecture 4.6) states that if a region of parameters featuring chaotic behavior exists (red region on plots (a) and (c)), then a period-doubling cascade must exist at its boundary. **(b)** Having fixed β at a low value, as indicated by the dotted line on plot (a), the green and blue regions as a function of the remaining parameters $(1/\tilde{Q}, \xi_d, \nu_d)$ cover the whole parameter space. This excludes the existence of a period-doubling cascade, and thus of chaotic behavior for any values of $(1/\tilde{Q}, \xi_d, \nu_d)$, unless the cascade is initiated by a first period-doubling of a subharmonic of period larger than $\bar{\tau}$. This absence of chaos would correspond to the parameter values of Figure 4.5(e), except now for a finite $\tilde{Q} < \infty$. **(c)** Fixing β at a higher value, as indicated by the dashed line on plot (a), there exists a parameter region (outside both green and blue region) where a period-doubling cascade can be expected, such that regions featuring chaotic behavior (red zone) can exist. Such chaotic behavior is indeed observed for parameter values as in Figure 4.5(f), also with a finite $\tilde{Q} < \infty$.

The general approach to prove the absence of chaotic behavior for small β is illustrated in Figure 4.7, and goes as follows.

- When the dissipation rate $1/\tilde{Q}$ dominates the regularity parameter β (green zone in Figure 4.7), we can prove that the system is contracting, i.e. any two close solutions converge towards each other, such that the asymptotic regime has to feature a single limit cycle that is globally attractive. This is valid for any values of the drive parameters (ξ_d, ν_d), see Section 4.3.2. Our goal is to extend the conclusion about the absence of chaos, from strong dissipation $1/\tilde{Q}$ to weak dissipation, while at the same time allowing for additional subharmonic solutions.

- For appropriately fixed β, the remaining parameters $(1/\tilde{Q}, \xi_d, \nu_d)$ thus feature a region where (4.24) converges to a single limit cycle, hence there is no chaos. If there exists another parameter region featuring chaotic behavior, then it has been conjectured that the boundary to this region has to feature a period-doubling cascade – see the Gambaudo-Tresser conjecture, here Conjecture 4.6 in Section 4.3.3.

- Thus, conversely, by excluding the possibility of period-doubling bifurcations in a parameter region overlapping with the green zone, we exclude the existence of a chaotic regime within this parameter region. For the particular system (4.24), we prove that period-doubling is indeed impossible, at least for solutions of period smaller than $\bar{\tau}$, provided β is small enough compared to $1/\bar{\tau}$. This criterion allows arbitrarily weak dissipation and any values for the drive parameters (blue zone in Figure 4.7). For this, see Corollary 4.11 in Section 4.3.4.

- All these elements together thus indicate that for low enough β, even for extremely small damping and for any values of drive parameters, the classical system should not transition into a chaotic regime. The addition of two remaining points would make this a rigorous result: (i) proving the Gambaudo-Tresser conjecture, which was recently done under extra technical conditions in [31], and (ii), proving a bound similar to Corollary 4.11 but independent of the period of the solution.

To simplify the mathematical analysis, in Section 4.3.1 we first perform a last change of variables on (4.24). We also derive the linearized dynamics around a trajectory of the system, i.e. the differential equation governing how small deviations from this trajectory will evolve over time.

4.3.1 Final change of variables and local linearization around a solution

The goal of our last change of variables is to obtain equal dissipation rates for both state variables. For this, we replace p by a hyperbolically-rotated quadrature, defining

$$\tilde{p} \coloneqq \frac{p + \frac{x}{2\tilde{Q}}}{\sqrt{1 - \frac{1}{4\tilde{Q}^2}}}, \quad \tilde{x} = x \,, \tag{4.25}$$

and we rescale time as:

$$s \coloneqq \sqrt{1 - \frac{1}{4\tilde{Q}^2}}\, \tau \,. \tag{4.26}$$

Defining the modified parameters

$$\tilde{\beta} = \frac{\beta}{1 - \frac{1}{4\tilde{Q}^2}}, \tag{4.27a}$$

$$\tilde{\nu}_d = \frac{\nu_d}{\sqrt{1 - \frac{1}{4\tilde{Q}^2}}}, \tag{4.27b}$$

$$\kappa = \frac{1}{2\tilde{Q}\sqrt{1 - \frac{1}{4\tilde{Q}^2}}}, \tag{4.27c}$$

we obtain the following model:

$$\frac{\mathrm{d}}{\mathrm{d}s}\tilde{x} = \quad \tilde{p} - \kappa\tilde{x}, \tag{4.28a}$$

$$\frac{\mathrm{d}}{\mathrm{d}s}\tilde{p} = -\tilde{x} - \kappa\tilde{p} - \tilde{\beta}\sin(\tilde{x} + \xi_d \sin(\tilde{\nu}_d s)). \tag{4.28b}$$

We define the vector field $f(\tilde{x}, \tilde{p}, s)$ such that

$$\frac{\mathrm{d}}{\mathrm{d}s}\begin{pmatrix}\tilde{x}\\ \tilde{p}\end{pmatrix} = f(\tilde{x}, \tilde{p}, s) \coloneqq \begin{pmatrix}\tilde{p} - \kappa\tilde{x}\\ -\tilde{x} - \kappa\tilde{p} - \tilde{\beta}\sin(\tilde{x} + \xi_d \sin(\tilde{\nu}_d s))\end{pmatrix}, \tag{4.29}$$

and denote the flow corresponding to system (4.29) by $\Psi_s : \mathbb{R}^2 \to \mathbb{R}^2, s \in \mathbb{R}$, such that by definition

$$\frac{\partial}{\partial s}\Psi_s(\tilde{x}_0, \tilde{p}_0) = f(\Psi_s(\tilde{x}_0, \tilde{p}_0), s). \tag{4.30}$$

The Poincaré map $\mathcal{P}$, which propagates any initial condition over one period $2\pi/\tilde{\nu}_d$, thus corresponds to

$$\mathcal{P} = \Psi_{\frac{2\pi}{\tilde{\nu}_d}}.$$

We now turn to local linearization. Given any solution $(\tilde{x}^{(b)}(s), \tilde{p}^{(b)}(s)) = \Psi_s(\tilde{x}_0^{(b)}, \tilde{p}_0^{(b)})$ of the system (4.29), we can investigate how small variations $(\Delta\tilde{x}_0, \Delta\tilde{p}_0)$ of the initial condition evolve under the same dynamics,

$$\Psi_s(\tilde{x}_0^{(b)} + \Delta\tilde{x},\ \tilde{p}_0^{(b)} + \Delta\tilde{p}) \quad = \quad (\tilde{x}^{(b)}(s) + \Delta\tilde{x}_s,\ \tilde{p}^{(b)}(s) + \Delta\tilde{p}_s)\ .$$

At the limit of infinitesimal $(\Delta\tilde{x}_0, \Delta\tilde{p}_0)$, the corresponding dynamics is given by the linearization of the vector field around the solution, i.e.:

$$\begin{aligned}\frac{\mathrm{d}}{\mathrm{d}s}\begin{pmatrix}\Delta\tilde{x}_s\\ \Delta\tilde{p}_s\end{pmatrix} &= \boldsymbol{\nabla}_z f(z, s)\big|_{z=(\tilde{x}^{(b)}(s), \tilde{p}^{(b)}(s))}\begin{pmatrix}\Delta\tilde{x}_s\\ \Delta\tilde{p}_s\end{pmatrix} \\ &= \begin{pmatrix}-\kappa & 1\\ -1 - \tilde{\beta}\cos\big(\tilde{x}^{(b)}(s) + \xi_d \sin(\tilde{\nu}_d s)\big) & -\kappa\end{pmatrix}\begin{pmatrix}\Delta\tilde{x}_s\\ \Delta\tilde{p}_s\end{pmatrix}.\end{aligned} \tag{4.31}$$

Once a solution $(\tilde{x}^{(b)}(s), \tilde{p}^{(b)}(s))$ is known, the linear time-dependent equation (4.31) enables the study of the system in that solution's vicinity. We will denote the flow corresponding to this linear system as $\Phi_s \in \mathbb{R}^{2\times 2}$, thus satisfying

$$\begin{pmatrix}\Delta\tilde{x}_s\\ \Delta\tilde{p}_s\end{pmatrix} = \Phi_s\begin{pmatrix}\Delta\tilde{x}_0\\ \Delta\tilde{p}_0\end{pmatrix}, \tag{4.32}$$

with

$$\frac{\mathrm{d}}{\mathrm{d}s}\Phi_s \;=\; \begin{pmatrix} -\kappa & 1 \\ -1-\tilde{\beta}\cos\big(\tilde{x}^{(b)}(s)+\xi_d\sin(\tilde{\nu}_d s)\big) & -\kappa \end{pmatrix}\Phi_s\;. \tag{4.33}$$

By integrating over n drive periods, we obtain the local linearization of the n'th power of the Poincaré map around the chosen initial condition:

$$\boldsymbol{\nabla}(\mathcal{P}^n)(\tilde{x}_0^{(b)},\tilde{p}_0^{(b)}) = \Phi_{2n\pi/\tilde{\nu}_d} \quad , \quad n\in\mathbb{N}. \tag{4.34}$$

In particular, when $(\tilde{x}_0^{(b)},\tilde{p}_0^{(b)})$ corresponds to a fixed point of $\mathcal{P}^n$, we can obtain the flow of the linearized system by applying a time-independent linear map:

$$\boldsymbol{\nabla}\Big(\mathcal{P}^{nk}\Big)(\tilde{x}_0^{(b)},\tilde{p}_0^{(b)}) = \Big(\boldsymbol{\nabla}(\mathcal{P}^n)(\tilde{x}_0^{(b)},\tilde{p}_0^{(b)})\Big)^k = \Phi_{2nk\pi/\tilde{\nu}_d} \quad , \quad k,n\in\mathbb{N}. \tag{4.35}$$

4.3.2 When $\frac{1}{\tilde{Q}}$ dominates β: single asymptotic limit cycle

If any two close trajectories asymptotically converge towards each other, then by induction the asymptotic regime of the system has to consist of a single trajectory. We here prove that our system (4.29) satisfies the first property, known as contraction in the dynamical systems theory [86], for $1/\tilde{Q}$ sufficiently large compared to $\tilde{\beta}$, and for any values of the drive parameters $(\xi_d,\tilde{\nu}_d)$. We further prove that the asymptotic trajectory must be a regular $2\pi/\tilde{\nu}_d$-periodic limit cycle.

Contraction thus analyzes local variations between two close trajectories, and therefore it studies the linearized vector field (4.31). In particular, contraction at a rate $r>0$ holds if we can prove that

$$\frac{\mathrm{d}}{\mathrm{d}s}\big(\Delta\tilde{x}^2+\Delta\tilde{p}^2\big) < -r\,(\Delta\tilde{x}^2+\Delta\tilde{p}^2)\;, \tag{4.36}$$

for any values of $\tilde{x}^{(b)}(s)$ and s in (4.31).

Lemma 4.3. *The system* (4.29) *is a contraction, i.e. it satisfies* (4.36) *for a fixed* $r>0$ *independently of* $\tilde{x}^{(b)}(s)$, $\tilde{p}^{(b)}(s)$ *and* s, *for any values of the drive parameters, provided*

$$\beta < \frac{\sqrt{1-\frac{1}{4\tilde{Q}^2}}}{\tilde{Q}}\;. \tag{4.37}$$

Proof. Writing out $\frac{\mathrm{d}}{\mathrm{d}s}\big(\Delta\tilde{x}^2+\Delta\tilde{p}^2\big)$ gives a quadratic expression in $(\Delta\tilde{x},\Delta\tilde{p})$, which satisfies (4.36) provided

$$(\kappa-r)(\Delta\tilde{x}^2+\Delta\tilde{p}^2)+\tilde{\beta}\cos\Big(\tilde{x}^{(b)}(s)+\xi_d\sin(\tilde{\nu}_d s)\Big)\Delta\tilde{x}\Delta\tilde{p}\geq 0\;.$$

This readily gives the bound $\tilde{\beta}/2<\kappa$, which translates into (4.37). □

Under condition (4.37), any trajectory of our system is thus attracted towards a single asymptotic solution. We can further prove that this solution must be a $2\pi/\tilde{\nu}_d$-periodic limit cycle. We separate the statement into two steps, as the first one will be useful in other contexts.

Lemma 4.4. *Any disk around the origin of radius larger than* $\tilde{\beta}/\kappa = \frac{2\beta\tilde{Q}}{\sqrt{1-\frac{1}{4\tilde{Q}^2}}}$ *remains positively invariant under the evolution of the system* (4.29)*, i.e. when starting on this disk the trajectory moves into its interior and stays there for all times.*

Proof. Writing out $\frac{\mathrm{d}}{\mathrm{d}s}\big(\tilde{x}^2+\tilde{p}^2\big)$, we readily see that it is negative as soon as $\kappa(\tilde{x}^2+\tilde{p}^2) > \tilde{\beta}|\tilde{p}|$, which holds under the stated condition on the radius. □

Lemma 4.5. *For any values of the parameters, the system* (4.29) *always features a solution that is a* $2\pi/\tilde{\nu}_d$*-periodic trajectory.*

Proof. The proof uses the Brouwer fixed-point theorem on the Poincaré map $\mathcal{P}$. This theorem states that any continuous function which maps a closed disk onto its interior must admit at least one fix point inside this disk. The function $\mathcal{P}$ is continuous as resulting from integrating a smooth vector field, and by Lemma 4.4 it maps any disk around the origin of radius larger than $\tilde{\beta}/\kappa$ onto its interior. Therefore $\mathcal{P}$ must always feature a fixed point, corresponding to a $2\pi/\tilde{\nu}_d$-periodic trajectory of (4.29). □

4.3.3 Linking chaos to period-doubling cascades

The system (4.29) is a *dissipative*, periodically-driven, planar, nonlinear system. For such systems, it has been conjectured that the only possible route to chaos upon varying parameters is through a period-doubling cascade starting from an initially-stable orbit. More precisely:

Conjecture 4.6. (Gambaudo, Tresser, [31, 46]) *In the space of* $\mathcal{C}^k$ *orientation-preserving embeddings of a planar disk, with* $k > 1$*, which are area-contracting, generically, maps which belong to the boundary of positive topological entropy have a set of periodic orbits which, except for a finite subset, is made of an infinite number of periodic orbits with periods* $m2^k$ *for a given* m *and all* $k \in \mathbb{N}$*.*

The conditions of Conjecture 4.6 hold for our Poincaré map $\mathcal{P}$ associated to (4.29), as a function of the parameters $(1/\tilde{Q}, \xi_d, \nu_d)$. Indeed:

- $\mathcal{P}$ is smooth for any parameter values, as resulting from the integration of a smooth vector field.
- $\mathcal{P}$ embeds any disk of radius larger than $\tilde{\beta}/\kappa$ into itself, as established by Lemma 4.4. Thus, for any fixed β and any strictly positive interval $\frac{1}{\tilde{Q}} \in [\frac{1}{\tilde{Q}_{\max}}, \frac{1}{\tilde{Q}_{\min}}] \subset \big(0, \frac{1}{2}\big)$, there exists a disk of sufficient radius for which the embedding holds for all parameter values.
- $\mathcal{P}$ is orientation-preserving and area-contracting for any $(1/\tilde{Q}, \xi_d, \nu_d)$ with $1/\tilde{Q} > 0$. These are both local features to be checked uniformly in $(\tilde{x}, \tilde{p})$ on the linearized Poincaré map $\boldsymbol{\nabla}\mathcal{P}(\tilde{x}, \tilde{p})$. Orientation is preserved if $\det(\boldsymbol{\nabla}\mathcal{P}) > 0$ and area is contracted if $|\det(\boldsymbol{\nabla}\mathcal{P})| < 1$. From (4.33), we have

$$\frac{\mathrm{d}}{\mathrm{d}s}\det(\Phi_s) = \mathrm{tr}\begin{pmatrix} -\kappa & 1 \\ -1-\tilde{\beta}\cos\big(\tilde{x}^{(b)}(s)+\xi_d\sin(\tilde{\nu}_d s)\big) & -\kappa \end{pmatrix}\det(\Phi_s) = -2\kappa\ \det(\Phi_s)$$

and integrating from $\det(\Phi_0) = 1$ up to $s = 2\pi/\tilde{\nu}_d$ we readily obtain

$$\det(\boldsymbol{\nabla}\mathcal{P}) = \exp\!\left(-\frac{4\pi\kappa}{\tilde{\nu}_d}\right) \in (0,1)\ .$$

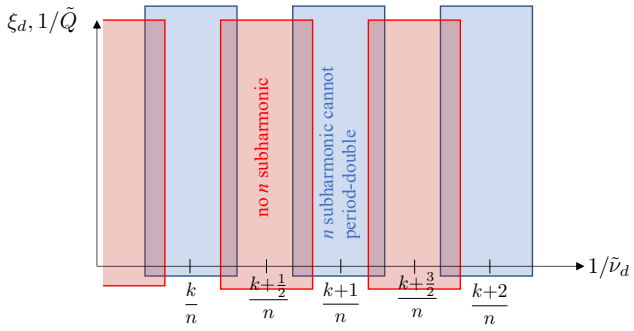

Figure 4.8: Splitting of the parameter space for the two parts of our proof excluding period-doubling bifurcation of a $2\pi n/\tilde{\nu}_d$-periodic solution of (4.29).

> Physically, these properties hold by virtue of $\mathcal{P}$ being generated by a weakly dissipative system, that reduces to a Hamiltonian system for $\kappa = 0$.

We illustrate how this conjecture will be used in the context of our study, see Figure 4.7(b)-(c). For fixed β, consider an open set of values for the parameters $(1/\tilde{Q}, \xi_d, \nu_d)$, which we will vary to define the set of maps. In particular, the values of $1/\tilde{Q}$ should span an interval ranging from the lowest damping expected, up to a value satisfying Lemma 4.3 in Section 4.3.2 (green zone on Fig.4.7(b)). Thanks to Lemma 4.3, the set of parameter values thus contains settings (green zone) for which the system asymptotically converges to a single harmonic orbit. According to Conjecture 4.6, if the set of parameter values also contains settings for which the system features "positive topological entropy", which is the technical definition of what we have been calling "chaos" (red zone on Figure 4.7(c)), then somewhere between these two types of settings there must be a boundary with a period-doubling cascade. In the next section, to conclude our study, we will thus try to exclude the existence of a parameter region featuring chaotic behavior, by establishing conditions that exclude its boundary, i.e. period-doubling (blue zone on Fig.4.7(b)).

We note that the Gambaudo-Tresser conjecture has recently been proven under extra technical conditions in [31].

4.3.4 A bound on β to exclude period-doubling

From the previous sections, we have identified that the transition to a chaotic regime when $(\xi, \nu_d, 1/\tilde{Q})$ are varied, must involve the period-doubling bifurcation of periodic orbits of the system. In this last section, we establish that taking β low enough excludes a period-doubling bifurcation for any subharmonic solution of (4.24), at least if the period of this subharmonic is lower than $\bar{\tau}$, with the bound on β depending on $\bar{\tau}$. The bound is uniformly valid for any values of the drive amplitude ξ_d and for arbitrarily low dissipation $1/\tilde{Q}$.

We thus consider as starting point a fixed maximal period of $\bar{\tau}$. If we want to exclude the period doubling of a given subharmonic solution of (4.24) of period $2\pi n/\nu_d$, we must assume that $2\pi n/\nu_d < \bar{\tau}$ remains valid for any values of ν_d, bounded away from zero. We then want to exclude that the considered solution undergoes a period-doubling bifurcation when varying $(\nu_d, \xi_d, 1/\tilde{Q})$ in the relevant parameter range. Our proof again works with the slightly changed

coordinates (4.29) and slightly modified parameters $(\tilde{\beta}, \tilde{\nu}_d)$, and it comprises two parts, see Figure 4.8:

- In Section 4.3.4.1, we perform a local study close to the considered subharmonic, establishing a bound on $\tilde{\beta}$ under which the premises for a period-doubling bifurcation can be excluded. This local study provides a conclusive bound only for some parameter region (blue zone on Figure 4.8).
- In Section 4.3.4.2, for another parameter region (red on Fig.4.8), we perform a global study in phase space, showing that for low enough $\tilde{\beta}$ the $2\pi n/\tilde{\nu}_d$-periodic solution cannot exist.

These two parameter regions are defined as bands with $1/\tilde{\nu}_d$ centered respectively around integer and half-integer multiples of $1/n$. (Recall that in (4.29) the natural frequency of the harmonic oscillator for $\tilde{\beta} = 0$ has been normalized to 1.) Making these two regions overlap (Section 4.3.4.3), we exclude any period-doubling bifurcation of this solution within the full parameter range.

4.3.4.1 Values of $\tilde{\beta}$ and $\tilde{\nu}_d$ excluding period-doubling

Consider a fixed point $(\tilde{x}^*, \tilde{p}^*)$ of the smooth map $\mathcal{P}^n$, corresponding to the continuous-time trajectory $(\tilde{x}_n(s), \tilde{p}_n(s))$ with $(\tilde{x}_n(0), \tilde{p}_n(0)) = (\tilde{x}^*, \tilde{p}^*)$, for some fixed parameter values. When varying parameters, the location and the stability of the fixed point must vary smoothly, unless it undergoes a bifurcation. A good introduction to basic bifurcation theory can be found in [57]. We are focusing on period-doubling bifurcations, where the initial solution becomes unstable while a stable periodic orbit of double the period appears in its vicinity. The important property for our purposes is that at any point where $(\tilde{x}_n(s), \tilde{p}_n(s))$ undergoes a period-doubling bifurcation, the linearized Poincaré map $\boldsymbol{\nabla}(\mathcal{P}^n)(\tilde{x}^*, \tilde{p}^*)$ must have an eigenvalue crossing -1 [57]. In order to exclude a period-doubling bifurcation, we thus set out to bound the eigenvalues of $\boldsymbol{\nabla}(\mathcal{P}^n)$ away from -1. Due to the absence of an exact expression for the subharmonic solution $(\tilde{x}_n(s), \tilde{p}_n(s))$, we approximate $\boldsymbol{\nabla}(\mathcal{P}^n)(\tilde{x}^*, \tilde{p}^*)$ by splitting the flow Ψ_s up into a known part, based on the linear part of the system, and an unknown part that we treat as a perturbation, proportional to $\tilde{\beta}$. We obtain the following result.

Lemma 4.7. *Fix $\tilde{\nu}_d > 0$, and $n \in \mathbb{N}, n \geq 1$. Choose the $m \in \mathbb{N}$ which minimizes $\left|1 - \frac{m}{n}\tilde{\nu}_d\right|$, and define the detuning*

$$\delta := 1 - \frac{m}{n}\tilde{\nu}_d. \tag{4.38}$$

for which thus $|\delta| \leq \frac{\tilde{\nu}_d}{2n}$. If

$$\exp\left(\tilde{\beta}\frac{4\pi n}{\tilde{\nu}_d}\right) - 1 \quad < \quad 2\cos\left(\bar{\delta}\frac{\pi n}{\tilde{\nu}_d}\right) \quad \text{, with} \quad |\delta| \leq \left|\bar{\delta}\right| \leq \frac{\tilde{\nu}_d}{2n}. \tag{4.39}$$

then $\boldsymbol{\nabla}(\mathcal{P}^n)(\tilde{x}, \tilde{p})$ obtained by integrating (4.33) cannot exhibit an eigenvalue -1 for any point $(\tilde{x}, \tilde{p}) \in \mathbb{R}^2$. Therefore, under condition (4.39), a $2\pi n/\tilde{\nu}_d$-periodic subharmonic cannot undergo a period-doubling bifurcation.

Proof. The proof is organized as follows.

- We first perform a change of variables that integrates out the time-independent part of the linearized dynamics determining, which is also independent of $\tilde{\beta}$.
- We then bound the spectral norm [3] of the flow operator corresponding to this linearized dynamics uniformly in the remaining parameters. This bounds the effect of the terms proportional to $\tilde{\beta}$.
- From this, we next bound the spectral norm of the difference between the flow operator at time $s = 0$ (which is the identity matrix) and the flow at any time s later.
- Finally, we use this proximity in spectral norm to deduce information about the eigenvalues of the original flow operator, in particular evaluating a parameter setting which guarantees that the eigenvalues cannot reach -1.

• *Change of variables:* We start by moving to a rotating frame with frequency $\frac{m}{n}\tilde{\nu}_d$, such that

$$\begin{pmatrix} u(s) \\ v(s) \end{pmatrix} \coloneqq \begin{pmatrix} \cos\left(\frac{m}{n}\tilde{\nu}_d s\right) & -\sin\left(\frac{m}{n}\tilde{\nu}_d s\right) \\ \sin\left(\frac{m}{n}\tilde{\nu}_d s\right) & \cos\left(\frac{m}{n}\tilde{\nu}_d s\right) \end{pmatrix} \begin{pmatrix} \tilde{x}(s) \\ \tilde{p}(s) \end{pmatrix}. \tag{4.40}$$

Note that for the flow $\Psi_s^{(n:m)}$ corresponding to the variables (u, v) we still have $\Psi_{T_n}^{(n:m)} = \Psi_{T_n} = \mathcal{P}^n$, where we introduced the total period

$$T_n = \frac{2\pi n}{\tilde{\nu}_d},$$

due to the periodicity of the change of variables, Applying the change of variables to (4.33), we obtain the following evolution equation for $\boldsymbol{\nabla}\Psi_s^{(n:m)}(u_0, v_0)$, the linearized flow around an arbitrary solution $(u(s), v(s))$ with $(u(0), v(0)) = (u_0, v_0)$:

$$\frac{\partial}{\partial s}\boldsymbol{\nabla}\Psi_s^{(n:m)}(u_0, v_0) = \left(-\kappa\begin{pmatrix} 1 & 0 \\ 0 & 1 \end{pmatrix} + \delta\begin{pmatrix} 0 & 1 \\ -1 & 0 \end{pmatrix} + \tilde{\beta}\,\Gamma_s^{(n:m)}(u(s), v(s), \xi_d)\right)\boldsymbol{\nabla}\Psi_s^{(n:m)}(u_0, v_0), \tag{4.41}$$

where

$$\Gamma_s^{(n:m)}(u(s), v(s), \xi_d) := \cos(\zeta(s))\begin{pmatrix} \sin\left(\frac{m}{n}\tilde{\nu}_d s\right)\cos\left(\frac{m}{n}\tilde{\nu}_d s\right) & \sin^2\left(\frac{m}{n}\tilde{\nu}_d s\right) \\ -\cos^2\left(\frac{m}{n}\tilde{\nu}_d s\right) & -\sin\left(\frac{m}{n}\tilde{\nu}_d s\right)\cos\left(\frac{m}{n}\tilde{\nu}_d s\right) \end{pmatrix},$$

with $\zeta(s) = u(s)\cos\left(\frac{m}{n}\tilde{\nu}_d s\right) + v(s)\sin\left(\frac{m}{n}\tilde{\nu}_d s\right) + \xi_d \sin(\tilde{\nu}_d s)$. We will drop the reference to the particular solution $(u_0(s), v_0(s))$ for notational convenience.

To conclude the proof we must bound the eigenvalues of $\boldsymbol{\nabla}\Psi_{T_n} = \boldsymbol{\nabla}\mathcal{P}^n$ away from -1. Since Ψ_0 is the identity map, $\boldsymbol{\nabla}\Psi_0 = \mathbb{1}$, where $\mathbb{1}$ is the 2×2 identity matrix, with eigenvalues $+1$. Our strategy is to show that the eigenvalues cannot move far away from 1 when integrating (4.41) over a time T_n. We can already explicitly integrate the time-independent part, corresponding to $\beta = 0$, by defining

$$X(s) = \exp\left(\left(\kappa\mathbb{1} - \delta\left(\begin{smallmatrix} 0 & 1 \\ -1 & 0 \end{smallmatrix}\right)\right)s\right)\boldsymbol{\nabla}\Psi_s\,,$$

yielding

$$\frac{\mathrm{d}}{\mathrm{d}s}X(s) = \tilde{\beta}R_{\delta s}\,\Gamma_s^{(n:m)}(\xi_d)\,R_{-\delta s}\,X(s), \tag{4.42}$$

[3] The spectral norm of a square matrix A is defined as the largest singular value of A, which is the square root of the largest eigenvalue of $A^\dagger A$.

where $R_{\delta s}$ is the rotation matrix

$$R_{\delta s} = \begin{pmatrix} \cos(\delta s) & -\sin(\delta s) \\ \sin(\delta s) & \cos(\delta s) \end{pmatrix}.$$

• *Bounding the norm of X:* We can write (4.42) as an integral equation:

$$X(s) = X(0) + \tilde{\beta} \int_0^s R_{\delta z}\, \Gamma_z^{(n:m)}(\xi_d)\, R_{-\delta z} X(z)\, \mathrm{d}z. \tag{4.43}$$

Taking the spectral norm of both sides, applying the triangle inequality, pulling the norm into the integral in the right hand side, and subsequently using the submultiplicativity of the spectral norm, we obtain

$$\|X(s)\| \leq \|X(0)\| + \tilde{\beta} \int_0^s \|X(z)\| \left\|\Gamma_z^{(n:m)}(\xi_d)\right\| \mathrm{d}z. \tag{4.44}$$

Since the entries of $\Gamma_z^{(n:m)}$ are all smaller than 1 in absolute value, uniformly in z and ξ_d, we have $\left\|\Gamma_s^{(n:m)}(\xi_d)\right\| \leq 2$. Plugging this into (4.44) and applying the simplest form of the Grönwall Lemma (recalled as Lemma 4.8 below) then yields

$$\|X(s)\| \leq \|X(0)\| e^{2\tilde{\beta}s} = e^{2\tilde{\beta}s}, \tag{4.45}$$

since $X(0) = \mathbb{1}$.

• *Tying X to the identity:* Now, consider again Equation (4.43):

$$X(s) - \mathbb{1} = \int_0^s \tilde{\beta} R_{\delta z}\, \Gamma_z^{(n:m)}(\xi_d)\, R_{-\delta z} X(z)\, \mathrm{d}z. \tag{4.46}$$

Analogously to the previous point, taking the spectral norm of both sides, subsequently pulling the norm into the integral into the right hand side, using the submultiplicativity of the spectral norm and the bound on $\|\Gamma\|$, we obtain

$$\|X(s) - 1\| \leq 2\tilde{\beta} \int_0^t \|X(s)\|\, \mathrm{d}s. \tag{4.47}$$

Plugging (4.45) in the right hand side and evaluating at $s = T_n$, we obtain

$$\|X(T_n) - \mathbb{1}\| \leq e^{2\tilde{\beta}T_n} - 1. \tag{4.48}$$

• *Confining the eigenvalues of $\boldsymbol{\nabla}\Psi_{T_n}$:* We have thus bounded how $X(T_n)$ departs from the identity, from which there remains to deduce a bound on the eigenvalues of

$$\boldsymbol{\nabla}\Psi_{T_n} = e^{-\kappa T_n} R_{-\delta T_n} X = e^{-\kappa T_n} R_{-\delta T_n} \quad + \quad e^{-\kappa T_n} R_{-\delta T_n} (X(T_n) - \mathbb{1})\ .$$

The last expression indicates how we intend to view $\boldsymbol{\nabla}\Psi_{T_n}$, namely as the flow corresponding to $\beta = 0$ plus a perturbation. The Bauer-Fike theorem (recalled as Theorem 4.9 below), bounds how eigenvalues behave under such perturbations. In this theorem, we use $p = \infty$ for the Schatten norm, which corresponds to the operator norm that we have used above. The norm of the perturbation in the right-hand side of (4.52) is bounded by $\left\|e^{-\kappa T_n} R_{-\delta T_n}(X(T_n) - 1)\right\| \leq$

$e^{-\kappa T_n}\Big(e^{2\tilde{\beta}T_n}-1\Big)$, and since $e^{-\kappa T_n}R_{-\delta T_n}$ is diagonalized by a unitary, the condition number equals 1. The Bauer-Fike theorem then says that for any eigenvalue μ of $\boldsymbol{\nabla}\Psi_{T_n}$, there exists an eigenvalue η of $e^{-\kappa T_n}R_{-\delta T_n}$ such that

$$|\eta-\mu| \leq e^{-\kappa T_n}\Big(e^{2\tilde{\beta}T_n}-1\Big). \tag{4.49}$$

Of course we know that $\eta = e^{(-\kappa\pm i\delta)T_n}$.

The final argument is thus: if any eigenvalue μ is sufficiently close to some $\eta = e^{(-\kappa\pm i\delta)T_n}$, while all these η are sufficiently far from -1, then each μ can be bounded away from -1. Explicitly, if

$$\Big|1+e^{(-\kappa\pm i\delta)T_n}\Big| > e^{-\kappa T_n}\Big(e^{2\tilde{\beta}T_n}-1\Big), \tag{4.50}$$

then

$$|\mu+1| = \Big|\eta - e^{(-\kappa\pm i\delta)T_n} + e^{(-\kappa\pm i\delta)T_n} + 1\Big| \geq \Big|1+e^{(-\kappa\pm i\delta)T_n}\Big| - \Big|\eta - e^{(-\kappa\pm i\delta)T_n}\Big| > 0. \tag{4.51}$$

Multiplying both sides of (4.50) by $e^{\kappa T_n}$, one readily sees that $\kappa = 0$ is the most constraining case, and working out the algebra for this case gives the stated criterion (4.39). □

We here recall the two lemmas used in the proof of Lemma 4.7:

Lemma 4.8. (Grönwall, [28]) *Consider the integral equation*

$$h(t) \leq c(t) + \int_0^t g(s)h(s)\,\mathrm{d}s,$$

with the scalar functions g, h and c all non-negative on the interval $[0,t]$, and c differentiable. Then

$$h(t) \leq c(0)\exp\left(\int_0^t g(s)\,\mathrm{d}s\right) + \int_0^t \frac{\mathrm{d}c}{\mathrm{d}t}(t)\left(\exp\left(\int_s^t g(\tau)\,\mathrm{d}\tau\right)\right)\mathrm{d}s.$$

We have used this Grönwall Lemma with both g and c constant. In particular, the second term on the right drops out.

Theorem 4.9. (Bauer-Fike, [9]) *Suppose $A \in \mathbb{C}^{n\times n}$ is a diagonalizable matrix, and $V \in \mathbb{C}^{n\times n}$ is the non-singular similarity transformation that brings A into its diagonal form Λ:*

$$\Lambda = V^{-1}AV.$$

Define the condition number

$$\kappa_p(V) := \frac{\|V\|_p}{\|V^{-1}\|_p},$$

with $\|\cdot\|_p$ the p-Schatten norm. Let μ be an eigenvalue of $A+B$, $B \in \mathbb{C}^{n\times n}$. Then there exists an eigenvalue η of A such that

$$|\eta-\mu| \leq \kappa_p(V)\|B\|_p. \tag{4.52}$$

We used the Bauer-Fike Theorem with the operator norm ($p = \infty$) and with a matrix A which is diagonalized by a unitary, such that $\kappa_p(V) = 1$.

Lemma 4.7 is useful only for part of the parameter space, represented by the blue bands in Fig. 4.8. Indeed, the criterion (4.39) requires $\tilde{\beta} = 0$ as $\bar{\delta}$ tends towards its maximal value $\frac{\tilde{\nu}_d}{2n}$, so part of the parameter values for δ are not covered by Lemma 4.7. Therefore, we next provide in Section 4.3.4.2 another result to cover these largest values of $\bar{\delta}$ (red bands in Fig. 4.8) while allowing for nonzero values for $\tilde{\beta}$. We will then combine both results in Section 4.3.4.3 to obtain our overall conclusion.

4.3.4.2 Values of $\tilde{\beta}$ and $\tilde{\nu}_d$ excluding an n-subharmonic

The rough idea can be sketched as follows. We consider a harmonic $2\pi/\tilde{\nu}_d$-periodic solution as a point of reference − we will show that such a solution must exist for any parameter values. If the natural dynamics for $\tilde{\beta} = 0$ corresponds to a trajectory where a half-integer number of laps around the harmonic orbit are completed over a period $2n\pi/\tilde{\nu}_d$, then in case of small $\tilde{\beta} > 0$ it is unlikely for a trajectory which completes an integer number of laps around the harmonic solution to exist *anywhere*. It then immediately follows that it is unlikely for any trajectory to exist that can possibly close on itself to form a periodic orbit. The only remaining trivial fixed point of $\mathcal{P}^n$ would be the unavoidable fixed point of $\mathcal{P}$ corresponding to the harmonic solution.

Lemma 4.10. *If the interval* $[(1-\tilde{\beta})\frac{1}{\tilde{\nu}_d},\ (1+\tilde{\beta})\frac{1}{\tilde{\nu}_d}]$ *contains no integer multiple of* $1/n$*, then the system* (4.29) *can feature no* $\frac{2\pi n}{\tilde{\nu}_d}$*-periodic solution other than a single* $2\pi/\tilde{\nu}_d$*-periodic solution.*

Proof. By Lemma 4.5 in Section 4.3.2, the system always features at least one $2\pi/\tilde{\nu}_d$-periodic solution. Let us denote it by $(x_1^*(s), p_1^*(s))$ and define the displaced variables

$$x_d(s) = \tilde{x}(s) - x_1^*(s) \tag{4.53a}$$
$$p_d(s) = \tilde{p}(s) - p_1^*(s), \tag{4.53b}$$

describing how other solutions behave compared to this solution. The corresponding equations of motion are, without approximation,

$$\frac{\mathrm{d}}{\mathrm{d}s}x_d = \quad p_d - \kappa x_d, \tag{4.54a}$$
$$\frac{\mathrm{d}}{\mathrm{d}s}p_d = -x_d - \kappa p_d - 2\tilde{\beta}\sin\Big(\frac{x_d}{2}\Big)\cos\Big(\frac{x_d}{2} + x_1^*(s) + \xi_d\sin(\tilde{\nu}_d s)\Big). \tag{4.54b}$$

In polar coordinates $x_d = R\cos(\theta)$, $p_d = R\sin(\theta)$, we obtain:

$$\frac{\mathrm{d}}{\mathrm{d}s}R = -\kappa R - \sin(\theta)2\tilde{\beta}\sin\left(\frac{R}{2}\cos(\theta)\right)\cos\left(\frac{R}{2}\cos(\theta) + x_1^*(s) + \xi_d\sin(\tilde{\nu}_d s)\right), \tag{4.55}$$
$$\frac{\mathrm{d}}{\mathrm{d}s}\theta = -1 - \tilde{\beta}\cos^2(\theta)\frac{\sin\big(\frac{R}{2}\cos(\theta)\big)}{\frac{R}{2}\cos(\theta)}\cos\left(\frac{R}{2}\cos(\theta) + x_1^*(s) + \xi_d\sin(\tilde{\nu}_d s)\right). \tag{4.56}$$

By definition, $x_d(s) = p_d(s) = 0$ (corresponding to $R = 0$) is a solution for any time s, and no other trajectories ever cross the point $R = 0$. Recognizing the expression $\frac{\sin(p_d/2)}{p_d/2} \in [-1, 1]$ in

(4.56), we can bound $|\frac{\mathrm{d}}{\mathrm{d}s}\theta + 1| \leq \tilde{\beta}$. A $\frac{2\pi n}{\tilde{\nu}_d}$-periodic solution has to make an integer number of laps m around the (periodically displaced) origin. We thus need

$$\theta(0) - \theta\left(\frac{2\pi n}{\tilde{\nu}_d}\right) = 2\pi m \in \left[\frac{2\pi n}{\tilde{\nu}_d}(1-\tilde{\beta}), \frac{2\pi n}{\tilde{\nu}_d}(1+\tilde{\beta})\right],$$

which is equivalent to the statement. □

Using the notation of Lemma 4.7, this criterion excludes the existence of an $(n{:}m)$-subharmonic

$$\text{for } |\delta^{(n:m)}| > \bar{\delta}, \text{ provided } \frac{2\pi n\tilde{\beta}}{\tilde{\nu}_d} < \frac{2\pi n\bar{\delta}}{\tilde{\nu}_d}\,. \tag{4.57}$$

4.3.4.3 Combining Lemma 4.7 and Lemma 4.10 into a uniform criterion on β

We now select $\bar{\delta}$ to have overlapping regions of $1/\tilde{\nu}_d$, as explained in Figure 4.8.

Corollary 4.11. *Consider a simply connected open set $\mathcal{S}_p$ of possible parameter values $(1/\tilde{Q}, \nu_d, \xi_d)$ with $\nu_d \geq \nu_{\min}$ and $\tilde{Q} \geq Q_{\min} > 1/2$. For some parameter setting in this set, consider a stable subharmonic solution of (4.24) of period smaller than or equal to $2\pi\bar{n}/\nu_d, \bar{n} \in \mathbb{N}, \bar{n} \geq 2$, and denote the largest period that this solution could possibly have when varying ν_d by $\bar{\tau} = 2\pi\bar{n}/\nu_{\min}$. If*

$$\beta < \frac{0.53}{\bar{\tau}}\sqrt{1 - \frac{1}{4Q_{\min}^2}}, \tag{4.58}$$

then this solution cannot undergo a period-doubling bifurcation when varying $(1/\tilde{Q}, \nu_d, \xi_d)$ in $\mathcal{S}_p$.

Proof. To cover the whole parameter space, we must match the value of $\bar{\delta}$ in both criteria, (4.39) and (4.57). Choosing $\bar{\delta}$ smaller makes (4.39) easier to achieve, yet it confines $1/\tilde{\nu}_d$ close to integer multiples of $1/n$. Conversely, choosing $\bar{\delta}$ larger makes (4.57) easier to achieve, while confining $1/\tilde{\nu}_d$ closer to half-integer multiples of $1/n$. The best compromise is obtained when both criteria yield the same bound on $\tilde{\beta}$. We thus equate the right hand sides of (4.39) and (4.57), to numerically find the optimal value $\bar{\delta} \simeq 0.537\frac{\tilde{\nu}_d}{2\pi n}$ for the boundary between red and blue regions of Figure 4.8. Substituting this value in (4.57), working back to the original variables using (4.27a), (4.27b) and imposing the condition for all parameter values then gives the stated criterion (4.58). □

Important remark: Corollary 4.11 speaks of a *subharmonic* in the strict sense, i.e. a $2n\pi/\tilde{\nu}_d$-periodic solution with $n \geq 2$. Indeed, when using Lemma 4.10 in the proof, we leave open the possible behavior of a $2\pi/\tilde{\nu}_d$-periodic solution. However, this poses no problem for our intended use of Corollary 4.11 to exclude a period-doubling cascade. Indeed, with the strict interpretation of Corollary 4.11, we thus leave open the possibility that a $2\pi/\tilde{\nu}_d$-periodic solution would undergo period-doubling, but the resulting subharmonic would then be covered by Corollary 4.11 such that further period-doubling is necessarily excluded.

Under the condition of Corollary 4.11, we are thus always in a zone where the considered subharmonic cannot undergo period-doubling, either because of Lemma 4.7 or because it cannot exist in the first place (Lemma 4.10). In other words, starting from a subharmonic of period $2\pi n/\tilde{\nu}_d$ we are necessarily in the blue zone of Fig. 4.8, and when moving towards the

red zone of Fig. 4.8 this subharmonic must disappear in a saddle-node bifurcation without the occurrence of period-doubling.

Note that this result is independent of the drive amplitude ξ_d and only requires an upper bound on the dissipation rate $1/\tilde{Q}$ that is trivial to meet in practice.

Finally, to apply the Gambaudo-Tresser Conjecture 4.6, the parameter set $\mathcal{S}_p$ of Corollary 4.11, with condition (4.58), should overlap with a zone where condition (4.37) of Lemma 4.3 holds (green zones on Fig. 4.7). Indeed, this would give rise to the conditions shown in Figure 4.7(b): for some parameter region we know that there is a single harmonic limit cycle, while for an overlapping region we know that there can be no period-doubling cascade (starting below $\bar{\tau}$), and thus according to the conjecture there can be no transition into a chaotic regime.

Let us thus analyze how to combine both conditions (4.37) and (4.58). Condition (4.58) holds for all $Q_{\min} \geq \underline{Q}$ if it holds for $\underline{Q}$. Conversely, for $\tilde{Q} > 1/\sqrt{2}$, the right hand side of (4.37) is decreasing in $\tilde{Q}$, so (4.37) holds for all $\tilde{Q} \leq \bar{Q}$ if it holds for $\bar{Q}$. For the regions satisfying (4.37) and (4.58) to overlap for a fixed β, we thus need $\underline{Q} < \bar{Q}$. By inspection, the limit is obtained at $1/\underline{Q} = 1/\bar{Q} = 0.53/\bar{\tau} < \sqrt{2}$. The associated constraint on β becomes:

$$\beta < \frac{0.53}{\bar{\tau}} \sqrt{1 - \left(\frac{0.53}{2\bar{\tau}}\right)^2}\,. \tag{4.59}$$

This concludes our analytical results in the context of preventing the classical system (4.24) from behaving chaotically, by preventing the period-doubling cascades that are conjectured to be a necessary precursor for chaotic behavior (Gambaudo-Tresser Conjecture 4.6) when $\tilde{Q} < \infty$. Since the bound (4.59) depends on the maximal period $\bar{\tau}$ of a given subharmonic solution, our results are only partial in nature, but we believe the discussion of this section provides theoretical indications that indeed for a finite small-enough value of β no period-doubling cascades should occur. Note that our arguments are mainly based on the fact that the Josephson potential and its first derivatives are uniformly bounded, so similar results should hold in other systems with these properties.

4.4 Enhancement of the quasienergy spectral gap

While in Section 4.1 we showed how the periodically-driven inductively-shunted transmon could be used for the confinement of Schrödinger cat states under appropriate resonance conditions of the drive, the detrimental effect of possible chaotic behavior was identified in Section 4.2. There we showed that we can tune the regularity parameter β to effectively suppress this chaotic behavior. In this section, we focus on this non-chaotic case, and while fixing the value of β to 0.5, we study the effect of a second parameter we call the quantum scaling parameter

$$\lambda = \left(\frac{2E_C}{E_L}\right)^{1/4},$$

which was introduced in Section 3.1.1. We previously argued that this parameter governs key properties of the quantum behavior of the system, as it can be entirely eliminated from the classical dynamics.

We numerically study the role of λ in the context of the confinement of 3-component Schrödinger cat states. For this we again focus on the Floquet decomposition of the driven

system. We fix $\beta = 0.5$ and study the asymptotic regime for various values of λ, while varying the drive parameters, focusing on the case of a $(3:1)$-resonance. We consider the quasienergy spectral gap $\Delta\varepsilon$ between the manifold of cat states $|\phi_k^\alpha(\tau)\rangle$ and the next-excited Floquet modes $|\eta_k^\alpha(\tau)\rangle$, defined in (4.12), and schematically illustrated in Figure 4.4. We previously argued that the magnitude of $|\Delta\varepsilon|$ captures the robustness of the cat subspace as a whole to sufficiently weak and sufficiently slowly-varying Hamiltonian perturbations.

Our findings are summarized on Figure 4.9. We investigate three different values $\lambda = 0.2, 0.3, 0.4$ and drive parameters ξ_d, ν_d leading to a constant mean photon number $\bar{n} = 9$ or 16 in the cat states $|\phi_k^\alpha\rangle$ (plots 4.9(a) and (b)). For these settings, Figures 4.9(c,d) show the quasienergy gap $\Delta\varepsilon$. For fixed $\bar{n}$, increasing λ is seen to ramp up the quasi-energy gap. Likewise, for fixed λ, increasing $\bar{n}$ is seen to ramp up the quasi-energy gap. The fact that the spectral gap increases also with the average number of photons could have been anticipated from previous work. Indeed, for the Kerr cat encoding [55], this gap equals $K|\alpha|^2$ where K is the quartic Kerr strength and $|\alpha|^2 = \bar{n}$, the cat state's average number of photons.

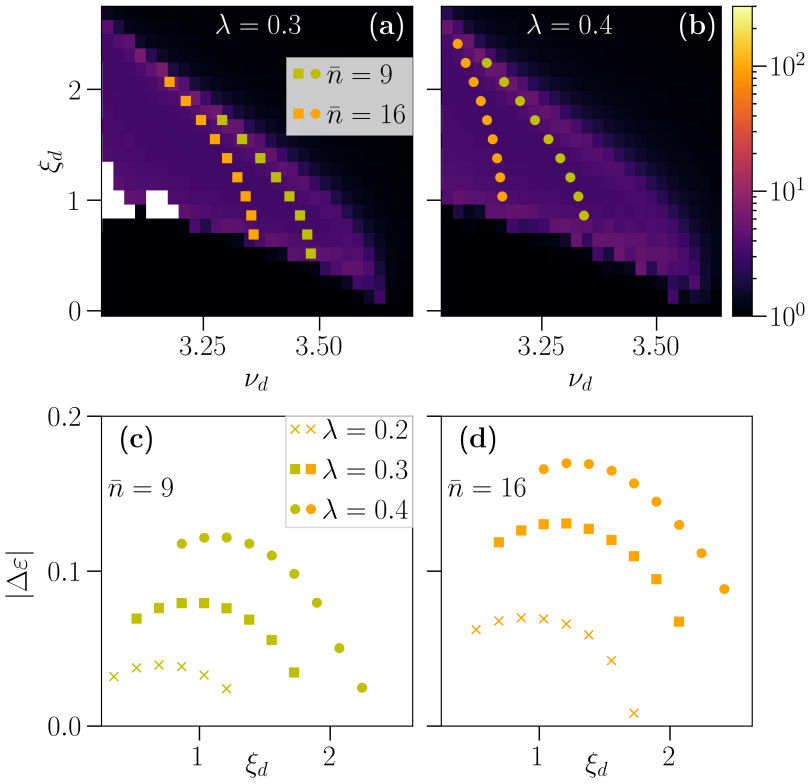

Figure 4.9: Behavior of the quantum system as a function of quantum scaling parameter λ for fixed $\beta = 0.5$. Plots (a) and (b) are similar to plot 4.5(a) and show that the system does not present a chaotic region for $\lambda = 0.2, 0.3, 0.4$. In the same plots, we represent the drive parameters leading to constant mean photon number $\bar{n} = 9$ or 16 in the asymptotic Schrödinger cat states. Plots (c) and (d) show the quasi-energy spectral gap ($\Delta\varepsilon$ in Figure 4.4(b)), corresponding to those drive parameters. For fixed $\bar{n}$, increasing λ ramps up the quasienergy gap.

In conclusion, we demonstrated the quantum signature of the classical transition to chaos as the breaking down of the confinement process and the appearance of a high-entropy asymptotic behavior. In this section, we showed that with the regularity parameter β fixed to avoid such transition, the quantum scaling parameter λ can be varied to control the quantum confinement strength in the subharmonic regime. It is thus possible to benefit from a strong nonlinear effect while maintaining the dynamics in a regular regime.

4.5 Conclusions

The work presented in this chapter is a natural continuation of work by the QUANTIC-team of Inria Paris in collaboration with the team of Michel Devoret at Yale University, after the inductively-shunted transmon was proposed as a novel circuit element that behaves more stable under the strong drives that are needed for state-of-the-art superconducting circuits experiments [126]. In [126], a resonator was driven in the strongly-dispersive regime and coupled to inductively-shunted transmon. It was shown that the AC-Stark shift of the resonator remained well-defined and varied smoothly with the effective number of photons in the resonator. This was contrasted to the case of the traditional transmon when considered in the exact same setting, where the AC-Stark shift of the resonator showed strong discontinuities. Moreover, the asymptotic behavior remained much more pure for the inductively-shunted transmon than for the regular transmon considered in the same setting. As a first axis of extension of [126], we explicitly focused on the *resonant* behavior of the circuit in a single-mode setup, showing its ability to mediate multi-photon processes, which has key applications in the field of bosonic encodings. Indeed, we have studied the confinement of highly non-classical states, namely Schrödinger cat states. It is within this concrete and topical application domain that we obtained a deeper understanding of the structural instabilities reported to plague practical nonlinear quantum devices. A first main contribution of this work was to explicitly ascribe this unwanted behavior to the possibility of complex dynamical behavior of the corresponding classical equations of motion: chaotic dynamics. This chaotic dynamics was studied wielding the proper tools from classical dynamical systems theory, namely by considering the Poincaré map. This excursion into classical dynamical systems furthermore allowed us to obtain a novel and dual understanding of the mentioned multi-photon processes on a classical level.

Using a change of variables detailed in Section 3.1.1, we identified renormalized circuit parameters that each govern different and complementary system properties. The identification of these parameters once again emphasizes the role of the inductively-shunted transmon as a ubiquitous model for nonlinear oscillators to be used for quantum information processing with superconducting circuits, as any device allows for a circuit model description composed of these same three basic building blocks: an inductor, a capacitor, and a Josephson junction. As an immediate contribution we exhaustively quantified the effect of the two effective circuit parameters β and λ on *regularity* and *anharmonicity* respectively, on either a classical or quantum level, and using either numerical or analytical tools. Besides these contributions which are inherently circuit-related, the methods proposed in this chapter can readily be applied to different systems, as analogous effective parameters can be identified for related families of systems that contain an inductive shunt. We argue that the ability to perform perturbation theory that is valid on a global level hinges on the presence of the inductive shunt, and this dissertation explores one such perturbation theory for the classical system in Chapter 5, utilizing the fact that the harmonic part of the system dominates the bounded nonlinearity. Applying

such an averaging-type of perturbation theory on the quantum level [15, 34, 88, 91, 125] for our specific system should be the subject of future work, explicitly identifying β as the perturbation parameter. These results are then to be contrasted with theoretical explanations of the strong-drive problem [100, 110] in general, and especially to other state-of-the-art perturbation techniques [101, 125] that identify different small parameters. This small parameter has been chosen to be $\sqrt{\frac{8E_C}{E_J}}$ in a transmon limit for example [101], rather than of $\beta = E_J/E_L$ in our case.

Regarding a more explicit connection to classical chaotic dynamics representing structural instabilities of the system, we presented a twofold argument why shunted junction models should be less prone to any perceivable chaotic dynamics altogether, when choosing correct circuit parameters. First, since the topology of phase space is that of a bounded disk, the Gambaudo-Tresser conjecture predicts the occurrence of a period-doubling cascade at the onset of chaos. Secondly, in Section 4.3, we argued that choosing β small enough should exclude period-doubling bifurcations altogether. We were able to prove this for low-enough-order subharmonic solutions, again utilizing the boundedness of the Josephson cosine potential with respect to the harmonic part of the potential. Future work could look into improving upon this result, obtaining a bound similar to (4.58) that scales more favorably with the period $\bar{\tau}$ of the considered subharmonic solution. The analytical results of Section 4.3 are not immediately applicable to models where an inductive shunt is absent, such as for the traditional transmon [73]. Firstly, an equivalent regularity parameter cannot immediately be identified, due to the absence of the inductive shunt ($E_L = 0$ in (3.1)). Secondly, for the transmon, the topology of phase space is equivalent to that of a cylinder, as the superconducting phase becomes a periodic variable. The conditions of the Gambaudo-Tresser conjecture are then not rigorously fulfilled, since one should be able to restrict the Poincaré map to an invariant subset of phase space with the topology of a compact disk.

Chapter 5

Classical study of subharmonic working points

Dans la Section 4.1, nous avons établi une correspondance entre des sousharmoniques stables de période $\frac{2\pi n}{\nu_d}$, indice $m \in \mathbb{N}$ et parité $r = m + n \mod 2$ d'une part, et le confinement de $(1+r)n$ états chats de Schrödinger à $(1+r)n$ composants d'autre part. Les résultats de la Section 4.2 nous ont donné une idée préliminaire sur comment choisir les paramètres du forçage pour rendre un tel processus de confinement multi-photons résonnant, dans le cas où $n = 3, m = 1$, et dans le cas non-chaotique de $\beta \simeq 0.5$. Dans ce chapitre, nous cherchons à établir un modèle simplifié qui décrit la condition de résonance des paramètres du forçage (ν_d, ξ_d) afin de créer des sous-harmoniques $(n : m)$ stables. Cette analyse suit la méthode générale de moyennisation géométrique. Nous appliquons cette technique perturbative dans le cas non-chaotique de $\beta \lesssim 0.5$, en considérant β comme une perturbation. Cependant, contrairement à la Section 4.3, nous saisisserons des effets $\mathcal{O}(\beta)$, et négligerons seulement les effets d'ordre $\mathcal{O}(\beta^2)$ en première instance. Le chapitre est présenté comme suit. Après un bref résumé sur la théorie de moyennisation géométrique des systèmes périodiques, nous obtenons une classe de modèles moyennisés au premier ordre qui élimine la dépendance en temps, pour tout $(n : m)$ fixé. Ensuite, nous analysons la structure des points d'équilibre de ce modèle moyenisé et nous la comparons aux simulations numériques de type Floquet-Markov. La résonance $(3 : 1)$ sert à nouveau d'illustration, et la même méthodologie peut facilement être appliquée à d'autres résonances.

In Section 4.1, we showed a clear correspondence between stable subharmonic solutions of period $\frac{2\pi n}{\nu_d}$, winding number $m \in \mathbb{N}$ and parity $r = m + n \mod 2$ on the one hand, and the confinement of $(1+r)n$ Schrödinger cat states with $(1+r)n$ components on the other hand. The results outlined in Section 4.2 gave us a preliminary numerical account of how the drive parameters should be chosen to render such a multi-photon confinement process resonant for $n = 3, m = 1$, in the non-chaotic case of $\beta \simeq 0.5$. In this chapter, we set out to obtain a simplified model that describes the resonance condition the drive parameters (ν_d, ξ_d) need to satisfy in order to create stable $(n : m)$-subharmonics for the classical system. This analysis is performed following the method of geometric averaging. We apply this perturbative technique in the non-chaotic case of $\beta \lesssim 0.5$, treating β as a perturbation. However, in contrast to Section 4.3, we will capture $\mathcal{O}(\beta)$ effects, and only neglect effects of $\mathcal{O}(\beta^2)$. The chapter is outlined as follows. After a short summary of the theory of geometric averaging for periodic systems, we obtain a class of first-order averaged models that eliminates the dependence on

time, for any fixed $(n:m)$. Next, we analyze the equilibrium point structure of this average model and compare to the numerical Floquet-Markov simulations. The (3:1) resonance again serves as an illustration of the general theory, and the same methodology can readily be applied to other resonances.

5.1 Summary of averaging theory

We will summarize the method of geometric averaging (originally due to Krylov and Bogoliubov [75]) using the notation of Section 3.2.1, in terms of a general T-periodic vector field describing the dynamics of a two-dimensional state variable $z \in \mathbb{R}^2$. What is new, is that the oscillations of the vector field as a function of time t are now assumed to be *fast* with respect to the magnitude of the vector field itself. To capture this, we introduce a small positive dimensionless variable $\varepsilon \ll 1$, and assume the following equations of motion for z,

$$\dot{z} = \varepsilon f(z,t), \quad z \in \mathbb{R}^2, t \in \mathbb{R}, \tag{5.1}$$

where f is now assumed of the same order as the frequency of its oscillations:

$$\|Tf\| = \mathcal{O}(1).$$

Another way to interpret this condition, is that the state of the system should not change significantly on the timescale of the oscillations present in the vector field. To (5.1) we can associate an *autonomous averaged* vector field, by neglecting its oscillations in time:

$$\bar{f}(\cdot) = \frac{1}{T}\int_0^T f(\cdot,t)\,\mathrm{d}t.$$

Based on the average vector field, one defines the averaged system

$$\dot{\bar{z}} = \varepsilon \bar{f}(\bar{z}), \quad \bar{z} \in \mathbb{R}^2, \tag{5.2}$$

whose solutions $\bar{z}(t)$ are meant to approximate those of the true system (5.1), for small values of ε. More precisely, the flow of the averaged system over one system-period provides a good approximation of the true Poincaré map of (5.1). Explicitly, and analogously to the introductory material in 3.2.1, we define

$$\mathcal{P}_\varepsilon \coloneqq \Psi_T, \text{ with } \quad \frac{\partial}{\partial t}\Psi_t(z_0) = \varepsilon f(\Psi_t(z_0),t), \quad \forall z_0 \in \mathbb{R}^2, t \in \mathbb{R}. \tag{5.3a}$$

A standard version of the averaging theorem for periodic systems can be found in chapter 4 of [57]. We will summarize the main conclusions relevant to this work. One can establish the following local correspondences between $\bar{f}$ and $\mathcal{P}_\varepsilon$, for small enough ε.

(i) Consider a solution $\bar{z}(t)$ of (5.2) and a solution $z(t)$ of (5.1), based at $\bar{z}_0$ and z_0 respectively. If $|\bar{z}_0 - z_0| = \mathcal{O}(\varepsilon)$, then $|\bar{z}(t) - z(t)| = \mathcal{O}(\varepsilon)$ on a timescale $0 < t < t_{\max} = \mathcal{O}\big(\frac{1}{\varepsilon}\big)$.

(ii) Consider a *hyperbolic equilibrium point* $\bar{z}^*$ of (5.2), namely

$$\bar{f}(\bar{z}^*) = 0, \tag{5.4}$$

where the *stability matrix* $A(\bar{z}^*) \coloneqq \boldsymbol{\nabla}\bar{f}(\bar{z}^*)$ only has eigenvalues with nonzero real parts. Then there exists an $\varepsilon_0 > 0$ such that for all $0 \leq \varepsilon < \varepsilon_0$, $\mathcal{P}_\varepsilon$ possesses a unique hyperbolic fixed point z^* of the same stability type as $\bar{z}^*$, with $z^* = \bar{z}^* + \mathcal{O}(\varepsilon)$.

(*iii*) Consider a trajectory $\bar{z}_s(t)$ in the stable manifold of the hyperbolic equilibrium point $\bar{z}^*$ of $\bar{f}$, and let $\mathcal{P}_\varepsilon^k(z_{s,0})$ be an orbit in the stable manifold of the corresponding fixed point z^* of $\mathcal{P}_\varepsilon$ (with still $z^* = \bar{z}^* + \mathcal{O}(\varepsilon)$). If $|\bar{z}_s(0) - z_{s,0}| = \mathcal{O}(\varepsilon)$, then $\left|\bar{z}_s(kT) - \mathcal{P}_\varepsilon^k(z_{s,0})\right| = \mathcal{O}(\varepsilon), \forall k \in \mathbb{N}$. Similar results apply for unstable manifolds of hyperbolic fixed points (in reversed time).

(*iv*) If for some system parameter $\mu = \mu_0$, the averaged vector field $\bar{f}^{(\mu)}$ of (5.2) undergoes a saddle-node bifurcation, then for ε small enough, the Poincaré map $\mathcal{P}_\varepsilon^{(\mu)}$ of (5.1) similarly undergoes a saddle-node bifurcation, for an ε-close parameter value $\mu_{0,\varepsilon}$.

Since in Section 4.1, the quantum-classical correspondence in the asymptotic regime was shown to involve stable periodic orbits of the Poincaré map, we are interested in characterizing these as a function of system parameters. The averaging theorem justifies characterizing the equilibrium points of an averaged vector field instead, if we can identify the corresponding small parameter ε. In the next section we will hence study the equilibrium points of the average vector field in a well-chosen frame. Before moving on to the next section, a final comment can be passed on to the interested reader.

Remark 5.1. While the above results tell us that local behavior of the averaged system carries over to the true system, the same does not hold for global properties of the flow. One example of such a global property is a homoclinic loop connecting a saddle-type equilibrium of $\bar{f}$ to itself. One can in general not expect such an exact identification of stable and unstable manifolds to hold for the true system (5.1). Determining if the two manifolds still intersect for small ε − and if so, if they intersect in a transversal manner − is a delicate matter, and requires a careful analysis for many classes of systems [50, 61]. On the other hand, there do exist results proving the topological equivalence of the phase portraits of $\mathcal{P}_0$ and $\mathcal{P}_\varepsilon$, under conditions of Morse-Smale-type structural stability of $\mathcal{P}_0$ (see for example theorem 4.4 in [57]), but this is beyond the scope of this work.

5.2 General properties of $(n : m)$-resonances

We recall the form of the classical system with symmetric dissipation rates in the two quadratures, introduced in (4.28):

$$\begin{aligned}\frac{\mathrm{d}}{\mathrm{d}s}\tilde{x} &= \quad \tilde{p} - \kappa\tilde{x},\\ \frac{\mathrm{d}}{\mathrm{d}s}\tilde{p} &= -\tilde{x} - \kappa\tilde{p} - \tilde{\beta}\sin(\tilde{x} + \xi_d \sin(\tilde{\nu}_d s)).\end{aligned}$$

Here, the frequency of oscillation is given by the normalized drive frequency $\tilde{\nu}_d$, and should be considered of order 1. To write our system in the normal form (5.1), amenable to averaging, we will move to a rotating frame with frequency $\frac{m}{n}\tilde{\nu}_d$, where m and n are two strictly positive coprime integers:

$$\tilde{x} = \cos\Big(\frac{m}{n}\tilde{\nu}_d s\Big)u + \sin\Big(\frac{m}{n}\tilde{\nu}_d s\Big)v, \tag{5.6a}$$

$$\tilde{p} = \cos\Big(\frac{m}{n}\tilde{\nu}_d s\Big)v - \sin\Big(\frac{m}{n}\tilde{\nu}_d s\Big)u. \tag{5.6b}$$

Recalling the definition of the detuning from (4.38),

$$\delta = 1 - \frac{m}{n}\tilde{\nu}_d, \tag{5.7}$$

the resulting equations of motion are

$$\begin{aligned}
\dot{u} = &\quad \delta u - \kappa u + \tilde{\beta}\sin\Big(\frac{m}{n}\tilde{\nu}_d s\Big)\sin\Big(u\cos\Big(\frac{m}{n}\tilde{\nu}_d s\Big) + v\sin\Big(\frac{m}{n}\tilde{\nu}_d s\Big) + \xi_d\sin(\tilde{\nu}_d s)\Big),\\
\dot{v} = &-\delta u - \kappa v - \tilde{\beta}\cos\Big(\frac{m}{n}\tilde{\nu}_d s\Big)\sin\Big(u\cos\Big(\frac{m}{n}\tilde{\nu}_d s\Big) + v\sin\Big(\frac{m}{n}\tilde{\nu}_d s\Big) + \xi_d\sin(\tilde{\nu}_d s)\Big),
\end{aligned}$$

where now δ can be considered small with respect to $\tilde{\nu}_d$. Note that we have changed the periodicity of the system, as the smallest common period of all time-dependent terms amounts to $2n\pi/\tilde{\nu}_d$. The equilibria found through an averaged model will thus correspond to $2n\pi/\tilde{\nu}_d$-periodic subharmonic solutions a priori. The averaged model is defined as

$$\dot{\bar{u}} = \quad \delta\bar{u} - \kappa\bar{u} + \tilde{\beta}\frac{\tilde{\nu}_d}{2n\pi}\int_0^{\frac{2n\pi}{\tilde{\nu}_d}} \sin\Big(\frac{m}{n}\tilde{\nu}_d s\Big)\sin\Big(\bar{u}\cos\Big(\frac{m}{n}\tilde{\nu}_d s\Big) + \bar{v}\sin\Big(\frac{m}{n}\tilde{\nu}_d s\Big) + \xi_d\sin(\tilde{\nu}_d s)\Big)\mathrm{d}s, \tag{5.9a}$$

$$\dot{\bar{v}} = -\delta\bar{u} - \kappa\bar{v} - \tilde{\beta}\frac{\tilde{\nu}_d}{2n\pi}\int_0^{\frac{2n\pi}{\tilde{\nu}_d}} \cos\Big(\frac{m}{n}\tilde{\nu}_d s\Big)\sin\Big(\bar{u}\cos\Big(\frac{m}{n}\tilde{\nu}_d s\Big) + \bar{v}\sin\Big(\frac{m}{n}\tilde{\nu}_d s\Big) + \xi_d\sin(\tilde{\nu}_d s)\Big)\mathrm{d}s. \tag{5.9b}$$

For the solutions of this model to correspond to the true system up to good accuracy, we a priori need to assume that

$$\begin{aligned}
\kappa\sqrt{\bar{u}^2+\bar{v}^2} &\ll \frac{\nu_d}{n},\\
|\delta|\sqrt{\bar{u}^2+\bar{v}^2} &\ll \frac{\nu_d}{n},\\
\tilde{\beta} &\ll \frac{\nu_d}{n}.
\end{aligned}$$

The general correspondences between the averaged model and the true system summarized in the previous section are asymptotic in nature however, so there are no clear a priori allowable values for (κ, δ, β) (and corresponding regions in phase space) for which averaging is valid. Explicit bounds on these values fall beyond the scope of this work. We will thus study the averaged model (5.9) *as is*, knowing there exist some small-enough values for (κ, δ, β) for which the obtained conclusions are valid for the true system. In Section 5.3 however, we compare the predictions of this averaged model to exact numerical Floquet-Markov simulations.

Analogously to the discussion in Section 3.2.1.2 on the stability types of the Poincaré map, we can define the stability type of an equilibrium point (u^*, v^*) in terms of the eigenvalues of the *stability matrix*

$$A(\bar{u}^*, \bar{v}^*) := \begin{pmatrix} \frac{\partial\dot{\bar{u}}}{\partial u} & \frac{\partial\dot{\bar{u}}}{\partial v} \\ \frac{\partial\dot{\bar{v}}}{\partial u} & \frac{\partial\dot{\bar{v}}}{\partial v} \end{pmatrix}\Bigg|_{\bar{u}=\bar{u}^*,\bar{v}=\bar{v}^*}. \tag{5.10}$$

Explicitly, we obtain

$$\begin{aligned}
A(\bar{u}^*, \bar{v}^*) = &\begin{pmatrix} -\kappa & \delta \\ -\delta & -\kappa \end{pmatrix} \qquad (5.11)\\
+\tilde{\beta}\frac{\tilde{\nu}_d}{2n\pi}&\begin{pmatrix} \int_0^{\frac{2n\pi}{\tilde{\nu}_d}} \sin\big(\frac{m}{n}\tilde{\nu}_d s\big)\cos\big(\frac{m}{n}\tilde{\nu}_d s\big)\cos(\zeta(s))\,\mathrm{d}s & \int_0^{\frac{2n\pi}{\tilde{\nu}_d}} \sin^2\big(\frac{m}{n}\tilde{\nu}_d s\big)\cos(\zeta(s))\,\mathrm{d}s \\ -\int_0^{\frac{2n\pi}{\tilde{\nu}_d}} \cos^2\big(\frac{m}{n}\tilde{\nu}_d s\big)\cos(\zeta(s))\,\mathrm{d}s & -\int_0^{\frac{2n\pi}{\tilde{\nu}_d}} \sin\big(\frac{m}{n}\tilde{\nu}_d s\big)\cos\big(\frac{m}{n}\tilde{\nu}_d s\big)\cos(\zeta(s))\,\mathrm{d}s \end{pmatrix},
\end{aligned}$$

with

$$\zeta(s) = \bar{u}^* \cos\Big(\frac{m}{n}\tilde{\nu}_d s\Big) + \bar{v}^* \sin\Big(\frac{m}{n}\tilde{\nu}_d s\Big) + \xi_d \sin(\tilde{\nu}_d s).$$

If both eigenvalues of A have strictly negative real parts, $(\bar{u}^*, \bar{v}^*)$ corresponds to a *stable node*. If A has one eigenvalue with strictly positive real part and a second with strictly negative real part, we speak of a *saddle point*. If both eigenvalues of A have strictly positive real parts, the equilibrium point corresponds to a *source*.

As was the case for the true Poincaré map (see Section 3.2.1.3), the dissipative nature of (5.9) dictates that also for the averaged model, equilibrium points $(\bar{u}^*, \bar{v}^*)$ necessarily correspond to either stable nodes or saddle points, and no sources are allowed. This is easy to see by considering $\mathrm{Tr}(A) \equiv -2\kappa$, so the eigenvalues of A must sum to -2κ. Furthermore, since A only has real entries, its eigenvalues are either both real, or are a complex conjugate pair. Then it easily follows that the eigenvalues $\eta_\pm$ of A can be written as

$$\eta_\pm = -\kappa \pm \chi,$$

where χ is either strictly positive or purely imaginary. Consequently, the only possible bifurcation mechanism is a *saddle-node bifurcation* where $\eta_+ = 0$, for $\chi = \kappa$. At this bifurcation point, a *saddle-node pair is either created or annihilated together* (depending in which direction one changes the system parameters). Denoting the total number of nodes by N_n, and the total number of saddle points by N_s, this implies that for any set of system parameters $(\kappa, \delta, \beta, \xi_d)$, $N_\mathrm{n} - N_\mathrm{s}$ remains constant. For system (5.9), we can prove that $N_\mathrm{n} - N_\mathrm{s} \equiv 1$. The main idea behind the proof is a standard topological argument based on the Poincaré index (see Proposition 1.8.4 of [57]) of a closed curve $\mathcal{C}$ encircling all the equilibria[1]. The index theorem equates $N_\mathrm{n} - N_\mathrm{s}$ to the number of turns made by the vector field when traversing the curve $\mathcal{C}$, and for our system this number of turns amounts to 1.

We now turn to finding the equilibrium points of (5.9). It is instructive to perform the equilibrium point analysis in polar coordinates,

$$\bar{u} = R\sin(\theta), \tag{5.12a}$$
$$\bar{v} = R\cos(\theta). \tag{5.12b}$$

The equivalent vector field for (θ, R) becomes

$$\dot{\theta} = \delta + \tilde{\beta}\frac{g^{(n:m)}(\theta, R, \xi_d)}{R}, \tag{5.13a}$$
$$\dot{R} = -\kappa R + \tilde{\beta} h^{(n:m)}(\theta, R, \xi_d), \tag{5.13b}$$

with

$$g^{(n:m)}(\theta, R, \xi_d) = \begin{cases} \sum_{k=-\infty}^{\infty} \cos(kn\theta)\mathcal{J}_{1+kn}(R)\mathcal{J}_{-km}(\xi_d) & , \quad m+n \text{ even}, \\ \sum_{k=-\infty}^{\infty} \cos(2kn\theta)\mathcal{J}_{1+2kn}(R)\mathcal{J}_{-2km}(\xi_d) & , \quad m+n \text{ odd}, \end{cases} \tag{5.14a}$$

$$h^{(n:m)}(\theta, R, \xi_d) = \begin{cases} -\sum_{k=-\infty}^{\infty} \sin(kn\theta)\mathcal{J}_{1+kn}(R)\mathcal{J}_{-km}(\xi_d) & , \quad m+n \text{ even}, \\ -\sum_{k=-\infty}^{\infty} \sin(2kn\theta)\mathcal{J}_{1+2kn}(R)\mathcal{J}_{-2km}(\xi_d) & , \quad m+n \text{ odd}, \end{cases} \tag{5.14b}$$

[1] We show in Section 5.2.2 that for $\kappa > 0$ all equilibria are necessarily situated in a bounded region of phase space.

where $\mathcal{J}_l$ is the l'th order Bessel function of the first kind. To make the notation more uniform, we will introduce the parity

$$r \coloneqq (m+n) \mod 2 = \begin{cases} 0 & , \quad m+n \text{ even}, \\ 1 & , \quad m+n \text{ odd}, \end{cases}$$

and drop the superscript $^{(n:m)}$ to make the notation less heavy, while it should be remembered that g and h depend on the pair of coprime integers (m,n). In this way we can write

$$g(\theta, R, \xi_d) = \sum_{k=-\infty}^{\infty} \cos((1+r)kn\theta)\mathcal{J}_{1+(1+r)kn}(R)\mathcal{J}_{-(1+r)km}(\xi_d), \tag{5.15a}$$

$$h(\theta, R, \xi_d) = -\sum_{k=-\infty}^{\infty} \sin((1+r)kn\theta)\mathcal{J}_{1+(1+r)kn}(R)\mathcal{J}_{-(1+r)km}(\xi_d). \tag{5.15b}$$

As an immediate observation, for any value of κ, β and δ, if either $n \geq 2$, or $n = 1$ and $r = 1$, the origin $R = 0$ corresponds to an equilibrium point, since $h(\theta, 0, \xi_d) = 0, \forall \theta, \xi_d$. Since we are interested in finding subharmonic solutions with $n > 1$, we can exclude the case $n = 1$, $r = 0$ however, so we can always assume the origin to be an equilibrium point. Subsequently excluding the origin, the remaining equilibria (θ^*, R^*) can be sought for by solving

$$\delta = -\tilde{\beta}\frac{g(\theta^*, R^*, \xi_d)}{R^*}, \tag{5.16a}$$

$$\kappa = \quad \tilde{\beta}\frac{h(\theta^*, R^*, \xi_d)}{R^*}. \tag{5.16b}$$

Thus excluding the origin, whenever we find a node (resp. saddle point) we know there must exist a corresponding saddle point (resp. node). For this reason, we do not focus on the stability type for now, and postpone this question to Section 5.3. The rest of this chapter is outlined as follows. First, a set of global symmetries of the set of equilibria is discussed. Next, in Section 5.2.2 we consider some insightful limiting cases, for which analytical conclusions can be obtained. Section 5.3 then details a numerical approach for characterizing the set of equilibria, for the case $m = 1, n = 3$.

5.2.1 Global symmetries

The averaged model (5.9) adheres to a global rotational symmetry, causing a degeneracy in the set of equilibria.

(*i*) The averaged vector field is invariant under rotation by an angle $\frac{2\pi}{n(1+r)}$, since $h(\theta + \frac{2\pi}{n(1+r)}, \cdot, \cdot) = h(\theta, \cdot, \cdot)$, and $g(\theta + \frac{2\pi}{n(1+r)}) = g(\theta, \cdot, \cdot)$. This means that for any trajectory $(\theta(s), R(s))$, another solution is obtained by considering $(\theta(s) + k\frac{2\pi}{n(1+r)}, R(s))$, $k = 1, \ldots, (1+r)n-1$. In particular, any equilibrium (θ^*, R^*) is part of a group of $(1+r)n$ equilibria of *the same stability type*.

(*ii*) In the Hamiltonian limit of $\kappa = 0$, $\dot{R} = 0$ is automatically satisfied for

$$\theta^* = \frac{k\pi}{n(1+r)}, k = 0, \ldots, (1+r)n-1, \tag{5.17}$$

readily identifying a subset of possible equilibria. Note that for any value of R^*, the detuning can be chosen to satisfy (5.16a), so such equilibria must exist for

$$\delta \in \Big[-\tilde{\beta} g_{\sup}, -\tilde{\beta} g_{\inf}\Big],$$

where

$$g_{\inf} \coloneqq \inf_{\theta^* \in \left\{0, \frac{\pi}{n(1+r)}\right\}, R>0} \frac{g(\theta^*, R^*, \xi_d)}{R},$$
$$g_{\sup} \coloneqq \sup_{\theta^* \in \left\{0, \frac{\pi}{n(1+r)}\right\}, R>0} \frac{g(\theta^*, R^*, \xi_d)}{R}$$

Since g is bounded, these limits are well-defined.

(*iii*) Still in the Hamiltonian case, an extra symmetry of (5.13) can be established:

$$\theta \to -\theta, \tag{5.18a}$$
$$s \to -s. \tag{5.18b}$$

The system is therefore called *reversible*, due to this time-reversal symmetry. (5.18) has no immediate extra consequences for any of the equilibria satisfying $\theta^* = k\frac{\pi}{n(1+r)}$, since the set is invariant under $\theta \to -\theta$. However, any equilibrium (θ^*, R^*) that is not of this form must necessarily come with a second equilibrium $(-\theta^*, R^*)$ of the same stability type. This symmetry is broken for $\kappa > 0$, but one can expect a certain approximate symmetry to hold, as an infinitesimal amount of dissipation can only change the phase portrait in a continuous manner.

5.2.2 Limiting behavior

There are two interesting limits to be considered in terms of the distance R to the origin.

- For $R \ll 1$, we can Taylor expand (5.13) to obtain up to leading order, for $n > 1$:

$$\dot{\theta} = \delta + \frac{\tilde{\beta}}{2}\mathcal{J}_0(\xi_d) + \mathcal{O}(R), \tag{5.19a}$$
$$\dot{R} = -\kappa R + \mathcal{O}\big(R^2\big). \tag{5.19b}$$

The origin of phase space is seen to be a stable node for $\kappa > 0$, and a center in the limit of $\kappa \to 0$. We call this equilibrium the *nominal point*. Close to the origin, the averaged model describes an essentially linear system (harmonic oscillator). The Josephson nonlinearity only shows itself in the fact that the frequency of this effective harmonic oscillator depends on the drive amplitude ξ_d, which is not the case for the response of a purely linear system. We call this drive-induced frequency shift the *AC-Stark shift* of the oscillator:

$$\Delta_{\mathrm{AC}} \coloneqq \frac{\tilde{\beta}}{2}(\mathcal{J}_0(\xi_d) - 1). \tag{5.20}$$

One important conclusion is that the AC-Stark shift shows oscillatory behavior with ξ_d, and remains bounded indefinitely as a function of the drive amplitude ξ_d.

- The opposite limit can also be taken. Consider a candidate equilibrium point (θ^*, R^*) and let $R^* \to \infty$. Since g is a bounded function of R, we obtain

$$\dot{\theta} = \delta + \mathcal{O}\left(\frac{1}{R^*}\right).$$

As $R^* \to \infty$, the value of $|\delta|$ that is allowed for an equilibrium point to occur tends to zero. In terms of the original drive frequency this implies

$$\tilde{\nu}_d = \frac{n}{m} + \mathcal{O}\left(\frac{1}{R^*}\right).$$

The effect of the nonlinearity of the Josephson junction thus effectively disappears, and we obtain a resonance condition based solely on the linear part of the system. We can apply the same reasoning to the dissipation rate κ, as also h is bounded in R. For an equilibrium point to occur at a distance R^*, we need

$$\kappa = \mathcal{O}\left(\frac{1}{R^*}\right).$$

- There is one more limit that allows for a simple analytical estimate, namely the limit of weak driving: $\xi_d \ll 1$. In this case we can replace the Bessel functions by an appropriate asymptotic expansion to obtain the leading-order contributions in (5.13). The asymptotic expansion

$$\mathcal{J}_l(\xi_d) \sim \frac{\xi_d^l}{2^l l!}, \quad l, \xi_d > 0 \tag{5.21}$$

is valid for $\xi_d \to 0$. We obtain the following leading-order equation:

$$\dot{\theta} = \delta + \tilde{\beta}\frac{\mathcal{J}_1(R)}{R} + \mathcal{O}\left(\frac{\xi_d^{(1+r)m}}{2^{(1+r)m}((1+r)m)!}\right), \tag{5.22a}$$

$$\dot{R} = -\kappa R - (-1)^m \tilde{\beta}\sin((1+r)n\theta)\frac{\xi_d^{(1+r)m}}{2^{(1+r)m}((1+r)m)!}\left(\mathcal{J}_{(1+r)n+1}(R) + (-1)^r \mathcal{J}_{(1+r)n-1}(R)\right)$$
$$+ \mathcal{O}\left(\frac{\xi_d^{2(1+r)m}}{2^{2(1+r)m}(2(1+r)m)!}\right). \tag{5.22b}$$

In this case, it is δ that first determines R^* such that $-\delta/\tilde{\beta} \simeq \mathcal{J}_1(R^*)/R^*$ (though possibly not uniquely), and the value of θ can then be chosen as to satisfy $\dot{R} = 0$ in (5.22b). Note that this last equation always allows for a solution θ^* as long as the dissipation rate κ is small enough. In the limit of $\kappa = 0$, $\theta^* = \frac{k\pi}{n(1+r)}, k = 0, \ldots, (1+r)n - 1$ provides a class of solutions. However, for decreasing ξ_d, the averaged model tells us that the oscillator must be increasingly high-Q to observe the corresponding subharmonic resonance. Indeed, using the boundedness of $\mathcal{J}_{(1+r)n\pm1}(R)/R$ for $n > 1$, it easily follows from (5.22b) that

$$\kappa < \frac{\tilde{\beta}\xi_d^{(1+r)m}}{2^{(1+r)m-1}((1+r)m)!} + \mathcal{O}\left(\frac{\xi_d^{2(1+r)m}}{2^{2(1+r)m}(2(1+r)m)!}\right)$$

must be satisfied for there to exist any equilibria. Note that odd-parity processes ($r = 1$) are suppressed, in the sense that asymptotically, for small ξ_d, one needs a much higher-Q system to observe them.

The general equilibrium point structure of the averaged model is quite complicated, and especially the sequence of bifurcations upon varying parameters is increasingly complicated. In the next subsection, we adopt a numerical approach to characterize this equilibrium point structure as a function of the drive parameters.

5.3 Numerical approach for $(n:m) = (3{:}1)$

Note that for any fixed equilibrium (θ^*, R^*), and any given drive amplitude ξ_d, one obtains the corresponding values of (κ, δ) by *forwardly* computing them from (5.13). If on the other hand, we want to fix the system parameters beforehand, and look for equilibrium points, one has to resort to a numerical root-finding algorithm. To avoid having to use root-finding algorithms in the two variables (θ, R) we make an observation. Note that the dissipation rate κ is fixed at the fabrication of the device, whereas δ corresponds to a drive-detuning that is typically adjusted online. This allows us to adopt the following strategy to find the equilibria of (5.13) as a function of $(\tilde{\beta}, \kappa, \delta, \xi_d)$, using a reliable *one-dimensional* root-finding algorithm. First fix the values of $\tilde{\beta}, \kappa$ *and* the R^*-value of the sought-for equilibrium. Next, from (5.13b), root-find possible θ^*-values that give rise to $\dot{R} = 0$. For this we used a simple algorithm based on sign changes of $\dot{R}$ as function of θ. If no such sign changes are found within 1000 uniform samples for θ in the interval $[0, 2\pi)$, we conclude that no equilibria exist for the given values of (κ, δ, R^*). For every θ^* that does give rise to $\dot{R} = 0$, from (5.13a), we can forwardly compute the (unique) value

$$\delta = -\tilde{\beta}\frac{g(\theta^*, R^*, \xi_d)}{R^*}$$

such that also $\dot{\theta} = 0$ and (θ^*, R^*) is indeed an equilibrium point. As a note aside, the point $R^* = 0$ should be omitted, as θ is ill-defined at the origin. From (5.19b), we know that the origin is always an equilibrium point however, and corresponds to a stable node when $\kappa > 0$.

Afterwards, the stability type of the corresponding equilibrium can be determined by performing a linearization analysis on (5.9). We recall that if the eigenvalues of

$$A(R^*\sin(\theta^*), R^*\cos(\theta^*)) = \left.\begin{pmatrix} \frac{\partial \dot{\bar{u}}}{\partial u} & \frac{\partial \dot{\bar{u}}}{\partial v} \\ \frac{\partial \dot{\bar{v}}}{\partial u} & \frac{\partial \dot{\bar{v}}}{\partial v} \end{pmatrix}\right|_{\bar{u}=R^*\sin(\theta^*), \bar{v}=R^*\cos(\theta^*)} . \tag{5.23}$$

both have strictly negative real parts, then (θ^*, R^*) corresponds to a stable node. If one of the eigenvalues has a strictly positive real part, then (θ^*, R^*) corresponds to a saddle point. In practice, it suffices to compute the determinant of (5.23). An analytical formula similar to (5.13), (5.14) can be derived for $A(R^*\sin(\theta^*), R^*\cos(\theta^*))$, and the expression is then evaluated numerically in (θ^*, R^*).

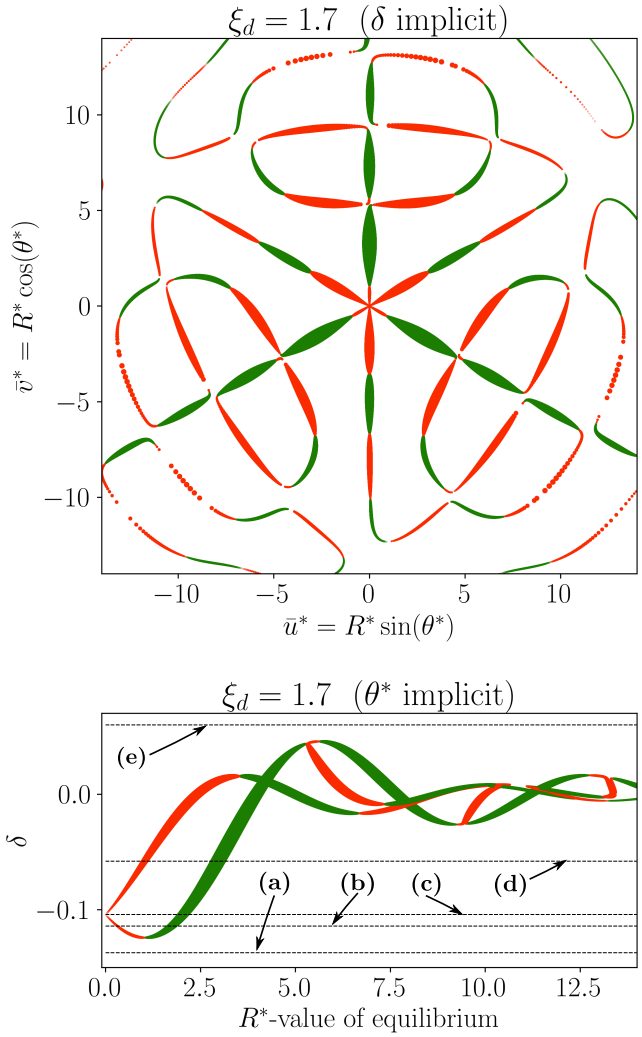

Figure 5.1: Numerical account of the bifurcation structure of the averaged model (5.13),(5.15) when varying the detuning δ, for $\tilde{\beta} = 0.5$, $\kappa = 10^{-5}$, and $\xi_d = 1.7$. The possible equilibria (θ^*, R^*) were determined by imposing $\dot{R} = 0$ (see (5.16b)). Two projections are given for the remaining relation $\delta = -\tilde{\beta} g(\theta^*, R^*, \xi_d)/R^*$, relating the detuning δ to the polar coordinates (θ^*, R^*) of the equilibrium point. **(top):** The possible equilibria satisfying $\dot{R} = 0$ (see (5.16b)) are plotted, omitting the corresponding (uniquely defined) value of δ. Stable nodes are shown in green, while saddle points are shown in red. One can clearly see the rotational symmetry over an angle $\frac{2\pi}{n(1+r)} = 2\pi/3$ of the equilibrium point structure, which was introduced in Section 5.2.1. Equilibria close to the origin ($R < 5$ here) occur approximately at angles $\theta = k\pi/3, k = 0, \ldots 5$. **(bottom):** δ is plotted as a function of R^*, omitting the corresponding value of θ^*. Correspondingly, every displayed point corresponds to a triplet of equilibria, at the same distance R from the origin, and angles $\pm 2\pi/3$ apart. At local extremal points of δ, a saddle-node bifurcation takes place, since three nodes and three saddles locally (dis)appear at these extrema. The bifurcation mechanisms from situation (a) to (e) are discussed in the text.

5.3.1 Bifurcation structure

In Figure 5.1, an account is given of the equilibrium point structure of the averaged model for $m = 1, n = 3$ (so an even-parity process, $r = 0$), as a function of the detuning δ, for fixed values of $\kappa = 10^{-5}, \tilde{\beta} = 0.5$ and $\xi_d = 1.7$. Two projections of the relation

$$\delta = -\tilde{\beta}\frac{g(\theta^*, R^*, \xi_d)}{R^*}$$

are given, linking the triplet (δ, θ^*, R^*). Stable nodes are shown in green, while saddle points are shown in red. On the top plot, the value of δ is implicit. One can clearly see the rotational symmetry over an angle $\frac{2\pi}{n(1+r)} = 2\pi/3$ of the equilibrium point structure, which was introduced in Section 5.2.1. On the bottom plot, the value of the angle θ^* is implicit. At local extrema of δ, a saddle-node bifurcation takes place, where three nodes and three saddles locally (dis)appear at these extrema. Combining the bottom and top plots of Figure 5.1, we can discuss the location of the equilibria and the bifurcations that take place, when increasing δ gradually from point (a) to point (e).

- For the most negative values of δ, no equilibria are found for $R > 0$. The only equilibrium resides in the origin (not shown), and the averaged model predicts the origin to be globally attractive for any $\kappa > 0$. This is straightforward to prove due to the absence of other equilibria.

- Upon increasing the value of δ, from point (a) to point (b), a threefold saddle-node bifurcation (around $R^* \simeq 1$) takes place, simultaneously creating three saddle-node pairs at angles $\theta^* \simeq 2k\pi/3, k = 0, 1, 2$. Upon further increasing the value of δ, the stable nodes move radially outward to larger values of R^*, while the saddle points move radially inward towards the origin.

- From point (b) to (d), the saddle points move through the origin, re-exiting at angles $\theta^* \simeq \pi/3 + 2k\pi/3, k = 0, 1, 2$ (note that in the origin θ^* can undergo a discontinuity). In situation (c), the three saddle points coalesce in the origin, creating a degenerate point [2]. The value of δ for situation (c) exactly compensates the AC-Stark shift (see (5.20)) of the oscillator:
$$\delta = -\frac{\tilde{\beta}}{2}\mathcal{J}_0(\xi_d) \simeq -0.1.$$

- When further increasing δ, moving from situation (d) to situation (e), many different saddle-node pairs are created and move towards other equilibria as a function of the detuning δ, before subsequently recombining and annihilating in another saddle-node bifurcation. Moreover, we see that equilibria are no longer restricted to the angles $\theta \simeq \frac{k\pi}{3}, k = 0, \ldots 5$, as equilibria branch off and move in the angular direction in between these radial axes. Beyond the numerical results displayed in Figure 5.1, we have no further analytical insight in this complicated bifurcation structure. This process continues

[2] One can show that for $\kappa = 0$ this indeed corresponds to a degenerate bifurcation point where the 4 equilibria exactly coincide, due to the global rotational symmetry of the vector field. For small non-zero κ this bifurcation must be regularized in saddle-node bifurcations very close to this degenerate point, providing an *unfolding* of this degenerate point in codimension 2, similar in nature to the cusp catastrophe (see e.g. Section 7.1 of [57]). The exact nature of the unfolding of this bifurcation in terms of the two parameters (κ, δ) has not been the study of this work however.

when further increasing δ, until eventually all equilibria are annihilated, corresponding to situation (e).

A schematic representation of the phase diagrams corresponding to the analogous situations (a) to (e) for the dissipationless case of $\kappa = 0$ is given in Figure 5.2 (top).

The bifurcation structure for different values of ξ_d looks qualitatively similar. Specifically, we observe that for values of $\xi_d \in [0, 2.2]$, when driving to compensate the AC-Stark shifted frequency of the oscillator ($\delta = -\tilde{\beta}\mathcal{J}_0(\xi_d)/2$) there exists a *unique* triplet of stable nodes (not shown here). The distance R^* of these nodes to the origin moreover increases monotonically from 0 to 3.3 with ξ_d going from 0 to 2.2, and for the corresponding angles we have $\theta^* \simeq 2k\pi/3, k = 0, 1, 2$. This is true independently of the value of $\tilde{\beta}$, for small enough dissipation rate κ. Driving the oscillator around its AC-Stark shifted frequency thus identifies one favorable working regime in which the global symmetries of (5.17) approximately hold, and in which the stable resonant nodes are unique. In the next section, we will indeed see that the drive parameters giving rise to a confined manifold of Schrödinger cat states for the quantum system generally follow the AC-Stark shift:

$$\delta = -\frac{\tilde{\beta}}{2}\mathcal{J}_0(\xi_d).$$

5.3.2 Comparison to Floquet-Markov simulations

In this section, we establish how the equilibrium point structure of the averaged classical model (5.13),(5.15) can predict the asymptotic behavior of the quantum system, as calculated by the numerical Floquet-Markov simulations outlined in Section 3.2.2. For this we consider the dissipationless case of $\kappa = 0$, as the Floquet-Markov simulations are set in the limit of a vanishing coupling rate to an environmental bath, and hence at a vanishing dissipation rate. The value of β is chosen as to be in a regular regime, $\beta = 0.5$. We again consider the case of the $(3:1)$-resonance as a guiding example, while the discussion can readily be applied to other resonances.

The general correspondence that can be established between the classical and quantum system was outlined in Section 4.1.3. For the case of the $(3:1)$-resonance, we saw that a stable 3-orbit

$$\left\{\left(x_l^{(3:1)}, p_l^{(3:1)}\right) | l = 0, 1, 2\right\}$$

of the Poincaré map $\mathcal{P}$ corresponds to a triplet of Floquet modes that are of the form of three-component Schrödinger cat states, and whose quasienergies were shown to be degenerate modulo $\nu_d/3$, indicating a multi-photon process where three oscillator photons are converted into one drive photon and vice versa. We recall that these Schrödinger cat states are given by the superpositions of distinguishable states in phase space that closely resemble coherent states $|\alpha_l\rangle$, $l = 0, 1, 2$. The amplitudes α_l of these coherent states were seen to approximately correspond (see e.g. Figure 4.3) to the three classical fixed points of $\mathcal{P}^3$,

$$\alpha_l \simeq \frac{x_l^{(3:1)} + i p_l^{(3:1)}}{\sqrt{2}}, \quad l = 0, 1, 2. \tag{5.24}$$

In this chapter, we have described a prominent class of stable $(3:1)$-subharmonics corresponding to stable nodes

$$(R^* \sin(\theta^* + 2l\pi/3), R^* \cos(\theta^* + 2l\pi/3)), l = 0, 1, 2$$

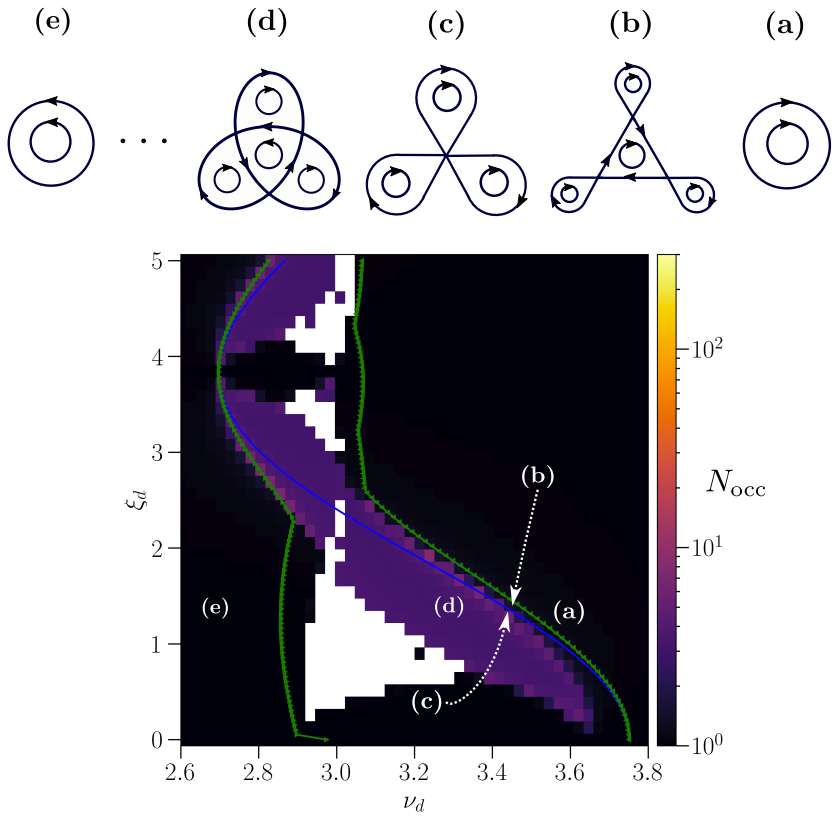

Figure 5.2: Comparison between the Floquet-Markov signatures of the $(3:1)$-resonant cat states, and the occurrence of $(3:1)$-fixed points of $\mathcal{P}^3$, as predicted by the averaged classical system (5.13), for $\beta = 0.5$, $\lambda = 0.2$, and $\kappa = 0$. **(Bottom):** The effective number of Floquet modes N_{occ} occupied by ρ_∞ at time $\tau = 0 \mod 2\pi/\nu_d$ is plotted in a color map plot, as a function of drive parameters (exact numerical Floquet-Markov simulations). The green lines delimit the region where the classical averaged model (5.9) predicts the existence of stable equilibria, and is seen to delimit the quantum resonance region where $N_{\mathrm{occ}} \simeq 3$ up to very good accuracy. The AC-Stark-shifted drive frequency as predicted by the averaged model (see (5.27)) is shown in blue. **(Top):** Schematic representation of the phase portraits of the averaged system for 5 points indicated in the bottom plot. The center in the middle corresponds to the origin of phase space. Moving from (a) to (e), the following bifurcation mechanisms take place. First, a saddle-node bifurcation occurs where three nodes and three saddles are created, represented in (b). The saddle-separatrices form (initially small) homoclinic loops. The corresponding saddle-points subsequently move radially inwards (typically very fast as a function of ν_d), until they coalesce (and perfectly coincide, due to the discrete rotational symmetry) in the origin. This is depicted in the degenerate situation (c), corresponding to the drive frequency ν_d that compensates for the AC-Stark shift, indicated by the blue line. At this point, the direction of rotation of the origin is reversed, and in (d) the three saddle-points form heteroclinic loops. The bifurcation process from (d) to (e) involves (often cascades of) saddle-node annihilations and creations (see Figure 5.1), when further lowering the value of ν_d (corresponding to increasing δ, see (5.7)). This entails exchanges in pairing between saddle-node triplets, before they eventually all cancel out, and only the center in the origin remains. This situation is depicted in situation (e).

of the first-order averaged model (5.9), which approximate solutions of the true system. Working back to the lab frame, by undoing the rotating-frame transformation (5.6), we obtain that the corresponding 3-orbit of the Poincaré map $\mathcal{P}$ corresponding to (5.5) is approximately of the form

$$\tilde{x}_l^{(3:1)} \simeq R^* \sin(\theta^* + 2l\pi/3), \tag{5.25a}$$

$$\tilde{p}_l^{(3:1)} \simeq R^* \cos(\theta^* + 2l\pi/3), \tag{5.25b}$$

Recall from Section 3.1.1.1 that both quadratures $\tilde{x}, \tilde{p}$ were scaled by the quantum scaling parameter (see (3.15)) λ to eliminate it from the classical equations of motion. The correspondence (5.24) can then be worked out for the 3-orbit of the form (5.25), yielding

$$\alpha_l \simeq i e^{-i\left(\frac{2\pi l}{3}+\theta^*\right)} \frac{R^*}{2\lambda}, l = 0, 1, 2. \tag{5.26}$$

With this correspondence in mind, we can now compare the classical averaged model to the numerical Floquet-Markov simulations of the infinite-time behavior of the quantum system. This is the subject of Figure 5.2(bottom). To characterize the asymptotic regime, as in Chapter 4, we consider the effective number of Floquet modes N_{occ} occupied by the asymptotic state $\rho_\infty(\tau)$, defined as

$$N_{\text{occ}} \coloneqq \exp(S(\rho_\infty)),$$

where $S(\rho_\infty)$ is the von Neumann entropy of the state,

$$S(\rho_\infty) \coloneqq -\operatorname{Tr}(\rho_\infty \ln(\rho_\infty)).$$

N_{occ} is plotted as a function of the drive parameters (ν_d, ξ_d) in Figure 5.2 (bottom). From a numerical point of view, we define the *resonance region* for the quantum system to be the set of drive parameters (ν_d, ξ_d) for which

$$N_{\text{occ}} \simeq 3,$$

since when ρ_∞ is given by a uniform mixture of 3 three-component Schrödinger cat states, N_{occ} amounts to exactly 3. This quantum resonance region corresponds to the purple region in Figure 5.2. The black region corresponds to an essentially pure state (displaced vacuum) for ρ_∞. For the drive parameters corresponding to the white points, the numerical simulations are inconclusive to determine ρ_∞ (see Remark 4.1).

Superimposed on the plot is the blue line, representing the drive parameters that exactly compensate for the AC-Stark shift of the oscillator, given by

$$\nu_d^{(3:1)} \coloneqq \frac{3}{1}\left(1 + \frac{\beta}{2}\mathcal{J}_0(\xi_d)\right). \tag{5.27}$$

We can see that the general shape of the resonance region follows the oscillation of this AC-Stark shifted resonance frequency. Plotted in green are the extremal values for the drive-detuning for which the averaged model exhibits stable nodes. These necessarily coincide with a saddle-node bifurcation of the average system, and analogously to the *global* extrema of the analogous curves shown in Figure 5.1(bottom). We can see that the green lines delimit the quantum resonance region ($N_{\text{occ}} \simeq 3$) up to very good approximation, and hence the averaged classical model accurately predicts the drive parameters that lead to a resonant situation for the quantum system. As a point of reference, the top of Figure 5.2 shows schematic diagrams

of the corresponding phase-portrait of the classical averaged model (for $\kappa = 0$). Examples of drive parameters that give rise to the respective phase portraits are indicated on the bottom plot of Figure 5.2. The drive parameters are chosen such that the averaged model predicts either a unique triplets of resonant equilibria (situations (b),(c),(d)), or that only the origin remains as a center (situations (a) and (e)).

In conclusion, we can see that the general shape of the quantum resonance region in terms of drive parameters is well-described by the classical averaged model of (5.9). Since (5.9) corresponds to the lowest-order model of the perturbative method of averaging, and the value of β chosen is quite large to be considered a perturbation (but small enough to be in the regular, non-chaotic regime, $\beta = 0.5$) was not a priori given. A first limitation of any classical model in predicting the quantum resonance region, is that the classical equations of motion (5.5) do not show any dependence on the quantum scaling parameter λ, which has a clear quantum effect studied in Section 4.4. We conclude with a few remarks on other limitations of classical models in predicting the resonance region for the quantum system, leading to some expected quantitative differences between the purple region and the green delimiting lines in Figure 5.2.

Remark 5.2. *(Tunneling and far equilibria).* A first aspect to be noted, is that the maximal number of Floquet modes occupied by ρ_∞ is seen to be $N_{\text{occ,max}} \simeq 3$. The possible Floquet modes that are occupied correspond to either three 3-component cat states (purple region, $N_{\text{occ}} \simeq 3$), or a single Floquet mode resembling a (dressed) vacuum state (black region, $N_{\text{occ}} \simeq 1$) [3]. Note that this is not what would be predicted by the classical averaged model in the equivalent limit of vanishing dissipation rate, since many resonant stable nodes can co-exist (see Figure 5.1(bottom)), and all have a non-vanishing basin of attraction. The reason for this limitation of the quantum-classical correspondence in the asymptotic regime is the specific dissipation model for the driven quantum system, consisting of a weak Hamiltonian coupling to an environmental bath. Indeed, by the extension of Fermi's golden rule to periodically-driven systems outlined in Section 3.2.2, the driven quantum system can directly transition between different Floquet modes, and is seen to converge to a mixture of Floquet modes that correspond to only a handful of the possible classical locally-stable nodes. When comparing the phase-space representation of ρ_∞ to the phase portrait of the classical Poincaré map, as in Figure 4.3, we observe (simulations not shown here) that the dominantly-occupied Floquet modes in the resonant case always corresponds to the classical stable resonant nodes that are *closest to the origin*, so in terms of the averaged model, have minimal values of R^*.

A possible explanation for this follows from an energetic argument, since coherent states that are further out into phase space correspond to a larger average number of photons,

$$\bar{n} \coloneqq |\alpha_l|^2 \simeq \frac{R^{*2}}{4\lambda^2},$$

and hence could be be less favorable thermodynamically since the environmental bath was assumed to be at zero temperature. This fact should also find a quantitative explanation through the application of semiclassical quantization methods based on the effective potential landscape associated to the nested irrational tori of the Poincaré map [11, 18]. For the regular, non-chaotic regime of periodically driven systems in a Floquet-Markov-limit similar to this

[3] The white points in Figure 5.2(bottom) indicate values for the drive parameters for which the numerical Floquet Markov simulations are inclusive to determine ρ_∞, since for these drive parameters, both a complete mixture of the three cat states on the one hand, and the dressed vacuum state on the other hand appear to be long-lived, and both span the kernel of the transition matrix R (see (3.48)) obtained from Fermi's golden rule outlined in Section 3.2.2. For a more detailed discussion, see Remark 4.1.

work, a Boltzmann distribution with a winding-number-dependent effective temperature has been shown to predict the distribution of Floquet modes [67]. Such an analysis falls beyond the scope of this dissertation however. As a last point, note that far-away resonant stable nodes might become relevant for the *transient*, finite-time behavior of the system. This is not the subject of this work however.

Remark 5.3. *(Basins of attraction).* A second main difference between the classical averaged model and the behavior of the quantum system lies in the fact that quantum states occupy a finite minimal surface area in phase space given by the Heisenberg uncertainty principle. In this way, classical stable nodes with a small basin of attraction [4] cannot be resolved by the quantum system, as the quantum wave-packet is forced to spread outside of the basin of attraction. Concretely, if the basin of attraction of a stable node is smaller than the surface in phase space occupied by a quantum coherent state $|\alpha_l\rangle$, the correspondence of Observation 4.1 should be expected to break down. Such small basins of attraction for the classical system occur close to a saddle-node bifurcation point for example, and we cannot expect the corresponding resonant stable nodes to give rise to a resonant quantum regime, The same argument holds when the resonant nodes are sufficiently close to the origin, as the quantum state spreads over multiple classical basins of attraction (not shown here). This potentially explains the black region around $\xi_d \in [0, 0.3], \nu_d \in [3.67, 3.73]$, as ν_d is close to the saddle-node bifurcations of the green curves, and moreover, for small values of ξ_d, the stable nodes are created close to the origin (not shown here).

Remark 5.4. *(Hilbert space truncation).* Lastly, from (5.26), we can see that the average number of photons of the coherent state $|\alpha_l\rangle$ is approximately given by

$$\bar{n} \coloneqq |\alpha_l|^2 \simeq \frac{R^{*2}}{4\lambda}.$$

Depending on the value of the quantum scaling parameter λ, many of the equilibria represented in Figure 5.1 thus correspond to a very high average number of photons in the oscillator. Indeed for a "nominal" experimental value of $\lambda = 0.2$, and for a reference value of $R = 3$, the corresponding mean number of photons amounts to

$$\bar{n} = \frac{R^2}{4\lambda^2} \simeq 56.$$

Hence equilibria of the averaged model corresponding to very large R^*-values are not captured by the numerical simulations, due to a finite truncation of the Hilbert space. Depending on the value of λ, we might not be able to capture such far-out equilibria of the classical system, as most of our simulations were performed using 300 Fock states. Therefore, the number of Fock states was chosen as to capture the coherent states corresponding to the stable nodes of the averaged model that are *closest* to the origin, for the smallest value of the quantum scaling parameter λ considered, namely $\lambda = 0.2$. Such an analysis reveals that 150 Fock states should suffice, and we see that the simulations have fully converged for 300 Fock states, for any purple or black point in Figure 5.2(bottom). We recall that the white points in Figure 5.2(bottom) are not due a truncation of Fock space. All the relevant individual Floquet modes have fully converged with 300 Fock states, but the specific mixture of Floquet modes in ρ_∞ is not uniquely defined for these points (see Remark 4.1).

[4] While the classical averaged model was analyzed for $\kappa = 0$, we refer to the resulting centers as "nodes" after all, since for any $\kappa > 0$, these correspond to stable nodes. Similarly, we refer to regions in phase space delimited by saddle separatrices as "basins of attraction" of the nodes, since in the limit of $\kappa \to 0$ but $\kappa > 0$, the true basins of attraction of the corresponding stable nodes are delimited by these saddle-separatrices.

5.4 Summary

In this chapter, we applied the method of geometric averaging to characterize a general set of $(n : m)$-subharmonic resonances as a function of drive parameters, treating the regularity parameter β as a perturbation. The averaged vector field was seen to split into two cases for the parity $r = (m+n) \mod 2$, where equilibria must come in sets of size $(1+r)n$ due to a global rotational symmetry of the system, as was the case for the quantum multi-photon process in Section 4.1.4. Considering the full Josephson cosine potential in the averaged model, the boundedness of the cosine potential showed itself in the following way. The frequency range for $\tilde{\nu}_d$ in which resonant equilibria exist was shown to be bounded from both sides, and also the AC-Stark shift of the oscillator was shown to be a bounded oscillating function of the drive amplitude ξ_d. Next, we outlined a simple algorithm to numerically characterize the bifurcation structure of equilibria as a function of drive parameters. These results were shown to be able to predict the equivalent resonance region in (ν_d, ξ_d) of the quantum system, providing an efficient and insightful way to select drive parameters that lead to a confined manifold of Schrödinger cat states.

An immediate extension of these results should be pursuing higher-order averaged models of increased accuracy, capturing terms of the order $\mathcal{O}(\beta^k), k \in \mathbb{N}, k \geq 2$ in the averaged vector field. While we have only obtained an explicit formula for the second-order average, capturing terms of order β^2, the global symmetries of Section 5.2.1 can be shown to persist up to *any* order of averaging, both for the Krylov-Bogoliubov-type averaging approach [75] as for Lie-group based averaging approaches for the Hamiltonian case [125]. This justifies pursuing higher-order models while retaining the same physical interpretation of an analogous multi-photon quantum process where $(1+r)n$ oscillator photons at frequency $m\nu_d/n$ are exchanged with $(1+r)m$ drive photons at frequency ν_d.

Part II

Dynamical decoupling of the close environment

In this part, we develop an approach for countering noise in practical quantum devices. An elementary setting is considered where a target system carrying quantum information is coupled to a small and identifiable environment subsystem that is the main source of noise for the target. We use techniques and insights from the field of dynamical decoupling (DD) to propose the following strategy: driving the environment subsystem as to decouple it from the target.

Context and motivation

Several experimental realizations for quantum hardware encounter the situation where a target system is directly coupled to a finite-dimensional environment subsystem whose decoherence is identified as the main source of induced decoherence on the target. One example of such environment systems are so-called two-level system (TLS) defects in the oxide layer of superconducting Josephson junctions, which typically decohere through phonon channels and are a main mechanism inducing decoherence of superconducting qubits [84, 95]. Another such identified environment would be spurious box modes that show some residual coupling to the target modes in microwave resonators.

The idea of Dynamical Decoupling (DD, see [129] and a large set of follow-up works) is to reduce the effective coupling between two quantum systems by using tailored control actions at a faster timescale than the Hamiltonian coupling. Starting from this idea, we propose to reduce induced decoherence on the target system by applying actions, in a very broad sense, on the *environment side*. The potential advantages are that those actions need not be particularly precise, and that they commute with any system operations one may want to perform. In fact, in Chapter 7 we show how even adding dynamics as noisy as pure decoherence channels on the environment can decrease the induced dissipation on the target system.

Environment-actuated decoupling also opens the door to refined contributions to analyzing the decoherence induced on the target system. The timescale separation between the effective inter-system coupling and all the dominant dynamics acting on the environment allows for treating the induced decoherence experienced by the target in a perturbative manner, through the method of adiabatic elimination [5, 6, 66, 106]. This mathematical approach remains fully compatible with control actions applied to the environment over all ranges of magnitudes. More so, since the goal is to *reduce* the effective coupling between the target system and the environment, the validity of the adiabatic elimination approach actually increases. Using an extension of the adiabatic elimination formalism (see Section. 6.3.1.2), supplemented with Floquet-Markov-type [54] adjustment of the environment decoherence channels themselves when accounting for ultra-strong driving (see Section 6.3.3), we calculate the induced decoherence rate on the target when applying coherent drives or further decoherence channels on the environment, paving the way for an optimization of the setting.

No control actions whatsoever can hope to decouple from purely Markovian decoherence. More concretely, in mathematical terms: adding Hamiltonian actions on a system does not enable to reduce the effect of a purely Lindbladian dissipation channel on the same system. DD has been considered to cancel spurious effects in two cases. In the first proposal [129], the goal is directly formulated as reducing the coupling to a spurious finite-dimensional "environment" system. The target and spurious environment are both modeled as Hamiltonian systems. Control sequences are designed to make the effective Hamiltonian coupling vanish up to a certain order, the successive orders typically being given by a Magnus expansion [16, 88] or

an equivalent Hamiltonian averaging technique [35]. As a result of the DD controls, the state of the target system undergoes a fast trajectory and its quantum information is preserved in a so-called toggling frame which must be safely followed. In a second type of approach, it is acknowledged that Lindbladian dissipation models are in fact often an approximation, stemming from a direct interaction with a large bath. Identifying the environment with this large bath in a Hamiltonian model and introducing the DD drives before making the typical approximations (Born-Markov or secular approximations) that lead to a Lindbladian model, one obtains that decoupling actions are able to counter low-frequency noise, thus effectively modifying and reducing the Lindbladian decoherence channels on the target when DD controls act faster than the cut-off frequency of the noise-spectrum of the bath [37, 41, 121]. The decoherence model in the present work can be seen as intermediate to these two viewpoints, as it considers a target system coupled to a small effective environment, which itself undergoes Lindbladian decoherence. The small environment thus captures memory effects in the decoherence of the target. Since we will be driving this small environment, its Lindbladian dissipation model will have to be revised when considering strong drives (see Section 6.3.3), just as in the approach of [37, 41, 121]

Throughout most of this part, as a first approach, we will consider that the dominant noisy environment, denoted as the "E" subsystem, consists of a two-level quantum system (TLS). Such settings commonly appear in practice as spurious levels coupled to superconducting devices [22, 95]. More general settings should feature qualitatively similar behavior and could be studied in future work.

This part is organized as follows. In Section 6, we consider the environment subject to periodic drives. While acting on the environment comes with the security of not deteriorating the target state directly in the case of control imprecision, we also cannot expect to control an environment system in a well-calibrated manner. Neither can we expect to have accurate knowledge of the bare environment Hamiltonian. Using a simple model for both these uncertainties, we show that for the case of a TLS environment, using sufficient time-scale separation in the applied drive enables efficient DD despite control imprecisions. As a trade-off for requesting a strong time-scale separation, we consider a very simple control signal, consisting of only one harmonic tone. The analysis is performed using a generalization of adiabatic elimination adapted to periodically-driven systems, inspired by the basic Floquet property, and which is novel to the best of our knowledge. This analysis method also differs from the more standard DD analysis based on a Magnus expansion [88] in a purely Hamiltonian setting. We obtain an explicit Lindblad model for the leading-order induced decoherence on the target. The procedure, explained in Section 6.3.1.2, would allow in principle to obtain further perturbative corrections in powers of the coupling strength.

Next we consider the limit of ultra-strong DD drives, which requires revising the Lindbladian dissipation model of the TLS. In Section 6.3.3, we rederive a Lindbladian model for the dissipation of the environment TLS, starting from a general model where the E-subsystem is coupled to a large bath through a Hamiltonian coupling. The obtained Lindbladian will explicitly account for the possibly ultra-strong drive on E, yielding a perturbative correction to the dissipators obtained in the undriven case. We will see that this correction becomes significant when the drive amplitude is non-negligible with respect to the bare frequency of the TLS. For the derivation we follow the standard approach of the Born-Markov approximation [19], followed by a secular approximation, averaging out over rapidly oscillating terms. Once this model for E is settled in the presence of strong driving, the decoherence that it induces on the target system will again be calculated using the time-periodic extension of

adiabatic elimination.

In Chapter 7, we consider the limit of extremely disorganized DD actions, adding decoherence channels instead of Hamiltonians to the environment subsystem. Indeed, increasing the decoherence strength on the environment also decreases its effective coupling with the target system, and the scaling for induced dissipation on the target often turns out to be favorable at higher environment decoherence. Using second-order adiabatic elimination formulas, we analyze the resulting behavior in detail, providing some general results and characterizing the optimal choice for typical settings with a TLS environment.

Model description

As a main setting throughout this part, we consider a general target system T undergoing Hamiltonian dynamics, and whose main source of decoherence is an undesired Hamiltonian interaction with an environment E which itself undergoes fast Lindbladian decoherence. We describe both the Hamiltonian coupling as well as the applied controls and their possible control imprecisions in a rotating frame w.r.t. the bare system frequencies of both T and E. In this frame, the general evolution is described by the following master equation:

$$\tfrac{d}{dt}\rho = -i[H_T + H_E + H_{TE},\, \rho] + \sum_k \kappa_k \mathcal{D}_{L_k}(\rho)\ . \tag{II.1}$$

Here we have introduced the general Lindbladian dissipator

$$\mathcal{D}_X(\rho) = X\rho X^\dagger - \frac{1}{2}\Big(X^\dagger X\rho + \rho X^\dagger X\Big).$$

The L_k represent various decoherence channels of E, at respective rates κ_k. The Hamiltonians H_T, H_E and H_{TE} respectively act on T, on E, and couple T with E. Note that as this part of the dissertation does not feature any classical physics, we omit the boldface notation for quantum observables or other operators for notational convenience.

The objective is to protect quantum information stored in the target system T. Standard DD works by applying well-designed sequences of control Hamiltonians H_T. In this work we rather assume $H_T = 0$ and analyze how one can decrease the induced decoherence on T by acting on the environment through H_E on the one hand, or through addition or modification of the κ_k on the other hand.

A prototypical example for E is a set of two-level-systems (TLSs), like defects in the oxide layer of superconducting Josephson junctions [22, 38, 84, 95]. At the dominating order, we can consider the contribution to the overall induced decoherence of each such TLS individually [43]. In a rotating frame of both the target system and TLS, we consider a general stationary coupling

$$H_{TE} = g(T_x \otimes \sigma_x + T_y \otimes \sigma_y + T_z \otimes \sigma_z)\ . \tag{II.2}$$

Here, g is a small coupling rate with the dimension of a frequency (using units where $\hbar = 1$), T_x, T_y and T_z are arbitrary Hermitian operators acting on the target system, and $\sigma_x, \sigma_y, \sigma_z$ are the Pauli operators on the TLS.

The TLSs themselves are thus assumed poorly protected and quickly dissipate according to a Lindbladian model, as described in (II.1). When adding coherent drives in Chapter 6, we typically assume the dominating dissipation channels

$$L_k \in \{\sigma_-,\ \sigma_+\}\ , \tag{II.3}$$

corresponding to loss and excitation in the σ_z-basis of E. When adding/tuning dissipation channels in Chapter 7, the environment side is treated purely on the basis of a given set of dissipation operators L_k whose rates κ_k may be adjustable in some range.

In this way we mainly consider the Lindbladian dissipation operators L_k as fixed, independently of the mechanisms added to reduce the coupling between T and E. Since our goal towards DD is to drive strongly, we also compute corrections to the dissipation on E for the case where ultra-strong driving has an effect on the dissipation model itself. For this, in Section 6.3.3, we rederive a modified Lindbladian starting from a model where E interacts with a large bath.

Chapter 6

Coherent decoupling with drives

Dans ce chapitre, nous appliquons des contrôles DD cohérents à un environnement décohérant à deux niveaux, afin de découpler celui-ci d'un système cible général, et donc de réduire la décohérence qu'il induit sur la cible. Ce chapitre est organisé comme suit. Nous commençons dans la Section 6.1 par introduire la méthode de DD, y compris les travaux précédents concernant les contrôles DD continus à force bornée en particulier, appliqués à travers H_T. Ensuite, nous transfèrons l'application des contrôles DD au côté environnement H_E. Dans la Section 6.2, nous proposons un signal de contrôle continu qui tient compte de l'imprécision inévitable du contrôle lorsqu'on agit sur l'environnement. Dans Section 6.3, nous calculons ensuite un modèle de Lindblad explicite pour la décohérence induite sur la cible lors de l'application des contrôles DD. Ceci engendre une extension de l'approche d'élimination adiabatique aux couplages périodiques dans le temps, qui fait l'objet de la Section 6.3.1.2. Nous analysons ensuite les expressions obtenues, mettant en évidence l'efficacité d'appliquer des contrôles DD à l'environnement. Pour rendre l'analyse complète, dans la Section 6.3.3, nous rediscutons les canaux de dissipation sur l'environnement lorsque les contrôles H_E deviennent significatifs par rapport aux fréquences nues de celui-ci.

In this chapter, we pursue the strategy of applying coherent dynamical decoupling (DD) drives to a decohering TLS-type environment, in order to decouple it from a general target system, and thereby reduce the decoherence it induces on the target system. The chapter is organized as follows. We start in Section 6.1 by recalling the concept of DD more explicitly, including previous work concerning continuous bounded-strength decoupling schemes in particular, applied through H_T. Next, we transpose the application of DD drives to the environment-side H_E. In Section 6.2 we propose a continuous DD control signal accounting for inevitable control imprecision when acting on the environment. In section 6.3, we then calculate an explicit Lindbladian model for the decoherence induced on the target when applying the DD controls. This involves an extension of the adiabatic elimination approach to time-periodic couplings which is the subject of Section 6.3.1.2. We analyze the obtained expressions, highlighting the efficiency of applying environment-side DD drives. For further consistency, in Section 6.3.3, we re-discuss the dissipation channels on the environment when the DD drives H_E become significant compared to bare system frequencies.

6.1 DD and related work

Established DD approaches consist in applying control pulses to the target system T that send its state rapidly wandering around its Hilbert space. The explicit objective is for the average effect over one wandering cycle of all relevant coupling operators to go to zero. The simplest example is the case of a target qubit T with only one coupling term involving σ_z. In this case, one can periodically apply π-pulses around the σ_x-axis of T, such that it effectively accumulates phase around $\pm\sigma_z$ half of the time respectfully, thus canceling the coupling effect on average if there is no other motion in the meantime. The shorter the period between subsequent pulses, the better T is being decoupled from E. This is the well-known spin echo sequence [60]. The generalization of this idea to general systems with arbitrary stationary couplings was introduced in [129], and versions replacing the instantaneous pulses with bounded drives in group-based decoupling schemes were established in [25, 70, 128, 131].

For the case of a target qubit T, a different type of bounded-drive DD scheme has been devised, using the combination of a static field and a simple monochromatic drive [24, 36, 37]. In [37] the control Hamiltonian to decouple a single qubit takes the form

$$H_T(t) = \frac{\omega}{2}\sigma_z + \frac{\omega}{4}(\cos(\omega t)\sigma_x + \sin(\omega t)\sigma_y). \tag{6.1}$$

Under this drive, the qubit state is made to rotate around the σ_x-axis in a frame which itself rotates around the σ_z-axis at double the frequency. Indeed, $H_T(t)$ has been designed to generate the unitary evolution

$$U_T(t) = e^{-i\frac{\omega}{2}\sigma_z t}e^{-i\frac{\omega}{4}\sigma_x t}$$

of the target qubit in absence of any further dynamics. We can clearly see the composition of two rotations around orthogonal axes of the Bloch sphere. The effectiveness of this DD scheme can be analyzed in a frame that eliminates the DD controls, called the toggling frame. Indeed, it is easy to verify that the first-order decoupling condition is satisfied [129]. This means that any constant operator on T which could be present in the coupling Hamiltonian averages out to 0 under this unitary evolution:

$$\frac{\omega}{2\pi}\int_0^{\frac{2\pi}{\omega}} U_T^\dagger(t)\sigma_a U_T(t)\, dt = 0, \quad \text{for } a \in \{x, y, z\}\,. \tag{6.2}$$

When this first-order decoupling condition is satisfied, the effect of any coupling between T and E can be made arbitrarily small by ramping up ω. This is proven by identifying the average coupling as the first and leading order of a Magnus expansion of the effective dynamics in powers of $\frac{g}{\omega}$.

Such results are hence typically established by focusing on the Hamiltonian part of the model, i.e. discarding the L_k in (II.1) and showing that the effective coupling between T and E is canceled up to some order(s). In such a setting, the DD treats T and E in a symmetric way, and one could in principle consider applying the DD drives to either system. The advantages of acting on E rather than on T would be that (i) we minimize the danger of perturbing quantum information with actuation imprecisions and (ii) we can keep applying DD drives irrespective of the system operations on T. Indeed, standard DD acting on T requires specific adaptations when T is also subject to actions manipulating the quantum information system, like logical gates [70]. On the downside, of course, we can hope to act on E only if it is well identified and

of reasonably small dimension, like for instance spurious TLSs [84, 95]. Furthermore, even if such a subsystem is well identified, its parameters are surely not as well characterized as for the target system, hence the control actions will unavoidably be imprecise. The situation is not as symmetric between T and E when one explicitly considers E to be a strongly decohering environment, i.e. when introducing the L_k in (II.1). We therefore provide an analysis that explicitly considers the decoupling Hamiltonian and the decoherence operators together.

The remainder of this chapter is organized as follows, In Section 6.2, we introduce the model for control imprecision of the DD drives, and propose how to mitigate this imprecision by building an additional timescale separation into the DD drives. Next, since the fastest timescale is given by the dynamics of E, we propose an analysis of the model (II.1) including the decoherence channels L_k. In Section 6.3, using adiabatic elimination techniques, we eliminate the fast subsystem E and directly compute the induced decoherence on T, rather than going through the computation of effective couplings with Hamiltonian averaging techniques such as the Magnus expansion. Lastly, the model with dissipation channels L_k acting on E has to be rediscussed under ultra-strong DD driving, as this model ultimately stems from interaction of E with further external degrees of freedom in a way that can also be affected by the driving. We perform such a derivation in Section 6.3.3, and subsequently use the same adiabatic elimination procedure to compute and discuss the induced decoherence rate of the target system.

6.2 Double-timescale DD proposal

The E subsystem, i.e. the spurious TLS, is not an accurately addressable subsystem. As such, we will not assume to know the eigenfrequency Ω_E of E exactly. To account for this, we split up Ω_E into its best-guess value $\bar{\Omega}_E$ and an uncertain constant deviation $\delta\Omega_E$:

$$\Omega_E = \bar{\Omega}_E + \delta\Omega_E.$$

With this decomposition, the model (II.2) is defined in a rotating frame w.r.t. $\bar{\Omega}_E$, and H_E features a residual unknown detuning:

$$H_E(t) = \frac{\delta\Omega_E}{2}\sigma_z + H_c(t).$$

Here, $H_c(t)$ stands for the applied control Hamiltonian.

As a second point of control imperfection, we will not assume that a calibration is carried out for the actual amplitude reaching E upon applying a signal in the lab. Hence, for the definition of H_c, we introduce the same decomposition for the control parameters into best-guess quantities and unknown deviations thereof. We propose to use a simple continuous signal similar to (6.1), meant to cancel the general coupling (II.2):

$$H_c(t) := \frac{\omega_1}{2}\sigma_z + \frac{\omega_2}{2}(\cos(\bar{\omega}_1 t)\sigma_x + \sin(\bar{\omega}_1 t)\sigma_y),$$

with

$$\omega_1 = \bar{\omega}_1 + \delta\omega_1, \tag{6.3}$$
$$\omega_2 = \bar{\omega}_2 + \delta\omega_2. \tag{6.4}$$

Note that the drive frequency $\bar{\omega}_1$ is well-known, whereas the amplitudes of the static field and of the $\sigma_{x,y}$-drive are only roughly known, involving uncertainties $\delta\omega_1$ and $\delta\omega_2$ respectively. Defining

$$\Delta = \delta\omega_1 + \delta\Omega_E,$$

the total Hamiltonian can be written as

$$H_E(t) := \frac{\Delta + \bar{\omega}_1}{2}\sigma_z + \frac{\omega_2}{2}(\cos(\bar{\omega}_1 t)\sigma_x + \sin(\bar{\omega}_1 t)\sigma_y). \tag{6.5}$$

Although our actual analysis will consider the full model with decoherence channels, we can already anticipate the implications of such control in a purely Hamiltonian setting.

The evolution of E under $H_E(t)$ alone can be understood by first moving to a rotating frame w.r.t. $\frac{\bar{\omega}_1}{2}\sigma_z$, yielding a remaining constant Hamiltonian $\frac{\Delta}{2}\sigma_z + \frac{\omega_2}{2}\sigma_x$. In this frame the state will rotate at a speed

$$\Lambda := \sqrt{\Delta^2 + \omega_2^2},$$

around the axis

$$\sigma_{\alpha x} = \cos(\alpha)\sigma_x + \sin(\alpha)\sigma_z,$$

where we have defined

$$\cos(\alpha) = \frac{\omega_2}{\Lambda}, \quad \sin(\alpha) = \frac{\Delta}{\Lambda}.$$

In the original frame, the associated propagator thus reads

$$U_E(t) := e^{-i\bar{\omega}_1\sigma_z t/2} e^{-i\Lambda\sigma_{\alpha x} t/2}\ . \tag{6.6}$$

The E subsystem undergoes two composite rotations around axes in the Bloch sphere which would be orthogonal in absence of the detuning Δ. We see that the presence of Δ prevents us from applying exact σ_x rotations, as would be required in a continuous-time analog of the spin echo strategy. As the angle is determined by Δ/ω_2, we should favor a large value of ω_2. Considering Δ of possibly the same order as $\bar{\omega}_1$, this would suggest to take $\omega_2 \gg \bar{\omega}_1 \gg g$, where the latter is the strength of the coupling Hamiltonian (II.2).

Next, applying the propagator associated to $H_E(t)$ to the coupling Hamiltonian (II.2), it is easy to verify that $U_E^\dagger(t)\sigma_x U_E(t)$ and $U_E^\dagger(t)\sigma_y U_E(t)$ only involve terms oscillating at frequencies $\pm\bar{\omega}_1$ and $\Lambda \pm \bar{\omega}_1$, while

$$U_E^\dagger(t)\sigma_z U_E(t) = \sin(\alpha)\sigma_{\alpha x} - \cos(\alpha)(e^{i\Lambda t}\sigma_{\alpha+} + e^{-i\Lambda t}\sigma_{\alpha-}),$$

where $\sigma_{\alpha\pm}$ are raising and lowering operators with respect to the eigenstates of $\sigma_{\alpha x}$. Having $\Lambda, \Lambda \pm \bar{\omega}_1, \pm\bar{\omega}_1 \gg g$, we can perform a rotating-wave approximation (RWA) and obtain the non-zero average coupling

$$g\sin(\alpha)\sigma_{\alpha x} = g\frac{\Delta}{\omega_2}\sigma_{\alpha x} + g\mathcal{O}\left(\frac{\Delta^3}{\omega_2^3}\right). \tag{6.7}$$

We thus see that taking $\omega_2 \gg \Delta$ in this formula indeed appears to reduce the effective coupling between T and E. This the RWA has to be justified however. We mention that the leading RWA-errors are of the order

$$\frac{g^2}{\Lambda}, \frac{g^2}{\Lambda \pm \bar{\omega}_1}, \frac{g^2}{\bar{\omega}_1}.$$

In conclusion, based with this Hamiltonian model, one can expect that one possible strategy is to ensure that $\omega_2 \gg \bar{\omega}_1 \gg g$, while we can allow for the uncertain detuning Δ to be of the order of $\bar{\omega}_1$ ($\Delta \sim \bar{\omega}_1$), as long as we still have that $\omega_2 \gg \Delta$. This general idea is subsequently confirmed by analyzing the full model (II.1), including the dissipation channels L_k on E, instead of only reasoning on the average coupling.

6.3 Analysis of decoherence on the target

In a rotating frame w.r.t. $\frac{\bar{\omega}_1}{2}\sigma_z$, and defining $T_\pm = T_x \pm iT_y$, the joint evolution of the target and TLS is described by the master equation

$$\begin{aligned}\tfrac{d}{dt}\rho = {} & \kappa_- \mathcal{D}_{\mathbb{1}_T\otimes\sigma_-}(\rho) + \kappa_+ \mathcal{D}_{\mathbb{1}_T\otimes\sigma_+}(\rho) \\ & - i\frac{\Lambda}{2}[\mathbb{1}_T \otimes \sigma_{\alpha x}, \rho] \\ & - ig\big[T_z \otimes \sigma_z + e^{i\bar{\omega}_1 t} T_- \otimes \sigma_+ + e^{-i\bar{\omega}_1 t} T_+ \otimes \sigma_-, \rho\big],\end{aligned} \tag{6.8}$$

where $\mathbb{1}_T$ stands for the identity operator on T. For now we assume drive-independent decoherence channels $L_k \in \{\sigma_-, \sigma_+\}$ on E. In the present section, we analyze the induced decoherence on T, by obtaining explicit formulas for its reduced dynamics due to adiabatic elimination of the environment E. For this we rely on a timescale separation as E dissipates with rates $\kappa_\pm \gg g$ dominating the coupling Hamiltonian. The work of [6] explains how to obtain the reduced dynamics of T as a power expansion in $g/\kappa_\pm$, considering a stationary coupling Hamiltonian as a perturbation. In Section 6.3.1.2, we derive a general extension of this adiabatic elimination approach for the case where the coupling Hamiltonian is time-periodic. The related formulas could be of independent interest to treat other cases where first performing a lowest-order RWA and subsequently adiabatically eliminating the fastly decohering degrees of freedom does not yield the correct leading-order induced decoherence.

6.3.1 Adiabatic elimination method

6.3.1.1 Summary of the formalism

Consider dynamics with the following timescale separation

$$\dot{\rho} = \mathcal{L}_0(\rho) + \varepsilon\mathcal{L}_1(\rho). \tag{6.9}$$

Here, ρ is a density operator acting on a Hilbert space $\mathcal{H}$, $\mathcal{L}_0$ a stationary Lindbladian of order 1, and $\mathcal{L}_1$ an order-one Lindbladian providing a perturbation, since $\varepsilon \ll 1$ is a small positive constant. We use the term "Lindbladian" in the broad sense, as we assume any Hamiltonian parts of the dynamics to be included in $\mathcal{L}_0$ or $\mathcal{L}_1$. The starting point is that the fast dynamics are degenerate, i.e. the linear superoperator $\mathcal{L}_0$, acting on the set of linear operators on $\mathcal{H}$, has a nontrivial kernel $\mathcal{M}_0$ associated to eigenvalue 0. Furthermore, this kernel is strongly attractive, in other words all the non-zero eigenvalues of $\mathcal{L}_0$ have a strictly negative real part, making up a gap in its spectrum.

The goal of adiabatic elimination, as described in [6], is then to obtain a reduced model describing the perturbation of this degenerate kernel under the full Lindblad dynamics $\mathcal{L}_0 + \varepsilon\mathcal{L}_1$, for small ε. This reduced model involves an invariant space $\mathcal{M}_r$ — dubbed the slow

or reduced subspace — of the same dimension as the kernel $\mathcal{M}_0$ of $\mathcal{L}_0$, and on which the perturbation of 0-eigenvalues now implies some slow dynamics.

Both the invariant space $\mathcal{M}_r$ and the associated slow dynamics $\mathcal{L}_s$ can be determined as a power series in ε. For this we parameterize the reduced model by a variable $\rho_s \in \mathcal{M}_s \simeq \mathcal{M}_r$ undergoing the dynamics

$$\dot{\rho}_s(t) = \mathcal{L}_{s,\varepsilon}(\rho_s(t)) = \sum_{k=1}^{\infty} \varepsilon^k \mathcal{L}_{s,k}(\rho_s) \ , \tag{6.10}$$

and we express how this variable is embedded in the full system, thus mapping the parameterization space $\mathcal{M}_s$ to the actual invariant eigenspace $\mathcal{M}_r$, via the linear map:

$$\rho(t) = \mathcal{K}_\varepsilon(\rho_s(t)) = \sum_{k=0}^{\infty} \varepsilon^k \mathcal{K}_k(\rho_s(t)). \tag{6.11}$$

Ideally, we want $\mathcal{L}_{s,\varepsilon}$ to have the typical Lindblad structure of positivity-preserving dynamics, and $\mathcal{K}_\varepsilon$ to be a Kraus map, such that density matrices in $\mathcal{M}_s$ are mapped to density operators in the total space. General expressions satisfying this structure have been obtained when truncating the series after 2nd order [4–6, 43]. For the specific case of quantum non-demolition photon-number measurements through a dispersive coupling to a driven ancilla-qubit, it was shown in [111] that this positivity-preserving structure persists up to *infinite* order, namely $\sum_{k=1}^{\infty} \varepsilon^k \mathcal{L}_{s,k}$ is explicitly of Lindblad form, and $\sum_{k=0}^{\infty} \varepsilon^k \mathcal{K}_k$ is explicitly given by a Kraus map.

Demanding that the equations (6.10),(6.11) be a solution of (6.9), the $\mathcal{L}_{s,k}$ and $\mathcal{K}_k$ can be progressively identified by matching terms of equal order in ε. Explicitly, one obtains

$$\begin{aligned}
\mathcal{L}_0(\mathcal{K}_0(\rho_s)) &= 0, \\
\mathcal{K}_0(\mathcal{L}_{s,1}(\rho_s)) &= \mathcal{L}_0(\mathcal{K}_1(\rho_s)) + \mathcal{L}_1(\mathcal{K}_0(\rho_s)), \\
\mathcal{K}_0(\mathcal{L}_{s,2}(\rho_s)) + \mathcal{K}_1(\mathcal{L}_{s,1}(\rho_s)) &= \mathcal{L}_0(\mathcal{K}_2(\rho_s)) + \mathcal{L}_1(\mathcal{K}_1(\rho_s)), \\
&\vdots
\end{aligned}$$

Since these equations should hold for any $\rho_s \in \mathcal{M}_s$, we write (with a slight abuse of notation, since all operators are linear):

$$\mathcal{L}_0\mathcal{K}_0 = 0, \tag{6.12a}$$
$$\mathcal{K}_0\mathcal{L}_{s,1} = \mathcal{L}_0\mathcal{K}_1 + \mathcal{L}_1\mathcal{K}_0, \tag{6.12b}$$
$$\mathcal{K}_0\mathcal{L}_{s,2} + \mathcal{K}_1\mathcal{L}_{s,1} = \mathcal{L}_0\mathcal{K}_2 + \mathcal{L}_1\mathcal{K}_1, \tag{6.12c}$$
$$\vdots$$

where a product of superoperators denotes their composition.

The solution is not unique since we have a choice in the parameterization of $\mathcal{M}_r$ via $\mathcal{M}_s$, but it has been proved that solutions exist [6]. At each order, we can first solve for $\mathcal{L}_{s,k}$ by projecting the corresponding equation with

$$\mathcal{R} := \lim_{t \to +\infty} \exp(\mathcal{L}_0 \, t)$$

onto the subspace corresponding to the zero eigenvalues of $\mathcal{L}_0$, i.e. the subspace whose perturbation we want to compute. Mathematically, this decouples the unknowns through $\mathcal{R}\mathcal{L}_0 =$

$\mathcal{L}_0\mathcal{R} = 0$ and choosing $\mathcal{R}\mathcal{K}_0 = \mathcal{K}_0$. This choice for $\mathcal{K}_0$ is natural since $\mathcal{M}_s$ is isomorphic to $\mathcal{M}_0$. In a second step, one can project the equations with $1 - \mathcal{R}$ to determine $\mathcal{K}_k$.

While this procedure is completely general, the context of this thesis mainly lies in a particular common setting, and we will apply this procedure to the case where $\mathcal{L}_0$ stabilizes one subsystem of a composite quantum system towards a unique steady state, and $\mathcal{L}_1$ expresses Hamiltonian coupling between this subsystem and another. The leading-order adiabatic elimination results for this case have been explicitly computed in [6]. However, for some points in Chapter 7 we have encountered situations where the set of steady states of $\mathcal{L}_0$ has a different structure. In these cases we resort to the general procedure outlined in this section.

6.3.1.2 Time-periodic extension

This section aims to develop an extension of the approach of adiabatic elimination in systems with strongly dissipative degrees of freedom, to the case where the perturbation displays a periodic time-dependence with a frequency comparable in magnitude to the fast dissipation rate. We consider dynamics with a similar timescale separation as before:

$$\dot{\rho} = \mathcal{L}_0(\rho) + \varepsilon\mathcal{L}_1(\rho, t), \tag{6.13}$$

where we impose the same assumptions on $\mathcal{L}_0$ as before, but now $\mathcal{L}_1(t)$ is a periodic Lindbladian perturbation of period $\frac{2\pi}{\omega}$. Furthermore, this perturbation should be rapidly oscillating:

$$\omega \gg \|\varepsilon\mathcal{L}_1\|.$$

Thanks to Floquet theory, we can expect $\mathcal{M}_0$ to be perturbed into a slightly altered attractive subspace which now moves periodically in time, and on which some slow dynamics is present.

We again parameterize the slow dynamics using a variable ρ_s living in a space $\mathcal{M}_s$ isomorphic to $\mathcal{M}_0$, and propose

$$\rho(t) = \mathcal{K}_\varepsilon(\rho_s(t), t), \tag{6.14a}$$
$$\dot{\rho}_s(t) = \mathcal{L}_{s,\varepsilon}(\rho_s(t)) \tag{6.14b}$$

as a solution staying in the "slow" invariant subspace of (6.13). Here, $\mathcal{K}_\varepsilon(\cdot, t)$ is a $\frac{2\pi}{\omega}$-periodic map characterizing the embedding of the perturbed slow subspace in the total space and $\mathcal{L}_{s,\varepsilon} : \mathcal{M}_s \to \mathcal{M}_s$ is a stationary superoperator parameterizing the slow dynamics. Plugging (6.14) into (6.13), we obtain an invariance equation:

$$\frac{\partial\mathcal{K}_\varepsilon}{\partial t}(t) + \mathcal{K}_\varepsilon(t)\mathcal{L}_{s,\varepsilon} = \mathcal{L}_0\mathcal{K}_\varepsilon(t) + \varepsilon\mathcal{L}_1(t)\mathcal{K}_\varepsilon(t), \tag{6.15}$$

where the domain of all terms is $\mathcal{M}_s$. We again expand both the stationary superoperator $\mathcal{L}_{s,\varepsilon}$ and the periodic map $\mathcal{K}_\varepsilon(t)$ in powers of ε,

$$\mathcal{K}_\varepsilon(t) = \mathcal{K}_0(t) + \varepsilon\mathcal{K}_1(t) + \varepsilon^2\mathcal{K}_2(t) + \cdots, \tag{6.16}$$
$$\mathcal{L}_{s,\varepsilon} = \mathcal{L}_{s,0} + \varepsilon\mathcal{L}_{s,1} + \varepsilon^2\mathcal{L}_{s,2} + \cdots. \tag{6.17}$$

Collecting (6.15) into powers in ε yields the set of recursive equations

$$\frac{\partial\mathcal{K}_0}{\partial t}(t) + \mathcal{K}_0(t)\mathcal{L}_{s,0} = \mathcal{L}_0\mathcal{K}_0(t), \tag{6.18}$$

$$\frac{\partial\mathcal{K}_k}{\partial t}(t) + \sum_{j=0}^{k}\mathcal{K}_j(t)\mathcal{L}_{s,k-j} = \mathcal{L}_0\mathcal{K}_k(t) + \mathcal{L}_1(t)\mathcal{K}_{k-1}(t) \quad , \quad k \geq 1. \tag{6.19}$$

We can choose $\mathcal{L}_{s,0} = 0$ and $\mathcal{K}_0$ time-independent and injective such that $\mathcal{R}\mathcal{K}_0 = \mathcal{K}_0$, since for $\varepsilon = 0$, the solutions in the slow subspace are stationary. For $k = 1$ we then obtain the following equation, to be satisfied by $\mathcal{L}_{s,1}$ and $\mathcal{K}_1$:

$$\frac{\partial \mathcal{K}_1}{\partial t}(t) + \mathcal{K}_0 \mathcal{L}_{s,1} = \mathcal{L}_0 \mathcal{K}_1(t) + \mathcal{L}_1(t)\mathcal{K}_0 \ . \tag{6.20}$$

We split this equation into four parts, by projecting either with $\mathcal{R}$ or $1 - \mathcal{R}$ on the one hand, and by considering the time-average $\bar{(\cdot)}$ versus the purely oscillating part of the equation that averages out to zero (also called the *ripple*) $\tilde{(\cdot)}$ on the other hand. Since in this way it will be clear which terms depend on time, we drop the t argument in what follows.

Applying $\mathcal{R}$ and the time-average to (6.20), we obtain

$$\mathcal{K}_0 \mathcal{L}_{s,1} = \mathcal{R}\bar{\mathcal{L}}_1 \mathcal{K}_0 \ . \tag{6.21}$$

This equation determines $\mathcal{L}_{s,1}$ uniquely, since $\mathcal{K}_0$ can be inverted on its image. The application of $\mathcal{R}$ to the perturbation (its average part here) corresponds to the Zeno-effect that is well-known for stationary systems.

Applying $\mathcal{R}$ to (6.20) and taking the ripple of the resulting equation, we get

$$\mathcal{R}\dot{\mathcal{K}}_1 = \mathcal{R}\tilde{\mathcal{L}}_1 \mathcal{K}_0, \tag{6.22}$$

of which a solution can be obtained via taking the *zero-average* time primitive, denoted by ∂_t^{-1}:

$$\mathcal{R}\mathcal{K}_1 = \mathcal{R}\partial_t^{-1}\tilde{\mathcal{L}}_1 \mathcal{K}_0 + \mathcal{R}\bar{\mathcal{G}}_1. \tag{6.23}$$

Note that ∂_t^{-1} is uniquely defined such that $\overline{\partial_t^{-1}\tilde{\mathcal{L}}_1} = 0$, hence the name zero-average primitive. Here $\bar{\mathcal{G}}_1$ is an integration constant, playing the role of a gauge choice. Equation (6.23) is reminiscent of an averaging procedure, where oscillating terms are transformed away using a coordinate change ε-close to identity (here $\mathcal{K}_0 + \varepsilon\mathcal{K}_1$) and generated by the integral of the oscillating terms; see [57] for a canonical treatment of this averaging procedure. This is not surprising, since within the slow subspace, the effect of $\mathcal{L}_0$ reduces to zero, and we retain a small oscillating perturbation, which is exactly the setting where averaging procedures work well.

Applying $1 - \mathcal{R}$ to (6.20) and taking the average of the resulting equation, we get

$$0 = \mathcal{L}_0(1 - \mathcal{R})\bar{\mathcal{K}}_1 + (1 - \mathcal{R})\bar{\mathcal{L}}_1 \mathcal{K}_0, \tag{6.24}$$

which has the formal solution

$$(1 - \mathcal{R})\bar{\mathcal{K}}_1 = -\mathcal{L}_0^{-1}(1 - \mathcal{R})\bar{\mathcal{L}}_1 \mathcal{K}_0. \tag{6.25}$$

Since $\mathcal{L}_0$ has a spectral gap, its restriction to the image of $(1 - \mathcal{R})$ can be rigorously inverted, because it has no eigenvalue zero there. This pseudo-inverse of $\mathcal{L}_0$ is equally present in stationary adiabatic elimination and it expresses how the stationary part of the perturbation perturbs the slow subspace up to first order.

Lastly, applying $1 - \mathcal{R}$ to (6.20) and taking the ripple of the resulting equation, we get

$$(1 - \mathcal{R})\dot{\mathcal{K}}_1 = \mathcal{L}_0(1 - \mathcal{R})\tilde{\mathcal{K}}_1 + (1 - \mathcal{R})\tilde{\mathcal{L}}_1 \mathcal{K}_0. \tag{6.26}$$

To determine $(1-\mathcal{R})\tilde{\mathcal{K}}_1$ from this equation, we introduce a decomposition into Fourier modes. We can write

$$(1-\mathcal{R})\tilde{\mathcal{L}}_1(t) = \sum_{n\in\mathbb{Z},n\neq 0} e^{int}(1-\mathcal{R})\tilde{\mathcal{L}}_{1,n},$$

for some superoperators $\tilde{\mathcal{L}}_{1,n}$, since $\tilde{\mathcal{L}}_1$ has zero average. Decomposing in the same way the tentative solution

$$(1-\mathcal{R})\tilde{\mathcal{K}}_1(t) = \sum_{n\in\mathbb{Z},n\neq 0} e^{int}(1-\mathcal{R})\mathcal{K}_{1,n},$$

and plugging this into (6.26), we see that for every $n \neq 0$, we are looking for the stationary superoperator $(1-\mathcal{R})\mathcal{K}_{1,n}$ such that

$$(\mathcal{L}_0 - in)(1-\mathcal{R})\mathcal{K}_{1,n} = -(1-\mathcal{R})\tilde{\mathcal{L}}_{1,n}\mathcal{K}_0. \tag{6.27}$$

This equation is the exact analog of (6.25) but for $n \neq 0$, capturing oscillating terms. Here we can really see that, since the time-dependence of $\mathcal{L}_1$ is as fast as the dissipation $\mathcal{L}_0$, the combined effect of the two has to be inverted to obtain the oscillating part of the correction to the slow subspace. We thus need $\mathcal{L}_0 - in$ to be invertible on the image of $1-\mathcal{R}$. Because $\mathcal{L}_0$ restricted to the image of $1-\mathcal{R}$ only has eigenvalues with a strictly negative real part, a shift in its spectrum by $-in, n \in \mathbb{Z}$, can never move an eigenvalue to the origin, and hence $\mathcal{L}_0 - in$ can formally be inverted in the above equation. This can be done for every fixed n separately, or if available, a diagonalization of $\mathcal{L}_0$ could allow us to define all inverses at once.

Equation (6.19) for $k \geq 2$ can be treated in an analogous way, and the general higher-order solution is

$$\mathcal{K}_0\mathcal{L}_{s,k} = \mathcal{R}\bar{\mathcal{A}}_k, \tag{6.28a}$$

$$\mathcal{R}\mathcal{K}_k = \mathcal{R}\partial_t^{-1}\Big(\tilde{\mathcal{A}}_k - \tilde{\mathcal{B}}_k\Big) + \mathcal{R}\bar{\mathcal{G}}_k, \tag{6.28b}$$

$$(1-\mathcal{R})\bar{\mathcal{K}}_k = -\mathcal{L}_0^{-1}(1-\mathcal{R})\big(\bar{\mathcal{A}}_k - \bar{\mathcal{B}}_k\big), \tag{6.28c}$$

$$(1-\mathcal{R})\tilde{\mathcal{K}}_k = -(\mathcal{L}_0 - \partial_t)^{-1}(1-\mathcal{R})\Big(\tilde{\mathcal{A}}_k - \tilde{\mathcal{B}}_k\Big), \tag{6.28d}$$

with

$$\mathcal{A}_k = \mathcal{L}_1\mathcal{K}_{k-1},$$
$$\mathcal{B}_k = \sum_{j=1}^{k-1}\mathcal{K}_j\mathcal{L}_{s,k-j}.$$

Here, $\mathcal{R}\bar{\mathcal{G}}_k$ is a general gauge choice that can be made at every order. All inverses are well-defined for the same reasons as before, and it is easy to check that the above recursive relation provides a solution, by plugging it into (6.19).

We will show that in the context of this chapter, $\mathcal{K}_0 + \varepsilon\mathcal{K}_1$ can be written as a Kraus map up to $\mathcal{O}(\varepsilon^2)$ terms, choosing $\bar{\mathcal{G}}_1 = 0$, so $\mathcal{R}\tilde{\mathcal{K}}_1 = \mathcal{R}\partial_t^{-1}\tilde{\mathcal{L}}_1\mathcal{K}_0$, and $\mathcal{R}\bar{\mathcal{K}}_1 = 0$. Furthermore, $\mathcal{L}_{s,1}$ is a Hamiltonian on the target T, and $\mathcal{L}_{s,2}$ is the sum of a Hamiltonian and a Lindbladian on T. Thus the proposed perturbative series preserves the quantum structure of Lindbladian reduced dynamics and completely positive trace preserving (CPTP) mappings up to second order. In fact, one can prove that this remains the case for a general bipartite scenario.

Theorem 6.1. *Consider the model* (6.13) *where the Lindbladian* $\mathcal{L}_0$ *acts only on one subsystem (F) of a bipartite quantum system, and exponentially stabilizes F towards a unique steady state at a rate* κ*; and,* $\mathcal{L}_1(t)$ *expresses a* $\frac{2\pi}{\omega}$*-periodic Hamiltonian coupling between the F-subsystem and the second one (S). Assume* $\varepsilon\|\mathcal{L}_1\| \ll \kappa$ *and* $\varepsilon\|\mathcal{L}_1\| \ll \omega$*. When choosing* $\bar{\mathcal{G}}_1 = 0$ *in* (6.23)*,* $\mathcal{L}_{s,1}$ *takes the form of a Hamiltonian,* $\mathcal{L}_{s,2}$ *is the sum of Hamiltonian and a Lindbladian term, and* $\mathcal{K}_0 + \varepsilon\mathcal{K}_1$ *can be written as a CPTP-map up to terms of order* ε^2*.*

Proof. Since $\mathcal{L}_0$ only acts on F, it trivially corresponds to a Lindbladian $\mathcal{L}_F$ acting on F such that $\mathcal{L}_0 = \text{identity} \otimes \mathcal{L}_F$. The proof then consists of a straightforward adaptation of Lemma 4 and 5 in appendix A of [7] to a general pseudo-inverse $(\mathcal{L}_F - in)^{-1}, n \in \mathbb{Z}$ instead of only ${\mathcal{L}_F}^{-1}$ considered in the original work. □

6.3.2 Case of strong driving

In this section, we assume that the DD driving does not alter the dissipation model of the E system. In Section 6.3.3, we consider such a correction, which arises when the DD drives are what we will define as *ultra-strong*. We recall that in a rotating frame w.r.t. $\frac{\bar{\omega}_1}{2}\sigma_z$, the joint evolution of the target and TLS is then described by the master equation

$$\begin{aligned}\tfrac{d}{dt}\rho = {}& \kappa_-\mathcal{D}_{\mathbb{1}_T\otimes\sigma_-}(\rho) + \kappa_+\mathcal{D}_{\mathbb{1}_T\otimes\sigma_+}(\rho) \\ & - i\frac{\Lambda}{2}[\mathbb{1}_T \otimes \sigma_{\alpha x}, \rho] \\ & - ig\big[T_z \otimes \sigma_z + e^{i\bar{\omega}_1 t}T_- \otimes \sigma_+ + e^{-i\bar{\omega}_1 t}T_+ \otimes \sigma_-, \rho\big].\end{aligned} \tag{6.29}$$

In the previous section we have derived a general extension of the adiabatic elimination approach for the present case where the coupling Hamiltonian is time-periodic. Before explicitly calculating the reduced model, we can make the general conclusions from this adiabatic elimination method more concrete for the bipartite case of $\mathcal{H} = \mathcal{H}_T \otimes \mathcal{H}_E$. The fast dynamics acts only on E, and quickly drives it to a unique steady state $\bar{\rho}_E$ were it not for the T-E coupling, which is considered the perturbation, since $g \ll \bar{\omega}_1, \Lambda, \kappa_\pm$. The small expansion parameter of the perturbative series can be identified as

$$\varepsilon = \frac{g}{\bar{\omega}_1} \ll 1,$$

with $\bar{\omega}_1$ the frequency of the driving as in (6.5). We will calculate $\bar{\rho}_E$ explicitly below, but it is clear that the unperturbed slow subspace $\mathcal{M}_0$ is given by the set of linear operators

$$X_T \otimes \bar{\rho}_E,$$

where X_T acts on $\mathcal{H}_T$. Hence, it is natural to choose $\mathcal{M}_s$ as the space of operators acting on $\mathcal{H}_T$, and

$$\mathcal{K}_0(\rho_s) = \rho_s \otimes \bar{\rho}_E.$$

In this way, $\mathcal{L}_{s,\varepsilon}$ is a superoperator corresponding to the target Hilbert space $\mathcal{H}_T$ alone, and the reduced model

$$\dot{\rho}_s = \mathcal{L}_{s,\varepsilon}(\rho_s) \tag{6.30}$$

can truly be seen as describing the induced decoherence on the target system. How the target becomes *entangled* with the environment will be described by the map $\mathcal{K}_\varepsilon$ up to first order in

ε. Given that the map $\mathcal{K}_\varepsilon(t)$ is periodic in time, with period $\frac{2\pi}{\bar{\omega}_1}$, the hybridization of the two systems changes periodically in time. This is one more reason for rightfully calling (6.30) a *reduced* model for the induced decoherence on T, since we have eliminated both the coupling to the TLS from the description, as well as a fast periodic micromotion given by $\mathcal{K}_\varepsilon(\cdot, t)$.

In line with standard adiabatic elimination for bipartite systems, a necessary condition for the convergence of the series is $g \ll \kappa_-$ (where we assume $\kappa_- > \kappa_+$ from physical reasons). The validity of the expansion thus depends on the two timescale separations $\bar{\omega}_1 \gg g$ and $\kappa_- \gg g$. However, we do not have to assume either $\bar{\omega}_1$ or κ_- to be larger than the other. In other words, we do not have to perform standard adiabatic elimination with κ_- before averaging over $\bar{\omega}_1$ or conversely.

Lastly we mention that a standard result for bipartite systems [6] with a *stationary* Hamiltonian coupling is that the induced decoherence will be of leading-order

$$\frac{g^2}{\kappa_-}.$$

This will provide a good point of comparison for the reduced models to follow.

We will now apply this formalism, and provide a full derivation of the reduced model. Next, we summarize the conclusions towards the DD benefits in Section 6.3.2.2.

6.3.2.1 Derivation of reduced model for strong driving

In the notation of Section 6.3.1.2, assuming $g \ll \bar{\omega}_1, \kappa_-$, we can thus define $\varepsilon = \frac{g}{\bar{\omega}_1}$,

$$\mathcal{L}_0 = -i\frac{\Lambda}{2}[\mathbb{1}_T \otimes \sigma_{\alpha x}, \cdot] + \kappa_- \mathcal{D}_{\mathbb{1}_T \otimes \sigma_-} + \kappa_+ \mathcal{D}_{\mathbb{1}_T \otimes \sigma_+},$$

and

$$\mathcal{L}_1(t) = -i\bar{\omega}_1 \big[T_z \otimes \sigma_z + e^{i\bar{\omega}_1 t} T_- \otimes \sigma_+ + e^{-i\bar{\omega}_1 t} T_+ \otimes \sigma_-, \cdot\big].$$

Order 0 computations

Since the E system represents a two-level system, involving just a few degrees of freedom, it is straightforward to verify that the fast dynamics $\mathcal{L}_0$ drives the environment to a unique steady state

$$\bar{\rho}_E = \frac{\mathbb{1}_E + \xi_\infty \sigma_+ + \xi_\infty^* \sigma_- + z_\infty \sigma_z}{2}, \tag{6.31}$$

with

$$\xi_\infty = -2\Lambda \cos(\alpha) \frac{\kappa_\Delta}{\kappa_\Sigma} \frac{2\Lambda \sin(\alpha) + i\kappa_\Sigma}{\kappa_\Sigma^2 + 2\Lambda^2\big(1 + \sin^2(\alpha)\big)},$$
$$z_\infty = -\frac{\kappa_\Delta}{\kappa_\Sigma} \frac{4\Lambda^2 \sin^2(\alpha) + \kappa_\Sigma^2}{\kappa_\Sigma^2 + 2\Lambda^2\big(1 + \sin^2(\alpha)\big)},$$

where we have defined

$$\kappa_\Sigma := \kappa_- + \kappa_+,$$
$$\kappa_\Delta := \kappa_- - \kappa_+.$$

As outlined in Section 6.2, we are mainly interested in the regime of strong driving where $\omega_2 \gg \kappa_\Sigma$, corresponding to the double-timescale DD driving introduced there. Hence, we here restrict ourselves to computing the leading order in $\frac{1}{\omega_2}$ of all quantities in this section. For this, $\cos(\alpha)$ should be put equal to 1 since α goes to zero as $\omega_2 \to \infty$, and it should be remembered that $\Lambda \sin(\alpha) = \Delta$. Thus,

$$\xi_\infty = -\frac{\kappa_\Delta}{\kappa_\Sigma}\frac{(i\kappa_\Sigma + 2\Delta)}{\omega_2} + \mathcal{O}\left(\frac{1}{\omega_2^2}\right),$$
$$z_\infty = -\frac{\kappa_\Delta}{\kappa_\Sigma}\frac{\left(\kappa_\Sigma^2 + 2\Delta^2\right)}{\omega_2^2} + \mathcal{O}\left(\frac{1}{\omega_2^3}\right).$$

The steady state therefore converges to the maximally mixed state in the limit of $\omega_2 \to \infty$.

For the projector $\mathcal{R}$ we have

$$\mathcal{R}(X_{\mathrm{TE}}) = \mathrm{Tr}_E(X_{\mathrm{TE}}) \otimes \bar{\rho}_E, \quad \forall X_{\mathrm{TE}}.$$

Order ε computations

- Equation (6.21) yields the following expression for the first-order reduced dynamics:

$$\begin{aligned}\varepsilon\mathcal{L}_{s,1}(\rho_s) \otimes \bar{\rho}_E &= \varepsilon\mathcal{R}(\overline{\mathcal{L}_1(\rho_s \otimes \bar{\rho}_E)}) \\ &= -ig\,\mathrm{Tr}_E([T_z \otimes \sigma_z, \rho_s \otimes \bar{\rho}_E]) \otimes \bar{\rho}_E \\ &= -igz_\infty[T_z, \rho_s] \otimes \bar{\rho}_E,\end{aligned}$$

  readily giving

$$\varepsilon\mathcal{L}_{s,1}(\rho_s) = -igz_\infty[T_z, \rho_s].$$

- Equation (6.23) in turn yields

$$\begin{aligned}\varepsilon\mathcal{R}\mathcal{K}_1(\rho_s) &= \varepsilon\mathcal{R}\partial_t^{-1}\tilde{\mathcal{L}}_1\mathcal{K}_0(\rho_s) \\ &= -\frac{g}{\bar{\omega}_1}\,\mathrm{Tr}_E(\left[e^{i\bar{\omega}_1 t}T_- \otimes \sigma_+ - e^{-i\bar{\omega}_1 t}T_+ \otimes \sigma_-, \rho_s \otimes \bar{\rho}_E\right]) \otimes \bar{\rho}_E \\ &= -\frac{ig}{2\bar{\omega}_1}\left[i\xi_\infty^* e^{i\bar{\omega}_1 t}T_- - i\xi_\infty e^{-i\bar{\omega}_1 t}T_+, \rho_s\right] \otimes \bar{\rho}_E, \qquad (6.33)\end{aligned}$$

  where we have put the integration constant to zero as a gauge choice.

- Equation (6.25) yields a second part of $\mathcal{K}_1$:

$$\begin{aligned}\varepsilon\mathcal{L}_0(1-\mathcal{R})\bar{\mathcal{K}}_1(\rho_s) &= -\varepsilon(1-\mathcal{R})\bar{\mathcal{L}}_1\mathcal{K}_0(\rho_s) \\ &= ig[T_z \otimes \sigma_z, \rho_s \otimes \bar{\rho}_E] \\ &\quad - ig\,\mathrm{Tr}_E([T_z \otimes \sigma_z, \rho_s \otimes \bar{\rho}_E]) \otimes \bar{\rho}_E \\ &= ig(T_z\rho_s \otimes \bar{\sigma}_z\bar{\rho}_E - \rho_s T_z \otimes \bar{\rho}_E\bar{\sigma}_z),\end{aligned}$$

with $\bar{\sigma}_z = \sigma_z - \mathrm{Tr}(\sigma_z\bar{\rho}_E)\mathbb{1}_E = \sigma_z - z_\infty \mathbb{1}_E$. Note that taking the partial trace over E on the right-hand side gives zero, since $\mathrm{Tr}(\bar{\sigma}_z\bar{\rho}_E) = 0$. Hence $\mathcal{L}_0$ can be inverted to obtain, formally,

$$\varepsilon(1-\mathcal{R})\bar{\mathcal{K}}_1(\rho_s) = ig\big(T_z\rho_s \otimes \mathcal{L}_0^{-1}(\bar{\sigma}_z\bar{\rho}_E) - \rho_s T_z \otimes \mathcal{L}_0^{-1}(\bar{\rho}_E\bar{\sigma}_z)\big). \tag{6.34}$$

To carry out the inversion we use matrix representations in the Pauli basis. In the standard Pauli basis $(\sigma_x, \sigma_y, \sigma_z)$, we obtain the following matrix representation for $\mathcal{L}_0$:

$$[\mathcal{L}_0] = \begin{pmatrix} -\frac{\kappa_\Sigma}{2} & -\Lambda\sin(\alpha) & 0 \\ \Lambda\sin(\alpha) & -\frac{\kappa_\Sigma}{2} & -\Lambda\cos(\alpha) \\ 0 & \Lambda\cos(\alpha) & -\kappa_\Sigma \end{pmatrix},$$

with $\det[\mathcal{L}_0] = -\frac{\kappa_\Sigma}{4}\big(\kappa_\Sigma^2 + 2\Lambda^2(1+\sin^2(\alpha))\big)$. For its inverse $\big[\mathcal{L}_0^{-1}\big]$ we hence obtain

$$\frac{1}{\det[\mathcal{L}_0]}\begin{pmatrix} \frac{\kappa_\Sigma^2}{2} + \Lambda^2\cos^2(\alpha) & -\kappa_\Sigma\Lambda\sin(\alpha) & \frac{\Lambda^2\sin(2\alpha)}{2} \\ \kappa_\Sigma\Lambda\sin(\alpha) & \frac{\kappa_\Sigma^2}{2} & -\frac{\kappa_\Sigma\Lambda\cos(\alpha)}{2} \\ \frac{\Lambda^2\sin(2\alpha)}{2} & \frac{\kappa_\Sigma\Lambda\cos(\alpha)}{2} & \frac{\kappa_\Sigma^2}{4} + \Lambda^2\sin^2(\alpha) \end{pmatrix}.$$

In turn, $\bar{\sigma}_z\bar{\rho}_E$ takes the following vector representation in the Pauli basis:

$$[\bar{\sigma}_z\bar{\rho}_E] = \frac{1}{2}\begin{pmatrix} -iy_\infty - x_\infty z_\infty \\ ix_\infty - y_\infty z_\infty \\ 1 - z_\infty^2 \end{pmatrix}.$$

Straightforward but elaborate calculations then give

$$\big[\mathcal{L}_0^{-1}(\bar{\sigma}_z\bar{\rho}_E)\big] = \frac{1}{8\det[\mathcal{L}_E]} \tag{6.35}$$
$$\begin{pmatrix} -4\kappa_\Sigma\omega_2\left(ix_\infty - y_\infty z_\infty\right)\sin(\alpha) - 2\omega_2^2\left(z_\infty^2 - 1\right)\sin(2\alpha) - 2\left(\kappa_\Sigma^2 + 2\omega_2^2\cos^2(\alpha)\right)\left(x_\infty z_\infty + iy_\infty\right) \\ 2\kappa_\Sigma\left(\kappa_\Sigma\left(ix_\infty - y_\infty z_\infty\right) + \omega_2\left(z_\infty^2 - 1\right)\cos(\alpha) - 2\omega_2\left(x_\infty z_\infty + iy_\infty\right)\sin(\alpha)\right) \\ 2\kappa_\Sigma\omega_2\left(ix_\infty - y_\infty z_\infty\right)\cos(\alpha) - 2\omega_2^2\left(x_\infty z_\infty + iy_\infty\right)\sin(2\alpha) + \left(1 - z_\infty^2\right)\left(\kappa_\Sigma^2 + 4\omega_2^2\sin^2(\alpha)\right) \end{pmatrix}.$$

Focusing on the leading-order in $\frac{1}{\omega_2}$ yields the following:

$$\big[\mathcal{L}_0^{-1}(\bar{\sigma}_z\bar{\rho}_E)\big] = \begin{pmatrix} \frac{-\Delta + i\kappa_\Delta}{\kappa_\Sigma\omega_2} \\ \frac{1}{2\omega_2} \\ \frac{\Delta(-\Delta+i\kappa_\Delta) - \frac{\kappa_\Sigma(2i\kappa_\Delta+\kappa_\Sigma)}{4}}{\kappa_\Sigma\omega_2^2} \end{pmatrix},$$

and further

$$\varepsilon(1-\mathcal{R})\bar{\mathcal{K}}_1(\rho_s) = \frac{g}{\Lambda}(iT_z \otimes \bar{M}_z)(\rho_s \otimes \bar{\rho}_E) + \frac{g}{\Lambda}(\rho_s \otimes \bar{\rho}_E)\big(iT_z \otimes \bar{M}_z\big)^\dagger,$$

with

$$\big[\bar{M}_z\big] = \begin{pmatrix} -\frac{2\Delta}{\kappa_\Sigma} \\ 1 \\ \frac{-4\Delta^2 + 4\kappa_\Delta^2 - \kappa_\Sigma^2}{2\kappa_\Sigma\omega_2} \\ \frac{\kappa_\Delta(2\Delta - \kappa_\Sigma)}{\kappa_\Sigma\omega_2} \end{pmatrix} + i\begin{pmatrix} \frac{2\kappa_\Delta}{\kappa_\Sigma} \\ 0 \\ \frac{4\Delta\kappa_\Delta}{\kappa_\Sigma\omega_2} \\ -\frac{2\kappa_\Delta^2}{\kappa_\Sigma\omega_2} \end{pmatrix}.$$

- For the last part of $\mathcal{K}_1$, consider (6.26):

$$\varepsilon(\mathcal{L}_0-\partial_t)(1-\mathcal{R})\tilde{\mathcal{K}}_1(\rho_s) = ig(1-\mathcal{R})\big(\big[e^{i\bar{\omega}_1 t}T_-\otimes\sigma_+ + e^{-i\bar{\omega}_1 t}T_+\otimes\sigma_-, \rho_s\otimes\bar{\rho}_E\big]\big). \quad (6.36)$$

Introducing

$$\bar{\sigma}_+ := \sigma_+ - \mathrm{Tr}(\sigma_+\bar{\rho}_E)\mathbb{1}_E = \sigma_+ - \frac{\xi_\infty^*}{2}\mathbb{1}_E,$$
$$\bar{\sigma}_- := \sigma_- - \mathrm{Tr}(\sigma_-\bar{\rho}_E)\mathbb{1}_E = \sigma_- - \frac{\xi_\infty}{2}\mathbb{1}_E,$$

we can write the right-hand side of (6.36) as

$$ig\big[e^{i\bar{\omega}_1 t}T_-\otimes\bar{\sigma}_+ + e^{-i\bar{\omega}_1 t}T_+\otimes\bar{\sigma}_-, \rho_s\otimes\bar{\rho}_E\big] = ige^{i\bar{\omega}_1 t}T_-\rho_s\otimes\bar{\sigma}_+\bar{\rho}_E + ige^{-i\bar{\omega}_1 t}T_+\rho_s\otimes\bar{\sigma}_-\bar{\rho}_E + \text{h.c.}$$

At this point we can split $(1-\mathcal{R})\tilde{\mathcal{K}}_1$ into two parts:

$$\begin{aligned}\varepsilon(1-\mathcal{R})\tilde{\mathcal{K}}_1(\rho_s) &= ige^{i\bar{\omega}_1 t}(\mathcal{L}_0 - i\bar{\omega}_1)^{-1}(T_-\rho_s\otimes\bar{\sigma}_+\bar{\rho}_E) + ige^{-i\bar{\omega}_1 t}(\mathcal{L}_0 + i\bar{\omega}_1)^{-1}(T_+\rho_s\otimes\bar{\sigma}_-\bar{\rho}_E) + \text{h.c.}\\ &= ige^{i\bar{\omega}_1 t}T_-\rho_s\otimes(\mathcal{L}_0 - i\bar{\omega}_1)^{-1}(\bar{\sigma}_+\bar{\rho}_E) + ige^{-i\bar{\omega}_1 t}T_+\rho_s\otimes(\mathcal{L}_0 + i\bar{\omega}_1)^{-1}(\bar{\sigma}_-\bar{\rho}_E) + \text{h.c.}\end{aligned} \quad (6.37)$$

We obtain the following matrix representations:

$$[\bar{\sigma}_+\bar{\rho}_E] = \frac{1}{8}\begin{pmatrix} -2z_\infty - (\xi_\infty + \xi_\infty^*)\,\xi_\infty^* + 2 \\ i\,(-2z_\infty - 1\,(\xi_\infty - \xi_\infty^*)\,\xi_\infty^* + 2) \\ (2-2z_\infty)\,\xi_\infty^* \end{pmatrix},$$

and

$$\det[\mathcal{L}_0 \mp i\bar{\omega}_1]\Big[(\mathcal{L}_0 \mp i\bar{\omega}_1)^{-1}\Big] =$$
$$\frac{1}{2}\begin{pmatrix} \kappa_\Sigma^2 + 3i\kappa_\Sigma\bar{\omega}_1 + 2\omega_2^2\cos^2(\alpha) - 2\bar{\omega}_1^2 & -2\omega_2\,(\kappa_\Sigma + i\bar{\omega}_1)\sin(\alpha) & \omega_2^2\sin(2\alpha) \\ 2\omega_2\,(\kappa_\Sigma + i\bar{\omega}_1)\sin(\alpha) & \kappa_\Sigma^2 + 3i\kappa_\Sigma\bar{\omega}_1 - 2\bar{\omega}_1^2 & -\omega_2\,(\kappa_\Sigma + 2i\bar{\omega}_1)\cos(\alpha) \\ \omega_2^2\sin(2\alpha) & \omega_2\,(\kappa_\Sigma + 2i\bar{\omega}_1)\cos(\alpha) & \frac{\kappa_\Sigma^2}{2} + 2i\kappa_\Sigma\bar{\omega}_1 + 2\omega_2^2\sin^2(\alpha) - 2\bar{\omega}_1^2 \end{pmatrix},$$

with

$$\det[\mathcal{L}_0 \mp i\bar{\omega}_1] = -\frac{\kappa_\Sigma^3}{4} + \frac{\kappa_\Sigma\omega_2^2\cos^2(\alpha)}{2} - \kappa_\Sigma\omega_2^2 + 2\kappa_\Sigma\bar{\omega}_1^2 \pm i\left(\frac{5\kappa_\Sigma^2\bar{\omega}_1}{4} - \omega_2^2\bar{\omega}_1 + \bar{\omega}_1^3\right).$$

Elaborate calculations then show that

$$(\mathcal{L}_0 - i\bar{\omega}_1)^{-1}(\bar{\sigma}_+\bar{\rho}_E) = \frac{1}{\kappa_\Sigma + i\bar{\omega}_1}\bar{M}_+\bar{\rho}_E, \quad (6.38a)$$
$$(\mathcal{L}_0 + i\bar{\omega}_1)^{-1}(\bar{\sigma}_-\bar{\rho}_E) = \frac{1}{\kappa_\Sigma - i\bar{\omega}_1}\bar{M}_-\bar{\rho}_E, \quad (6.38b)$$

with $\bar{M}_\pm$ operators such that $\mathrm{Tr}\big(\bar{M}_\pm \bar{\rho}_E\big) = 0$, and that, up to leading-order in $\frac{1}{\omega_2}$ take the form

$$\big[\bar{M}_+\big] = \frac{1}{2}\begin{pmatrix} -1 + \mathcal{O}\Big(\frac{1}{\omega_2}\Big) \\ -\frac{(\kappa_\Sigma + 2i\bar{\omega}_1)\big(4\Delta^2\kappa_\Delta + \kappa_\Sigma\big(2\Delta\kappa_\Delta + 2i\Delta\kappa_\Sigma - 2\Delta\bar{\omega}_1 + 2\kappa_\Delta\kappa_\Sigma + 2i\kappa_\Delta\bar{\omega}_1 - \kappa_\Sigma^2 - 3i\kappa_\Sigma\bar{\omega}_1 + 2\bar{\omega}_1^2\big)\big)}{2\kappa_\Sigma\omega_2^2(i\kappa_\Sigma - 2\bar{\omega}_1)} + \mathcal{O}\Big(\frac{1}{\omega_2^3}\Big) \\ \frac{-\Delta + i\kappa_\Delta - \frac{i\kappa_\Sigma}{2} + \bar{\omega}_1}{\omega_2} + \mathcal{O}\Big(\frac{1}{\omega_2^2}\Big) \\ \frac{\kappa_\Delta}{\omega_2} + \mathcal{O}\Big(\frac{1}{\omega_2^2}\Big) \end{pmatrix},$$

$$\big[\bar{M}_-\big] = \frac{1}{2}\begin{pmatrix} -1 + \mathcal{O}\Big(\frac{1}{\omega_2}\Big) \\ -\frac{(\kappa_\Sigma - 2i\bar{\omega}_1)\big(4\Delta^2\kappa_\Delta + \kappa_\Sigma\big(2\Delta\kappa_\Delta + 2i\Delta\kappa_\Sigma + 2\Delta\bar{\omega}_1 + 2\kappa_\Delta\kappa_\Sigma - 2i\kappa_\Delta\bar{\omega}_1 + \kappa_\Sigma^2 - 3i\kappa_\Sigma\bar{\omega}_1 - 2\bar{\omega}_1^2\big)\big)}{2\kappa_\Sigma\omega_2^2(i\kappa_\Sigma + 2\bar{\omega}_1)} + \mathcal{O}\Big(\frac{1}{\omega_2^3}\Big) \\ \frac{-\Delta + i\kappa_\Delta + \frac{i\kappa_\Sigma}{2} + \bar{\omega}_1}{\omega_2} + \mathcal{O}\Big(\frac{1}{\omega_2^2}\Big) \\ \frac{\kappa_\Delta}{\omega_2} + \mathcal{O}\Big(\frac{1}{\omega_2^2}\Big) \end{pmatrix}.$$

Hence we can write

$$\bar{M}_+ = \bar{M}_- = -\frac{\sigma_x}{2} + \mathcal{O}\Big(\frac{1}{\omega_2}\Big). \tag{6.39}$$

Putting all this together, we can write

$$\begin{aligned}\varepsilon(1-\mathcal{R})\tilde{\mathcal{K}}_1(\rho_s) =& \Big(\frac{ig}{\kappa_\Sigma + i\bar{\omega}_1} e^{i\bar{\omega}_1 t} T_- \otimes \bar{M}_+\Big)(\rho_s \otimes \bar{\rho}_E) + (\rho_s \otimes \bar{\rho}_E)\Big(\frac{ig}{\kappa_\Sigma + i\bar{\omega}_1} e^{i\bar{\omega}_1 t} T_- \otimes \bar{M}_+\Big)^\dagger \\ &+ \Big(\frac{ig}{\kappa_\Sigma - i\bar{\omega}_1} e^{-i\bar{\omega}_1 t} T_+ \otimes \bar{M}_-\Big)(\rho_s \otimes \bar{\rho}_E) + (\rho_s \otimes \bar{\rho}_E)\Big(\frac{ig}{\kappa_\Sigma - i\bar{\omega}_1} e^{-i\bar{\omega}_1 t} T_+ \otimes \bar{M}_-\Big)^\dagger.\end{aligned}$$

Order ε^2 computations

For the second-order reduced dynamics, (6.28) for $k = 2$ gives

$$\begin{aligned}\mathcal{K}_0\mathcal{L}_{s,2}(\rho_s) &= \mathcal{L}_{s,2}(\rho_s) \otimes \bar{\rho}_E \\ &= \mathcal{R}\overline{\mathcal{L}_1\mathcal{K}_1}(\rho_s) = \mathrm{Tr}_E(\overline{\mathcal{L}_1\mathcal{K}_1}(\rho_s)) \otimes \bar{\rho}_E,\end{aligned}$$

such that

$$\mathcal{L}_{s,2}(\rho_s) = \mathrm{Tr}_E(\bar{\mathcal{L}}_1(1-\mathcal{R})\bar{\mathcal{K}}_1(\rho_s)) + \mathrm{Tr}_E\Big(\overline{\tilde{\mathcal{L}}_1\mathcal{R}\tilde{\mathcal{K}}_1(\rho_s)}\Big) + \mathrm{Tr}_E\Big(\overline{\tilde{\mathcal{L}}_1(1-\mathcal{R})\tilde{\mathcal{K}}_1(\rho_s)}\Big). \tag{6.40}$$

It is straightforward to verify that

$$\mathrm{Tr}_E(\bar{\mathcal{L}}_1(1-\mathcal{R})\bar{\mathcal{K}}_1(\rho_s)) = \frac{\bar{\omega}_1^2}{\omega_2}\mathrm{Tr}\big(\sigma_z\bar{M}_z\bar{\rho}_E\big)\big(T_z^2\rho_s - T_z\rho_s T_z\big) + \frac{\bar{\omega}_1^2}{\omega_2}\mathrm{Tr}\Big(\sigma_z\bar{\rho}_E\bar{M}_z^\dagger\Big)\big(\rho_s T_z^2 - T_z\rho_s T_z\big),$$

and using

$$\mathrm{Tr}\big(\sigma_z\bar{M}_z\bar{\rho}_E\big) = -\frac{4\Delta^2 + \kappa_\Sigma^2}{2\kappa_\Sigma\omega_2} + i\frac{\kappa_\Delta\,(2\Delta - \kappa_\Sigma)}{\kappa_\Sigma\omega_2},$$

we obtain that

$$\mathrm{Tr}_E(\bar{\mathcal{L}}_1(1-\mathcal{R})\bar{\mathcal{K}}_1(\rho_s)) = \bar{\omega}_1^2\frac{\left(4\Delta^2+\kappa_\Sigma^2\right)}{\kappa_\Sigma\omega_2^2}\mathcal{D}_{T_z}(\rho_s) - i\bar{\omega}_1^2\frac{\kappa_\Delta\left(-2\Delta+\kappa_\Sigma\right)}{\kappa_\Sigma\omega_2^2}\left[T_z^2,\rho_s\right].$$

For the second term in equation (6.40) we get

$$\mathrm{Tr}_E\left(\overline{\tilde{\mathcal{L}}_1\mathcal{R}\tilde{\mathcal{K}}_1(\rho_s)}\right) = i\frac{\xi_\infty}{2}\bar{\omega}_1\,\mathrm{Tr}(\sigma_+\bar{\rho}_E)[T_-,[T_+,\rho_s]] - i\frac{\xi_\infty^*}{2}\bar{\omega}_1\,\mathrm{Tr}(\sigma_-\bar{\rho}_E)[T_+,[T_-,\rho_s]],$$

and using $\mathrm{Tr}(\sigma_+\bar{\rho}_E) = \frac{\xi_\infty^*}{2}$ we obtain that

$$\mathrm{Tr}_E\left(\overline{\tilde{\mathcal{L}}_1\mathcal{R}\tilde{\mathcal{K}}_1(\rho_s)}\right) = -i\frac{\xi_\infty^*\xi_\infty}{4}\bar{\omega}_1[[T_+,T_-],\rho_s].$$

For the third term in equation (6.40) we obtain

$$\begin{aligned}\mathrm{Tr}_E\left(\overline{\tilde{\mathcal{L}}_1(1-\mathcal{R})\tilde{\mathcal{K}}_1(\rho_s)}\right) = {}& a_+(T_-T_+\rho_s - T_+\rho_sT_-) - a_-^*(T_-\rho_sT_+ - \rho_sT_+T_-)\\ &+ a_-(T_+T_-\rho_s - T_-\rho_sT_+) - a_+^*(T_+\rho_sT_- - \rho_sT_-T_+),\end{aligned}$$

with

$$\begin{aligned}a_+ &= \frac{\mathrm{Tr}\big(\sigma_+\bar{M}_-\bar{\rho}_E\big)}{\kappa_\Sigma - i\bar{\omega}_1}\bar{\omega}_1^2,\\ a_- &= \frac{\mathrm{Tr}\big(\sigma_-\bar{M}_+\bar{\rho}_E\big)}{\kappa_\Sigma + i\bar{\omega}_1}\bar{\omega}_1^2.\end{aligned}$$

Retaining the leading-order terms in $\frac{1}{\omega_2}$ for a_+ and a_-, we readily obtain

$$\mathrm{Tr}_E\left(\overline{\tilde{\mathcal{L}}_1(1-\mathcal{R})\tilde{\mathcal{K}}_1(\rho_s)}\right) = \frac{\kappa_\Sigma\bar{\omega}_1^2}{\kappa_\Sigma^2+4\bar{\omega}_1^2}\big(\mathcal{D}_{T_-}+\mathcal{D}_{T_-}\big) + i\frac{\bar{\omega}_1^3}{\kappa_\Sigma^2+4\bar{\omega}_1^2}[[T_+,T_-],\rho_s].$$

Summary

Putting all of the calculations of this section together, we arrive at the following second-order reduced model.

For the slow dynamics we obtain an explicit Lindbladian model

$$\begin{aligned}\mathcal{L}_{s,\varepsilon}(\rho_s) = &-i\big[\omega_{s,z,1}T_z + \omega_{s,z,2}T_z^2 + \omega_{s,c}[T_+, T_-], \rho_s\big] \\ &+ \kappa_{s,z}\mathcal{D}_{T_z}(\rho_s) + \kappa_{s,\pm}\big(\mathcal{D}_{T_-} + \mathcal{D}_{T_+}\big) + \mathcal{O}\big(g\varepsilon^2\big),\end{aligned} \tag{6.41}$$

with, up to leading order in $\frac{1}{\omega_2}$,

$$\omega_{s,z,1} = -\frac{\kappa_\Delta g\left(4\Delta^2 + \kappa_\Sigma^2\right)}{2\kappa_\Sigma\omega_2^2}, \tag{6.42a}$$

$$\omega_{s,z,2} = \frac{\kappa_\Delta g^2\left(-2\Delta + \kappa_\Sigma\right)}{2\kappa_\Sigma\omega_2^2}, \tag{6.42b}$$

$$\omega_{s,c} = \frac{g^2\bar{\omega}_1}{\kappa_\Sigma^2 + 4\bar{\omega}_1^2}, \tag{6.42c}$$

$$\kappa_{s,z} = \frac{g^2\left(4\Delta^2 + \kappa_\Sigma^2\right)}{\kappa_\Sigma\omega_2^2}, \tag{6.42d}$$

$$\kappa_{s,\pm} = \frac{\kappa_\Sigma g^2}{\kappa_\Sigma^2 + 4\bar{\omega}_1^2}\,. \tag{6.42e}$$

For the embedding of the slow subspace we obtain a completely positive map up to second order terms:

$$\mathcal{K}_\varepsilon(\rho_s) = K_\varepsilon(\rho_s \otimes \bar{\rho}_E)K_\varepsilon^\dagger + \mathcal{O}(\varepsilon^2), \tag{6.43}$$

with, up to leading-order in $\frac{1}{\omega_2}$ for every term,

$$\begin{aligned}K_\varepsilon := 1 &- i\frac{\kappa_\Delta}{\kappa_\Sigma}\frac{g}{\omega_2}H_s \otimes \mathbb{1}_E + i\frac{g}{\omega_2}T_z \otimes \sigma_y - i\frac{2g\Delta}{\kappa_\Sigma\omega_2}T_z \otimes \sigma_x \\ &- i\frac{g}{\sqrt{\kappa_\Sigma^2 + 4\bar{\omega}_1^2}}H_{s,\pm} \otimes \sigma_x - 2\frac{\kappa_\Delta}{\kappa_\Sigma}\frac{g}{\omega_2}T_z \otimes \sigma_x,\end{aligned} \tag{6.44}$$

and we have defined

$$H_s = -\frac{\kappa_\Sigma + 2i\Delta}{2\bar{\omega}_1}e^{i\bar{\omega}_1 t}T_- - \frac{\kappa_\Sigma - 2i\Delta}{2\bar{\omega}_1}e^{-i\bar{\omega}_1 t}T_+, \tag{6.45a}$$

$$H_{s,\pm} = \frac{(\kappa_\Sigma - 2i\bar{\omega}_1)e^{i\bar{\omega}_1 t}T_- + (\kappa_\Sigma + 2i\bar{\omega}_1)e^{-i\bar{\omega}_1 t}T_+}{\sqrt{\kappa_\Sigma^2 + 4\bar{\omega}_1^2}}. \tag{6.45b}$$

Remark 6.1. We here reported the leading-order of all different terms in $\frac{1}{\omega_2}$, hence approximating the exact expression of $\mathcal{K}_1$ as defined in (6.33), (6.34) and (6.37) in the limit of large ω_2. When using the exact expressions, it is straightforward to show that $\mathrm{Tr}(\mathcal{K}_1(\rho_s)) = 0$, since (6.33), (6.35) and (6.38), are traceless expressions. We then obtain that $\mathrm{Tr}_E(\mathcal{K}_\varepsilon(\rho_s)) = \mathrm{Tr}(\mathcal{K}_0(\rho_s)) + \varepsilon\,\mathrm{Tr}(\mathcal{K}_1(\rho_s)) + \mathcal{O}(\varepsilon^2) = \mathrm{Tr}(\rho_s) + \mathcal{O}(\varepsilon^2)$, and thus up to order ε^2, $\mathcal{K}_\varepsilon$ is also trace-preserving, and hence CPTP.

6.3.2.2 Discussion of DD benefits

As a concrete result of this section, and in line with the double-timescale DD proposal detailed in Section 6.2, we can focus on the limiting case of strong driving, where ω_2 dominates the other parameters, and we additionally only consider the induced decoherence channels.

Corollary 6.2. *Define $\frac{1}{\Omega_2^k}$ to signify any dimensionless term consisting of the product of $\frac{1}{\omega_2^k}$ with any product of powers of the other rates $\bar{\omega}_1, \kappa_\pm$ or Δ, excluding ω_2. The decoherence rates defined by* (6.48) *display the following asymptotic behavior for large ω_2:*

$$\begin{aligned} \kappa_{s,z} &= \frac{g^2\left(4\Delta^2+\kappa_\Sigma^2\right)}{\kappa_\Sigma \omega_2^2} && \text{(6.46a)} \\ &+ \frac{g^2}{\omega_2}\mathcal{O}\left(\frac{1}{\Omega_2^3}\right) \\ \kappa_{s,\pm} &= \frac{\kappa_\Sigma g^2}{\kappa_\Sigma^2+4\bar{\omega}_1^2} && \text{(6.46b)} \\ &+ \frac{g^2}{\omega_2}\mathcal{O}\left(\frac{1}{\Omega_2}\right). \end{aligned}$$

All these rates vanish in the limit $\bar{\omega}_1 \to \infty, \omega_2 \to \infty$ where still $\bar{\omega}_1 \ll \omega_2$, quantitatively confirming the DD benefits. The general form of these expressions can be understood intuitively as follows. The expressions involve the sum $\kappa_\Sigma = \kappa_- + \kappa_+$ because the strongest drive $\omega_2\sigma_x$ constantly exchanges the roles of ground and excited states in E. This also explains why $\kappa_{s,+} \simeq \kappa_{s,-}$. The rates $\kappa_{s,\pm}$ then take the standard Purcell-type expression resulting from Jaynes-Cummings-type coupling under detuning $\frac{\bar{\omega}_1}{2}$. The main DD effect here is the $\bar{\omega}_1$-detuning reducing the effective coupling between T and E. The first term of $\kappa_{s,z}$ in fact has a similar form, where κ_-, κ_+ terms do not appear in the denominator because they are dominated by ω_2^2. This is no coincidence, since the Hamiltonian part is like the usual Jaynes-Cummings coupling, up to exchanging the roles of σ_x and σ_z. Indeed, neglecting the detuning Δ, we are applying a constant drive along the σ_x direction (in the $\bar{\omega}_1$ rotating frame), orthogonal to the coupling in the σ_z direction. Those two contributions would not be present if we were only considering the average coupling as derived in (6.7). They thus express the limitations, in presence of $\kappa_\pm$, of the RWA performed in Section 6.2. The effect of the average coupling remaining in (6.7) is captured by the second term of $\kappa_{s,z}$. One can recognize the standard induced decoherence formula of type "$\tilde{g}^2/\tilde{\kappa}$" where $\tilde{g}$ is replaced by the average coupling $g\frac{\Delta}{\omega_2}$ as derived in Section 6.2.

As a last comment, Hamiltonian contributions to the reduced model can by definition be calibrated, so we do not set out to suppress them using the DD drives, as the terms do not represent induced decoherence. Although this was not the explicit goal of our DD driving, we can however see that the DD controls suppress also the Hamiltonian contributions (see the expressions for $\omega_{s,z,1}, \omega_{s,z,2}, \omega_{s,c}$ in (6.42)) asymptotically for large $\bar{\omega}_1$ and ω_2.

6.3.2.3 Optimization: cold TLS and reducing ω_2

The general formulas (6.46) quantify how DD controls containing two drives with amplitudes $\omega_2 \gg \bar{\omega}_1$ reduce the decoherence induced on T under general conditions. They can guide parameter choices in particular situations, as long as we assume large ω_2.

However, this does not mean that driving strongly in both $\bar{\omega}_1$ and ω_2 is always the best choice. Indeed, in very particular settings, it may be even better to take some of the drives at their minimal value. In other words, intermediate values of the drives would be the worst case. Assume for instance the extreme situation of dispersive coupling to a zero-temperature bath, i.e. $T_x = T_y = \kappa_+ = 0$. Then, in absence of controls (in fact as long as $\omega_2 = 0$), the TLS is attracted towards its ground state, and the resulting effect on T would be purely Hamiltonian. This raises the question of how to choose ω_2 to minimize the T_z-decoherence. We now answer this question, as an illustration of how to use our framework for design choices.

The *exact* decoherence rates $\kappa_{s,z}, \kappa_{s,\pm}$ (without considering the limiting case of large ω_2 as above) are defined by

$$\kappa_{s,z} = -2g^2 \mathrm{Re}(\mathrm{Tr}(\sigma_z X_z)), \tag{6.47a}$$
$$\kappa_{s,\pm} = -2g^2 \mathrm{Re}(\mathrm{Tr}(\sigma_\pm X_\mp)), \tag{6.47b}$$

where X_z and $X_\mp$ respectively satisfy the following matrix equations:

$$\begin{aligned}(\sigma_z - \mathrm{Tr}(\sigma_z \bar{\rho}_E))\bar{\rho}_E = &-\frac{i}{2}[\omega_2\sigma_x + \Delta\sigma_z, X_z] \\ &+ \kappa_- \mathcal{D}_{\sigma_-}(X_z) + \kappa_+ \mathcal{D}_{\sigma_+}(X_z),\end{aligned} \tag{6.48a}$$

$$\begin{aligned}(\sigma_\mp - \mathrm{Tr}(\sigma_\mp\, \bar{\rho}_E))\bar{\rho}_E = &-\frac{i}{2}[\omega_2\sigma_x + \Delta\sigma_z, X_\mp] \\ &\pm i\bar{\omega}_1 X_\mp + \kappa_- \mathcal{D}_{\sigma_-}(X_\mp) + \kappa_+ \mathcal{D}_{\sigma_+}(X_\mp).\end{aligned} \tag{6.48b}$$

Here, $\bar{\rho}_E$ is the unique steady state of the Lindbladian acting on E, given in (6.31), of which we recall the definition here:

$$-\frac{i}{2}[\omega_2\sigma_x + \Delta\sigma_z, \bar{\rho}_E] + \kappa_- \mathcal{D}_{\sigma_-}(\bar{\rho}_E) + \kappa_+ \mathcal{D}_{\sigma_+}(\bar{\rho}_E) = 0.$$

Given the number of variables in play, expressions for the dissipation rates are algebraically complicated and were computed with the help of a computer algebra system (SymPy [90]). We obtain the following expression for $\kappa_{s,z}$:

$$\begin{aligned}\kappa_{s,z} = &\frac{8g^2\kappa_+\kappa_- \left(4\Delta^2 + (\kappa_- + \kappa_+)^2\right)\left(16\Delta^2\omega_2^2 + \left(4\Delta^2 + (\kappa_- + \kappa_+)^2\right)^2\right)}{(\kappa_- + \kappa_+)^3\left(4\Delta^2 + (\kappa_- + \kappa_+)^2 + 2\omega_2^2\right)^3} \\ &+ \frac{8g^2\left(4\Delta^2 + (\kappa_- + \kappa_+)^2\right)(\kappa_- + \kappa_+)^2\omega_2^2\left(2\kappa_-^2 + 2\kappa_+^2 + \omega_2^2\right)}{(\kappa_- + \kappa_+)^3\left(4\Delta^2 + (\kappa_- + \kappa_+)^2 + 2\omega_2^2\right)^3}.\end{aligned} \tag{6.49}$$

One can indeed see that this reduces to (6.42d) for asymptotically large ω_2. The bath temperature is characterized by n_{th}, the mean number of thermal photons, such that $\kappa_- = \kappa_1(1+n_{\mathrm{th}})$ and $\kappa_+ = \kappa_1 n_{\mathrm{th}}$. Straightforward algebraic manipulations of (6.49) allow for an optimization study, which we summarize in the following result.

Theorem 6.3. *The induced decoherence rate $\kappa_{s,z}$ as defined in* (6.49) *shows the following dependence on ω_2:*

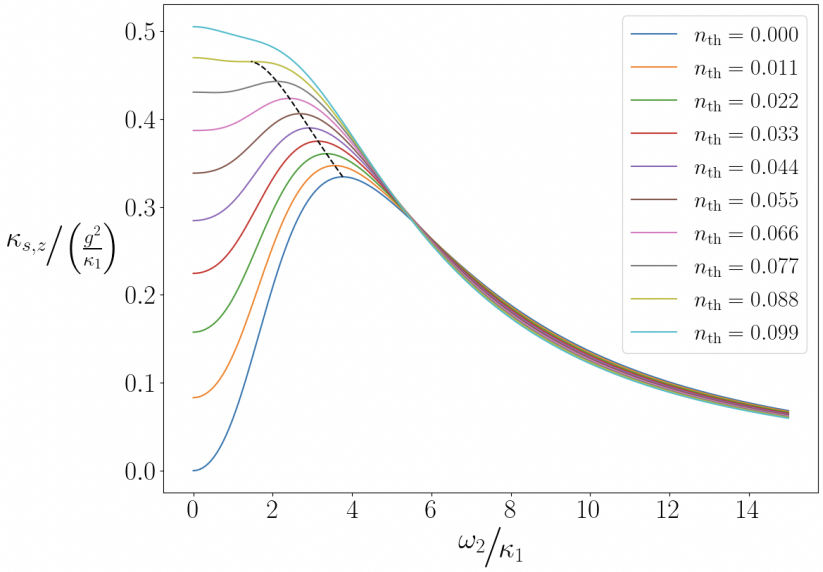

Figure 6.1: Dependence of $\kappa_{s,z}$ as defined in (6.49) on $\frac{\omega_2}{\kappa_1}$, for various values of $n_{\rm th}$ between 0 and 0.1 and at fixed $\frac{\Delta}{\kappa_1} = 2$. The dashed black line indicates the local maximum in ω_2 when it is present. In the latter cases, induced decoherence $\kappa_{s,z}$ is minimized either at $\omega_2 = 0$ or at the largest achievable ω_2, depending on its value.

- *If* $n_{th} < \frac{\sqrt{3}}{3} - \frac{1}{2} \simeq 0.077$ *, then* $\kappa_{s,z}$ *displays a single local maximum as a function of* ω_2*, for any values of* Δ *and* κ_1*. The optimal value of* ω_2 *is either zero or the maximal achievable one, depending on the experimentally achievable bound on the latter.*

- *If* $n_{th} > \frac{\sqrt{3}}{3} - \frac{1}{2} \simeq 0.077$ *and*

$$\frac{\Delta^2}{\kappa_1^2} < \frac{(2n_{th}+1)^2\left(2\sqrt{3}(2n_{th}+1)+\sqrt{12n_{th}^2+12n_{th}-1}\right)}{4\sqrt{12n_{th}^2+12n_{th}-1}} \,, \tag{6.50}$$

  then $\kappa_{s,z}$ *also displays a single local maximum as a function of* ω_2*, with the same conclusions for its optimization.*

- *If* $n_{th} > \frac{\sqrt{3}}{3} - \frac{1}{2} \simeq 0.077$ *and* (6.50) *is not satisfied, then* $\kappa_{s,z}$ *is monotonically decreasing in* ω_2*.*

In the last case, in other words when Δ is large, ramping up ω_2 is always advantageous. In the first two cases, the value of ω_2 minimizing $\kappa_{s,z}$ will depend on how its value at the maximal achievable ω_2 compares to its value at $\omega_2 = 0$, which reads:

$$\kappa_{s,z}(\omega_2 = 0) = \frac{8g^2 n_{\rm th}\left(n_{\rm th}+1\right)}{\kappa_1\left(8n_{\rm th}^3 + 12n_{\rm th}^2 + 6n_{\rm th} + 1\right)} \,. \tag{6.51}$$

A numerical illustration of the dependence of $\kappa_{s,z}$ on ω_2 and $n_{\rm th}$ is provided in Figure 6.1.

Note that Theorem 6.3 and Figure 6.1 have been established by analyzing a single algebraic formula. Indeed, the adiabatic elimination method on the one hand yields explicit formulas for the induced decoherence rates, preventing the need for solving differential equations for each

parameter setting. On the other hand, our extended formalism as explained in Section 6.3.1.2 does not require to select between either the dissipation being the largest time-scale (standard adiabatic elimination), or drive frequencies $\bar{\omega}_1, \omega_2$ being the largest timescale (domain of averaging techniques like RWA). A single formula thus allows us to consistently cover the full range of parameter values.

We can also look at the values of induced decoherence rates $\kappa_{s,\pm}$ for $\omega_2 = 0$, yielding:

$$\kappa_{s,-} = \frac{4\kappa_- g^2}{(\kappa_- + \kappa_+)^2 + 4(\bar{\omega}_1 + \Delta)^2}, \tag{6.52a}$$

$$\kappa_{s,+} = \frac{4\kappa_+ g^2}{(\kappa_- + \kappa_+)^2 + 4(\bar{\omega}_1 + \Delta)^2}. \tag{6.52b}$$

As expected when taking $\omega_2 = 0$, the initial κ_- and κ_+ remain separated, such that $\kappa_{s,+}$ remains small for a cold bath. We can also note that ω_2 was decoupling the effect of $\Delta\sigma_z$, and its absence reintroduces this detuning in addition to $\bar{\omega}_1$ in (6.52). Regarding the DD effect, we can see that also in the case of $\omega_2 = 0$, we rely on large $\bar{\omega}_1$ to reduce the induced decoherence channels $\kappa_{s,\pm}$. In absence of ω_2 however, there may be a danger of being counterproductive by hitting $\bar{\omega}_1 \approx -\Delta$, which renders the DD ineffective.

As a last point, we can obtain exact second-order expressions for the Hamiltonian terms in T_z as well, again without the asymptotic limit of large ω_2. The exact first-order slow dynamics $\mathcal{L}_{s,1}$ is given by the Hamiltonian $\omega_{s,z,1} T_z$, with

$$\omega_{s,z,1} = -\frac{\kappa_- - \kappa_+}{\kappa_- + \kappa_+} \frac{4\Delta^2 + (\kappa_- + \kappa_+)^2}{4\Delta^2 + (\kappa_- + \kappa_+)^2 + 2\omega_2^2}.$$

Regarding the system parameters, we can see that this contribution is largest for a TLS coupled to a cold bath, and disappears in the limit of a hot bath, where $\kappa_- = \kappa_+$. Since the imperfect detuning Δ appears, we cannot expect to have exact knowledge of $\omega_{s,z,1}$. However, if Δ can be assumed constant, then the term can be calibrated experimentally and corrected for. Remark that such a Lamb-shift type Hamiltonian is present in the absence of driving as well, and only the frequency is altered through the driving. Regarding the DD control, the term goes as $\sim \frac{1}{\omega_2^2}$ for large ω_2, and hence it is suppressed for strong driving, although this was not explicitly part of our initial goal. For the first Hamiltonian term at second order, we obtain

$$\omega_{s,z,2} = -\frac{16\Delta\kappa_\Delta\omega_2^2 g^2}{\kappa_\Sigma \left(4\Delta^2 + \kappa_\Sigma^2 + 2\omega_2^2\right)^2}.$$

We obtain the same conclusion as for $\omega_{s,z,1}$, namely that $\omega_{s,z,2}$ is minimal for a hot bath, and decreases as $\frac{1}{\omega_2^2}$ under the DD controls. The full expressions for the remaining Hamiltonian term − e.g. the exact expression for ω_c − is more involved, and is not mentioned here.

The calculations in this section illustrate how our formulas could be used to optimize the DD drive parameters. In Chapter 7, we will instead optimize the relative strengths of *dissipation rates* in various situations, showing that the optimal parameter choice can similarly jump from strongest possible to weakest possible dissipation on E, depending on the constraints on the allowable values of the dissipation rates. For instance, expressions like (6.51) seem to indicate that even in the absence of any drives, the lowest temperature (i.e. the lowest value of n_{th}) is not necessarily inducing the lowest $\kappa_{s,z}$. This specific example will be treated in Section 7.4.1.

6.3.3 Case of ultra-strong driving

A Lindbladian dissipation model like equation (II.1) is an idealization meant to summarize interactions of the TLS with further external degrees of freedom, e.g. a large bath involving phonon modes. Therefore, when significantly modifying the system Hamiltonian, in other words when we choose to add "ultra-strong" DD drives on the TLS, the dissipation model may have to be revised, depending on the type of bath and noise spectrum behind its derivation. One might be tempted to design DD drives to purposefully modify the Lindbladian itself [37, 41, 121]. However, in the context of the present work this is typically a secondary effect. This section provides explicit formulas for such a bath reconsideration, in order to check to which point our conclusions of Corollary 6.2 remain consistent.

We thus leave aside system T for a while and go back to the lab frame for the TLS system E in order to reconsider its decoherence channels. We can safely neglect the coupling of E and T at this stage, as it involves a weaker Hamiltonian, even further weakened by the DD drives, and it would thus only appear at higher orders in any possible modification of the Lindbladian dissipator of E. We model the TLS relaxation as stemming from an interaction of E with a large bath B that can be assumed memoryless. For the sake of concreteness, the interaction Hamiltonian is taken to be $\gamma\sigma_x \otimes R$, such that

$$H_{EB} = \frac{\Omega_E}{2}\sigma_z \otimes \mathbb{1}_B + \tilde{H}_c(t) \otimes \mathbb{1}_B + \gamma\sigma_x \otimes R + \mathbb{1}_E \otimes H_B \ . \tag{6.53}$$

Here R is a Hermitian operator acting on the bath Hilbert space, γ is some small positive coupling rate, H_B is the bare bath Hamiltonian and $\tilde{H}_c(t)$ is the DD drive, expressed in the lab frame. For this reason, (6.53) also includes the TLS bare frequency Ω_E. As is common practice, we can consider a bath of harmonic oscillators, for which the coupling along σ_x leads to a Jaynes-Cummings-type interaction with the different modes; similar conclusions hold for more general couplings and baths [19, 30, 48].

Moving to the rotating frame of both systems, and introducing the drive as in (6.5), we obtain the total Hamiltonian

$$H_E(t) \otimes \mathbb{1}_B + \gamma(\sigma_+ e^{i\bar{\Omega}_E t} + \sigma_- e^{-i\bar{\Omega}_E t}) \otimes \tilde{R}(t), \tag{6.54}$$

with $\tilde{R}(t) = e^{iH_B t} R e^{-iH_B t}$. Performing the toggling frame transformation defined in (6.6) yields

$$\gamma\tilde{E}(t) \otimes \tilde{R}(t), \tag{6.55}$$

with $\tilde{E}(t) = e^{i(\bar{\Omega}_E+\bar{\omega}_1)t}E_+(t) + e^{-i(\bar{\Omega}_E+\bar{\omega}_1)t}E_-(t)$, where we have defined

$$\begin{aligned} E_+(t) &:= e^{i\frac{\Lambda}{2}\sigma_{\alpha x}}\sigma_+ e^{-i\frac{\Lambda}{2}\sigma_{\alpha x}} \\ &= \frac{\cos(\alpha)}{2}\sigma_{\alpha x} + i\frac{1+\sin(\alpha)}{2}e^{i\Lambda t}\sigma_{\alpha+} \\ &\quad + i\frac{1-\sin(\alpha)}{2}e^{-i\Lambda t}\sigma_{\alpha-}, \end{aligned} \tag{6.56a}$$

$$E_-(t) := E_+^\dagger(t). \tag{6.56b}$$

At this point we introduce the modified bare E-frequency $\tilde{\Omega}_E = \bar{\Omega}_E + \bar{\omega}_1$. In line with the conclusions in Section 6.2, we will consider $\bar{\omega}_1 \ll \Omega_E$, so $\tilde{\Omega}_E \simeq \Omega_E$.

In the interaction frame of (6.55), the evolution equation of the joint density matrix ρ_{EB} is thus

$$\dot{\rho}_{EB}(t) = -i\gamma\Big[\tilde{E}(t)\otimes\tilde{R}(t), \rho_{EB}(t)\Big]. \tag{6.57}$$

We can write this as an integral equation,

$$\rho_{EB}(t) = \rho_{EB}(0) - i\gamma\int_0^t \Big[\tilde{E}(s)\otimes\tilde{R}(s), \rho_{EB}(s)\Big]\mathrm{d}s,$$

and reinjecting this into (6.57), we obtain

$$\dot{\rho}_{EB}(t) = -i\gamma\Big[\tilde{E}(t)\otimes\tilde{R}(t), \rho_{EB}(0)\Big] - \gamma^2\int_0^t \Big[\tilde{E}(t)\otimes\tilde{R}(t), \Big[\tilde{E}(s)\otimes\tilde{R}(s), \rho_{EB}(s)\Big]\Big]\mathrm{d}s. \tag{6.58}$$

Up until here, no approximations have been made, so (6.58) is exact. At this point we follow the standard procedure of the Born-Markov approximation [19, 30, 48], assuming the bath to be very large and unaffected by the weak coupling with the E system, such that it remains in a steady state $\bar{\rho}_B$ that is invariant under H_B ($[H_B, \bar{\rho}_B] = 0$). Without loss of generality we can take $\mathrm{Tr}(R\,\bar{\rho}_B) = 0$, since otherwise this would just lead to a modification of the bare E-Hamiltonian. Lastly, we assume the correlation time of the bath to be the shortest timescale present in the joint system. Taking the partial trace of both sides in (6.58) and performing these approximations yields a Markovian equation for E:

$$\frac{\dot{\rho}_E(t)}{\gamma^2} = \int_0^\infty \mathrm{Tr}\Big(\Big[\Big[\tilde{E}(t-s)\otimes\tilde{R}(t-s), \rho_E(t)\otimes\bar{\rho}_B\Big], \tilde{E}(t)\otimes\tilde{R}(t)\Big]\Big)\mathrm{d}s.$$

The right-hand side can be further worked out by defining the two-point correlation function $g(z)$ of the bath as

$$g(z) := \mathrm{Tr}\Big(\tilde{R}(t)\tilde{R}(t-z)\,\bar{\rho}_B\Big), z, t \in \mathbb{R},$$

yielding

$$\frac{\dot{\rho}_E(t)}{\gamma^2} = \int_{-\infty}^\infty g(z)\Big(\Big[\tilde{E}(t-z)\rho_E(t), \tilde{E}(t)\Big] + \Big[\tilde{E}(t), \rho_E(t)\tilde{E}(t+z)\Big]\Big)\mathrm{d}z. \tag{6.59}$$

Plugging in the expression of $\tilde{E}(t)$ as in (6.56), terms oscillating at frequencies $\pm 2\tilde{\Omega}_E, \pm 2\Lambda, 2\tilde{\Omega}_E \pm 2\Lambda, -2\tilde{\Omega}_E \pm 2\Lambda$ appear. Regarding oscillations as a function of z, we define the spectral density of the bath G as

$$G(\nu) := \int_{-\infty}^\infty e^{i\nu z} g(z)\,\mathrm{d}z, \forall \nu \in \mathbb{R}\,. \tag{6.60}$$

This still leaves the treatment of terms oscillating as a function of t. The bare TLS frequency $\tilde{\Omega}_E$ can always be assumed very large w.r.t. $\dot{\rho}_E$ in (6.59), justifying averaging over terms oscillating at frequencies $\pm\tilde{\Omega}_E$. The RWA introduces an error of order $\frac{\kappa^2}{\Omega_E}$, where κ is the typical dissipation rate obtained in the end. Since we assume the bare frequency of the TLS to be much larger than the dissipation rate, we can neglect this term. Thus, concretely, averaging (6.59) over t with only the frequencies $\pm 2\tilde{\Omega}_E$, yields

$$\begin{aligned}\frac{\dot{\rho}_E(t)}{\gamma^2} = &\int_{-\infty}^\infty g(z)e^{i\tilde{\Omega}_E z}\big([E_-(t-z)\rho_E, E_+(t)] + [E_-(t)\rho_E, E_+(t+z)]\big)\\ &+\int_{-\infty}^\infty g(z)e^{-i\tilde{\Omega}_E z}\big([E_+(t-z)\rho_E, E_-(t)] + [E_+(t), \rho_E E_-(t+z)]\big).\end{aligned}$$

A final approximation is needed to obtain a Lindbladian model. There are two possibilities for this approximation, and for any value of ω_2 at least one of them is valid in the context of our DD protocol.

As a first possible condition, when the drive amplitude ω_2 is dominated by the bare qubit frequency Ω_E, the noise spectral density G of the bath (defined in (6.60)) can typically be considered flat in the ranges $\pm[\Omega_E - \omega_2,\ \Omega_E + \omega_2]$. We thus shift the z dependency of E_- and E_+ towards $g(z)$ and assume $G(\tilde{\Omega}_E \pm \Lambda) \simeq G(\tilde{\Omega}_E) \simeq G(\Omega_E)$ when integrating over z. Finally, moving back to the lab frame by undoing (6.6), the Jaynes-Cummings-type coupling assumed in (6.53) then yields stationary dissipators in σ_- and σ_+, as assumed in the beginning of this chapter:

$$\dot{\rho}_E(t) = \kappa_- \mathcal{D}_{\sigma_-} + \kappa_+ \mathcal{D}_{\sigma_+}, \tag{6.61a}$$

$$\text{with} \quad \kappa_\mp \simeq 2\gamma^2\, G(\pm\Omega_E). \tag{6.61b}$$

As a second possible condition to obtain a Lindbladian model, the case of ultra-strong driving precisely assumes that we can similarly average over frequencies $\pm\Lambda$ and, avoiding parametric resonance, over the frequencies $2\tilde{\Omega}_E \pm 2\Lambda$ and $-2\tilde{\Omega}_E \pm 2\Lambda$. Again, this approximation remains valid if these frequencies are much larger than the obtained dissipation rate, to be checked a posteriori. Performing this last secular approximation yields instead:

$$\dot{\rho}_E(t) = \kappa_{\alpha x} \mathcal{D}_{\sigma_{\alpha x}} + \kappa_{\alpha -} \mathcal{D}_{\sigma_{\alpha -}} + \kappa_{\alpha +} \mathcal{D}_{\sigma_{\alpha +}}, \tag{6.62a}$$

$$\text{with} \quad \kappa_{\alpha x} := \frac{\gamma^2}{2}\Big(G(\tilde{\Omega}_E) + G(-\tilde{\Omega}_E)\Big)\cos^2(\alpha), \tag{6.62b}$$

$$\kappa_{\alpha -} := \frac{\gamma^2}{2} G(\tilde{\Omega}_E + \Lambda)(1+\sin(\alpha))^2 + \frac{\gamma^2}{2} G(-\tilde{\Omega}_E + \Lambda)(1-\sin(\alpha))^2, \tag{6.62c}$$

$$\kappa_{\alpha +} := \frac{\gamma^2}{2} G(-\tilde{\Omega}_E - \Lambda)(1+\sin(\alpha))^2 + \frac{\gamma^2}{2} G(\tilde{\Omega}_E - \Lambda)(1-\sin(\alpha))^2, \tag{6.62d}$$

and where we recall that

$$\cos(\alpha) = \frac{\omega_2}{\Lambda},$$
$$\sin(\alpha) = \frac{\Delta}{\Lambda},$$
$$\sigma_{\alpha x} = \cos(\alpha)\sigma_x + \sin(\alpha)\sigma_z,$$

and $\sigma_{\alpha\pm}$ are lowering and raising operators with respect to the eigenstates of $\sigma_{\alpha x}$.

The choice between a model with fixed decoherence operators $L_k \in \{\sigma_-,\ \sigma_+\}$, or with drive-corrected ones $L_k \in \{\sigma_{\alpha x},\ \sigma_{\alpha -},\ \sigma_{\alpha +}\}$, depends on whether it is a better approximation to consider G flat on the scale of ω_2/Ω_E, or to consider an RWA based on $\Lambda \gg \kappa_{\alpha x}, \kappa_{\alpha -}, \kappa_{\alpha +}$. The former approach leads to an error of order $\kappa\frac{\Lambda}{\Omega_E}$, whereas the latter leads to an error of order $\frac{\kappa^2}{\Lambda}$. The two approximations are compatible however and commute with one another when both are justified, i.e. when $\kappa_{\pm,\alpha\pm,\alpha x} \ll \Lambda \ll \tilde{\Omega}_E$. Indeed, first assuming a locally flat bath spectrum to obtain (6.61), next transforming the σ_- and σ_+ dissipators to the rotating frame w.r.t. $\frac{\Lambda}{2}\sigma_{\alpha x}$, and finally performing an RWA over frequencies $\pm\Lambda$,$2\tilde{\Omega}_E \pm 2\Lambda$ and $-2\tilde{\Omega}_E \pm 2\Lambda$ yields exactly the dissipators associated to (6.62) with ω_1 and $\Lambda \simeq \omega_2$ put to zero in the bath spectrum G. Note that it is consistent to effectively equate *two* dissipation channels κ_+, κ_- together with a *strong static drive* $\frac{\Lambda}{2}\sigma_{\alpha x}$, to *three* dissipation channels $\kappa_{\alpha -}, \kappa_{\alpha +}, \kappa_{\alpha z}$ in the

rotating frame. Since the drive makes the state rotate, the average effect of the dissipation is described by three dissipation channels in the rotating frame instead of two.

In summary, as long as the driving amplitude ω_2 remains an order of magnitude smaller than the bare frequency Ω_E, we retrieve the original model of (6.29) and the final form for the induced dissipation of the target system described in Corollary. 6.2. When ω_2 becomes too large (ultra-strong driving) and only the second type of approximation is justified, we must revise the dissipation model. In the rest of this section, we derive formulas for the induced decoherence on T under this revised dissipation model and just considering general, non-vanishing rates $\kappa_{\alpha x,\alpha-,\alpha+}$.

Reflection

We can briefly comment on how to consider the dissipation rates (6.62) as a function of our DD parameters.

- The effect of $\frac{\bar{\omega}_1}{2}\sigma_z$ just adds up to $\bar{\Omega}_E$, so for $\omega_2 = 0$ the bath noise spectrum G is probed at altered frequencies $\pm(\bar{\Omega}_E + \bar{\omega}_1)$ to evaluate the excitation and loss rates.
- The stronger drive of amplitude ω_2 introduces the periodic time-dependence in the TLS Hamiltonian (6.5). According to the general Floquet-Markov theory [54], the eigenbasis in which the TLS decoheres is then given by the Floquet Hamiltonian associated to E, in a frame given by a periodic change of variables (often called the micromotion), and Lindbladian dissipation rates are found by evaluating the bath noise spectrum at the Floquet quasi-energies. In our case, the periodic change of variables just corresponds to going to the rotating frame w.r.t. $\frac{\bar{\omega}_1}{2}\sigma_z$, where we obtain a constant Hamiltonian $\frac{\Lambda}{2}\sigma_{\alpha x}$ on E. This special situation implies that the Floquet decomposition trivializes to the more standard rotating-frame and averaging approach, but with correspondingly modified dissipation channels on E.

6.3.3.1 Derivation of reduced model for ultra-strong driving

Again in a rotating frame w.r.t. $\frac{\bar{\omega}_1}{2}\sigma_z$, the joint evolution of the target and TLS is thus described by the master equation

$$\begin{aligned}\tfrac{d}{dt}\rho = \kappa_{\alpha-}\mathcal{D}_{\mathbb{1}_T\otimes\sigma_{\alpha-}}(\rho) + \kappa_{\alpha+}\mathcal{D}_{\mathbb{1}_T\otimes\sigma_{\alpha+}}(\rho) + \kappa_{\alpha x}\mathcal{D}_{\mathbb{1}_T\otimes\sigma_{\alpha x}}(\rho) - i\frac{\Lambda}{2}[\mathbb{1}_T\otimes\sigma_{\alpha x},\rho] \\ - ig\big[T_z\otimes\sigma_z + e^{i\bar{\omega}_1 t}T_-\otimes\sigma_+ + e^{-i\bar{\omega}_1 t}T_+\otimes\sigma_-,\rho\big].\end{aligned} \tag{6.63}$$

In the notation of Section 6.3.1.2, we can write $\varepsilon = \frac{g}{\bar{\omega}_1}$,

$$\mathcal{L}_0 = -i\frac{\Lambda}{2}[\mathbb{1}_T\otimes\sigma_{\alpha x},\cdot] + \kappa_{\alpha x}\mathcal{D}_{\mathbb{1}_T\otimes\sigma_{\alpha x}} + \kappa_{\alpha-}\mathcal{D}_{\mathbb{1}_T\otimes\sigma_{\alpha-}} + \kappa_{\alpha+}\mathcal{D}_{\mathbb{1}_T\otimes\sigma_{\alpha+}},$$

and we have

$$\mathcal{L}_1(t) = -i\bar{\omega}_1\big[T_z\otimes\sigma_z + e^{i\bar{\omega}_1 t}T_-\otimes\sigma_+ + e^{-i\bar{\omega}_1 t}T_+\otimes\sigma_-,\cdot\big].$$

Again the exact expressions of the reduced model are algebraically complicated and computed with the help of a computer algebra system (SymPy). We here report a full derivation in the limit where ω_2 is the fastest timescale in the joint system.

Order 0 computations

It is straightforward to verify that the fast dynamics $\mathcal{L}_0$ drives the environment to a unique steady state

$$\bar{\rho}_E = \frac{\mathbb{1}_E + x_{\alpha,\infty}\sigma_{\alpha x}}{2},$$

with

$$x_{\alpha,\infty} = \frac{\kappa_{\alpha_+} - \kappa_{\alpha_-}}{\kappa_{\alpha_+} + \kappa_{\alpha_-}}.$$

For the following it is instructive to define

$$\kappa_{\alpha_\Sigma} := \kappa_{\alpha-} + \kappa_{\alpha+},$$
$$\kappa_{\alpha_\Delta} := \kappa_{\alpha-} - \kappa_{\alpha+},$$

so $x_{\alpha,\infty} = -\frac{\kappa_{\alpha_\Delta}}{\kappa_{\alpha_\Sigma}}$. Remark that the steady-state is independent of the driving amplitude Λ. For the projector $\mathcal{R}$ we have

$$\mathcal{R}(X_{\mathrm{TE}}) = \mathrm{Tr}_E(X_{\mathrm{TE}}) \otimes \bar{\rho}_E, \quad \forall X_{\mathrm{TE}}.$$

Order ε computations

- Equation (6.21) yields the following expression for the first-order reduced dynamics:

$$\begin{aligned}\varepsilon\mathcal{L}_{s,1}(\rho_s) \otimes \bar{\rho}_E &= \varepsilon\mathcal{R}(\overline{\mathcal{L}_1(\rho_s \otimes \bar{\rho}_E)}) \\ &= -ig\,\mathrm{Tr}_E([T_z \otimes \sigma_z, \rho_s \otimes \bar{\rho}_E]) \otimes \bar{\rho}_E \\ &= -igx_{\alpha,\infty}\sin(\alpha)[T_z, \rho_s] \otimes \bar{\rho}_E,\end{aligned}$$

  readily giving

$$\varepsilon\mathcal{L}_{s,1}(\rho_s) = -igx_{\alpha,\infty}\sin(\alpha)[T_z, \rho_s]. \tag{6.64}$$

- Equation (6.23) in turn yields

$$\begin{aligned}\varepsilon\mathcal{R}\mathcal{K}_1(\rho_s) &= \varepsilon\mathcal{R}\partial_t^{-1}\tilde{\mathcal{L}}_1\mathcal{K}_0(\rho_s) \\ &= -\frac{g}{\bar{\omega}_1}\,\mathrm{Tr}_E(\left[e^{i\bar{\omega}_1 t}T_- \otimes \sigma_+ - e^{-i\bar{\omega}_1 t}T_+ \otimes \sigma_-, \rho_s \otimes \bar{\rho}_E\right]) \otimes \bar{\rho}_E \\ &= -ix_{\alpha,\infty}\cos(\alpha)\frac{g}{2\bar{\omega}_1}\left[ie^{i\bar{\omega}_1 t}T_- - ie^{-i\bar{\omega}_1 t}T_+, \rho_s\right] \otimes \bar{\rho}_E,\end{aligned}$$

  where we have put the integration constant to zero as a gauge choice.

- Equation (6.25) yields a second part of $\mathcal{K}_1$:

$$\begin{aligned}\varepsilon\mathcal{L}_0(1-\mathcal{R})\bar{\mathcal{K}}_1(\rho_s) &= -\varepsilon(1-\mathcal{R})\bar{\mathcal{L}}_1\mathcal{K}_0(\rho_s) \\ &= ig[T_z \otimes \sigma_z, \rho_s \otimes \bar{\rho}_E] - ig\,\mathrm{Tr}_E([T_z \otimes \sigma_z, \rho_s \otimes \bar{\rho}_E]) \otimes \bar{\rho}_E \\ &= ig(T_z\rho_s \otimes \bar{\sigma}_z\bar{\rho}_E - \rho_s T_z \otimes \bar{\rho}_E\bar{\sigma}_z),\end{aligned}$$

with $\bar{\sigma}_z = \sigma_z - \mathrm{Tr}(\sigma_z \bar{\rho}_E)\mathbb{1}_E = \sigma_z - x_{\alpha,\infty}\sin(\alpha)\mathbb{1}_E$. Remark that taking the partial trace over E on the right-hand side gives zero, since $\mathrm{Tr}(\bar{\sigma}_z\bar{\rho}_E) = 0$. Hence $\mathcal{L}_0$ can be inverted to obtain, formally,

$$\varepsilon(1-\mathcal{R})\bar{\mathcal{K}}_1(\rho_s) = ig\big(T_z\rho_s \otimes \mathcal{L}_0^{-1}(\bar{\sigma}_z\bar{\rho}_E) - \rho_s T_z \otimes \mathcal{L}_0^{-1}(\bar{\rho}_E\bar{\sigma}_z)\big).$$

For this inversion we again use matrix representations in the Pauli basis.
In a rotated Pauli basis $(\cos(\alpha)\sigma_z - \sin(\alpha)\sigma_x,\ \sigma_y,\ \sigma_{\alpha x})$, we obtain the following matrix representation for $\mathcal{L}_0$:

$$[\mathcal{L}_0] = \begin{pmatrix} -\frac{\kappa_{\alpha_\Sigma}}{2} - 2\kappa_{\alpha x} & -\Lambda & 0 \\ \Lambda & -\frac{\kappa_{\alpha_\Sigma}}{2} - 2\kappa_{\alpha x} & 0 \\ 0 & 0 & -\kappa_{\alpha_\Sigma} \end{pmatrix},$$

with

$$\det[\mathcal{L}_0] = -\frac{\kappa_{\alpha_\Sigma}\left(4\Lambda^2 + \kappa_{\alpha_\Sigma}^2 + 8\kappa_{\alpha_\Sigma}\kappa_{\alpha x} + 16\kappa_{\alpha x}^2\right)}{4}.$$

For its inverse we obtain

$$\left[\mathcal{L}_0^{-1}\right] = \frac{1}{\det[\mathcal{L}_0]}\begin{pmatrix} \frac{\kappa_{\alpha_\Sigma}\left(\kappa_{\alpha_\Sigma}+4\kappa_{\alpha x}\right)}{2} & -\Lambda\kappa_{\alpha_\Sigma} & 0 \\ \Lambda\kappa_{\alpha_\Sigma} & \frac{\kappa_{\alpha_\Sigma}\left(\kappa_{\alpha_\Sigma}+4\kappa_{\alpha x}\right)}{2} & 0 \\ 0 & 0 & \Lambda^2 + \frac{\kappa_{\alpha_\Sigma}^2}{4} + 2\kappa_{\alpha_\Sigma}\kappa_{\alpha x} + 4\kappa_{\alpha x}^2 \end{pmatrix}.$$

In turn, $\bar{\sigma}_z\bar{\rho}_E$ takes the following vector representation in the Pauli basis:

$$[\bar{\sigma}_z\bar{\rho}_E] = \begin{pmatrix} -\frac{i\kappa_{\alpha_\Delta}\cos(\alpha)}{2\kappa_{\alpha_\Sigma}} \\ \frac{\cos(\alpha)}{2} \\ \frac{\left(-\kappa_{\alpha_\Delta}^2 + \kappa_{\alpha_\Sigma}^2\right)\sin(\alpha)}{2\kappa_{\alpha_\Sigma}^2} \\ 0 \end{pmatrix}.$$

Straightforward calculations then give

$$\left[\mathcal{L}_0^{-1}(\bar{\sigma}_z\bar{\rho}_E)\right] = \begin{pmatrix} \frac{\left(2\Lambda\kappa_{\alpha_\Sigma} + i\kappa_{\alpha_\Delta}\left(\kappa_{\alpha_\Sigma}+4\kappa_{\alpha x}\right)\right)\cos(\alpha)}{\kappa_{\alpha_\Sigma}\left(4\Lambda^2+\kappa_{\alpha_\Sigma}^2+8\kappa_{\alpha_\Sigma}\kappa_{\alpha x}+16\kappa_{\alpha x}^2\right)} \\ \frac{\left(2i\Lambda\kappa_{\alpha_\Delta} - \kappa_{\alpha_\Sigma}\left(\kappa_{\alpha_\Sigma}+4\kappa_{\alpha x}\right)\right)\cos(\alpha)}{\kappa_{\alpha_\Sigma}\left(4\Lambda^2+\kappa_{\alpha_\Sigma}^2+8\kappa_{\alpha_\Sigma}\kappa_{\alpha x}+16\kappa_{\alpha x}^2\right)} \\ \frac{\left(\kappa_{\alpha_\Delta} - \kappa_{\alpha_\Sigma}\right)\left(\kappa_{\alpha_\Delta}+\kappa_{\alpha_\Sigma}\right)\sin(\alpha)}{2\kappa_{\alpha_\Sigma}^3} \end{pmatrix}.$$

Focusing on the leading-order in $\frac{1}{\omega_2}$ yields

$$\left[\mathcal{L}_0^{-1}(\bar{\sigma}_z\bar{\rho}_E)\right] = \frac{1}{2\omega_2}\begin{pmatrix} 1 \\ \frac{i\kappa_{\alpha_\Delta}}{\kappa_{\alpha_\Sigma}} \\ \frac{\Delta\left(\kappa_{\alpha_\Delta}^2 - \kappa_{\alpha_\Sigma}^2\right)}{\kappa_{\alpha_\Sigma}^3} \end{pmatrix} + \mathcal{O}\left(\frac{1}{\omega_2^2}\right),$$

and further

$$\varepsilon(1-\mathcal{R})\bar{\mathcal{K}}_1(\rho_s) = i\frac{g}{\omega_2}\left[T_z \otimes \bar{M}_z, \rho_s \otimes \bar{\rho}_E\right],$$

with

$$\big[\bar{M}_z\big] = \begin{pmatrix} 1 \\ 0 \\ -\frac{\Delta}{\kappa_{\alpha_\Sigma}} \\ -\frac{\Delta\kappa_{\alpha_\Delta}}{\kappa_{\alpha_\Sigma}^2} \end{pmatrix} + \mathcal{O}\Big(\frac{1}{\omega_2}\Big).$$

- For the last part of $\mathcal{K}_1$, consider (6.26):

$$\varepsilon(\mathcal{L}_0 - \partial_t)(1-\mathcal{R})\tilde{\mathcal{K}}_1(\rho_s) = ig(1-\mathcal{R})\big(\big[e^{i\bar{\omega}_1 t}T_- \otimes \sigma_+ + e^{-i\bar{\omega}_1 t}T_+ \otimes \sigma_-, \rho_s \otimes \bar{\rho}_E\big]\big). \quad (6.65)$$

Introducing

$$\bar{\sigma}_+ := \sigma_+ - \mathrm{Tr}(\sigma_+\bar{\rho}_E)\mathbb{1}_E = \sigma_+ + \frac{\kappa_{\alpha_\Delta}\cos(\alpha)}{2\kappa_{\alpha_\Sigma}}\mathbb{1}_E,$$
$$\bar{\sigma}_- := \sigma_- - \mathrm{Tr}(\sigma_-\bar{\rho}_E)\mathbb{1}_E = \sigma_- + \frac{\kappa_{\alpha_\Delta}\cos(\alpha)}{2\kappa_{\alpha_\Sigma}}\mathbb{1}_E,$$

we can write the right-hand side of (6.65) as

$$ig\big[e^{i\bar{\omega}_1 t}T_- \otimes \bar{\sigma}_+ + e^{-i\bar{\omega}_1 t}T_+ \otimes \bar{\sigma}_-, \rho_s \otimes \bar{\rho}_E\big] = ige^{i\bar{\omega}_1 t}T_-\rho_s\otimes\bar{\sigma}_+\bar{\rho}_E + ige^{-i\bar{\omega}_1 t}T_+\rho_s\otimes\bar{\sigma}_-\bar{\rho}_E + \text{h.c.}$$

At this point we can split $(1-\mathcal{R})\tilde{\mathcal{K}}_1$ up into two parts:

$$\begin{aligned}\varepsilon(1-\mathcal{R})\tilde{\mathcal{K}}_1(\rho_s) &= ige^{i\bar{\omega}_1 t}(\mathcal{L}_0 - i\bar{\omega}_1)^{-1}(T_-\rho_s \otimes \bar{\sigma}_+\bar{\rho}_E) + ige^{-i\bar{\omega}_1 t}(\mathcal{L}_0 + i\bar{\omega}_1)^{-1}(T_+\rho_s \otimes \bar{\sigma}_-\bar{\rho}_E) + \text{h.c.} \\ &= ige^{i\bar{\omega}_1 t}T_-\rho_s \otimes (\mathcal{L}_0 - i\bar{\omega}_1)^{-1}(\bar{\sigma}_+\bar{\rho}_E) + ige^{-i\bar{\omega}_1 t}T_+\rho_s \otimes (\mathcal{L}_0 + i\bar{\omega}_1)^{-1}(\bar{\sigma}_-\bar{\rho}_E) + \text{h.c.}\end{aligned}$$

We obtain the following matrix representations:

$$\big[\bar{\sigma}_+\bar{\rho}_E\big] = \begin{pmatrix} \frac{i\left(\kappa_{\alpha_\Delta}\sin(\alpha)+\kappa_{\alpha_\Sigma}\right)}{4\kappa_{\alpha_\Sigma}} \\ -\frac{\kappa_{\alpha_\Delta}+\kappa_{\alpha_\Sigma}\sin(\alpha)}{4\kappa_{\alpha_\Sigma}} \\ \frac{\left(-\kappa_{\alpha_\Delta}^2+\kappa_{\alpha_\Sigma}^2\right)\cos(\alpha)}{4\kappa_{\alpha_\Sigma}^2} \end{pmatrix},$$
$$\big[\bar{\sigma}_-\bar{\rho}_E\big] = \begin{pmatrix} \frac{i\left(\kappa_{\alpha_\Delta}\sin(\alpha)-\kappa_{\alpha_\Sigma}\right)}{4\kappa_{\alpha_\Sigma}} \\ \frac{\kappa_{\alpha_\Delta}-\kappa_{\alpha_\Sigma}\sin(\alpha)}{4\kappa_{\alpha_\Sigma}} \\ \frac{\left(-\kappa_{\alpha_\Delta}^2+\kappa_{\alpha_\Sigma}^2\right)\cos(\alpha)}{4\kappa_{\alpha_\Sigma}^2} \end{pmatrix},$$

and

$$\Big[(\mathcal{L}_0 \mp i\bar{\omega}_1)^{-1}\Big] =$$
$$\begin{pmatrix} \frac{-2\kappa_{\alpha_\Sigma}-8\kappa_{\alpha x}\mp 4i\bar{\omega}_1}{4\Lambda^2+\kappa_{\alpha_\Sigma}^2+8\kappa_{\alpha_\Sigma}\kappa_{\alpha x}\pm 4i\kappa_{\alpha_\Sigma}\bar{\omega}_1+16\kappa_{\alpha x}^2\pm 16i\kappa_{\alpha x}\bar{\omega}_1-4\bar{\omega}_1^2} & \frac{4\Lambda}{4\Lambda^2+\kappa_{\alpha_\Sigma}^2+8\kappa_{\alpha_\Sigma}\kappa_{\alpha x}\pm 4i\kappa_{\alpha_\Sigma}\bar{\omega}_1+16\kappa_{\alpha x}^2\pm 16i\kappa_{\alpha x}\bar{\omega}_1-4\bar{\omega}_1^2} & 0 \\ -\frac{4\Lambda}{4\Lambda^2+\kappa_{\alpha_\Sigma}^2+8\kappa_{\alpha_\Sigma}\kappa_{\alpha x}\pm 4i\kappa_{\alpha_\Sigma}\bar{\omega}_1+16\kappa_{\alpha x}^2\pm 16i\kappa_{\alpha x}\bar{\omega}_1-4\bar{\omega}_1^2} & \frac{-2\kappa_{\alpha_\Sigma}-8\kappa_{\alpha x}\mp 4i\bar{\omega}_1}{4\Lambda^2+\kappa_{\alpha_\Sigma}^2+8\kappa_{\alpha_\Sigma}\kappa_{\alpha x}\pm 4i\kappa_{\alpha_\Sigma}\bar{\omega}_1+16\kappa_{\alpha x}^2\pm 16i\kappa_{\alpha x}\bar{\omega}_1-4\bar{\omega}_1^2} & 0 \\ 0 & 0 & \frac{1}{-\kappa_{\alpha_\Sigma}\mp i\bar{\omega}_1} \end{pmatrix}.$$

Again focusing on the leading-order in $\frac{1}{\omega_2}$, putting $\cos(\alpha)$ to 1, and using $\Lambda\sin(\alpha)=\Delta$, we obtain

$$(\mathcal{L}_0 - i\bar{\omega}_1)^{-1}(\bar{\sigma}_+\bar{\rho}_E) = -\left(\frac{1}{2\omega_2}B^\dagger + \frac{\cos(\alpha)}{2(\kappa_{\alpha_\Sigma}+i\bar{\omega}_1)}\left(\frac{\kappa_{\alpha_\Delta}}{\kappa_{\alpha_\Sigma}}\mathbb{1}_E + \sigma_{\alpha x}\right)\right)\bar{\rho}_E,$$
$$(\mathcal{L}_0 + i\bar{\omega}_1)^{-1}(\bar{\sigma}_-\bar{\rho}_E) = -\left(\frac{1}{2\omega_2}B + \frac{\cos(\alpha)}{2(\kappa_{\alpha_\Sigma}-i\bar{\omega}_1)}\left(\frac{\kappa_{\alpha_\Delta}}{\kappa_{\alpha_\Sigma}}\mathbb{1}_E + \sigma_{\alpha x}\right)\right)\bar{\rho}_E,$$

with

$$[B] = \begin{pmatrix} \frac{\Delta - \frac{i\kappa_{\alpha_\Sigma}}{2} - 2i\kappa_{\alpha x} - \bar{\omega}_1}{\omega_2} + \mathcal{O}\left(\frac{1}{\omega_2^2}\right) \\ -i + \mathcal{O}\left(\frac{1}{\omega_2}\right) \\ 0 \\ 0 \end{pmatrix}.$$

Putting all this together, we can write

$$\varepsilon(1-\mathcal{R})\tilde{\mathcal{K}}_1(\rho_s) = -i\frac{g}{2\Lambda}\left[e^{i\bar{\omega}_1 t}T_-\otimes B^\dagger + e^{-i\bar{\omega}_1 t}T_+\otimes B, \rho_s\otimes\bar{\rho}_E\right]$$
$$-i\frac{g\cos(\alpha)}{2\sqrt{\kappa_\Sigma^2+\bar{\omega}_1^2}}\left[\left(\frac{\kappa_\Sigma - i\bar{\omega}_1}{\sqrt{\kappa_\Sigma^2+\bar{\omega}_1^2}}e^{i\bar{\omega}_1 t}T_- + \frac{\kappa_\Sigma + i\bar{\omega}_1}{\sqrt{\kappa_\Sigma^2+\bar{\omega}_1^2}}e^{-i\bar{\omega}_1 t}T_+\right)\otimes\left(\frac{\kappa_{\alpha_\Delta}}{\kappa_{\alpha_\Sigma}}\mathbb{1}_E + \sigma_{\alpha x}\right), \rho_s\otimes\bar{\rho}_E\right].$$

Order ε^2 computations

For the second-order reduced dynamics, (6.28) for $k=2$ gives

$$\mathcal{K}_0\mathcal{L}_{s,2}(\rho_s) = \mathcal{L}_{s,2}(\rho_s)\otimes\bar{\rho}_E = \mathcal{R}\overline{\mathcal{L}_1\mathcal{K}_1}(\rho_s) = \mathrm{Tr}_E(\overline{\mathcal{L}_1\mathcal{K}_1}(\rho_s))\otimes\bar{\rho}_E$$

so

$$\mathcal{L}_{s,2}(\rho_s) = \mathrm{Tr}_E(\bar{\mathcal{L}}_1(1-\mathcal{R})\bar{\mathcal{K}}_1(\rho_s)) + \mathrm{Tr}_E\left(\overline{\tilde{\mathcal{L}}_1\mathcal{R}\tilde{\mathcal{K}}_1(\rho_s)}\right) + \mathrm{Tr}_E\left(\overline{\tilde{\mathcal{L}}_1(1-\mathcal{R})\tilde{\mathcal{K}}_1(\rho_s)}\right). \quad (6.66)$$

It is straightforward to verify that

$$\mathrm{Tr}_E(\bar{\mathcal{L}}_1(1-\mathcal{R})\bar{\mathcal{K}}_1(\rho_s)) = \frac{\bar{\omega}_1^2}{\omega_2}\mathrm{Tr}\big(\sigma_z\bar{M}_z\bar{\rho}_E\big)\big(T_z^2\rho_s - T_z\rho_s T_z\big) + \frac{\bar{\omega}_1^2}{\omega_2}\mathrm{Tr}\big(\sigma_z\bar{\rho}_E\bar{M}_z\big)\big(\rho_s T_z^2 - T_z\rho_s T_z\big),$$

and using

$$\mathrm{Tr}\big(\sigma_z\bar{M}_z\bar{\rho}_E\big) = \frac{i\kappa_{\alpha_\Delta}}{\kappa_{\alpha_\Sigma}} + \frac{\Delta^2\left(\frac{\kappa_{\alpha_\Delta}^2}{\kappa_{\alpha_\Sigma}^2}-1\right)}{\kappa_{\alpha_\Sigma}\omega_2} - \frac{\kappa_{\alpha_\Sigma}}{2\omega_2} - \frac{2\kappa_{\alpha x}}{\omega_2} + \mathcal{O}\left(\frac{1}{\omega_2^2}\right),$$

we obtain that

$$\mathrm{Tr}_E(\bar{\mathcal{L}}_1(1-\mathcal{R})\bar{\mathcal{K}}_1(\rho_s)) = \left(2\frac{\Delta^2\left(1-\frac{\kappa_{\alpha_\Delta}^2}{\kappa_{\alpha_\Sigma}^2}\right)}{\kappa_{\alpha_\Sigma}} + \kappa_{\alpha_\Sigma} + 4\kappa_{\alpha x}\right)\frac{\bar{\omega}_1^2}{\omega_2^2}\mathcal{D}_{T_z}(\rho_s) - i\frac{\kappa_{\alpha_\Delta}\bar{\omega}_1^2}{\kappa_{\alpha_\Sigma}\omega_2}\big[T_z^2,\rho_s\big] + \mathcal{O}\left(\frac{1}{\omega_2^3}\right).$$

For the second term in equation (6.66) we obtain

$$\mathrm{Tr}_E\left(\overline{\tilde{\mathcal{L}}_1\mathcal{R}\tilde{\mathcal{K}}_1(\rho_s)}\right) = -i\cos(\alpha)\frac{\kappa_{\alpha_\Delta}}{2\kappa_{\alpha_\Sigma}}\bar{\omega}_1\,\mathrm{Tr}(\sigma_+\bar{\rho}_E)[T_-,[T_+,\rho_s]]+i\cos(\alpha)\frac{\kappa_{\alpha_\Delta}}{2\kappa_{\alpha_\Sigma}}\bar{\omega}_1\,\mathrm{Tr}(\sigma_-\bar{\rho}_E)[T_+,[T_-,\rho_s]],$$

and using $\mathrm{Tr}(\sigma_+\bar{\rho}_E) = \mathrm{Tr}(\sigma_-\bar{\rho}_E) = -\frac{\kappa_{\alpha_\Delta}\cos(\alpha)}{2\kappa_{\alpha_\Sigma}}$ we get

$$\mathrm{Tr}_E\left(\overline{\tilde{\mathcal{L}}_1\mathcal{R}\tilde{\mathcal{K}}_1(\rho_s)}\right) = -i\left(\frac{\kappa_{\alpha_\Delta}}{\kappa_{\alpha_\Sigma}}\right)^2\frac{\cos^2(\alpha)}{4}\bar{\omega}_1[[T_+,T_-],\rho_s].$$

For the third term in equation (6.66) we obtain

$$\begin{aligned}\mathrm{Tr}_E\left(\overline{\tilde{\mathcal{L}}_1(1-\mathcal{R})\tilde{\mathcal{K}}_1(\rho_s)}\right) &= \frac{\bar{\omega}_1^2}{2\Lambda}\big(c_+(T_+\rho_sT_- - T_-T_+\rho_s) + c_-^*(T_-\rho_sT_+ - \rho_sT_+T_-)\big)\\ &+ \frac{\bar{\omega}_1^2}{2\Lambda}\big(c_-(T_-\rho_sT_+ - T_+T_-\rho_s) + c_+^*(T_+\rho_sT_- - \rho_sT_-T_+)\big)\\ &+ \frac{d\,\bar{\omega}_1^2}{\kappa_\Sigma^2+\bar{\omega}_1^2}(\kappa_\Sigma + i\bar{\omega}_1)(T_-\rho_sT_+ - T_-T_+\rho_s + T_+\rho_sT_- - \rho_sT_+T_-)\\ &+ \frac{d\,\bar{\omega}_1^2}{\kappa_\Sigma^2+\bar{\omega}_1^2}(\kappa_\Sigma - i\bar{\omega}_1)(T_+\rho_sT_- - T_+T_-\rho_s + T_-\rho_sT_+ - \rho_sT_-T_+),\end{aligned}$$

with

$$\begin{aligned}c_+ &= \mathrm{Tr}(\sigma_+B\bar{\rho}_E),\\ c_- &= \mathrm{Tr}\Big(\sigma_-B^\dagger\bar{\rho}_E\Big),\\ d &= \mathrm{Tr}(\sigma_+(\mathbb{1}_E+\sigma_{\alpha x})\bar{\rho}_E) = \mathrm{Tr}(\sigma_-(\mathbb{1}_E+\sigma_{\alpha x})\bar{\rho}_E) = \frac{1}{2}\left(1-\frac{\kappa_{\alpha_\Delta}^2}{\kappa_{\alpha_\Sigma}^2}\right)\cos^2(\alpha).\end{aligned}$$

Using

$$\begin{aligned}c_+ &= -\frac{i\kappa_{\alpha_\Delta}}{2\kappa_{\alpha_\Sigma}} + \frac{4i\Delta+\kappa_{\alpha_\Sigma}+4\kappa_{\alpha x}-2i\bar{\omega}_1}{4\omega_2} + \mathcal{O}\left(\frac{1}{\omega_2^2}\right),\\ c_- &= -\frac{i\kappa_{\alpha_\Delta}}{2\kappa_{\alpha_\Sigma}} + \frac{-4i\Delta+\kappa_{\alpha_\Sigma}+4\kappa_{\alpha x}+2i\bar{\omega}_1}{4\omega_2} + \mathcal{O}\left(\frac{1}{\omega_2^2}\right),\end{aligned}$$

we readily obtain

$$\begin{aligned}\mathrm{Tr}_E\left(\overline{\tilde{\mathcal{L}}_1(1-\mathcal{R})\tilde{\mathcal{K}}_1(\rho_s)}\right) &= \left(\frac{\kappa_{\alpha_\Sigma}d\,\bar{\omega}_1^2}{\kappa_{\alpha_\Sigma}^2+\bar{\omega}_1^2} + \frac{\kappa_{\alpha_\Sigma}+4\kappa_{\alpha x}}{4\omega_2^2}\bar{\omega}_1^2 + \mathcal{O}\left(\frac{1}{\omega_2^3}\right)\right)\big(\mathcal{D}_{T_-}(\rho_s)+\mathcal{D}_{T_+}(\rho_s)\big)\\ &+ i\left(\frac{\bar{\omega}_1^3\,d}{2\big(\kappa_{\alpha_\Sigma}^2+\bar{\omega}_1^2\big)} + \mathcal{O}\left(\frac{1}{\omega_2^2}\right)\right)[[T_+,T_-],\rho_s]\\ &+ i\left(\frac{\bar{\omega}_1^2}{4\omega_2}\frac{\kappa_{\alpha_\Delta}}{\kappa_{\alpha_\Sigma}} + \mathcal{O}\left(\frac{1}{\omega_2^3}\right)\right)[T_+T_- + T_-T_+,\rho_s].\end{aligned}$$

Summary

Putting all of the calculations of this section together, we obtain the following second-order reduced model.

For the slow dynamics we obtain an explicit Lindbladian model. We summarize its form while only keeeping the leading-order in $1/\omega_2$:

$$\begin{aligned}\mathcal{L}_{s,\varepsilon}(\rho_s) = &-i\big[\omega_{s,z,1}T_z + \omega_{s,z,2}T_z^2 + \omega_{s,\mathrm{c}}[T_+,T_-] + \omega_{s,\mathrm{a}}(T_+T_- + T_-T_+),\rho_s\big] \\ &+ \kappa_{s,z}\mathcal{D}_{T_z}(\rho_s) + \kappa_{s,\pm}\big(\mathcal{D}_{T_-} + \mathcal{D}_{T_+}\big) + \mathcal{O}\big(g\varepsilon^2\big)\end{aligned} \tag{6.67}$$

with

$$\omega_{s,z,1} = -\frac{\kappa_{\alpha_\Delta}}{\kappa_{\alpha_\Sigma}}\frac{g\Delta}{\omega_2}, \tag{6.68a}$$

$$\omega_{s,z,2} = \frac{\kappa_{\alpha_\Delta} g^2}{\kappa_{\alpha_\Sigma}\omega_2}, \tag{6.68b}$$

$$\omega_{s,\mathrm{c}} = \left(\frac{\kappa_{\alpha_\Delta}}{\kappa_{\alpha_\Sigma}}\right)^2 \frac{g^2}{4\bar{\omega}_1} - \frac{1}{4}\left(1 - \frac{\kappa_{\alpha_\Delta}^2}{\kappa_{\alpha_\Sigma}^2}\right)\frac{\bar{\omega}_1 g^2}{\kappa_{\alpha_\Sigma}^2 + \bar{\omega}_1^2}, \tag{6.68c}$$

$$\omega_{s,\mathrm{a}} = -\frac{\kappa_{\alpha_\Delta}}{\kappa_{\alpha_\Sigma}}\frac{g^2}{4\omega_2}, \tag{6.68d}$$

$$\kappa_{s,z} = \left(\frac{\Delta^2\left(1 - \frac{\kappa_{\alpha_\Delta}^2}{\kappa_{\alpha_\Sigma}^2}\right)}{\kappa_{\alpha_\Sigma}\omega_2} + \frac{\kappa_{\alpha_\Sigma}}{2\omega_2} + \frac{2\kappa_{\alpha x}}{\omega_2}\right)\frac{2g^2}{\omega_2}, \tag{6.68e}$$

$$\kappa_{s,\pm} = \frac{1}{2}\left(1 - \frac{\kappa_{\alpha_\Delta}^2}{\kappa_{\alpha_\Sigma}^2}\right)\frac{\kappa_{\alpha_\Sigma} g^2}{\kappa_{\alpha_\Sigma}^2 + \bar{\omega}_1^2} + \frac{g^2\left(\kappa_{\alpha_\Sigma} + 4\kappa_{\alpha x}\right)}{4\omega_2^2}\,. \tag{6.68f}$$

For the embedding of the slow subspace we obtain, up to second-order terms:

$$\mathcal{K}_\varepsilon(\rho_s) = e^{-iH_\varepsilon}(\rho_s \otimes \bar{\rho}_E)e^{iH_\varepsilon} + \mathcal{O}(\varepsilon^2), \tag{6.69}$$

with

$$H_\varepsilon := \frac{\kappa_{\alpha_\Delta}}{\kappa_{\alpha_\Sigma}}\frac{g}{2\bar{\omega}_1}H_s \otimes \mathbb{1}_E + \frac{g}{2\sqrt{\kappa_{\alpha_\Sigma}^2 + \bar{\omega}_1^2}}H_{s,\pm} \otimes (\mathbb{1}_E + \sigma_{\alpha,x}) - \frac{g}{\omega_2}T_z \otimes \bar{M}_z - \frac{g}{2\omega_2}H_s \otimes \sigma_y. \tag{6.70}$$

Here we have defined

$$H_s = ie^{-i\bar{\omega}_1 t}T_+ - ie^{i\bar{\omega}_1 t}T_-, \tag{6.71a}$$

$$H_{s,\pm} = \frac{(\kappa_{\alpha_\Sigma} - i\bar{\omega}_1)e^{i\bar{\omega}_1 t}T_- + (\kappa_{\alpha_\Sigma} + i\bar{\omega}_1)e^{-i\bar{\omega}_1 t}T_+}{\sqrt{\kappa_{\alpha_\Sigma}^2 + \bar{\omega}_1^2}}, \tag{6.71b}$$

$$\bar{M}_z = \sigma_{\alpha x} - \frac{\Delta}{\kappa_{\alpha_\Sigma}}\left(\frac{\kappa_{\alpha_\Delta}}{\kappa_{\alpha_\Sigma}}\mathbb{1}_E + \sigma_{\alpha x}\right). \tag{6.71c}$$

It is easy to verify that H_ε is Hermitian, since H_s, $H_{s,\pm}$ and $\bar{M}_z$ are Hermitian, and hence

$\mathcal{K}_\varepsilon$ can be written as an entangling unitary up to $\mathcal{O}(\varepsilon^2)$. In particular, $\mathcal{K}_\varepsilon$ is therefore a CPTP map up to $\mathcal{O}(\varepsilon^2)$ terms.

6.3.3.2 Discussion

We can summarize the DD benefits as follows

Corollary 6.4. *Consider the same notation* $\frac{1}{\Omega_2^k}$ *as in Thm. 6.2. The induced decoherence rates associated to the model* (6.63) *display the following asymptotic behavior for large* ω_2*:*

$$\kappa_{s,z} = \frac{(\kappa_{\alpha_\Sigma} + 4\kappa_{\alpha x})g^2}{\omega_2^2} + 2\frac{\Delta^2}{\omega_2^2}\frac{g^2\left(1-\frac{\kappa_{\alpha_\Delta}^2}{\kappa_{\alpha_\Sigma}^2}\right)}{\kappa_{\alpha_\Sigma}} + \frac{g^2}{\omega_2}\mathcal{O}\Big(\frac{1}{\Omega_2^2}\Big), \tag{6.72a}$$

$$\kappa_{s,\pm} = \frac{\kappa_{\alpha_\Sigma} g^2\left(1-\frac{\Delta^2}{\omega_2^2}\right)\left(1-\frac{\kappa_{\alpha_\Delta}^2}{\kappa_{\alpha_\Sigma}^2}\right)}{2\left(\kappa_{\alpha_\Sigma}^2+\bar{\omega}_1^2\right)} + \frac{g^2\left(4\kappa_{\alpha x}+\kappa_{\alpha_\Sigma}\right)}{4\omega_2^2} + \frac{g^2}{\omega_2}\mathcal{O}\Big(\frac{1}{\Omega_2^2}\Big), \tag{6.72b}$$

with $\kappa_{\alpha\Sigma} = \kappa_{\alpha-} + \kappa_{\alpha+}$ *and* $\kappa_{\alpha\Delta} = \kappa_{\alpha-} - \kappa_{\alpha+}$.

All these rates vanish in the limit $\bar{\omega}_1 \ll \omega_2; \bar{\omega}_1, \omega_2 \to \infty$, quantitatively confirming the DD benefits. These rates can be understood intuitively in a similar way as for (6.46). The extra factor $(1-\frac{\kappa_{\alpha_\Delta}^2}{\kappa_{\alpha_\Sigma}^2} = 1 - x_{\alpha,\infty}^2)$ accounts for the generally nonzero average value $x_{\alpha,\infty}$ of $\sigma_{\alpha x}$ in the TLS steady state. A larger $x_{\alpha,\infty}$ reduces the dissipative part at the expense of a deterministic, Hamiltonian term (see Section 6.3.3.1). In $\kappa_{s,\pm}$, we have now kept a term of order $1/\omega_2^2$ because the dominating contribution of $\kappa_{\alpha x}$ only appears at this order.

Taking into account the modified dissipation model for E therefore does affect induced decoherence for T, with significant changes if $\kappa_{\alpha-} \gg \kappa_{\alpha+}$ such that $\kappa_{\alpha\Delta} \simeq \kappa_{\alpha\Sigma}$. However, with a bath model at the origin of (6.62), this would only happen under very peculiar conditions. The standard conclusions with a reasonably flat bath noise spectrum, and $\alpha \ll 1$, are not too different from (6.46). They quantitatively confirm the DD benefits under this model too.

As a last point, also the Hamiltonian terms in (6.68) are suppressed asymptotically for large $\bar{\omega}_1$ and ω_2, although this was not explicitly part of our goal.

6.4 Summary

In this chapter, we have shown that one can apply coherent drives to an environment subsystem as to decouple it from a target system. As environment subsystem, we here focused on the benchmark case of a two-level system (TLS). The inevitable control imprecision that comes with acting on the environment subsystem was mitigated by building an extra timescale separation into the DD drives, while the DD drives can still be chosen to contain only two frequencies in the lab frame, and are hence straightforward to implement. Given the strongly dissipative nature of the TLS, the effectiveness of the DD driving was established by studying the dependence of the leading-order induced decoherence rates, as computed by the method of adiabatic elimination, as a function of the DD drive amplitudes. For this, in Section 6.3.1.2, the adiabatic elimination approach was extended to systems with periodic driving, providing a novel model reduction method that may be of independent interest. As a last consistency check with both the lossy nature of the TLS on the one hand, and the possibly very strong driving

amplitudes on the other hand, in Section 6.3.3, we rederived a corrected dissipation model for the TLS that explicitly takes into account the driving. The novel adiabatic elimination method of Section 6.3.1.2 was then applied to this case in Section 6.3.3.1, confirming the effectiveness of the DD driving to suppress the induced decoherence on the target also in this case. Addressing an environment subsystem with coherent drives thus provides a novel strategy for countering noise, whenever such a prominent environment subsystem can readily be identified as the main source of noise for the target device.

As a possible line of future work, one should set out to obtain an explicit convergence radius of the time-periodic adiabatic elimination approach in the small parameter ε, and set out to obtain explicit formulas for higher order terms in the reduced model for the specific case of bipartite systems. Another line of future work is to tailor the design of coherent DD drives for environment-side decoupling to existing quantum computing hardware where it could subsequently be implemented. A concrete experimental platform could further identify which specific classes of actions on the environment are the most viable, and a tailored driving scheme can be developed. While this chapter considered actions on the environment side to be coherent drives, the next chapter considers the limit of vanishing control precision, where applying such *noisy* drives can be considered as adding pure dissipation channels to the environment side.

Chapter 7

Purely dissipative decoupling

Dans le chapitre précédent, nous avons montré que d'appliquer des drives imprécis sur l'environment E peut diminuer la décohérence qu'il induit sur la cible T, par un mécanisme où l'environnement et le système cible sont découplé de manière dynamique. Ce chapitre a pour but de pousser cette idée plus loin: peut-on découpler les deux systèmes en forçant E avec un Hamiltonien dont l'amplitude est du bruit pur, ou, autrement dit, peut-on obtenir DD (c'est-à-dire réduire la décohérence induite) en rajoutant de la décohérence, sous la forme d'opérateurs de Lindblad, à l'environnement. Cette question est converti en un problème de contrôle où des différents taux de dissipation Markovienne de E sont considérés comme accordables dans une certaine gamme. Les taux de décohérence induits sur le système cible sont ensuite analysés en utilisant l'approche standard de l'élimination adiabatique pour des systèmes bipartites et stationnaires [6], dont les formules pertinentes sont rappelées dans la Section 7.2. Ensuite, nous établissons certaines propriétés des formules d'élimination adiabatique dans le contexte de la minimisation de la décohérence induite. Le reste du chapitre traite les cas physiques les plus pertinents pour un environnement à deux niveaux (TLS), pour un système cible général. Dans les sections 7.4.1 et 7.4.2, nous considérons que le TLS converge vers un état stable unique sous ses canaux de dissipation, et nous considérons le cas d'un couplage dispersif et presque résonnant au système cible respectivement. Pour le cas d'un couplage dispersif, le problème d'optimisation peut être décrit en termes d'une température de bain effective déterminant la décohérence induite sur la cible. Cette nouvelle étude confirme l'idée générale selon laquelle il est avantageux d'avoir soit l'environnement dans un état pur, soit dans un état hautement entropique. Dans le cas d'un couplage presque résonnant, il reste deux canaux de décohérence induite, et nous étudions si l'augmentation d'un seul canal de dissipation hermitien sur l'environnement peut le découpler de la cible arbitrairement bien. Ceci nous amène à une dernière situation considéré. Dans la Section 7.4.3 nous considérons le cas où le TLS ne converge pas vers un état stable unique, mais seulement une partie de ses cohérences subissent une décroissance rapide. Pour le cas d'un couplage dispersif avec la cible, nous confirmons à nouveau l'idée qu'un état stationnaire de l'environnement moyennement entropique correspond au scénario le plus défavorable pour la cible.

In Chapter 6 we showed that the addition of *imprecise* drives on E can decrease the decoherence that it induces on the target system T, as environment and target system can be seen to dynamically decouple. This chapter explores the question if we can push this idea one step further by asking: can we decouple the two systems by driving E with a Hamiltonian whose amplitude is *pure noise*. In other words, can we achieve dynamical decoupling (i.e. lower the

induced decoherence by definition) by *adding decoherence*, in the form of entropy-increasing Lindblad operators, to the environment? This question is translated into a control problem where various rates of Markovian dissipation channels of E are considered tunable within a given range. The induced decoherence rates on the target system are subsequently analyzed using the standard adiabatic elimination approach for stationary bipartite systems [6], the relevant formulas of which are given in Section 7.2. In Section 7.3 we establish general properties of the adiabatic elimination formulas in the context of the minimization of the induced decoherence. The remainder of the chapter addresses the most relevant physical settings for the case of a TLS environment, while the target system is kept fully general. In Sections 7.4.1 and 7.4.2 we assume the TLS to converge to a unique steady state under its dissipation channels, and we consider the case of a dispersive and almost-resonant coupling to the target system respectively. For the case of dispersive coupling, the optimization problem can be described in terms of one effective bath temperature determining the induced decoherence. This novel study confirms the general idea that it is good practice to have either minimal mixing on the environment, or rather maximal mixing. For the case of an almost-resonant coupling, two induced decoherence channels remain, and we investigate if increasing one Hermitian dissipation channel on the environment can decouple it from the target arbitrarily well. This brings us to a last setting considered. In Section 7.4.3 we consider the case where the TLS does not converge to a unique steady-state, but only part of its coherences undergo fast decay. For the case of a dispersive coupling to the target, we again confirm the idea that an intermediate amount of mixing on the environment corresponds to the worst-case scenario for the target.

7.1 Idea and control setting

We can calculate what happens when driving a quantum system with a Hamiltonian H whose amplitude is pure noise. For this, consider $\mathrm{d}W_t$ to be the increment at time t of a Brownian motion process, and denote the expectation value as $\mathbb{E}$:

$$\begin{aligned}\rho(t+\mathrm{d}t) =& \mathbb{E}\left(e^{-iH\mathrm{d}W_t}\rho(t)e^{iH\mathrm{d}W_t}\right)\\ =&\rho(t) - i[H,\rho(t)]\,\mathbb{E}(\mathrm{d}W_t) + \left(H\rho(t)H - \frac{H^2}{2}\rho(t) - \rho(t)\frac{H^2}{2}\right)\mathbb{E}(\mathrm{d}W_t^2)\\ =&\rho(t) + \mathcal{D}_H(\rho(t))\,\mathrm{d}t\ ,\end{aligned}$$

This leads to a Lindblad-type decoherence with Hermitian decoherence channel H for the state ρ. We can also consider adding non-Hermitian decoherence channels, such as the qubit relaxation channel $\mathcal{D}_{\sigma_-}$. Since engineering a very strong such cooling on the environment is known to be experimentally challenging, with active efforts to cool down quantum devices, a more reasonable setting of this type could be to let E be subject to

$$\mathcal{L}_E = \kappa_1(1+n_{th})\mathcal{D}_{\sigma_-} + \kappa_1 n_{th}\mathcal{D}_{\sigma_+}\ , \tag{7.1}$$

with lower and upper bounds on κ_1 and on n_{th}. The question is then which parameter choice minimizes the induced decoherence on T. We will see in Section 7.4.1 that under realistic constraints on n_{th}, a minimal value of n_{th} is not always the best choice. More generally, we can consider settings where the environment is subject to the dissipation

$$\mathcal{L}_E = \sum_k \kappa_k \mathcal{D}_{L_k}\ , \tag{7.2}$$

with the rates κ_k of the decoherence channels jointly tunable within a given set. The way in which these κ_k are tuned in practice can depend on the particular experiment. They might result from (noisy) drives and secular approximations, or for models such as (7.1) they might guide target values of κ_1 and n_{th} at the experiment design stage.

We will focus on a setting where the joint state of the system and environment are described by a master equation of the form (II.1) with $H_T = 0$, i.e.

$$\frac{d}{dt}\rho = -i[H_{TE} + H_E, \rho] + \mathcal{L}_E \ , \tag{7.3}$$

where now H_E is time-independent and fixed, and the Lindbladian $\mathcal{L}_E$ takes the form (7.2) with tunable κ_k associated to operators L_k acting on E only. Note that for notational convenience we have dropped the identities in $\mathbb{1}_T \otimes H_E$, $\mathbb{1}_T \otimes L_k$. With a slight abuse of notation, we will also use the same notation $\mathcal{L}_E$ when acting either on the E-state ρ_E alone, or on the total state ρ, as $\mathcal{L}_E$ acts as the identity on the target T in any case.

For a more general setting one may want to add a tunable H_E as in Chapter 6, but for a more efficient presentation we here chose to study both effects separately (see [43] for examples on tuning both the κ_k and a *time-independent* drive H_E). The question is again what values of the κ_k minimize the induced decoherence on T. In the absence of time-dependent drives, this induced decoherence can be computed directly with standard adiabatic elimination formulas [6]. We will show that the DD principle carries through at this purely dissipative level. Namely, selecting large values of κ_k, which strongly shake the environment, can lead to much less induced decoherence than selecting the κ_k which make the environment as pure as possible.

7.2 Adiabatic elimination formulas

The model (7.3) exhibits a clear timescale separation, where we assume that

$$\|\mathcal{L}_E\| \gg \|H_{\mathrm{TE}}\|.$$

Such a timescale separation can be leveraged to obtain a reduced model for the slowly-evolving degrees of freedom, through the general method of *adiabatic elimination* [5, 6]. The general purpose of adiabatic elimination is to eliminate all fast dissipative dynamics and only retain the degrees of freedom which evolve slowly, and which are thus best protected from decoherence. A standard setting is when a fast dissipating system (here E) is weakly coupled to another system (here T). Under appropriate conditions, the coupling induces a weak hybridization of the two subsystems, in which a subsystem close to T can be viewed as an autonomous system of state ρ_s undergoing slow decoherence and slow Hamiltonian dynamics. Approximation formulas have been developed to compute this hybridization and slow dynamics at various orders [6].

We here recall this standard adiabatic elimination setting to keep this chapter self-contained, and since this formulation is now standard in the literature, we report explicit formulas for the leading-order induced decoherence for bipartite systems, that are explicitly in the form of Lindbladian decoherence on the target system T. We focus on the formulas expressing the *dissipation* on ρ_s, thus induced on T by its coupling to E, taking the viewpoint that a constant hybridization and Hamiltonian can, by definition, be calibrated. The following procedure gives the dominating terms of the dissipation, provided the environment E alone has a unique steady state and the latter is strongly attractive compared to the coupling rate with T.

- Denote by $\bar{\rho}_E$ the unique steady state of the environment dynamics, thus taking $H_{TE} = 0$ in (7.3).
- Writing $H_{TE} = \sum_k T_k \otimes E_k$, for each E_k compute $\tilde{E}_k \bar{\rho}_E = E_k \bar{\rho}_E - \mathrm{Tr}(E_k \bar{\rho}_E)\bar{\rho}_E$.
- For each k, solve for a traceless operator Q_k in $-i[H_E, Q_k] + \mathcal{L}_E(Q_k) = -\tilde{E}_k \bar{\rho}_E$.
- Construct the matrix X with components $X_{k,j} = \mathrm{Tr}\Big(Q_j E_k^\dagger + E_j Q_k^\dagger\Big)$. This matrix is positive semidefinite and the induced decoherence on T, at second order adiabatic elimination, is given by

$$\mathcal{L}_{T,\mathrm{induced}} = \sum_k \mathcal{D}_{L_{T,k}}, \tag{7.4}$$

  where $L_{T,k} = \sum_j \Lambda_{j,k} T_j$ for any decomposition $X = \Lambda\Lambda^\dagger$.

  In particular, the Lindbladian describing the induced decoherence at this order of approximation involves jump operators $L_{T,k}$ that are simply linear combinations of the coupling operators T_j in H_{TE}. When there is only a single coupling term, $H_{TE} = T_1 \otimes E_1$, the scalar X readily yields the induced decoherence rate on the target T associated to the dissipation operator T_1.

We will use the result of this procedure to analyze how the dissipation induced on a target system can be reduced by varying the κ_k in (7.2). One should bear in mind that this is only the dominating term, in an approximate formula which is valid when dissipation on the environment is *fast*. Thus, conclusions encouraging us to consider minimal dissipation on the environment should be taken with caution. However, we will often encounter the conclusion that more dissipation in the environment is better for the target, and this regime is precisely the one well covered by the adiabatic elimination conditions.

Moreover, when treating the example of a TLS environment in more detail, we will illustrate how to adapt the adiabatic elimination procedure when the dynamics on E alone do not strongly attract it to a unique steady state. For this scenario, a more general approach formulated purely in terms of linear systems was introduced in Section 6.3.1.1. There, the slow degrees of freedom were parametrized by a general subspace of operators isomorphic to the kernel of the fast Lindbladian superoperator. One contribution of ours is to work out this more general approach for typical cases of a TLS-type environment, and to interpret the results. This will be the subject of Section 7.4.3.

7.3 Some general properties

Before proceeding with our running example of a TLS environment, we can give some general results on induced decoherence as computed with the above procedure. These are very much in line with the DD viewpoint that shaking the environment *more* should lead to *less* effect on the target system.

Proposition 7.1. *When H_E is fixed and is either of the same order as H_{TE} or smaller, multiplying all the κ_k by $\alpha > 1$ decreases the decoherence induced on the target system by a factor α. The same conclusion holds for any H_E if it can be multiplied by $\alpha > 1$ together with the κ_k.*

Proof. There are two ways to consider H_E. Under the first condition, we consider it as part of the perturbation, with a coupling $\tilde{H}_{TE} = H_{TE} + \mathbb{1}_T \otimes H_E$. Under the second condition, we consider it as part of the fast dynamics, and simply scale it together with all other Lindbladian contributions on the environment. In the adiabatic elimination procedure outlined in Section 7.2, both cases will not change $\bar{\rho}_E$ nor the $\tilde{E}_k$, yet the Q_k will become α times smaller. Thus the induced decoherence matrix X becomes α times smaller and so will the rates deduced from it. Another viewpoint is to make a change of timescale re-establishing the initial dissipation rate on the environment. In this new timescale, the coupling to the target system is decreased by α. According to the 2nd order adiabatic elimination formulas, the induced decoherence is *quadratic* in the coupling strength. Therefore, the lower coupling more than compensates for the change of timescale.

□

Proposition 7.2. *Consider $H_E = 0$ and that all the decoherence channels L_k on the environment are Hermitian and can be tuned individually. Then, as soon as adiabatic elimination conditions are satisfied, the diagonal elements of the induced decoherence matrix X are all minimized by taking the maximal value of κ_k for each L_k on the environment.*

Proof. We say "as soon as" because if the conditions are satisfied for some set of parameters, then they still hold when we increase the dissipation rates. We summarize the main ideas of the proof, whose full version is available in [42]. First, note that the unique steady state $\bar{\rho}_E$ of the environment under Hermitian L_k must be proportional to the identity, irrespective of the tuning choice. One can then formulate an optimization problem for each diagonal element of X, expressing the computations of the adiabatic elimination procedure outlined above as constraints with Lagrange multipliers. The necessary optimality conditions then ensure that X can be minimal only at the extreme values of the κ_k. A local analysis shows that if X depends on its value, then κ_k must be *maximal* to minimize the X-element. □

Since we know that X is positive semidefinite, the implications of Proposition 7.2 on its diagonal have similar consequences for the induced decoherence rates.

Finally, we can try to give criteria under which the induced decoherence on T can vanish at the limit where some κ_k become very large. Note that this is the limit where adiabatic elimination becomes increasingly more valid.

Proposition 7.3. *Consider* (7.3) *and let*

$$\mathcal{L}_E = \mathcal{L}_a + \tfrac{1}{\delta}\mathcal{L}_b \ ,$$

such that, for fixed $\mathcal{L}_a$ and $\mathcal{L}_b$, the κ_k remain within their authorized domain as δ tends to 0*. In other words, $\mathcal{L}_b$ is the part of the dissipation on E whose rates can possibly tend to infinity. If $\mathcal{L}_b$ has a unique steady state, then the decoherence induced on the target system vanishes as δ tends to* 0*. Otherwise, the dynamics can first be reduced by non-standard, first-order quantum adiabatic elimination of $\mathcal{L}_b$, before studying the potentially remaining induced decoherence on T.*

Proof. Note that the general procedure described in Section 6.3.1.1 makes no distinction between T and E subsystems, and simply eliminates the fastest dynamics.

First consider the case where $\mathcal{L}_b$ has a unique steady state. We can thus consider $\frac{1}{\delta}\mathcal{L}_b$ as the fast dynamics to eliminate, with respect to the slower dynamics including $\mathcal{L}_a$ and Hamiltonians H_E and H_{TE}. As $1/\delta$ gets infinite, the first-order adiabatic elimination yields finite contributions to the dynamics, while all higher-order terms become infinitesimal. One easily checks from the general procedure that, in presence of $\mathcal{L}_a$ and H_E possibly acting on E (thus *slow* dynamics with respect to $1/\delta$), the specific first-order adiabatic elimination formula outlined in Section 7.2 remains unchanged, i.e., the induced dynamics on T reduces to a Hamiltonian, without any decoherence.

Next consider the case where $\mathcal{L}_b$ would not have a unique steady state. In other words, as a superoperator, some of its eigenvalues would have 0 real part, while the other eigenvalues have negative real parts of the order $\mathcal{O}(1/\delta)$. From dynamical systems theory, we know that we can eliminate all the latter. Mathematically, this requires a separation between fast and slow dynamics not at the level of the Hilbert space, but rather at the level of operators ρ_E. More precisely, among the linear operators Q on E, we will distinguish a subspace of operators associated to fast decaying eigenvectors of $\mathcal{L}_b$, and a complementary subspace S_E associated to non-decaying eigenvectors. The "slow dynamics" with respect to $1/\delta$, after adiabatic elimination of $\mathcal{L}_b$, would describe the evolution of operators of the form

$$\rho_s = \sum_k c_k Q_{T,k} \otimes Q_{\tilde{E},k} \ ,$$

with $Q_{T,k}$ any linear operators on the target system T, $Q_{\tilde{E},k}$ belonging to S_E, and scalar coefficients c_k. The structure of such a subspace of operators can take various forms (see the examples in the Section 7.4.3). Nevertheless, the procedure for iteratively computing the reduced dynamics and the embedding of the true slow subspace at various orders follows the same procedure, since this was formulated at the general level of superoperators in Section 6.3.1.1. In particular, as for the case where $\mathcal{L}_b$ features a unique steady state, when $1/\delta$ becomes infinite, the first-order adiabatic elimination yields finite contributions to the slow dynamics, while all higher-order terms become infinitesimal. □

In order to give somewhat more substance to this second case, where $\mathcal{L}_b$ has no unique steady state, we mention the following general possibilities. More explicit examples are worked out in Section 7.4.3.

(*i*) In some cases, after adiabatic elimination of $\mathcal{L}_b$, the reduced dynamics may no longer involve a coupling between T and E. This means that there would be no induced decoherence on T when $1/\delta$ becomes infinite.

In most cases, however, a part of the Hamiltonian coupling H_{TE} will remain after eliminating $\mathcal{L}_b$. In this case, we can pursue the analysis of induced decoherence by a second round of adiabatic elimination, where we now consider part of the dynamics of $\mathcal{L}_a$ and H_E on the environment as the next-fastest timescale, while the interaction due to the original H_{TE} occurs at a yet slower timescale. Since this second time-scale separation remains finite, the second round of adiabatic elimination will generally have to be pursued at various orders, and obtaining a vanishing induced decoherence at all orders, as requested in Proposition 7.3, would be exceptional. One can readily start by treating the dominating order of dissipation.

(*ii*) Note that the "fast" dynamics implied by $\mathcal{L}_a$ and H_E after first-order adiabatic elimination of $\mathcal{L}_b$ does not necessarily features a unique steady state, even if $\mathcal{L}_a + \frac{1}{\delta}\mathcal{L}_b$ and H_E

together had a unique steady state on E for any finite δ. Indeed, when only scaling up $\frac{1}{\delta}\mathcal{L}_b$, it is possible that some eigenvalues of

$$\mathcal{L}_a + \tfrac{1}{\delta}\mathcal{L}_b - i[H_E, \cdot]$$

converge towards zero.

For instance, consider the case where E consists of two subsystems E_1 and E_2, with no dissipation on E_1 (we can take $\mathcal{L}_a = 0$), while $\mathcal{L}_b$ has a unique steady state on E_2, and H_E couples E_1 with E_2. In other words, E_1 and E_2 are in the standard form for adiabatic elimination of the dissipative subsystem E_2, coupled with a Hamiltonian to E_1, see Section 7.2. For any finite δ, the formulas of Section 7.2 for adiabatic elimination of $\mathcal{L}_b$ predict induced decoherence at second order on E_1, proportional to $H_E\delta$. Similarly to our observations for T coupled to E, as the dissipation $\frac{1}{\delta}\mathcal{L}_b$ increases, the induced decoherence E_1 *decreases*. At the limit of infinitesimal δ, the induced decoherence also vanishes and we no longer have a unique steady state on E_1.

(*iii*) Cases such as the example of point (*ii*) seem to require particular substructures of the environment dynamics. It is therefore rather common that after eliminating $\frac{1}{\delta}\mathcal{L}_b$, the remaining fast dynamics would still feature a unique steady state on E. In this case, the general procedure of adiabatic elimination can be pursued to obtain a reduced model on T alone.

If, furthermore, the dynamics after eliminating $\mathcal{L}_b$ takes the form of dissipation towards a unique steady state on what remains of E, with weak Hamiltonian coupling to T, then we can readily apply the second-order adiabatic elimination formulas of Section 7.2. This enables to directly either conclude to the negative (there remains induced decoherence even at second-order), or observe that at least the dominating order of dissipation vanishes (thus according to second-order adiabatic elimination formulas with finite $\mathcal{L}_a$).

(*iv*) To give a conclusive result, we must specify the setting even more. Like in point (*iii*), assume that the dynamics obtained after eliminating $\mathcal{L}_b$ indeed still takes the form of dissipation on E with a Hamiltonian coupling to T, while the dissipation on E leads to a unique steady state $\bar{\rho}_E$. If $\bar{\rho}_E$ is of full rank, then the induced decoherence cannot vanish. If $\bar{\rho}_E$ is of reduced rank, then the induced decoherence cannot vanish if the Hamiltonian coupling acts inside the space supported by $\bar{\rho}_E$.

This can be proven as follows.

We consider the system obtained after first-order adiabatic elimination of $\mathcal{L}_b$, according to the procedure of Section 6.3.1.1, as being the new target-environment model, and consider this to be the new starting situation, using the same notation. Without loss of generality, we assume that the E_k have been redefined such that $\mathrm{Tr}(E_k\,\bar{\rho}_E) = 0$, and also that each E_k is Hermitian. We denote by $\mathcal{L}_E$ the remaining Lindbladian dissipation on this reduced environment. The proof ideas are similar to those for proving positivity of X in the adiabatic elimination theory paper [6].

The goal is thus to investigate when the induced decoherence matrix X in Section 7.2 might vanish. Since X is nonnegative, we can focus on its diagonal. This means, we want each diagonal element $x_k := \mathrm{Tr}\Big(E_k(Q_k + Q_k^\dagger)\Big) = 0$. Here Q_k is the solution of

$\mathcal{L}_E(Q_k) = -E_k\bar{\rho}_E$. Using the integral formula for the inverse of a negative operator, we can write $Q_k = \int_0^\infty \exp[\mathcal{L}_E t](E_k\bar{\rho}_E)dt$ and thus

$$\begin{aligned} x_k &= \mathrm{Tr}\left(E_k \int_0^\infty \exp[\mathcal{L}_E t](E_k\bar{\rho}_E)dt\right) \\ &= \mathrm{Tr}\left(\int_0^\infty \exp[\mathcal{L}_E^* t](E_k)dt\ (E_k\bar{\rho}_E)\right) \\ &= \mathrm{Tr}(M_k\ (E_k\bar{\rho}_E)) \end{aligned}$$

where $\mathcal{L}^*$ denotes the dual superoperator of $\mathcal{L}$, and M_k must satisfy $\mathcal{L}_E^*(M_k) = -E_k$. Replacing E_k in this way in the expression of x_k and using that $\mathcal{L}_E(\bar{\rho}_E) = 0$, we get after a few computations:

$$x_k = \sum_j \mathrm{Tr}\Big([M_k, D_j]\ \bar{\rho}_E\ [M_k, D_j]^\dagger\Big)\ ,$$

with D_j the dissipation channel operators of $\mathcal{L}_E$.

Now, when $\bar{\rho}_E$ has full rank, the only way to get $x_k = 0$ is to have $[M_k, D_j] = 0$ for all D_j. But this would imply $\mathcal{L}_E^*(M_k) = 0$, contradicting how M_k must be computed. When $\bar{\rho}_E$ has reduced rank we apply the same argument to the block-diagonal part corresponding to the support of $\bar{\rho}_E$.

Remark 7.1. The example mentioned in (*ii*) above motivates some of the assumptions in Proposition 7.1 and Proposition 7.2. Indeed, considering this example for finite δ, we see that by ramping up $\frac{1}{\delta}\mathcal{L}_b$ we effectively induce lower dissipation on E_1. Thus if T was coupled to E_1, then its environment E_1 would become less dissipative, while if T was coupled to E_2 then its environment E_2 would become more dissipative. The induced effect on T must be inconclusive for determining what happens when ramping up only the dissipation channels in $\mathcal{L}_b$ without further knowledge of subsystems, and this fact can be attributed to the presence of a fixed $H_E \neq 0$, hence playing an essential role here.

As a practical take-away message, we see that it is important to consider which parts of E are directly coupled to T, and which parts are coupled indirectly. From a theoretical point of view, it may be interesting to consider networks of subsystems and study how varying parameters on each subsystem can affect the induced decoherence on a single target system T.

7.4 Minimizing decoherence induced by a TLS environment

We now focus in more detail on the case of a TLS environment. We consider Hermitian dissipation channels plus relaxation in a thermal environment:

$$\begin{aligned} \mathcal{L}_E &= \kappa_x\mathcal{D}_{\sigma_x} + \kappa_y\mathcal{D}_{\sigma_y} + \kappa_z\mathcal{D}_{\sigma_z} \\ &+ \kappa_-\mathcal{D}_{\sigma_-} + \kappa_+\mathcal{D}_{\sigma_+}\ . \end{aligned} \tag{7.5}$$

We assume that $\kappa_x, \kappa_y, \kappa_z$ are each tunable independently within a given interval e.g. $[\,\underline{\kappa}_x,\ \overline{\kappa}_x\,]$, while $\kappa_- = \kappa_1\,(1 + n_{\mathrm{th}})$, $\kappa_+ = \kappa_1\,n_{\mathrm{th}}$, with typically independent bounds on the coupling strength κ_1 and temperature characteristic n_{th}.

We will first consider two typical couplings between E and T, almost-resonant and dispersive respectively, while assuming that E always has a strongly attractive unique steady state. This happens as soon as two of the $\kappa_x, \kappa_y, \kappa_z$ assume significant nonzero values, or κ_1 assumes a significant nonzero value. When this is not the case, we can still apply adiabatic elimination but on a modified state space splitting. We illustrate what this implies for induced decoherence in a third example treated in Section 7.4.3. Note that for this example the induced decoherence cannot be calculated using the formula (7.4), as E does not feature a unique steady state on the fastest timescale. The formulas for the induced decoherence on the target will be derived using the general approach outlined in Section 6.3.1.1.

7.4.1 Dispersive coupling

As a first case, we consider (7.5) in conjunction with the coupling Hamiltonian:

$$H_{TE} = g\, T_z \otimes \sigma_z \ .$$

This models the typical situation of dipolar coupling between the target system and a TLS which is detuned far off-resonantly (dispersive coupling limit).

Following the adiabatic elimination procedure, we first compute the steady state of the fast TLS relaxation alone:

$$\bar{\rho}_E = \frac{\mathbb{1} + \bar{z}\sigma_z}{2} \quad \text{with} \quad \bar{z} = \tfrac{-\kappa_1}{(1+2n_{\rm th})\kappa_1 + 2(\kappa_x+\kappa_y)} \ .$$

From the coupling operator σ_z in E, we then compute

$$\tilde{\sigma}_z \bar{\rho}_E = \tfrac{1-\bar{z}^2}{2}\sigma_z \ .$$

Next we must solve

$$\mathcal{L}_E(Q) = -\tilde{\sigma}_z \bar{\rho}_E \ ,$$

which fortunately reduces to a scalar equation for the coefficient of σ_z. Plugging the solution into the formula for the dissipation matrix gives:

$$X = \tfrac{1-\bar{z}^2}{(1+2n_{\rm th})\kappa_1 + 2(\kappa_x+\kappa_y)} = \tfrac{4c_+c_-}{(c_++c_-)^3},$$

where

$$\begin{aligned} c_- &= (1+n_{\rm th})\kappa_1 + \kappa_x + \kappa_y, \\ c_+ &= n_{\rm th}\kappa_1 + \kappa_x + \kappa_y. \end{aligned}$$

This is the induced decoherence rate acting on T with the operator T_z. We note that κ_z plays no role here and we can make the following observations.

- One checks that, for any values of the other parameters, this induced decoherence rate decreases when κ_1 increases. Thus we should fix κ_1 at its maximal bound. For κ_1 dominating, the induced decoherence decreases as $1/\kappa_1$.
- Once the value of κ_1 is fixed, we can write $\kappa_x + \kappa_y = \kappa_1 n_b$ such that the induced decoherence becomes a function of $n_{\rm eff} = n_{\rm th} + n_b$ only, namely

$$X = \tfrac{4n_{\rm eff}(n_{\rm eff}+1)}{(2n_{\rm eff}+1)^3} \ . \tag{7.6}$$

This function increases from $X = 0$ at $n_{\text{eff}} = 0$ towards a maximum at $n_{\text{eff}} = \frac{\sqrt{3}-1}{2} \approx 0.366$, then slowly decreases to 0 as n_{eff} tends to infinity. Note that the adiabatic elimination approximation remains well valid near $n_{th} = 0$, as long as κ_1 itself is significantly larger than the coupling Hamiltonian.

Thus, the minimal induced decoherence will be obtained either at the lower or at the upper bound of n_{eff}, depending on their values. In other words, if a very low temperature can be achieved to keep the TLS close to its ground state then this is favorable, but otherwise it is better to make it as mixing as possible. The judge on "very low temperature" is the formula (7.6).

- Comparing to Propositions: There is nothing significant to say regarding Proposition 7.1.

  Proposition 7.2 applies rigorously when $\kappa_1 = 0$. Taking κ_1 very low, we would indeed be in a regime where $n_{\text{eff}} \approx n_b = \frac{\kappa_x+\kappa_y}{\kappa_1}$ is large, and we have seen that as soon as $n_b > \frac{\sqrt{3}-1}{2}$ it is beneficial to increase n_b, be it through κ_x or κ_y. On the contrary, if κ_1 is the dominating dissipation, then increasing κ_x or κ_y is not necessarily beneficial, as we may be in the regime $n_{\text{eff}} < \frac{\sqrt{3}-1}{2}$. This supports the condition that all dissipation operators must be Hermitian for Proposition 7.2 to apply.

  Regarding Proposition 7.3, as soon as κ_1 or two other dissipation channels can be increased indefinitely, we are in the situation where $\mathcal{L}_b$ has a unique steady state, and the induced decoherence goes to zero. There remains the case where only a single Hermitian channel can be increased indefinitely.

  - Taking this channel to be κ_z, the elimination of $\mathcal{L}_b$ yields a reduced state space of the type $p_g\rho_g \otimes |g\rangle\langle g| + (1-p_g)\rho_e \otimes |e\rangle\langle e|$ with free parameters p_g, ρ_g, ρ_e. The remaining fast dynamics will stabilize the value $p_g = \bar{p}_g$ independently of the coupled target system T. The case $\kappa_x = \kappa_y = n_{th} = 0$, thus with κ_1 stabilizing $|g\rangle\langle g|$ as $\bar{p}_g = 1$, would yield a rank-deficient $\bar{\rho}_E$ for which induced decoherence completely vanishes, even for finite κ_z. Otherwise, induced decoherence will always be finite.
  - Taking the possibly infinitely strong channel to be κ_x (the case of κ_y is analogous), the elimination of $\mathcal{L}_b$ yields a reduced space of similar form but with $|+\rangle, |-\rangle$ replacing $|g\rangle, |e\rangle$. At first-order adiabatic elimination of $\mathcal{L}_b$, the dispersive coupling Hamiltonian cancels and there only remains dissipation pushing p_+ towards $1/2$. Hence, driving κ_x (or κ_y) towards infinity is sufficient to drive the induced decoherence on T towards 0. Since this stabilizes the most mixed environment state, this might not have been the most intuitive guess. The choice of κ_y as possibly infinitely strong dissipation rate can be treated entirely analogously.

7.4.2 Almost-resonant coupling (Jaynes-Cummings)

As a second case, we consider (7.5) with adjustable κ_k, in conjunction with the fixed Hamiltonian:

$$\begin{aligned} H_E &= \tfrac{\Delta}{2}\mathbb{1} \otimes \sigma_z, && (7.7)\\ H_{TE} &= 2g(T_+ \otimes \sigma_- + T_- \otimes \sigma_+) && (7.8)\\ &= g(T_x \otimes \sigma_x + T_y \otimes \sigma_y)\ , \end{aligned}$$

where $T_x = T_- + T_+$ and $T_y = -i(T_- - T_+)$.

In the adiabatic elimination formulas, the fast TLS dynamics now includes both $H_E = \frac{\Delta}{2}\sigma_z$ and $\mathcal{L}_E$. Note that this remains valid when Δ is not dominating g, because we only need fast *dissipation*. However, when Δ does take a large value, it enables to have a strongly attractive unique TLS steady state even if only either κ_x or κ_y is nonzero. The steady state of the TLS alone is

$$\bar{\rho}_E = \frac{\mathbb{1} + \bar{z}\sigma_z}{2} \quad \text{, with} \quad \bar{z} = \tfrac{-\kappa_1}{(1+2n_{\rm th})\kappa_1 + 2(\kappa_x+\kappa_y)} \ .$$

For the coupling operators σ_x and σ_y, we then compute

$$\tilde{\sigma}_x\bar{\rho}_E = \tfrac{\sigma_x - i\bar{z}\sigma_y}{2} \quad , \quad \tilde{\sigma}_y\bar{\rho}_E = \tfrac{\sigma_y + i\bar{z}\sigma_x}{2} \ .$$

The solution of

$$-i[H_E, Q_k] + \mathcal{L}_E(Q_k) = -\tilde{\sigma}_k\bar{\rho}_E \tag{7.9}$$

for $k \in \{x, y\}$ is rather simple in Bloch coordinates, as the dynamics decouple the coefficients of σ_x, σ_y from those of $\sigma_z, \mathbb{1}$. We can thus write $Q_k = q_{k,x}\sigma_x + q_{k,y}\sigma_y$ and the left-hand side of (7.9) simply becomes

$$\tfrac{\Delta}{2}(q_{k,x}\sigma_y - q_{k,y}\sigma_x) - 2(\kappa_y + \kappa_z + (1+2n_{\rm th})\tfrac{\kappa_1}{4})q_{k,y}\sigma_y - 2(\kappa_x + \kappa_z + (1+2n_{\rm th})\tfrac{\kappa_1}{4})q_{k,x}\sigma_x \ .$$

Equating the components in σ_x and σ_y gives the solutions, from which we construct the dissipation matrix:

$$X = \frac{1}{\frac{\Delta^2}{4} + c_x c_y} \begin{pmatrix} c_y & i\bar{z}\frac{c_y+c_x}{2} \\ -i\bar{z}\frac{c_y+c_x}{2} & c_x \end{pmatrix} , \tag{7.10}$$

with

$$c_{x,y} = \kappa_{x,y} + \kappa_z + \tfrac{(1+2n_{\rm th})\kappa_1}{4}. \tag{7.11}$$

The parameters now define not only the induced decoherence rate, but also the associated decoherence operators (unitary combinations of T_x, T_y). Considering all decoherence operators equally detrimental for the target system, we typically look at the spectrum of X. We can make the following observations.

- Δ: increasing the detuning between E and T always decreases induced decoherence, and the induced decoherence can tend to zero as Δ becomes infinite.

- Reducing induced decoherence to zero at a finite value of Δ requires to increase *both* c_x and c_y to infinity — this will be impossible if only κ_x or κ_y can be made arbitrarily large.

- c_x, c_y, sum of rates: The sum of induced decoherence rates (trace of X) as a function of c_x, c_y shows a saddle point in $c_x = c_y = \Delta/2$, where induced decoherence is maximal as a function of $c_x + c_y$ and minimal as a function of $|c_x - c_y|$. Which side gives the minimum induced decoherence will thus depend on the available range of κ_k.

  In particular, for $\Delta = 0$, induced decoherence will always decrease when we increase $\kappa_z, \kappa_1, n_{\rm th}, \kappa_x, \kappa_y$. Thus even if we have the option $n_{\rm th} = 0$ to attract the TLS towards a pure state with only σ_-, it is better to not do so and rather increase the TLS temperature and other rates. This difference with respect to dispersive coupling of course stems from

the fact that a ground state for E, although pure, has no particular advantage under resonant coupling.

In particular, for large Δ, it appears better to choose low dissipation on the TLS. This can be understood as keeping the TLS frequency well-defined, avoiding any leakage towards the frequencies to which the target system is sensitive. However, one has to be careful of the fact that the formulas are only valid if the dissipation on the TLS remains significantly larger than its coupling to the target system. Otherwise, the correct viewpoint would rather be to first take the dispersive coupling limit and only then analyze the system, as in Section 7.4.1.

- c_x, c_y, individual rates: The difference between the two induced decoherence rates may be interesting to track when thinking e.g. of the interest of having biased noise [92]. At a fixed value of the sum, the difference increases when $|c_x - c_y|$ gets larger (thus κ_x increasing and κ_y decreasing), or when $\bar{z}^2$ gets larger (thus e.g. κ_1 increasing and n_{th} decreasing).

  In particular, for $\bar{z} = 0$, increasing only e.g. κ_x (and thus also c_x) decreases one induced decoherence rate as $\frac{1}{c_x + \Delta^2/(4c_y)}$ (thus to 0 as κ_x becomes infinite), but increases the other rate as $\frac{1}{c_y + \Delta^2/(4c_x)}$ (or thus at best keeps it constant if $\Delta = 0$, with finite limit $1/c_y$ as κ_x becomes infinite).

- Comparing to Propositions: The two regimes of Proposition 7.1 are clearly visible here. The one where Δ and all κ_k are scaled by α is trivial. The case where Δ is fixed shows two aspects: if Δ is small, then Proposition 7.1 says that it is better to increase the κ_k, as we see from the explicit formulae (7.10), (7.11) here. However, if Δ is fixed and large, then Proposition 7.1 does not apply and we see indeed with (7.10), (7.11) that the situation is not as clear. In other words, the saddle at $c_x = c_y = \Delta/2$ is precisely consistent with the first case of Proposition 7.1.

  Proposition 7.2 applies at least when $\Delta = 0$ (and $\kappa_1 = 0$). It predicts that in this setting, increasing any of κ_x or κ_y can only be beneficial. In the particular case $\bar{z} = 0$ mentioned in the previous item, we see how a nonzero Δ moderates this conclusion.

  Regarding Proposition 7.3, as for the dispersive coupling, the only nontrivial situation is when only a single Hermitian channel can be increased indefinitely.

  - Taking this channel to be κ_z, the elimination of $\mathcal{L}_b$ cancels the Hamiltonian coupling. Thus, although convergence on E happens at a finite rate as we need $\mathcal{L}_a$ to finally converge to $\bar{\rho}_E$, the induced decoherence on T goes to 0 as κ_z becomes infinite.
  - Taking this channel to be κ_x, the elimination of $\mathcal{L}_b$ yields a reduced state space of the type

    $$p_+\rho_+ \otimes |+\rangle\langle+| \; + \; (1-p_+)\rho_- \otimes |-\rangle\langle-| \,,$$

    with free parameters p_+, ρ_+, ρ_-. The remaining fast dynamics stabilizes $p_+ = 1/2$ independently of T, while the Hamiltonian coupling reduces to

    $$-ig[T_x, \rho_+] \otimes |+\rangle\langle+| + ig[T_x, \rho_-] \otimes |-\rangle\langle-| \;\; .$$

    Since $\bar{\rho}_E$ has full rank, the associated T_x-decoherence is bound to stay finite, even when κ_x tends to infinity.

7.4.3 Partly dissipative environment

We now address a setting where the fast dissipation of the TLS does not converge to a unique steady state $\bar{\rho}_E$. A typical example would be (7.5) where only κ_z is large. If this were the only dynamics on the environment E, then the dynamics of the target T would depend on the environment's initial state. The intermediate case which we discuss here assumes that we also have the unavoidable κ_-, κ_+ dissipation, but with rates comparable to the coupling rate g between E and T.

Since adiabatic elimination fundamentally works by splitting the fast and slow dynamics, it should thus eliminate only the fast decay of E under $\kappa_z \mathcal{D}_{\sigma_z}$, i.e. the quickly vanishing coherences among the $|e\rangle$ and $|g\rangle$ states of E. The κ_-, κ_+ dissipation on E has to be considered as a part of the slow dynamics, which are dynamics on both the target system as well as on the populations of $|e\rangle\langle e|$ or $|g\rangle\langle g|$ of the environment E. To illustrate what this implies for the target system, we again investigate the two typical cases for the Hamiltonian coupling between T and E.

7.4.3.1 Dispersive coupling:

First consider the case of a dispersive coupling:

$$\tfrac{d}{dt}\rho = \kappa_z \mathcal{D}_{\sigma_z}(\rho) + \kappa_- \mathcal{D}_{\sigma_-}(\rho) + \kappa_+ \mathcal{D}_{\sigma_+}(\rho) - ig[T_z \otimes \sigma_z, \rho] \,, \tag{7.12}$$

where we recall that κ_z is assumed much larger than the other rates. The set of states of the form $\rho = \rho_g \otimes |g\rangle\langle g| + \rho_e \otimes |e\rangle\langle e|$, corresponding to the set where $\mathcal{D}_{\sigma_z}(\rho) = 0$, is exactly invariant under (7.12). To consider only valid states ρ, the two slow variables ρ_g, ρ_e must both be positive semidefinite, but only the sum of their traces must amount to one, $\mathrm{Tr}(\rho_g) + \mathrm{Tr}(\rho_e) = 1$. The dynamics for the slow variables ρ_g and ρ_e are given by:

$$\begin{aligned} \tfrac{d}{dt}\rho_g &= \kappa_- \rho_e - \kappa_+ \rho_g + ig[T_z, \rho_g], \\ \tfrac{d}{dt}\rho_e &= \kappa_+ \rho_g - \kappa_- \rho_e - ig[T_z, \rho_e] \,. \end{aligned}$$

The dynamics for the populations of the $|g\rangle$ and $|e\rangle$ states are subsequently given by.

$$\tfrac{d}{dt}\,\mathrm{Tr}(\rho_g) = \kappa_-\,\mathrm{Tr}(\rho_e) - \kappa_+\,\mathrm{Tr}(\rho_g), \tag{7.13}$$

$$\tfrac{d}{dt}\,\mathrm{Tr}(\rho_e) = \kappa_+\,\mathrm{Tr}(\rho_g) - \kappa_-\,\mathrm{Tr}(\rho_e). \tag{7.14}$$

In particular, the environment populations admit steady state values where $\mathrm{Tr}(\rho_g) = w$ and $\mathrm{Tr}(\rho_e) = 1 - w$, with

$$w = \frac{\kappa_-}{\kappa_+ + \kappa_-}.$$

Now consider an initial separable state between T and E with steady-state environment populations, thus

$$\rho(0) = \rho_T(0) \otimes (w|g\rangle\langle g| + (1-w)|e\rangle\langle e|).$$

In the eigenbasis of T_z, the diagonal elements of $\rho_T(t) \coloneqq \mathrm{Tr}_E(\rho(t))$ are stationary. However, as ρ_g and ρ_e perform opposite rotations along the Hamiltonian T_z, the off-diagonal elements

of ρ_T will undergo induced decay. More precisely, for each pair of eigenvalues λ_j, λ_k of T_z, the corresponding off-diagonal elements will decay according to the eigenvalues

$$\begin{aligned} r_\pm &= -\kappa_1(n_{\rm th}+\tfrac{1}{2}) \pm \sqrt{\kappa_1^2(n_{\rm th}+\tfrac{1}{2})^2 - L^2 + i\kappa_1 L} \\ &\quad \text{with } \; L = g(\lambda_j - \lambda_k), j \neq k \; . \end{aligned}$$

(i) When L is small compared to $\kappa_1(n_{\rm th}+\frac{1}{2}) = (\kappa_- + \kappa_+)/2$, we would be in the regime where adiabatic elimination of E still holds. The slowest eigenvalue is approximately given by

$$r_- \simeq \; i\tfrac{L}{(2n_{\rm th}+1)} - \tfrac{L^2}{\kappa_1(2n_{\rm th}+1)}\big(\, 1 - \tfrac{1}{(2n_{\rm th}+1)^2} \,\big) \; .$$

In the second term we thus recover the typical expression for the induced decoherence rate in "$\tilde{g}^2/\kappa$" obtained by adiabatic elimination, with an additional factor accounting for the fact that induced decoherence vanishes if the environment is exclusively in $|g\rangle$. An optimization similar to the one in Section 7.4.1 applies, showing that the induced decay rate obtains a maximum for some intermediate value of $n_{\rm th}$, and tends to zero for both $n_{\rm th} \to 0$ and $n_{\rm th} \to \infty$. On the other hand, a larger dissipation rate κ_1 on E always implies lower induced decoherence on T.

(ii) When L is large compared to $\kappa_1(n_{\rm th}+\frac{1}{2})$, the eigenvalues are approximately given by

$$r_- \simeq \kappa_- + iq \text{ and } r_+ \simeq \kappa_+ - iq$$

for some real parameter q. Thus the induced decoherence rates on T are equal to the ones of excitation and loss on E, irrespective of the value of L. Contrary to the previous case, it is thus better to keep environment dissipation low.

These two cases in fact illustrate the transition from the situation where highest environment dissipation is better ("surprising" conclusion of adiabatic elimination) to the case where lowest dissipation is better (truly, i.e., not only according to the standard formula for adiabatic elimination of E, whose validity decreases). According to both these limiting cases, an intermediate dissipation rate appears worst. Note that we are comparing the environment dissipation to $L = g(\lambda_j - \lambda_k)$, so in a single multi-level system the different cases can arise for different off-diagonal elements. We were able to cover both limits (i) and (ii) by identifying an exact invariant subspace of operators of (7.12).

7.4.3.2 Resonant coupling:

Consider the model

$$\tfrac{d}{dt}\rho = \kappa_z \mathcal{D}_{\sigma_z}(\rho) + \kappa_- \mathcal{D}_{\sigma_-}(\rho) + \kappa_+ \mathcal{D}_{\sigma_+}(\rho) - ig[T_x \otimes \sigma_x + T_y \otimes \sigma_y, \; \rho] \; , \qquad (7.15)$$

where again only κ_z is assumed to be larger than the other rates. This specific Hamiltonian coupling does not allow for identifying the slow invariant subspace by simple inspection, so we apply the general adiabatic elimination procedure as outlined in Section 6.3.1.1.

The fast dynamics happens at timescale κ_z, while the slow timescales correspond to κ_-, κ_+, g. In the notation of Section 6.3.1.1, the fast dynamics corresponds to

$$\mathcal{L}_0 = \mathcal{D}_{\sigma_z},$$

and the projector $\mathcal{R}$ onto the kernel of $\mathcal{L}_0$ reads

$$\mathcal{R}(\rho) = \exp(+\infty\mathcal{D}_{\sigma_z})(\rho) = |g\rangle\langle g|\,\rho\,|g\rangle\langle g| + |e\rangle\langle e|\,\rho\,|e\rangle\langle e|\,.$$

We consider $\kappa_-/\kappa_z, \kappa_+/\kappa_z$ and g/κ_z to all be of order ε, where $\varepsilon \ll 1$. This leads us to write, still in the notation of Section 6.3.1.1,

$$\varepsilon\mathcal{L}_1 = -ig[T_x \otimes \sigma_x + T_y \otimes \sigma_y, \cdot] + \kappa_-\mathcal{D}_{\sigma_-} + \kappa_+\mathcal{D}_{\sigma_+}.$$

Following the general approach outlined in Section 6.3.1.1, we parameterize the slow dynamics in a space isomorphic with the image of $\mathcal{R}$, namely

$$\rho_s = (\rho_g,\ \rho_e),$$

where both ρ_g and ρ_e are positive semidefinite operators, with additionally $\mathrm{Tr}(\rho_g + \rho_e) = 1$. Indeed, the linear superoperator

$$\mathcal{K}_0(\rho_s) = \rho_g \otimes |g\rangle\langle g| + \rho_e \otimes |e\rangle\langle e|$$

maps this reduced state onto the steady states of the fast dynamics $\mathcal{D}_{\sigma_z}$. To obtain a reduced model for the slow dynamics, the general equations to be solved (see (6.12)) go as follows,

$$\mathcal{L}_0(\mathcal{K}_0(\rho_s)) = 0, \tag{7.16a}$$
$$\mathcal{K}_0(\mathcal{L}_{s,1}(\rho_s)) = \mathcal{L}_0(\mathcal{K}_1(\rho_s)) + \mathcal{L}_1(\mathcal{K}_0(\rho_s)), \tag{7.16b}$$
$$\mathcal{K}_0(\mathcal{L}_{s,2}(\rho_s)) + \mathcal{K}_1(\mathcal{L}_{s,1}(\rho_s)) = \mathcal{L}_0(\mathcal{K}_2(\rho_s)) + \mathcal{L}_1(\mathcal{K}_1(\rho_s)), \tag{7.16c}$$

leading to the truncated reduced model

$$\frac{\mathrm{d}}{\mathrm{d}t}\rho_s = \varepsilon\mathcal{L}_{s,1}(\rho_s) + \mathcal{L}_{s,2}(\rho_s), \tag{7.17a}$$
$$\rho(t) = \mathcal{K}_0(\rho_s(t)) + \varepsilon\mathcal{K}_1(\rho_s(t)). \tag{7.17b}$$

$\mathcal{K}_0$ was chosen such that (7.16a) is readily satisfied. Applying $\mathcal{R}$ to (7.16b), using $\mathcal{R}\mathcal{K}_0 = \mathcal{K}_0$, and $\mathcal{R}\mathcal{L}_0 = 0$, and finally splitting up

$$\mathcal{L}_{s,1} = (\mathcal{L}_{g,1}, \mathcal{L}_{e,1}),$$

we obtain

$$\begin{aligned}\varepsilon\mathcal{L}_{g,1}(\rho_s) \otimes |g\rangle\langle g| + \varepsilon\mathcal{L}_{e,1}(\rho_s) \otimes |e\rangle\langle e| = &-ig\mathcal{R}([T_x \otimes \sigma_x + T_y \otimes \sigma_y, \rho_g \otimes |g\rangle\langle g| + \rho_e \otimes |e\rangle\langle e|]) \\ &+ \mathcal{R}\big(\big(\kappa_-\mathcal{D}_{\sigma_-} + \kappa_+\mathcal{D}_{\sigma_+}\big)(\rho_g \otimes |g\rangle\langle g| + \rho_e \otimes |e\rangle\langle e|)\big).\end{aligned}$$

This can be worked out to yield

$$\begin{aligned}\varepsilon\,\mathcal{L}_{g,1}(\rho_s) = {}&\kappa_-\langle g|\mathcal{D}_{\sigma_-}(\rho_g \otimes |g\rangle\langle g| + \rho_e \otimes |e\rangle\langle e|)|g\rangle \\ &+ \kappa_+\langle g|\mathcal{D}_{\sigma_+}(\rho_g \otimes |g\rangle\langle g| + \rho_e \otimes |e\rangle\langle e|)|g\rangle,\end{aligned} \tag{7.18a}$$
$$\begin{aligned}\varepsilon\,\mathcal{L}_{e,1}(\rho_s) = {}&\kappa_-\langle e|\mathcal{D}_{\sigma_-}(\rho_g \otimes |g\rangle\langle g| + \rho_e \otimes |e\rangle\langle e|)|e\rangle, \\ &+ \kappa_+\langle e|\mathcal{D}_{\sigma_+}(\rho_g \otimes |g\rangle\langle g| + \rho_e \otimes |e\rangle\langle e|)|e\rangle,\end{aligned} \tag{7.18b}$$

while the Hamiltonian term maps $|g\rangle\langle g|$ and $|e\rangle\langle e|$ onto the coherences $|g\rangle\langle e|$ and $|e\rangle\langle g|$, which get annihilated by $\mathcal{R}$. Working out (7.18) one can show that the slow dynamics $\varepsilon\mathcal{L}_{s,1}$ corresponds to

$$\tfrac{d}{dt}\rho_g = \kappa_-\rho_e - \kappa_+\rho_g \ \ , \ \ \tfrac{d}{dt}\rho_e = \kappa_+\rho_g - \kappa_-\rho_e \ .$$

The coupling Hamiltonian thus vanishes and the state of T remains stationary in the sense that at this order, we have $\frac{d}{dt}(\rho_g + \rho_e) = 0$. Next, we go back to (7.16b) without applying $\mathcal{R}$, and parameterize $\mathcal{K}_1(\rho_s) = \sum_{j,k\in\{g,e\}} \mathcal{K}_{j,k}(\rho_s) \otimes |j\rangle\langle k|$. We observe that $\mathcal{K}_{e,e} \otimes |e\rangle\langle e|$ and $\mathcal{K}_{g,g} \otimes |g\rangle\langle g|$ cancel under the application of $\mathcal{L}_0 = \kappa_z\mathcal{D}_z$, and therefore these are gauge degrees of freedom associated to the non-uniqueness of the parameterization. We can choose $\mathcal{K}_{e,e} = \mathcal{K}_{g,g} = 0$ for simplicity. The remaining equations impose

$$\begin{aligned} \varepsilon\,\mathcal{K}_{e,g}(\rho_s) &= \tfrac{-g\,i}{2\kappa_z}(T_x\rho_g - \rho_e T_x + iT_y\rho_g - i\rho_e T_y) \\ \varepsilon\,\mathcal{K}_{g,e}(\rho_s) &= \tfrac{-g\,i}{2\kappa_z}(T_x\rho_e - \rho_g T_x + i\rho_g T_y - iT_y\rho_e) \ . \end{aligned}$$

This can be plugged into (7.16c), to which we again apply $\mathcal{R}$ in order to obtain $\mathcal{L}_{s,2}$. In the term $\mathcal{L}_1(\mathcal{K}_1(\rho_s))$, now only the Hamiltonian contribution remains as it can map terms of the form $|g\rangle\langle e|$, $|e\rangle\langle g|$ in $\mathcal{K}_1(\rho_s)$ to terms in $|e\rangle\langle e|$, $|g\rangle\langle g|$ which are conserved by $\mathcal{R}$. Simple algebraic computations then yield the combined dissipative dynamics

$$\tfrac{d}{dt}\tilde{\rho}_s = \varepsilon\mathcal{L}_{s,1}(\tilde{\rho}_s) + \tfrac{g^2}{\kappa_z}\mathcal{D}_{(T_x+iT_y)\otimes|e\rangle\langle g|}(\tilde{\rho}_s) + \tfrac{g^2}{\kappa_z}\mathcal{D}_{(T_x-iT_y)\otimes|g\rangle\langle e|}(\tilde{\rho}_s) \ ,$$

with $\tilde{\rho}_s = \mathcal{K}_0(\rho_s) = \rho_g \otimes |g\rangle\langle g| + \rho_e \otimes |e\rangle\langle e|$. The second-order dissipation combines $(|e\rangle, |g\rangle)$-population mixing on E with induced decoherence on T. To get an idea of the latter, we can consider the (quite academic) special case where $T_x = T_y$ and again obtain autonomous dynamics for T, namely

$$\tfrac{d}{dt}(\rho_g + \rho_e) = \tfrac{2g^2}{\kappa_z}\mathcal{D}_{T_x}(\rho_g + \rho_e) \ .$$

Taking $T_x = T_y$ implies that the target T only has one coupling term in $T_{x,y} \otimes (\sigma_x + \sigma_y)$ to the environment E. Thus, unlike for the case of a dispersive coupling, the induced decoherence (up to second order) appears to be independent of the values of κ_-, κ_+ as long as they remain small compared to κ_z.

7.5 Conclusions

Protecting a target quantum system from decoherence is a major objective towards quantum technology. Although quantum information loss on a target physical system is often expressed via Markovian decoherence channels, it is generally acknowledged that this only approximates more intricate dynamics of a larger system. Adding dynamics at the fast timescales of this larger system may thus allow us to change the induced decoherence on target, and ideally reduce it. This is essentially the idea behind $1/f$ noise countering methods, and spin echo or quantum dynamical decoupling (DD) techniques, among others.

In the present chapter, we have expressed the not-entirely-Markovian dissipation on the target system T as a Hamiltonian coupling to a low-dimensional environment subsystem E, which itself undergoes Markovian dissipation modeled by a Lindbladian. This is in line with initial DD settings [129], which focus on the Hamiltonian part of T and E.

The specificity of our proposal is to mitigate decoherence of the target system T by acting on the intermediate environment E instead of on T. Such actions cannot be assumed as

precise as on T, but they need not be. Indeed, we explicitly quantified how not only strong and imprecise coherent drives (see Chapter 6), but also adding pure decoherence channels on E (without introducing direct Markovian dissipation on T itself, see Chapter 7), effectively reduces the decoherence induced on T. Maybe surprisingly, we observe how only particular circumstances would favor a very pure environment as compared to a very mixing one.

The reduction of induced decoherence on T when increasing the decoherence on E should not be too unfamiliar to researchers that are familiar with adiabatic elimination and the "g^2/κ" formula. In light of this chapter, this is interpreted as a DD effect, which can arise both through coherent or incoherent driving, and which can be quantified precisely in both cases.

Indeed, having all fast dynamics on subsystem E, we can go beyond Hamiltonian decoupling arguments and develop an adiabatic elimination procedure yielding explicit formulas for the decoherence of T induced by dissipation on E. The resulting formulas are valid in the limit of strong dissipation on E, which is precisely the regime that is typically favored. They allow us to explicitly examine trade-offs and dependencies on parameters, as we illustrated on various typical settings when E is a two-level system.

The explicit formulas for the decoherence of the target developed in this chapter led to the conclusion that a fastly mixing environment is generally favorable for the target, as this leads to lower induced decoherence rates. This fact had not been studied previously in the context of multiple decoherence channel on the intermediate environment E. In Sections 7.4.1 and 7.4.3.1, we treated the only potential counterexample to this rule, which is the case of a dispersive coupling to the target. Using an optimization study we quantified how the achievable lower bounds on the temperature of the bath coupled to E allows to decide between keeping the steady state of E either as pure as possible, or as entropic as possible. The fact that an intermediate amount of mixing is the worst possible case for E was confirmed both in the standard setting of adiabatic elimination, where E is assumed to relax to a unique steady state on the fast timescale, but also in a novel setting where E is assumed to undergo only strong dephasing, as in Section 7.4.3.1. This last setting allowed for explicitly describing the crossover between the case where highest environment dissipation is favorable, which corresponds to the counterintuitive conclusion of this work, to the case where lowest dissipation on E is favorable.

For the case of a resonant coupling between T and E, we explicitly showed that increasing the dissipation rates of the environment is always beneficial, with typical dissipation channels on E. A last contribution of this work was to show this in the novel setting where the only dissipation channel on the fastest timescale is a dephasing channel (Section 7.4.3.2), again generalizing the adiabatic elimination methodology to eliminate more general degrees of freedom, to obtain explicit formulas for the induced decoherence.

Part III

Conclusions

This dissertation considers the study of periodically-driven open quantum systems, focusing on two main applications for countering physical noise in quantum devices: bosonic codes in Part I, and an extension of quantum dynamical decoupling in Part II.

The first part of the dissertation set out to provide solutions for strong-drive limitations of current superconducting circuits experiments. Our contribution was to identify that these limitations are due to chaotic classical dynamics leading to wave-packet explosion of the quantum state [23], and to provide a clear recipe of how to suppress this chaos for a ubiquitous single-mode nonlinear device: the inductively-shunted transmon. For this, $\beta = E_J/E_L$ was identified as the parameter governing the regularity of the operating regime. To display the remaining nonlinear potential of the device in the regular, non-chaotic regime, we demonstrated its ability for robust confinement of a manifold of Schrödinger cat states. These cat states have immediate applications in the field of bosonic encodings, which have been shown to allow for hardware-efficient quantum error correction. We showed that $\lambda = (2E_C/E_L)^{1/4}$ could be increased independently to enhance the spectral gap separating the cat state manifold from higher-excited states. These results were established using numerical Floquet-Markov simulations, focusing on the long-time asymptotic behavior of the system. Besides these results based on numerical simulations, we pursued the parallel path of studying the classical version of the system using analytical methods. In Section 4.3 we provided a theoretical explanation for the absence of chaos for small enough β in terms of the blocking of a main route to chaos of the classical system, namely the avoidance of period-doubling cascades. Once in the non-chaotic regime of small β, we characterized the bifurcation structure of $(n : m)$-subharmonics as a function of drive parameters (ν_d, ξ_d) using a first-order averaged model in Chapter 5.

This work focused on the case of a nonlinear oscillator with a single degree of freedom and periodic drives, for two main reasons. First, a single degree of freedom nonlinear oscillator with periodic drives corresponds to the minimal number of dimensions required for chaotic behavior to come into play. At the same time, nontrivial parametric processes can be activated on a single-mode nonlinear oscillator, as exemplified by the manifold of cat states created by an $(n : m)$-multi-photon process between oscillator and drive photons. As a last point, and crucial to the methodology employed throughout this dissertation, periodic systems benefit from specific theoretical tools developed for their analysis, namely the Poincaré map and the Floquet decomposition for the classical and quantum system respectively.

The premise of working quantum computational devices is to faithfully combine physical subsystems to perform complex operations on these interconnected systems. Superconducting devices are composed of multiple modes, and are coupled through nonlinear elements that require *multiple drives*, applied at different frequencies. Multiple drive tones are regularly used for spectroscopy experiments [81] probing AC-Stark shifts [115], quantum limited amplification [87], and additional drives are typically utilized for readout [55]. Pertaining to cat qubits in particular, reservoir engineering approaches considering a two-mode system [80, 82] involving two drive tones provide a mechanism for confining cat states, different from the one considered in this work. The main advantage of this approach is that they allow for allow active stabilization of the code space, using a dissipative mechanism. The main direction for further research related to Part I is to extend the developed methodology to *multi-mode systems, including multiple drives*. As a first step, an analogous change of variables as in Section 3.1.1 should be performed to identify an effective circuit parameter that governs the regularity of the operating regime for multi-mode systems. Such an analysis should be possible also for the case of other inductively-shunted junction models, such as the Asymmetrically-Threaded SQUID (ATS) [82]. Depending on the type of application, one or more effective circuit pa-

rameters should be identified that enhance the rate of a parametric process, analogous to the role of λ in this work.

As a second point of extension, the inclusion of drives at multiple frequencies calls for new theoretical techniques fulfilling the analogous role of Floquet theory (resp. the Poincaré map) in the case of periodic quantum (resp. classical) systems. On the quantum side, for periodic systems the Floquet decomposition allowed for studying the relevant asymptotic behavior in a way that is inaccessible via numerical time-domain simulations. An extension of Floquet theory to quasiperiodic driving [17, 96] should be considered that is amenable to a straightforward numerical implementation. On the classical side, averaging techniques for quasiperiodic systems [119] should be utilized to find the correct operating points. One theoretical reason for caution when applying these techniques, is the general problem of small denominators. Indeed, focusing on two incommensurate driving frequencies ω_2, ω_2, where ω_1/ω_2 is not a rational number, there are infinitely many points where a quasi-resonance condition is met,

$$k\omega_1 \simeq l\omega_2 \quad , \quad k, l \in \mathbb{Z},$$

potentially causing the corresponding perturbation series to blow up. For a fixed Diophantine condition [112] between ω_1 and ω_2, and in the Hamiltonian case, averaging techniques are available that lead to a remainder term that is exponentially small in the perturbation parameter [119]. Such perturbation series do not allow for sweeping the driving frequencies in a continuous manner a priori, as one would inevitably cross rational resonance conditions. This would thus pose extra technical challenges to be overcome for quasiperiodic driving.

As last point of possible future work pertaining to Part I, the present study could benefit from a more quantitative quantum-classical correspondence in a "mildly" chaotic regime. Indeed, we cannot expect very small chaotic regions in phase space to influence the behavior of the quantum system, as a physical quantum state cannot resolve arbitrary small regions in phase space. In the context of improving on the result of Section 4.3 to exclude chaotic behavior for the classical system, this would allow us to relax the goal to only *excluding sufficiently large chaotic areas* in phase space. While our result in Section 4.3 leveraged a finite nonzero dissipation rate, a study of the measure of chaotic regions could be performed in the dissipationless case, on the Hamiltonian system. There exists an arsenal of theoretical techniques for doing so in the field of KAM theory [2, 93, 94]. These techniques work by perturbing an integrable system away from integrability, characterized by a small perturbation parameter. Of particular relevance are averaging techniques [98] showing that if chaotic regions exist, these are typically exponentially small in the perturbation parameter [50, 61], provided the unperturbed (integrable) Hamiltonian system does not exhibit any homoclinic connections. We believe that such results could be leveraged when considering β as the perturbation parameter in our case.

In Part II of this dissertation, we proposed a novel, inherently robust strategy for countering noise for a practical class of target quantum devices. We proposed to drive an environment subsystem as to decouple it from the target system, whenever the former can readily be identified and presents the main source of noise for the target. The performance of such an approach was benchmarked for the case of a two-level-system (TLS) environment, and analyzed using adiabatic elimination [5, 8] techniques to obtain the main figure of merit, namely the induced decoherence rate of the target system. Having obtained explicit expressions for the induced decoherence rate for the typical physical settings, we performed an optimization study, revealing a general guideline: only very particular circumstances would favor a very

pure environment as compared to a very mixing one.

As a possible line of future work, this environment-side decoupling approach could be tailored to existing quantum computing hardware where it could subsequently be implemented. The approaches of Chapters 6 and 7 consider two different limits of ways in which one can expect to be able to drive an environment subsystem: coherent drives with considerable control imprecision versus the limit of driving the environment with pure noise. It should be clear that actions with an intermediate degree of control imprecision should benefit from the same DD effect. A concrete experimental platform could further identify which specific classes of actions on the environment are the most viable, and a tailored driving scheme can be developed.

A final point of future work is in the context of model reduction based on physical timescale separations. In Section 6.3.1.2, we extended the adiabatic elimination method to the case of periodic driving, while in Section 7.4.3 an extension was made to a double timescale separation, where the environment subsystem shows a fast dissipative decay, and a slower one. In this case, we have given examples where the two different timescale separations are used one after the other to obtain a reduced model in two consecutive steps. The characterization of the interplay between different such timescale separations has not been exhaustively explored in the literature, and clear rules need to be established for when one can eliminate fast timescales in a certain order, or if all have to be eliminated together. Such a study is key for checking the validity of present day successive approximations. A concrete problem that has drawn our attention is that of a rapidly oscillating Lindbladian system, where the driving is significantly faster than the dissipation rate. It is an open question whether one can perform an averaging-type perturbation method while preserving the structure of Markovian open quantum systems, i.e. use a change of variables that preserves positivity of the quantum state, and obtain a stationary *Lindbladian* model with positive dissipation rates. Previous work shows that such a *Floquet Lindbladian* typically exists in the adiabatic limit of slowly varying drives, and in the limit of fast driving [113, 114] for the exact system (corresponding to averaging up to infinite order). The gauge choice of the averaging transformation that yields finite perturbative expansions of Lindblad form has yet to be determined, if such a gauge choice exists in general.

We conclude that while we have made concrete contributions to the problem of strong-drive limitations of current superconducting circuits experiments, and provided a novel strategy for countering noise with a dynamical decoupling methodology, the work presented in this dissertation could in turn serve as the basis for exploring open questions towards the analysis of open quantum systems and novel model reduction methods.

Bibliography

[1] D. Aharonov and M. Ben-Or. Fault-Tolerant Quantum Computation with Constant Error Rate. *SIAM Journal on Computing*, 38(4):1207–1282, jul 2008. ISSN 00975397. doi: 10.1137/S0097539799359385. URL https://epubs.siam.org/doi/epdf/10.1137/S0097539799359385.

[2] V. I. Arnold. Proof of a theorem of A. N. Kolmogorov on the invariance of quasi-periodic motions under small perturbations of the Hamiltonian. In *Collected Works: Representations of Functions, Celestial Mechanics and KAM Theory, 1957 - 1965*, pages 267–294. Springer, Berlin, Heidelberg, 2009. ISBN 978-3-642-01742-1. doi: 10.1007/978-3-642-01742-1_21. URL https://link.springer.com/chapter/10.1007/978-3-642-01742-1_21.

[3] F. Arute, K. Arya, R. Babbush, D. Bacon, J. C. Bardin, R. Barends, R. Biswas, S. Boixo, F. G. S. L. Brandao, D. A. Buell, B. Burkett, Y. Chen, Z. Chen, B. Chiaro, R. Collins, W. Courtney, A. Dunsworth, E. Farhi, B. Foxen, A. Fowler, C. Gidney, M. Giustina, R. Graff, K. Guerin, S. Habegger, M. P. Harrigan, M. J. Hartmann, A. Ho, M. Hoffmann, T. Huang, T. S. Humble, S. V. Isakov, E. Jeffrey, Z. Jiang, D. Kafri, K. Kechedzhi, J. Kelly, P. V. Klimov, S. Knysh, A. Korotkov, F. Kostritsa, D. Landhuis, M. Lindmark, E. Lucero, D. Lyakh, S. Mandrà, J. R. McClean, M. McEwen, A. Megrant, X. Mi, K. Michielsen, M. Mohseni, J. Mutus, O. Naaman, M. Neeley, C. Neill, M. Y. Niu, E. Ostby, A. Petukhov, J. C. Platt, C. Quintana, E. G. Rieffel, P. Roushan, N. C. Rubin, D. Sank, K. J. Satzinger, V. Smelyanskiy, K. J. Sung, M. D. Trevithick, A. Vainsencher, B. Villalonga, T. White, Z. J. Yao, P. Yeh, A. Zalcman, H. Neven, and J. M. Martinis. Quantum supremacy using a programmable superconducting processor. *Nature*, 574 (7779):505–510, 2019. ISSN 1476-4687. doi: 10.1038/s41586-019-1666-5. URL https://doi.org/10.1038/s41586-019-1666-5.

[4] R. Azouit, A. Sarlette, and P. Rouchon. Convergence and adiabatic elimination for a driven dissipative quantum harmonic oscillator. *Proceedings of the IEEE Conference on Decision and Control*, 2016-Febru:6447–6453, 2016. ISSN 07431546. doi: 10.1109/CDC.2015.7403235. URL https://doi.org/10.1109/CDC.2015.7403235.

[5] R. Azouit, A. Sarlette, and P. Rouchon. Adiabatic elimination for open quantum systems with effective Lindblad master equations. In *2016 IEEE 55th Conference on Decision and Control, CDC 2016*, pages 4559–4565, 2016. ISBN 9781509018376. doi: 10.1109/CDC.2016.7798963. URL https://doi.org/10.1109/CDC.2016.7798963.

[6] R. Azouit, F. Chittaro, A. Sarlette, and P. Rouchon. Towards generic adiabatic elim-

ination for bipartite open quantum systems. *Quantum Sci. Technol*, 2, 2017. doi: 10.1088/2058-9565/aa7f3f. URL https://doi.org/10.1088/2058-9565/aa7f3f.

[7] R. Azouit, F. Chittaro, A. Sarlette, and P. Rouchon. Structure-preserving adiabatic elimination for open bipartite quantum systems. In *IFAC-PapersOnLine*, volume 50, pages 13026–13031. Elsevier, jul 2017. doi: 10.1016/j.ifacol.2017.08.2000. URL https://doi.org/10.1016/j.ifacol.2017.08.2000.

[8] R. Azouit, F. Chittaro, A. Sarlette, and A. Sarlette. Towards generic adiabatic elimination for bipartite open quantum systems, 2017. ISSN 23318422. URL https://arxiv.org/abs/1704.00785.

[9] F. L. Bauer and C. T. Fike. Norms and exclusion theorems. *Numerische Mathematik 1960 2:1*, 2(1):137–141, dec 1960. ISSN 0945-3245. doi: 10.1007/BF01386217. URL https://link.springer.com/article/10.1007/BF01386217.

[10] C. H. Bennett and G. Brassard. Quantum cryptography: Public key distribution and con tos5. In *Proceedings of the International Conference on Computers, Systems and Signal Processing*, 1984.

[11] F. Bensch, H. J. Korsch, B. Mirbach, and N. Ben-Tal. EBK quantization of quasi-energies. *Journal of Physics A: Mathematical and General*, 25(24):6761–6777, dec 1992. ISSN 03054470. doi: 10.1088/0305-4470/25/24/027. URL https://iopscience.iop.org/article/10.1088/0305-4470/25/24/027.

[12] C. Berke, E. Varvelis, S. Trebst, A. Altland, and D. P. DiVincenzo. Transmon platform for quantum computing challenged by chaotic fluctuations. dec 2020. URL https://arxiv.org/abs/2012.05923.

[13] A. Blais, A. L. Grimsmo, S. M. Girvin, and A. Wallraff. Circuit quantum electrodynamics. *Reviews of Modern Physics*, 93(2), 2021. ISSN 15390756. doi: 10.1103/RevModPhys.93.025005. URL https://journals.aps.org/rmp/abstract/10.1103/RevModPhys.93.025005.

[14] A. Blais, A. L. Grimsmo, S. M. Girvin, and A. Wallraff. Circuit quantum electrodynamics. *Reviews of Modern Physics*, 93(2):025005, may 2021. ISSN 15390756. doi: 10.1103/RevModPhys.93.025005. URL https://journals.aps.org/rmp/abstract/10.1103/RevModPhys.93.025005.

[15] S. Blanes, F. Casas, J. A. Oteo, and J. Ros. The Magnus expansion and some of its applications. *Physics Reports*, 470(5-6):151–238, 2009. ISSN 03701573. doi: 10.1016/j.physrep.2008.11.001. URL http://www.sciencedirect.com/science/article/pii/S0370157308004092.

[16] S. Blanes, F. Casas, J. A. Oteo, and J. Ros. The Magnus expansion and some of its applications. *Physics Reports*, 470(5):151–238, Jan. 2009. ISSN 0370-1573. doi: 10.1016/j.physrep.2008.11.001. URL https://www.sciencedirect.com/science/article/pii/S0370157308004092.

[17] P. M. Blekher, H. R. Jauslin, and J. L. Lebowitz. Floquet Spectrum for Two-Level Systems in Quasiperiodic Time-Dependent Fields. *Journal of Statistical Physics*, 68, 1992. doi: 10.1007/BF01048846. URL https://doi.org/10.1007/BF01048846.

[18] H. P. Breuer and M. Holthaus. A semiclassical theory of quasienergies and Floquet wave functions. *Annals of Physics*, 211(2):249–291, nov 1991. ISSN 1096035X. doi: 10.1016/0003-4916(91)90206-N. URL https://www.sciencedirect.com/science/article/pii/000349169190206N.

[19] H.-P. Breuer and F. Petruccione. *The Theory of Open Quantum Systems*. Oxford University Press, Oxford, 2007. ISBN 978-0-19-921390-0. doi: 10.1093/acprof:oso/9780199213900.001.0001. URL https://oxford.universitypressscholarship.com/10.1093/acprof:oso/9780199213900.001.0001/acprof-9780199213900.

[20] M. Burgelman, P. Forni, and A. Sarlette. Quantum dynamical decoupling by shaking the close environment, 2022.

[21] P. Campagne-Ibarcq, A. Eickbusch, S. Touzard, E. Zalys-Geller, N. E. Frattini, V. V. Sivak, P. Reinhold, S. Puri, S. Shankar, R. J. Schoelkopf, L. Frunzio, M. Mirrahimi, and M. H. Devoret. Quantum error correction of a qubit encoded in grid states of an oscillator. *Nature*, 584(7821):368–372, 2020. ISSN 14764687. doi: 10.1038/s41586-020-2603-3. URL https://www.nature.com/articles/s41586-020-2603-3.

[22] T. Capelle, E. Flurin, E. Ivanov, J. Palomo, M. Rosticher, S. Chua, T. Briant, P.-F. Cohadon, A. Heidmann, T. Jacqmin, and S. Deléglise. Probing a Two-Level System Bath via the Frequency Shift of an Off-Resonantly Driven Cavity. *Physical Review Applied*, 13 (3):034022, Mar. 2020. doi: 10.1103/PhysRevApplied.13.034022. URL https://link.aps.org/doi/10.1103/PhysRevApplied.13.034022.

[23] G. G. Carlo, G. Benenti, and D. L. Shepelyansky. Dissipative Quantum Chaos: Transition from Wave Packet Collapse to Explosion. *Physical Review Letters*, 95(16):164101, Oct. 2005. doi: 10.1103/PhysRevLett.95.164101. URL https://link.aps.org/doi/10.1103/PhysRevLett.95.164101.

[24] A. Z. Chaudhry and J. Gong. Decoherence control: Universal protection of two-qubit states and two-qubit gates using continuous driving fields. *Physical Review A*, 85(1), 2012. ISSN 10502947. doi: 10.1103/PhysRevA.85.012315. URL https://doi.org/10.1103/PhysRevA.85.012315.

[25] P. Chen. Geometric continuous dynamical decoupling with bounded controls. *Physical Review A*, 73(2), 2006. ISSN 10502947. doi: 10.1103/PhysRevA.73.022343. URL https://doi.org/10.1103/PhysRevA.73.022343.

[26] R. Y. Chiao, M. J. Feldman, D. W. Peterson, B. A. Tucker, and M. T. Levinsen. Phase instability noise in Josephson junctions. In *AIP Conference Proceedings*, volume 44, pages 259–263. AIP, 2008. doi: 10.1063/1.31349. URL http://aip.scitation.org/doi/abs/10.1063/1.31349.

[27] J. M. Chow, J. M. Gambetta, A. W. Cross, S. T. Merkel, C. Rigetti, and M. Steffen. Microwave-activated conditional-phase gate for superconducting qubits. *New Journal of Physics*, 15(11):115012, nov 2013. ISSN 13672630. doi: 10.1088/1367-2630/15/11/115012. URL https://iopscience.iop.org/article/10.1088/1367-2630/15/11/115012.

[28] E. A. Coddington and N. Levinson. *Theory of Ordinary Differential Equations*. McGraw-Hill, 1955. ISBN 978-0-07-099256-6.

[29] J. Cohen and M. Mirrahimi. Dissipation-induced continuous quantum error correction for superconducting circuits. *Physical Review A*, 90(6):62344, dec 2014. doi: 10.1103/PhysRevA.90.062344. URL https://link.aps.org/doi/10.1103/PhysRevA.90.062344.

[30] C. Cohen-Tannoudji, J. Dupont-Roc, and G. Grynberg. *Processus d'interaction entre photoons et atomes*. EDP Sciences/CNRS Editions, 2001.

[31] S. Crovisier, E. Pujals, and C. Tresser. Mildly dissipative diffeomorphisms of the disk with zero entropy. 2020. URL http://arxiv.org/abs/2005.14278.

[32] D. D'Humieres, M. R. Beasley, B. A. Huberman, and A. Libchaber. Chaotic states and routes to chaos in the forced pendulum. *Physical Review A*, 26(6):3483–3496, dec 1982. ISSN 10502947. doi: 10.1103/PhysRevA.26.3483. URL https://link.aps.org/doi/10.1103/PhysRevA.26.3483.

[33] G. Duffing. *Erzwungene Schwingungen bei veränderlicher Eigenfrequenz und ihre technische Bedeutung*. Sammlung Vieweg 41/42. Vieweg, 1918.

[34] A. Eckardt and E. Anisimovas. High-frequency approximation for periodically driven quantum systems from a Floquet-space perspective. *New Journal of Physics*, 17(9): 093039, Sept. 2015. ISSN 1367-2630. doi: 10.1088/1367-2630/17/9/093039. URL https://doi.org/10.1088/1367-2630/17/9/093039.

[35] A. Eckardt and E. Anisimovas. High-frequency approximation for periodically driven quantum systems from a Floquet-space perspective. *New Journal of Physics*, 17(9): 93039, sep 2015. doi: 10.1088/1367-2630/17/9/093039. URL https://doi.org/10.1088/1367-2630/17/9/093039.

[36] F. F. Fanchini and R. D. J. Napolitano. Continuous dynamical protection of two-qubit entanglement from uncorrelated dephasing, bit flipping, and dissipation. *Physical Review A*, 76(6), 2007. ISSN 10502947. doi: 10.1103/PhysRevA.76.062306. URL https://doi.org/10.1103/PhysRevA.76.062306.

[37] F. F. Fanchini, J. E. M. Hornos, and R. D. J. Napolitano. Continuously decoupling single-qubit operations from a perturbing thermal bath of scalar bosons. *Physical Review A*, 75(2), 2007. ISSN 10502947. doi: 10.1103/PhysRevA.75.022329. URL https://doi.org/10.1103/PhysRevA.75.022329.

[38] L. Faoro and L. B. Ioffe. Quantum two level systems and kondo-like traps as possible sources of decoherence in superconducting qubits. *Physical Review Letters*, 96(4), oct 2006. ISSN 10797114. doi: 10.1103/PhysRevLett.96.047001. URL https://doi.org/10.1103/PhysRevLett.96.047001.

[39] R. P. Feynman. Simulating physics with computers. *International Journal of Theoretical Physics*, 21(6):467–488, 1982. ISSN 1572-9575. doi: 10.1007/BF02650179. URL https://doi.org/10.1007/BF02650179.

[40] G. Floquet. Sur les équations différentielles linéaires à coefficients périodiques. *Annales scientifiques de l'École Normale Supérieure*, 12:47–88, 1883. ISSN 0012-9593. doi: 10.24033/ASENS.220. URL https://doi.org/10.24033/asens.220.

[41] K. M. Fonseca-Romero, S. Kohler, and P. Hänggi. Coherence stabilization of a two-qubit gate by ac fields. *Physical Review Letters*, (14). ISSN 00319007. doi: 10.1103/PhysRevLett.95.140502. URL https://link.aps.org/doi/10.1103/PhysRevLett.95.140502.

[42] P. Forni and A. Sarlette. Minimizing decoherence on target in bipartite open quantum systems. In *Proceedings of the IEEE Conference on Decision and Control*, volume 2019-Decem, pages 1369–1376. Institute of Electrical and Electronics Engineers Inc., dec 2019. ISBN 9781728113982. doi: 10.1109/CDC40024.2019.9029583. URL https://doi.org/10.1109/CDC40024.2019.9029583.

[43] P. Forni, A. Sarlette, T. Capelle, E. Flurin, S. Deleglise, and P. Rouchon. Adiabatic Elimination for Multi-Partite Open Quantum Systems with Non-Trivial Zero-Order Dynamics. In *Proceedings of the IEEE Conference on Decision and Control*, volume 2018-Decem, pages 6614–6619. Institute of Electrical and Electronics Engineers Inc., jan 2019. ISBN 9781538613955. doi: 10.1109/CDC.2018.8619205. URL https://doi.org/10.1109/CDC.2018.8619205.

[44] A. G. Fowler, M. Mariantoni, J. M. Martinis, and A. N. Cleland. Surface codes: Towards practical large-scale quantum computation. *Physical Review A*, 86(3):032324, sep 2012. ISSN 10502947. doi: 10.1103/PhysRevA.86.032324. URL https://journals.aps.org/pra/abstract/10.1103/PhysRevA.86.032324.

[45] J. Féjoz. *13. Introduction to KAM theory with a view to celestial mechanics*, pages 387–433. De Gruyter, 2017. doi: doi:10.1515/9783110430394-013. URL https://doi.org/10.1515/9783110430394-013.

[46] J.-M. Gambaudo and C. Tresser. How Horseshoes are Created. In E. Tirapegui and W. Zeller, editors, *Instabilities and Nonequilibrium Structures III*, Mathematics and Its Applications, pages 13–25. Springer, Dordrecht, 1991. doi: 10.1007/978-94-011-3442-2_2. URL https://link.springer.com/chapter/10.1007/978-94-011-3442-2_2.

[47] Y. Y. Gao, B. J. Lester, Y. Zhang, C. Wang, S. Rosenblum, L. Frunzio, L. Jiang, S. M. Girvin, and R. J. Schoelkopf. Programmable Interference between Two Microwave Quantum Memories. *Physical Review X*, 8(2), 2018. ISSN 21603308. doi: 10.1103/PhysRevX.8.021073. URL https://doi.org/10.1103/PhysRevX.8.021073.

[48] C. Gardiner, P. Zoller, and P. Zoller. *Quantum Noise: A Handbook of Markovian and Non-Markovian Quantum Stochastic Methods with Applications to Quantum Optics*. Springer Science & Business Media, Aug. 2004. ISBN 978-3-540-22301-6.

[49] R. Gautier, A. Sarlette, and M. Mirrahimi. Combined Dissipative and Hamiltonian Confinement of Cat Qubits. 2021. URL https://arxiv.org/abs/2112.05545.

[50] V. G. Gelfreich. Melnikov method and exponentially small splitting of separatrices. *Physica D: Nonlinear Phenomena*, 101(3-4):227–248, 1997. ISSN 01672789. doi: 10.1016/S0167-2789(96)00133-9. URL https://doi.org/10.1016/S0167-2789(96)00133-9.

[51] V. Gorini, A. Kossakowski, and E. C. Sudarshan. Completely positive dynamical semigroups of N-level systems. *Journal of Mathematical Physics*, 17(5):821–825, aug 1975. ISSN 00222488. doi: 10.1063/1.522979. URL https://aip.scitation.org/doi/abs/10.1063/1.522979.

[52] D. Gottesman. Class of quantum error-correcting codes saturating the quantum Hamming bound. *Physical Review A*, 54(3):1862–1868, sep 1996. ISSN 10941622. doi: 10.1103/PhysRevA.54.1862. URL https://journals.aps.org/pra/abstract/10.1103/PhysRevA.54.1862.

[53] D. Gottesman, A. Kitaev, and J. Preskill. Encoding a qubit in an oscillator. *Physical Review A*, 64(1):123101–1231021, aug 2001. ISSN 10502947. doi: 10.1103/PhysRevA.64.012310. URL https://doi.org/10.1103/PhysRevA.64.012310.

[54] M. Grifoni and P. Hänggi. Driven quantum tunneling. *Physics Reports*, 304(5-6):229–354, 1998. ISSN 03701573. doi: 10.1016/S0370-1573(98)00022-2. URL https://doi.org/10.1016/S0370-1573(98)00022-2.

[55] A. Grimm, N. E. Frattini, S. Puri, S. O. Mundhada, S. Touzard, M. Mirrahimi, S. M. Girvin, S. Shankar, and M. H. Devoret. Stabilization and operation of a Kerr-cat qubit. *Nature*, 584(7820):205–209, aug 2020. ISSN 14764687. doi: 10.1038/s41586-020-2587-z. URL https://www.nature.com/articles/s41586-020-2587-z.

[56] L. K. Grover. Framework for fast quantum mechanical algorithms. In *Conference Proceedings of the Annual ACM Symposium on Theory of Computing*, pages 53–62, New York, New York, USA, 1998. ACM. doi: 10.1145/276698.276712. URL http://portal.acm.org/citation.cfm?doid=276698.276712.

[57] J. Guckenheimer and P. Holmes. *Nonlinear Oscillations, Dynamical Systems, and Bifurcations of Vector Fields*. Applied Mathematical Sciences. Springer New York, 2002. ISBN 9780387908199.

[58] J. Guillaud and M. Mirrahimi. Repetition Cat Qubits for Fault-Tolerant Quantum Computation. *Physical Review X*, 91(4):041053, dec 2019. ISSN 21603308. doi: 10.1103/PhysRevX.9.041053. URL https://journals.aps.org/prx/abstract/10.1103/PhysRevX.9.041053.

[59] J. Guillaud and M. Mirrahimi. Error rates and resource overheads of repetition cat qubits. *Physical Review A*, 103(4), 2021. ISSN 24699934. doi: 10.1103/PhysRevA.103.042413. URL https://journals.aps.org/pra/abstract/10.1103/PhysRevA.103.042413.

[60] E. Hahn. Spin Echoes. *Physical Review*, 80(4):580–594, 1950. ISSN 0031-899X. doi: 10.1103/PhysRev.80.580. URL https://doi.org/10.1103/PhysRev.80.580.

[61] P. J. Holmes, J. E. Marsden, and J. Scheurle. Exponentially small splittings of separatrices with applications to KAM theory and degenerate bifurcations. *Hamiltonian Dynamical Systems*, 81:213–244, 1988. doi: 10.1090/conm/081/986267. URL https://authors.library.caltech.edu/20129/.

[62] B. A. Huberman, J. P. Crutchfield, and N. H. Packard. Noise phenomena in Josephson junctions. *Applied Physics Letters*, 37(8):750–752, oct 1980. ISSN 00036951. doi: 10.1063/1.92020. URL http://aip.scitation.org/doi/10.1063/1.92020.

[63] J. R. Johansson, P. D. Nation, and F. Nori. QuTiP 2: A Python framework for the dynamics of open quantum systems. *Computer Physics Communications*, 184(4):1234–1240, apr 2013. ISSN 00104655. doi: 10.1016/j.cpc.2012.11.019. URL https://doi.org/10.1016/j.cpc.2012.11.019.

[64] B. D. Josephson. Possible new effects in superconductive tunnelling. *Physics Letters*, 1(7):251–253, jul 1962. ISSN 00319163. doi: 10.1016/0031-9163(62)91369-0. URL https://doi.org/10.1016/0031-9163(62)91369-0.

[65] T. Kato. *Perturbation Theory for Linear Operators*, volume 132 of *Classics in Mathematics*. Springer Berlin Heidelberg, Berlin, Heidelberg, 1995. ISBN 978-3-540-58661-6. doi: 10.1007/978-3-642-66282-9. URL http://link.springer.com/10.1007/978-3-642-66282-9.

[66] E. M. Kessler. Generalized Schrieffer-Wolff formalism for dissipative systems. *Physical Review A*, 86(1):012126, jul 2012. ISSN 10502947. doi: 10.1103/PhysRevA.86.012126. URL https://journals.aps.org/pra/abstract/10.1103/PhysRevA.86.012126.

[67] R. Ketzmerick and W. Wustmann. Statistical mechanics of Floquet systems with regular and chaotic states. *Physical Review E*, 82(2), may 2010. doi: 10.1103/PhysRevE.82.021114. URL https://doi.org/10.1103/PhysRevE.82.021114.

[68] K. Khodjasteh and L. Viola. Dynamically error-corrected gates for universal quantum computation. *Physical Review Letters*, 102(8), 2009. ISSN 00319007. doi: 10.1103/PhysRevLett.102.080501. URL https://doi.org/10.1103/PhysRevLett.102.080501.

[69] K. Khodjasteh and L. Viola. Dynamical quantum error correction of unitary operations with bounded controls. *Physical Review A*, 80(3), 2009. ISSN 10502947. doi: 10.1103/PhysRevA.80.032314. URL https://doi.org/10.1103/PhysRevA.80.032314.

[70] K. Khodjasteh and L. Viola. Dynamical quantum error correction of unitary operations with bounded controls. *Physical Review A*, 80(3), 2009. ISSN 10502947. doi: 10.1103/PhysRevA.80.032314. URL https://doi.org/10.1103/PhysRevA.80.032314.

[71] M. Kjaergaard, M. E. Schwartz, J. Braumüller, P. Krantz, J. I-J Wang, S. Gustavsson, and W. D. Oliver. Superconducting Qubits: Current State of Play. *Annual Review of Condensed Matter Physics*, 11(1):369–395, 2020. doi: 10.1146/annurev-conmatphys-031119-050605. URL https://doi.org/10.1146/annurev-conmatphys-031119-050605.

[72] E. Knill, R. Laflamme, and W. H. Zurek. Resilient Quantum Computation. *Science*, 279(5349):342–345, jan 1998. ISSN 00368075. doi: 10.1126/science.279.5349.342. URL https://www.science.org/doi/abs/10.1126/science.279.5349.342.

[73] J. Koch, T. M. Yu, J. Gambetta, A. A. Houck, D. I. Schuster, J. Majer, A. Blais, M. H. Devoret, S. M. Girvin, and R. J. Schoelkopf. Charge-insensitive qubit design derived from the Cooper pair box. *Physical Review A*, 76(4):042319, oct 2007. ISSN 10502947.

doi: 10.1103/PhysRevA.76.042319. URL https://journals.aps.org/pra/abstract/10.1103/PhysRevA.76.042319.

[74] A. Kolmogorov. On the conservation of conditionally periodic motions under small perturbation of the hamiltonian. In *Dokl. Akad. Nauk. SSR*, volume 98, pages 2–3, 1954.

[75] N. M. Krylov and N. N. Bogoliubov. *Méthodes approchées de la mécanique non linéaire dans leur application à l'étude de la perturbation des mouvements périodiques et de divers phénomènes de résonance s'y rapportant.* Publié par l'Académie des sciences d'Ukraine, Kyiv, 1935.

[76] W.-J. Kuo and D. A. Lidar. Quadratic Dynamical Decoupling: Universality Proof and Error Analysis. *Physical Review A*, 84(4), jun 2011. doi: 10.1103/PhysRevA.84.042329. URL https://doi.org/10.1103/PhysRevA.84.042329.

[77] J. W. Lee, D. V. Averin, G. Benenti, and D. L. Shepelyansky. Model of a deterministic detector and dynamical decoherence. *Physical Review A*, 72(1), 2005. ISSN 10502947. doi: 10.1103/PhysRevA.72.012310. URL https://doi.org/10.1103/PhysRevA.72.012310.

[78] Z. Leghtas, G. Kirchmair, B. Vlastakis, R. J. Schoelkopf, M. H. Devoret, and M. Mirrahimi. Hardware-Efficient Autonomous Quantum Memory Protection. *Physical Review Letters*, 111(12):120501, Sept. 2013. doi: 10.1103/PhysRevLett.111.120501. URL https://link.aps.org/doi/10.1103/PhysRevLett.111.120501.

[79] Z. Leghtas, U. Vool, S. Shankar, M. Hatridge, S. M. Girvin, M. H. Devoret, and M. Mirrahimi. Stabilizing a Bell state of two superconducting qubits by dissipation engineering. *Physical Review A*, 88(2):023849, Aug. 2013. doi: 10.1103/PhysRevA.88.023849. URL https://link.aps.org/doi/10.1103/PhysRevA.88.023849.

[80] Z. Leghtas, S. Touzard, I. M. Pop, A. Kou, B. Vlastakis, A. Petrenko, K. M. Sliwa, A. Narla, S. Shankar, M. J. Hatridge, M. Reagor, L. Frunzio, R. J. Schoelkopf, M. Mirrahimi, and M. H. Devoret. Confining the state of light to a quantum manifold by engineered two-photon loss. *Science*, 347(6224):853–857, 2015. ISSN 10959203. doi: 10.1126/science.aaa2085. URL https://doi.org/10.1126/science.aaa2085.

[81] R. Lescanne, L. Verney, Q. Ficheux, M. H. Devoret, B. Huard, M. Mirrahimi, and Z. Leghtas. Escape of a Driven Quantum Josephson Circuit into Unconfined States. *Physical Review Applied*, 11(1), 2019. ISSN 23317019. doi: 10.1103/PhysRevApplied.11.014030. URL https://doi.org/10.1103/PhysRevApplied.11.014030.

[82] R. Lescanne, M. Villiers, T. Peronnin, A. Sarlette, M. Delbecq, B. Huard, T. Kontos, M. Mirrahimi, and Z. Leghtas. Exponential suppression of bit-flips in a qubit encoded in an oscillator. *Nature Physics*, 16(5):509–513, jul 2020. ISSN 17452481. doi: 10.1038/s41567-020-0824-x. URL https://doi.org/10.1038/s41567-020-0824-x.

[83] G. Lindblad. On the generators of quantum dynamical semigroups. *Communications in Mathematical Physics*, 48(2):119–130, 1976. ISSN 00103616. doi: 10.1007/BF01608499. URL https://link.springer.com/article/10.1007/BF01608499.

[84] J. Lisenfeld, A. Bilmes, S. Matityahu, S. Zanker, M. Marthaler, M. Schechter, G. Schön, A. Shnirman, G. Weiss, and A. V. Ustinov. Decoherence spectroscopy with individual two-level tunneling defects. *Scientific reports*, 6:23786, 2016. ISSN 2045-2322. doi: 10.1038/srep23786. URL https://doi.org/10.1038/srep23786.

[85] S. Lloyd and S. L. Braunstein. Quantum computation over continuous variables. *Physical Review Letters*, 82(8):1784–1787, feb 1999. ISSN 10797114. doi: 10.1103/PhysRevLett.82.1784. URL https://journals.aps.org/prl/abstract/10.1103/PhysRevLett.82.1784.

[86] W. Lohmiller and J. J. E. Slotine. On contraction analysis for non-linear systems. *Automatica*, 34(6):683–696, 1998. ISSN 00051098. doi: 10.1016/S0005-1098(98)00019-3. URL http://web.mit.edu/nsl/www/preprints/contraction.pdf.

[87] C. Macklin, K. O'Brien, D. Hover, M. E. Schwartz, V. Bolkhovsky, X. Zhang, W. D. Oliver, and I. Siddiqi. A near-quantum-limited Josephson traveling-wave parametric amplifier. *Science*, 350(6258):307–310, oct 2015. ISSN 10959203. doi: 10.1126/science.aaa8525. URL https://www.science.org/doi/10.1126/science.aaa8525.

[88] W. Magnus. On the exponential solution of differential equations for a linear operator. *Communications on Pure and Applied Mathematics*, 7(4):649–673, nov 1954. ISSN 10970312. doi: 10.1002/cpa.3160070404. URL http://doi.wiley.com/10.1002/cpa.3160070404.

[89] A. Metelmann and A. Clerk. Quantum-Limited Amplification via Reservoir Engineering. *Physical Review Letters*, 112(13):133904, apr 2014. doi: 10.1103/PhysRevLett.112.133904. URL https://link.aps.org/doi/10.1103/PhysRevLett.112.133904.

[90] A. Meurer, C. P. Smith, M. Paprocki, O. Čertík, S. B. Kirpichev, M. Rocklin, A. Kumar, S. Ivanov, J. K. Moore, S. Singh, T. Rathnayake, S. Vig, B. E. Granger, R. P. Muller, F. Bonazzi, H. Gupta, S. Vats, F. Johansson, F. Pedregosa, M. J. Curry, A. R. Terrel, v. Roučka, A. Saboo, I. Fernando, S. Kulal, R. Cimrman, and A. Scopatz. Sympy: symbolic computing in python. *PeerJ Computer Science*, 3:e103, Jan. 2017. ISSN 2376-5992. doi: 10.7717/peerj-cs.103. URL https://doi.org/10.7717/peerj-cs.103.

[91] T. Mikami, S. Kitamura, K. Yasuda, N. Tsuji, T. Oka, and H. Aoki. Brillouin-Wigner theory for high-frequency expansion in periodically driven systems: Application to Floquet topological insulators. *Physical Review B*, 93(14):144307, apr 2016. ISSN 24699969. doi: 10.1103/PhysRevB.93.144307. URL https://journals.aps.org/prb/abstract/10.1103/PhysRevB.93.144307.

[92] M. Mirrahimi, Z. Leghtas, V. V. Albert, S. Touzard, R. J. Schoelkopf, L. Jiang, and M. H. Devoret. Dynamically protected cat-qubits: A new paradigm for universal quantum computation. *New Journal of Physics*, 16, 2014. ISSN 13672630. doi: 10.1088/1367-2630/16/4/045014. URL https://doi.org/10.1088/1367-2630/16/4/045014.

[93] J. Moser. Convergent series expansions for quasi-periodic motions. *Mathematische Annalen*, 169(1):136–176, 1967. ISSN 00255831. doi: 10.1007/BF01399536. URL https://doi.org/10.1007/BF01399536.

[94] J. K. Moser. On the Theory of Quasiperiodic Motions. *SIAM Review*, 8(2):145–171, 1966. ISSN 0036-1445. doi: 10.1137/1008035. URL https://doi.org/10.1137/1008035.

[95] C. Müller, J. Lisenfeld, A. Shnirman, and S. Poletto. Interacting two-level defects as sources of fluctuating high-frequency noise in superconducting circuits. *Physical Review B*, 92(035442), 2015. doi: 10.1103/PhysRevB.92.035442. URL https://doi.org/10.1103/PhysRevB.92.035442.

[96] J. A. Murdock. On the Floquet Problem for Quasiperiodic Systems. *Proceedings of the American Mathematical Society*, 68(2):179–184, 1978. ISSN 0002-9939. doi: 10.2307/2041767. URL https://www.jstor.org/stable/2041767.

[97] Y. Nakamura, Y. A. Pashkin, and J. S. Tsai. Coherent control of macroscopic quantum states in a single-Cooper-pair box. *Nature*, 398(6730):786–788, 1999. ISSN 1476-4687. doi: 10.1038/19718. URL https://doi.org/10.1038/19718.

[98] A. I. Neishtadt. The separation of motions in systems with rapidly rotating phase. *Journal of Applied Mathematics and Mechanics*, 48(2):133–139, 1984. doi: 10.1016/0021-8928(84)90078-9. URL https://doi.org/10.1016/0021-8928(84)90078-9.

[99] G. A. Paz-Silva and D. A. Lidar. Optimally combining dynamical decoupling and quantum error correction. *Scientific reports*, 3:1530, 2013. ISSN 2045-2322. doi: 10.1038/srep01530. URL https://doi.org/10.1038/srep01530.

[100] A. Petrescu, M. Malekakhlagh, and H. E. Türeci. Lifetime renormalization of driven weakly anharmonic superconducting qubits. II. The readout problem. *Physical Review B*, 101(13), aug 2020. ISSN 24699969. doi: 10.1103/PhysRevB.101.134510. URL https://doi.org/10.1103/PhysRevB.101.134510.

[101] A. Petrescu, C. L. Calonnec, C. Leroux, A. Di Paolo, P. Mundada, S. Sussman, A. Vrajitoarea, A. A. Houck, and A. Blais. Accurate methods for the analysis of strong-drive effects in parametric gates. 2021. URL https://arxiv.org/abs/2107.02343.

[102] J. Preskill. Quantum Computing in the NISQ era and beyond. *Quantum*, 2:79, Aug. 2018. doi: 10.22331/q-2018-08-06-79. URL https://quantum-journal.org/papers/q-2018-08-06-79/.

[103] S. Puri, L. St-Jean, J. A. Gross, A. Grimm, N. E. Frattini, P. S. Iyer, A. Krishna, S. Touzard, L. Jiang, A. Blais, S. T. Flammia, and S. M. Girvin. Bias-preserving gates with stabilized cat qubits. *Science Advances*, 6(34):5901–5922, aug 2020. ISSN 23752548. doi: 10.1126/sciadv.aay5901. URL https://www.science.org/doi/full/10.1126/sciadv.aay5901.

[104] H. Qi, J. P. Dowling, and L. Viola. Optimal digital dynamical decoupling for general decoherence via Walsh modulation. *Quantum Information Processing*, 16(11):1–18, oct 2017. ISSN 1573-1332. doi: 10.1007/S11128-017-1719-3. URL https://link.springer.com/article/10.1007/s11128-017-1719-3.

[105] M. D. Reed, L. Dicarlo, B. R. Johnson, L. Sun, D. I. Schuster, L. Frunzio, and R. J. Schoelkopf. High-fidelity readout in circuit quantum electrodynamics using the jaynes-cummings nonlinearity. *Physical Review Letters*, 105(17):173601, oct 2010. ISSN

00319007. doi: 10.1103/PhysRevLett.105.173601. URL https://journals.aps.org/prl/abstract/10.1103/PhysRevLett.105.173601.

[106] F. Reiter and A. S. Sørensen. Effective operator formalism for open quantum systems. *Physical Review A*, 85(3):032111, mar 2012. ISSN 10502947. doi: 0.1103/PhysRevA.85.032111. URL https://journals.aps.org/pra/abstract/10.1103/PhysRevA.85.032111.

[107] R. K. Ritala and M. M. Salomaa. Odd and even subharmonics and chaos in RF SQUIDS. *Journal of Physics C: Solid State Physics*, 16(14):477, may 1983. ISSN 00223719. doi: 10.1088/0022-3719/16/14/008. URL https://iopscience.iop.org/article/10.1088/0022-3719/16/14/008.

[108] R. K. Ritala and M. M. Salomaa. Chaotic dynamics of periodically driven rf superconducting quantum interference devices. *Physical Review B*, 29(11):6143–6154, jun 1984. ISSN 01631829. doi: 10.1103/PhysRevB.29.6143. URL https://journals.aps.org/prb/abstract/10.1103/PhysRevB.29.6143.

[109] H. Sambe. Steady states and quasienergies of a quantum-mechanical system in an oscillating field. *Physical Review A*, 7(6):2203–2213, 1973. ISSN 10502947. doi: 10.1103/PhysRevA.7.2203. URL https://journals.aps.org/pra/pdf/10.1103/PhysRevA.7.2203.

[110] D. Sank, Z. Chen, M. Khezri, J. Kelly, R. Barends, B. Campbell, Y. Chen, B. Chiaro, A. Dunsworth, A. Fowler, E. Jeffrey, E. Lucero, A. Megrant, J. Mutus, M. Neeley, C. Neill, P. J. O'Malley, C. Quintana, P. Roushan, A. Vainsencher, T. White, J. Wenner, A. N. Korotkov, and J. M. Martinis. Measurement-Induced State Transitions in a Superconducting Qubit: Beyond the Rotating Wave Approximation. *Physical Review Letters*, 117(19):190503, nov 2016. ISSN 10797114. doi: 10.1103/PhysRevLett.117.190503. URL https://journals.aps.org/prl/abstract/10.1103/PhysRevLett.117.190503.

[111] A. Sarlette, P. Rouchon, A. Essig, Q. Ficheux, and B. Huard. Quantum adiabatic elimination at arbitrary order for photon number measurement. In *IFAC-PapersOnLine*, volume 53, pages 250–256, 2020. doi: 10.1016/j.ifacol.2020.12.131. URL https://www.sciencedirect.com/science/article/pii/S2405896320303876.

[112] W. M. Schmidt. *Diophantine Approximation*. Lecture Notes in Mathematics 785. Springer-Verlag Berlin Heidelberg, 1 edition, 1980. ISBN 3540097627,9783540097624. doi: 10.1007/978-3-540-38645-2. URL https://link.springer.com/book/10.1007/978-3-540-38645-2.

[113] A. Schnell, A. Eckardt, and S. Denisov. Is there a Floquet Lindbladian? *Physical Review B*, 101(10), sep 2020. ISSN 24699969. doi: 10.1103/PhysRevB.101.100301. URL https://doi.org/10.1103/PhysRevB.101.100301.

[114] A. Schnell, S. Denisov, and A. Eckardt. High-frequency expansions for time-periodic Lindblad generators. *Physical Review B*, 104(16):165414, Oct. 2021. doi: 10.1103/PhysRevB.104.165414. URL https://link.aps.org/doi/10.1103/PhysRevB.104.165414.

[115] D. I. Schuster, A. Wallraff, A. Blais, L. Frunzio, R. S. Huang, J. Majer, S. M. Girvin, and R. J. Schoelkopf. Ac Stark shift and dephasing of a superconducting qubit strongly coupled to a cavity field. *Physical Review Letters*, 94(12), aug 2005. ISSN 00319007. doi: 10.1103/PhysRevLett.94.123602. URL http://doi.org/10.1103/PhysRevLett.94.123602.

[116] Seth Lloyd. Universal Quantum Simulators. *Science*, 273(5278):1073–1078, 1996. URL http://www.jstor.org/stable/2899535.

[117] S. Shankar, M. Hatridge, Z. Leghtas, K. M. Sliwa, A. Narla, U. Vool, S. M. Girvin, L. Frunzio, M. Mirrahimi, and M. H. Devoret. Autonomously stabilized entanglement between two superconducting quantum bits. *Nature*, 504(7480):419–422, 2013. ISSN 1476-4687. doi: 10.1038/nature12802. URL https://doi.org/10.1038/nature12802.

[118] P. W. Shor. Polynomial-time algorithms for prime factorization and discrete logarithms on a quantum computer. *SIAM Review*, 41(2):303–332, aug 1999. ISSN 00361445. doi: 10.1137/S0036144598347011. URL https://doi.org/10.1137/S0036144598347011.

[119] C. Simó. Averaging under Fast Quasiperiodic Forcing. In J. Seimenis, editor, *Hamiltonian Mechanics: Integrability and Chaotic Behavior*, NATO ASI Series, pages 13–34. Springer US, Boston, MA, 1994. ISBN 978-1-4899-0964-0. doi: 10.1007/978-1-4899-0964-0_2. URL https://doi.org/10.1007/978-1-4899-0964-0_2.

[120] S. H. Strogatz. *Nonlinear Dynamics and Chaos: With Applications to Physics, Biology, Chemistry, and Engineering*. CRC Press, May 2018. ISBN 978-0-429-97219-5.

[121] K. Szczygielski and R. Alicki. Markovian theory of dynamical decoupling by periodic control. *Physical Review A - Atomic, Molecular, and Optical Physics*, 92(2):1–14, 2015. ISSN 10941622. doi: 10.1103/PhysRevA.92.022349. URL https://doi.org/10.1103/PhysRevA.92.022349.

[122] Y. Taur and P. L. Richards. Parametric amplification and oscillation at 36 GHz using a point-contact Josephson junction. *Journal of Applied Physics*, 48(3):1321–1326, mar 1977. ISSN 00218979. doi: 10.1063/1.323777. URL http://aip.scitation.org/doi/10.1063/1.323777.

[123] J. P. Tillich and G. Zemor. Quantum LDPC codes with positive rate and minimum distance proportional to the square root of the blocklength. *IEEE Transactions on Information Theory*, 60(2):1193–1202, 2014. ISSN 00189448. doi: 10.1109/TIT.2013.2292061. URL https://doi.org/10.1109/TIT.2013.2292061.

[124] B. van der Pol. VII. Forced oscillations in a circuit with non-linear resistance. (Reception with reactive triode). *The London, Edinburgh, and Dublin Philosophical Magazine and Journal of Science*, 3(13):65–80, jan 2009. ISSN 1941-5982. doi: 10.1080/14786440108564176. URL https://www.tandfonline.com/doi/abs/10.1080/14786440108564176.

[125] J. Venkatraman, X. Xiao, R. G. Cortiñas, and M. H. Devoret. On the static effective Hamiltonian of a rapidly driven nonlinear system. 2021.

[126] L. Verney, R. Lescanne, M. H. Devoret, Z. Leghtas, and M. Mirrahimi. Structural Instability of Driven Josephson Circuits Prevented by an Inductive Shunt. *Physical Review Applied*, 11(2), 2019. ISSN 23317019. doi: 10.1103/PhysRevApplied.11.024003. URL https://doi.org/10.1103/PhysRevApplied.11.024003.

[127] L. Viola. On Quantum Control via Encoded Dynamical Decoupling. *Physical Review A*, 66(November 2001):12, 2001. ISSN 1050-2947. doi: 10.1103/PhysRevA.66.012307. URL https://journals.aps.org/pra/abstract/10.1103/PhysRevA.66.012307.

[128] L. Viola and E. Knill. Robust dynamical decoupling of quantum systems with bounded controls. *Physical review letters*, 90(3):037901, jan 2003. ISSN 0031-9007. doi: 10.1103/PhysRevLett.90.037901. URL https://doi.org/10.1103/PhysRevLett.90.037901.

[129] L. Viola, E. Knill, and S. Lloyd. Dynamical Decoupling of Open Quantum Systems. *Physical Review Letters*, 82(12):2417–2421, 1999. doi: 10.1103/PhysRevLett.82.2417. URL http://link.aps.org/doi/10.1103/PhysRevLett.82.2417.

[130] U. Vool and M. Devoret. Introduction to quantum electromagnetic circuits. *International Journal of Circuit Theory and Applications*, 45(7):897–934, 2017. ISSN 1097-007X. doi: 10.1002/cta.2359. URL https://onlinelibrary.wiley.com/doi/10.1002/cta.2359.

[131] P. Wocjan. Efficient decoupling schemes with bounded controls based on Eulerian orthogonal arrays. *Physical Review A*, 73(6), 2006. ISSN 10502947. doi: 10.1103/PhysRevA.73.062317. URL https://doi.org/10.1103/PhysRevA.73.062317.

[132] Y. Wu and X. Yang. Strong-coupling theory of periodically driven two-level systems. *Physical Review Letters*, 98(1):013601, jan 2007. ISSN 00319007. doi: 10.1103/PhysRevLett.125.012701. URL https://journals.aps.org/prl/abstract/10.1103/PhysRevLett.98.013601.

[133] W. H. Zurek. Decoherence and the transition from quantum to classical. *Physics Today*, 44(10):36, 1991. ISSN 00319228. doi: 10.1063/1.881293. URL https://physicstoday.scitation.org/doi/10.1063/1.881293.

RÉSUMÉ

Vu la fragilité de l'information quantique, elle nécessite une intervention active afin de supprimer les erreurs logiques des ordinateur quantiques. Ceci a suscité le développement d'approches au niveau du hardware et contrôle, pour complémenter ou même faciliter les méthodes de correction d'erreurs quantiques. L'analyse de la dynamique des sytèmes quantiques contrôlés ou forcés se montre difficile pourtant, et caractériser leur points de fonctionnements s'avère souvent impossible sans l'aide des modèles réduits de la dynamique suffisamment raffinés. Cette thèse s'intéresse à deux approches de protection d'erreurs complémentaires, agissant uniquement au niveau du hardware.
La premiére approche a pour objectif le confinement d'un espace code composé d'états chats de Schrödinger d'un oscillateur quantique non linéaire, en le forçant de manière périodique. On définit le confinement des états chats à l'aide de la théorie de Floquet, et on characterise les différrents points de fonctionnement, ainsi que le comportement chaotique qui se présente, en fonction des paramètres du circuit et le forçage, de manière exhaustive. Par la suite on montre comment choisir les paramètres du circuit pour enlever le comportement chaotique dans son intégralité. L'oscillateur quantique considéré étant omniprésent dans le domaine des circuits supraconducteur, ces résultats devraient éliminer des limitations pertinentes des méthodes paramétriques de ce domaine le plus avancé des technologies quantiques.
La deuxième partie de cette thèse traite une approche nouvelle de protection d'erreurs des appareils quantiques concrets, en les considérant comme systèmes quantiques ouverts de manière explicite. On considère un système cible, couplé a un sous-système de son environnement bien défini, qui à la fois représente le mécanisme de relaxation principal pour la cible. On applique la méthodologie du "dynamical decoupling" de la manière suivante: forcer le sous-système de l'environnement afin de découpler la cible de celui-ci. Nous analysons cette nouvelle stratégie, du modèle à la figure de mérite, sur l'exemple omniprésent d'un système à deux niveaux. Comme contribution en terme de modèles réduits, une extension de la méthode d'élimination adiabatique à des systèmes périodiques et des sous-espaces d'états plus généraux est présentée. Ceci permet de combiner des approximations différentes par séparation d'échelle de temps (moyennisation, convergence rapide) sans devoir les hiérarchiser.

MOTS CLÉS

systémes dynamiques, chaos, théories des perturbations, circuits supraconducteurs, chats de Schrödinger, théorie de Floquet, élimination adiabatique, découplage dynamique

ABSTRACT

The vulnerability of quantum information to decoherence requires active intervention to prevent logical errors in a functioning quantum computer. This has led to the development of approaches countering noise from a hardware or control perspective that are complementary to, or facilitate code-based quantum error correction techniques. At the same time, difficulties arise in analyzing the dynamical behavior of controlled or driven quantum systems, and the characterization of their desired operating regimes requires reduced models of the dynamics at hand that are both refined and tractable. This dissertation presents a theoretical study of two complementary approaches to protect quantum information on a concrete, hardware-only level.
The first is the confinement of a computational manifold of Schrödinger cat states through the application of periodic drives to a quantum nonlinear oscillator, ubiquitous in the field of superconducting circuits. We describe the confinement of the cat states using the language of Floquet theory, and provide an exhaustive account of the different possible operating regimes, as well as of possible chaotic behavior of such systems as a function of circuit and drive parameters. Furthermore, we provide a practical recipe for the circuit parameters as to suppress the detrimental chaotic behavior, alleviating some of the current limitations of parametric engineering in superconducting circuits.
In the second part, we develop a novel approach for countering noise in practical quantum devices, explicitly considering them as open quantum systems. An elementary setting is considered in which a target system carrying quantum information is coupled to a small and identifiable environment subsystem that represents the main source of noise for the target. We extend the methodology of dynamical decoupling to propose the following: drive the environment subsystem such as to decouple it from the target. This strategy shows the main advantage that imprecisions of the driving do not directly deteriorate the information encoded in the target system. We analyze this novel strategy from model to figure of merit, on the benchmark example of a two-level system environment. The contribution towards model reduction consists of an extension of the method of adiabatic elimination to periodic systems and more general state spaces. This allows for combining different approximations based on timescale separations (such as averaging, and fast dissipative convergence) without having to order the different fast timescales, hence treating them on an equal footing.

KEYWORDS

Schrödinger cat states, Floquet theory, dynamical systems, chaos, adiabatic elimination, perturbation theory, superconducting circuits, dynamical decoupling